

University of Alberta
Department of Civil &
Environmental Engineering



Structural Engineering Report No. 196

Flexural Behavior of High Strength Concrete Columns

by
Hisham H.H. Ibrahim
and
J.G. MacGregor

March, 1994

Flexural Behavior of High Strength Concrete Columns

by

Hisham H.H. Ibrahim

J.G. MacGregor

Structural Engineering Report 196

Department of Civil and Environmental Engineering

University of Alberta
Edmonton, Alberta

March, 1994

Abstract

The use of high strength concrete (HSC) and ultra-high strength concrete (UHSC) has become more common in many reinforced concrete members. Most reinforced concrete design codes use equations that were based on tests using low strength concrete. The use of these equations for the design of HSC members may lead to unsafe design. Recent analytical work showed that the ACI rectangular stress block is unconservative for the design of HSC sections subjected to axial loads with small eccentricities. Other experimental work on the ductility of HSC columns concluded that the effect of confinement in the ductility of the concrete columns is reduced by increasing the concrete strength.

The experimental phase of this investigation involved testing 21 columns under the action of two applied loads in order to maintain zero strain at predetermined point through the test. The controlled parameters were concrete strength, shape of the cross-section, and confinement steel (diameter, spacing and volumetric ratio).

The analytical work included studying the flexural stress-strain relationships of HSC and UHSC sections and the effect of lateral confinement on the ductility of the section.

The validity of the ACI rectangular stress block for the design of rectangular and triangular HSC and UHSC sections was investigated using data from the tests reported here and previous tests, and new equations for the parameters of the ACI rectangular stress block are suggested.

Different analytical models that describe the behavior of confined HSC sections were compared with the test results. A modification of one of these models which gives a better fit to the test data is suggested. The parameters of the modified model are determined based on the concrete strength, section geometry and confining reinforcement.

Table of Contents

Chapter		Page
1-	Introduction	1
	1.1 General	1
	1.2 Statement of the Problems	1
	1.3 Objectives and Scope	2
	1.4 Thesis Arrangement	2
2-	Literature Review	3
	2.1 General	3
	2.2 Tests of C-Shaped Specimens	3
	2.2.1 Tests of Specimens with Plain Concrete Test Region	3
	2.2.2 Tests of Specimens with Reinforcement in the Test Region	6
	2.3 Empirical Models for the Stress-Strain Curve for HSC	9
	2.3.1 Model by Shah et al. (1983)	9
	2.3.2 Model by Muguruma et al. (1983), (1989)	10
	2.3.3 Model by Yong et al. (1988)	12
	2.3.4 Model by Bjerkeli et al. (1990)	14
3-	Experimental Program	21
	3.1 General	21
	3.2 Test Specimens	21
	3.2.1 Rectangular Specimens	21
	3.2.2 Triangular Specimens	21
	3.3 Materials	22
	3.3.1 Concrete	22
	3.3.1.1 Mix Constituents	22
	3.3.1.1.1 Cement	22
	3.3.1.1.2 Sand	22
	3.3.1.1.3 Coarse Aggregates	22
	3.3.1.1.4 Silica Fume	22
	3.3.1.1.5 Super-plasticizer	23
	3.3.1.2 Mix Properties	23
	3.3.1.3 Mechanical Properties	23
	3.3.1.3.1 Compression Tests of Cylinders	23

	3.3.1.3.2 Fracture Energy of Concrete	24
	3.3.2 Reinforcement	24
	3.4 Specimen Preparation	25
	3.5 Test Set-Up	26
	3.6 Test Method	27
	3.7 Test Arrangement	28
	3.8 Instrumentation	28
	3.9 Test Procedure	29
4-	Analysis of Test Results	54
	4.1 General	54
	4.2 Problems Encountered in Testing	54
	4.2.1 The Actual Position of the Neutral Axis	54
	4.2.2 Effect of Cracking on the Control System	56
	4.2.3 Concrete Cylinder Compression Tests	57
	4.2.4 P_2 Load Cell	58
	4.3 Plain Concrete Specimens	58
	4.3.1 Strain Gauge Configurations	58
	4.3.2 Strain Measurements	58
	4.3.2.1 Assumption of Linear Strain Distribution	58
	4.3.2.2 Poisson's Ratio	59
	4.3.2.3 Longitudinal Strain Distribution	59
	4.3.2.4 Transverse Strain Distribution on Compression Face	60
	4.3.2.5 Transverse Strain Distribution on Side Faces	61
	4.3.3 General Behavior and Failure Modes	61
	4.3.4 Moment about the Neutral axis	63
	4.3.5 Discussion of Post Peak Behavior of Concrete	63
	4.4 Reinforced Concrete Specimens	66
	4.4.1 Average Longitudinal strain	66
	4.4.2 General Behavior and Failure Modes	68
	4.4.3 Moment about the Neutral Axis	71
	4.4.4 Lateral Steel Requirements by the Code	73
5-	Design Parameters	103
	5.1 General	103
	5.2 Stress-Strain Relationship in Flexure	103
	5.2.1 Mathematical Approach	103

5.2.2	Accuracy of the Analysis	106
5.2.3	Comparison between different Stress-Strain Curves	107
5.2.4	Summary of the Stress-Strain Curves of the Specimens	108
5.3	Stress Block Parameters K_1 , K_2 , K_3 and ϵ_u	109
5.3.1	Rectangular Specimens	109
5.3.2	Triangular Specimens	110
6-	Flexural Stress-Strain Curves of the Confined Core	124
6.1	General	124
6.2	Behavior of the Concrete Cover	124
6.2.1	Previous Work	124
6.2.2	Observed Behavior of the Concrete Cover	125
6.2.3	Simplified Assumptions for the Behavior of the Cover	127
6.3	Mathematical Approach	127
6.4	Stress-Strain Curves of the Rectangular Specimens	128
6.5	Stress-Strain Curves of the Triangular Specimens	129
7-	Design Equations	135
7.1	General	135
7.2	Stress-Strain Relationships in Different Design Codes	135
7.2.1	US Code ACI 318-89 and Canadian Code CAN3-A23.3-M84	135
7.2.2	Norwegian Code NS 3473-1989	135
7.2.3	Finnish Code Rak MK4 1989	136
7.2.4	CEB/FIP Model MC90	136
7.3	Interaction Diagrams for Concrete Columns	136
7.4	Derivation of Factors for Use in the ACI Design Procedures	137
7.4.1	Structure to Cylinder Compression Strength Ratio, K_3	137
7.4.2	ACI Design Parameters of the Rectangular Stress Block	139
7.4.3	Proposed Parameters for the Rectangular Stress Block	141
7.4.4	Design of Triangular Compression Zones	142
7.4.5	Limiting Strain	143
7.5	Conclusions and Design Recommendations	144
8-	Modeling the Behavior of the Rectangular Specimens	158
8.1	General	158
8.2	Analytical Analysis	158

	8.2.1 Modeling of Concrete Cover and Concrete Core	158
	8.2.2 Method of Analysis	159
	8.3 Comparison between the Tests and the Calculated Behavior	160
	8.3.1 Maximum Moment Capacity	160
	8.3.2 Loading Path	161
	8.4 Modifications to the Model by Bjerkeli et al.	162
	8.4.1 Reviewing the Equations of the Model	162
	8.4.2 Reasons for Modifications	164
	8.4.3 Discussion and Suggested Modifications for some of the Equations	164
	8.5 Comparison between the Tests and the Modified Model	166
	8.6 Equations of the Modified Model for Confined Concrete	167
9-	Summary, Conclusions and Recommendations	180
	9.1 Summary	180
	9.2 Conclusions	180
	9.3 Recommendations for Future Study	183
	References	184
Appendix	A Derivation of Equations 5.9 and 5.10 for Triangular Specimens	190
Appendix	B Procedures for obtaining the Stress-Strain Curves of the Rectangular Cross-Sections	193
Appendix	C Data from Eccentrically Loaded Plain and Reinforced Concrete Columns	194

List of Tables

Table	Page
3.1 Details of the Rectangular Specimens	30
3.2 Details of Cross-Section for the Rectangular Specimens	31
3.3 Details of the Triangular Specimens	32
3.4 Cement Composition	33
3.5 Sand Composition	34
3.6 Coarse Aggregates Composition	34
3.7 Mix Designs	35
3.8 Results of Concrete Tests for the Rectangular Specimens	36
3.9 Results of Concrete Tests for the Triangular Specimens	37
3.10 Properties of Reinforcement Steel	38
3.11 Eccentricities of Applied Loads for Each Specimens	39
4.1 Neutral Axis Depth of Different Specimens	74
5.1 Stress Block Parameters for the Rectangular Specimens	112
5.2 Stress Block Parameters for the Triangular Specimens	113
7.1 The Stress Block Parameters of the Norwegian Code NS 3473-1989	145
7.2 Data Required to Generate the Stress-Strain Diagram of the CEB/FIP Model MC90	145
8.1 Maximum Moment Capacity @ the C.L	168
8.2 Maximum Moment Capacity @ the N.A	169
8.3 Comparison of Modified Model to Test Values of Maximum Moment Capacity @ the C.L	170
8.4 Comparison of Modified Model to Test Values of Maximum Moment Capacity @ the N.A	170

List of Figures

Figure	Page
2.1 C-Shaped Specimen of Hognestad et al.	17
2.2 Stress-Strain Curves for Plain Concrete by Shah et al.	18
2.3 Idealized Stress Strain Curves by Murguma et al.	18
2.4 Empirical Model by Yong et al.	19
2.5 Empirical Model by Bjerkeli et al.	19
2.6.a Vertical section	
Compressive arches between the confinement reinforcement layers	20
2.6.b Horizontal section	
Compressive arches between longitudinal bars	20
2.6.c Idealized "confining pressure" f_r	20
3.1 Concrete Dimensions for the Rectangular Specimens	40
3.2 Details of Reinforcement for the Rectangular Specimens	41
3.3 Concrete Dimensions for the Triangular Specimens	42
3.4 Details of Reinforcement for the Triangular Specimens	43
3.5 Cylinder Compression Test	44
3.6 Stress-Strain Curves for 100 mm Cylinders	44
3.7 Details of Notched Beam Test	45
3.8 Stress Strain Curves for No.10 Bar	46
3.9 Stress Strain Curves for No.15 Bar	46
3.10 Stress Strain Curves for No.8 Bar	47
3.11 Assembling of the Steel Cage for Specimen T3 on the Floor	47
3.12 Placing of the Steel Cage of Specimens V16 inside the Form	48
3.13 Details of Test Measurements	49
3.14 Details of Test Set-up	50
3.15 Cylinder Compression Tests with Different Rate of Loading	51
3.16 Details of LVDT Locations	52
3.17 Test Set-Up for the Rectangular Specimens	53
3.18 Test Set-Up for the Triangular Specimens	53
4.1 Strain Gauge Configuration on the Back Face of the Specimens	75
4.2 Readings of the Strain Gauges on the Back Face of Specimen T1	76
4.3 Neutral axis Depth of Specimen V8	76
4.4 Neutral Axis Depth of Specimen V1	77
4.5 Neutral Axis depth of Specimen T1	77

4.6	Neutral Axis Depth of Specimen V2	78
4.7	Calibration Equations for P₂ Load Cell	78
4.8	Strain Gauge Configurations for Specimen V4	79
4.9	Strain Gauge Configurations for Specimen V5	80
4.10	Strain Gauge Configurations for Specimen V6	81
4.11	Strain Gauge Configurations for Specimens T1 and T4	82
4.12	Strain Distribution for Specimen V4	83
4.13	Strain Distribution for Specimen V6	83
4.14	Strain Distribution for Specimen T4	83
4.15	Poisson's Ratio Calculated at Different Locations for Specimen V5	84
4.16	Average Poisson's Ratio	84
4.17	Longitudinal Strain Distribution at the Compression Face of Specimen V4 Using the 4 in. Gauges	85
4.18	Longitudinal strain Distribution at the Compression Face of Specimen V4 Using the 1 in. Gauges	86
4.19	Longitudinal Strain Distribution at the Back Face of Specimen V4	86
4.20	Transverse Strain Distribution at the Right Side of the Compression Face of Specimen V5	87
4.21	Transverse Strain Distribution at the Left Side of the Compression Face of Specimen V5	87
4.22	Transverse Strain at 100 mm from the Back Face of Specimen V5	88
4.23	Transverse Strain at 150 mm from the Back Face of Specimen V5	88
4.24	Transverse Strain at 200 mm from the Back Face of Specimen V5	88
4.25	Transverse Strain Distribution on the Side Faces of Specimen V5 near Failure	89
4.26	Side Face of Specimen V5 after Testing	90
4.27	Compression Face of Specimen V6 after Testing	90
4.28	Normalized Moment about the Neutral Axis for the Rectangular Specimens	91
4.29	Moment about the Neutral Axis for the Triangular Specimens	91
4.30	Average Longitudinal Strain at the Compression Face of Specimen V11	92
4.31	Average Longitudinal Strain at the Back Face of Specimen V11	92
4.32	Compression Face of Specimen V11 after Testing	93
4.33	Compression Face of Specimen V17 after Testing	93
4.34	Compression and Side Faces of Specimen V7 after Testing	94
4.35	Compression and Side Faces of Specimen V12 after Testing	94
4.36	Compression and Side Faces of Specimen V15 after Testing	95

4.37	Tension Cracks and Spalling of the Cover at the Back Face of Specimen V15	95
4.38	Compression and Side Faces of Specimen V16 after Testing	96
4.39	Cracks Appear in the Side and the Back Faces of Specimen V16	96
4.40	View from the Tip of Specimen T5 after Testing	97
4.41	Side View of Specimen T5 after Testing	97
4.42	Normalized Moment about the Neutral Axis for the Rectangular Specimens	98
4.43	Normalized Moment about the Neutral Axis for the Triangular Specimens	99
4.44	Effect of Increasing the Volumetric Ratio of Confinement Reinforcement	100
4.45	Effect of Tie Spacing on the Normalized Moment	100
4.46	Effect of Testing Method	101
4.47	Effect of Changing Neutral axis Position	101
4.48	Effect of Section Geometry	102
5.1	Measured and Calculated Loads for Specimens V1 and V16	114
5.2	Measured and Calculated Moments for Specimens V1 and V16	114
5.3	Measured and Calculated Loads for Specimens T1 and T5	115
5.4	Measured and Calculated Moments for Specimens T1 and T5	115
5.5	Stress-Strain Curves for Specimen V6	116
5.6	Stress-Strain Curves for Specimen V14	116
5.7	Stress-Strain Curves for Specimen T1	117
5.8	Stress-Strain Curves for Specimen T4	117
5.9	Stress-Strain Curves for Specimen T2	118
5.10	Stress-Strain Curves for Specimen T6	118
5.11	Stress-Strain Curves for the HSC Rectangular Specimens	119
5.12	Stress-Strain Curves for the UHSC Rectangular Specimens	119
5.13	Stress-Strain Curves for the Triangular Specimens	120
5.14	Stress Block Parameters for the Rectangular Sections	121
5.15	Stress Block Parameters for the Triangular Specimens	122
5.16	Details of the Cross-Section of the Triangular Specimens	123
6.1	Strain Gauges at the Left Side of the Compression Face of V13	130
6.2	Strain Gauges at the Right Side of the Compression Face of V13	130
6.3	Strain Gauges at 200 mm from the Zero Strain Face of V13	131
6.4	Boundaries between Concrete Cover and Concrete Core for the Rectangular Specimens	132
6.5	Boundaries between Concrete Cover and Concrete Core for the Triangular Specimens	132

6.6	Stress-Strain Curves of the Confined Core of the HSC Rectangular Specimens	133
6.7	Stress-Strain Curves of the Confined Core of the UHSC Rectangular Specimens	133
6.8	Stress-Strain Curves of the Confined Core of the HSC Triangular Specimens	134
6.9	Stress-Strain Curves of the Confined Core of the UHSC Triangular Specimens	134
7.1	Schematic Stress-Strain Diagram for the Norwegian Code NS 3473-1989	146
7.2	Stress-Strain Diagram for the Finnish Code Rak MK4 1989	147
7.3	Stress-Strain Diagram for Uniaxial Compression MC90	147
7.4	Interaction Diagrams of Different Design Codes	148
7.5	Values of K_3 from Tests of C-Shaped Specimens	149
7.6	Values of K_3 from Tests of Concentrically Loaded Columns	149
7.7	ACI Normalized Interaction Diagram for Rectangular Plain Concrete Sections	150
7.8	Tests of the C-Shaped Specimens Compared with the ACI Code	151
7.9	Mean Values of δ versus the Concrete Strength	151
7.10	Proposed Equation for $\beta_1/2$ Compared to Tests of C-Shaped Specimens	152
7.11	Proposed Equation for α_1 Compared to Tests of Concentrically Loaded Columns	152
7.12	Equations for $\alpha_1\beta_1$ Compared to Tests of C-Shaped Specimens	153
7.13	Tests of the C-Shaped Specimens Compared with U of A	154
7.14	Mean Value of δ versus the Compression Strength	154
7.15	Tests of Specimen V8 with Compression Strength of 129.3 MPa	155
7.16	Tests of Specimen V13 with Compression Strength of 72.5 MPa	155
7.17	ACI Normalized Interaction Diagram for Triangular Plain Concrete Sections	156
7.18	Values of δ for the Triangular Specimens versus the Compression Strength	157
8.1	Calculations of the Lateral Deflection of the Specimen	171
8.2	Flow Chart of the Computer Analysis	172
8.3	Test and Calculated Behavior of Specimen V13	173
8.4	Test and Calculated Behavior of Specimen V15	173
8.5	Test and Calculated Behavior of Specimen V16	174
8.6	Test and Calculated Behavior of Specimen V17	174
8.7	Test and Calculated Behavior of the Modified Model for V1	175

8.8	Test and Calculated Behavior of the Modified Model for V7	175
8.9	Test and Calculated Behavior of the Modified Model for V8	176
8.10	Test and Calculated Behavior of the Modified Model for V11	176
8.11	Test and Calculated Behavior of the Modified Model for V12	177
8.12	Test and Calculated Behavior of the Modified Model for V13	177
8.13	Test and Calculated Behavior of the Modified Model for V15	178
8.14	Test and Calculated Behavior of the Modified Model for V16	178
8.15	Test and Calculated Behavior of the Modified Model for V17	179

List of Symbols

a_1	eccentricity of the primary load measured from the neutral axis position
a_2	eccentricity of the secondary load measured from the neutral axis position
a_{si}	horizontal distance from the position of the neutral axis to the vertical center line of each reinforcement bar
A_c	the core area enclosed by the center line of the outer tie
A_{sh}	total effective area of ties in direction under consideration
A_{si}	cross-section area of each reinforcement bar
b	width of the rectangular cross-section
b	width of the base of the triangular cross-section
B	width of the concrete core of the rectangular cross-section measured from the center line
c	center to center distance between the longitudinal bars
C	total applied loads during the test
C_c	loads carried by the concrete section only
d_{so}	shorter out-to-out of ties
E_c	modulus of elasticity for concrete in compression
E_o	secant modulus of elasticity at the peak stress
f_u	stress at the less strained fibers during the test
f_c	compressive stress in plain concrete section
f_c	calculated compressive stress at the most compressed fibers during the test
f_c'	cylinder compressive strength of concrete at the time of testing
f_{cy}	stress value at the horizontal part of the descending branch of confined concrete section
f_o	loads carried by the concrete section during the test divided by the area of the cross-section
f_r	lateral confining pressure in the concrete
f_u	stress carried by each reinforcement bar
f_y	yield stress of confining reinforcement
f_u	peak stress of confined concrete section
h	depth of the rectangular or triangular cross-sections
h_t	actual depth of the tested triangular cross-section
h'	out-to-out of ties in the direction under consideration
H	depth of the concrete core of the rectangular cross-section measured from the center line

K_1	ratio of the average compressive stress to the maximum compressive stress
K_2	ratio of distance between the extreme fiber and the resultant of compressive stress to distance between the extreme fiber and the neutral axis
K_{2t}	value of K_2 obtained from the test of triangular cross-section
K_3	ratio of the maximum compressive stress to the cylinder strength
K_g	geometry factor
K_{g1}	geometry factor associated with the development of vertical arches
K_{g2}	geometry factor associated with the development of horizontal arches
m_o	moments carried by the concrete section during the test divided by the area times the depth of the cross-section
M	total applied moments during the test
M_c	moments carried by the concrete section only
n	number of laterally supported longitudinal bars
(n, m)	coordinates of different points in the normalized interaction diagram
(n_t, m_t)	coordinates of the test point, R_t , in the normalized interaction diagram
R_c	point in the normalized interaction diagram that has the same slope angle of the test point R_t
R_t	point that represent the maximum capacity of each specimen plotted in the normalized interaction diagram
s_p	spacing between ties
P_1	primary load during testing
P_2	secondary load during testing
z	slope of the descending branch of the stress-strain curve
α_1	ratio of the maximum compressive stress to the cylinder strength according to the ACI code
β_1	depth of the equivalent rectangular stress block according to the ACI code
δ	percentage ratio of the difference between the test point, R_t , and the point in the normalized interaction diagram with the same slope angle, R_c , to the point, R_c
δ	percentage ratio of the difference between the calculated and test values of maximum capacity to the test values of maximum capacity
ϵ	compressive strain in concrete
$\epsilon_{.85}$	strain value at $0.85 f_c$ for confined concrete section
$\epsilon'_{.85}$	strain value at $0.85 f_c'$ for plain concrete
ϵ_c	measured strain at the most compressed fibers during the test

ϵ_u	strain value corresponding to the maximum moment obtained about the neutral axis during each test
ϵ_s	strain value at the peak stress
σ	compressive stress in confined concrete section
θ	slope angel of the point that represent the maximum capacity of the specimen in the normalized interaction diagram, R_t
ζ	ratio of the neutral axis depth to the cross-section depth
ζ_c	ratio of the neutral axis depth to the cross-section depth for the point, R_c , in the interaction duagram
ζ_t	ratio of the neutral axis depth to the cross-section depth for the test point , R_t

1- Introduction

1.1 General

The use of high strength concrete and ultra-high strength concrete (HSC up to 100 MPa, UHSC higher than 100 MPa) has become more common in reinforced concrete members where the design is mainly governed by the cross-section strength rather than the serviceability requirements. This includes heavily loaded reinforced concrete columns, medium and long span bridges and special structures such as off shore oil platforms. Most reinforced concrete design codes use equations including empirical constants for the design of structural members. These equations are based on tests using low strength concrete. During the last few years extensive experimental and analytical work has been carried out using high strength concrete. Empirical expressions to substitute in some of the currently used relationships have been proposed. More work is required to better understand the behavior of HSC.

1.2 Statement of the Problems

In North America design of reinforced concrete for flexure is based on a rectangular compression stress block. Garcia et al. (1990) suggest that the ACI rectangular stress block is unconservative by up to 12% for the design of HSC rectangular sections subjected to axial loads with small eccentricities. The results of this analytical work are based on stress-strain curves of concentrically loaded cylinders with a peak stress equal to $0.85 f'_c$. The code equations were based on tests by Kaar et al. (1978a) and Nedderman (1973), where the sections were subjected to axial forces with small eccentricities. Garcia et al. (1990) and Leslie et al. (1976) have proposed non-rectangular stress blocks for design of HSC sections. Swartz et al. (1985) and Leslie et al. (1976) suggest that the code value of 0.003 for the ultimate compressive strain is not conservative for design of HSC sections.

Mattock et al. (1961) conducted a test series on low strength concrete beams with triangular compression zones. They concluded that the use of the ACI rectangular stress block yields a sufficiently accurate estimate of the ultimate strength of these beams. There is no experimental work on HSC specimens to support this conclusion. It is important to check whether a full stress block could be developed after the tip reached high strains.

Bjerkeli et al. (1990), Yong et al. (1988), and Mugaruma et al. (1988) studied the ductility of HSC columns. Most of the tested columns were concentrically loaded. They concluded that the effect of confinement in the ductility of the concrete columns is reduced by increasing the concrete strength. They proposed analytical models to calculate

the behavior of the confined sections. This work needs to be extended for eccentrically loaded columns where the sections are subjected to strain gradient.

1.3 Objectives and Scope

The experimental program was designed to study the validity of the rectangular stress block for the design of rectangular and triangular HSC and UHSC sections.

To achieve these goals, 21 C- shaped specimens were tested. The program included two phases, the first phase consisted of tests of 15 rectangular cross-section specimens, the second phase consisted of tests of 6 triangular cross-section specimens. The rectangular specimens included 3 plain concrete specimens while the triangular specimens included 2 plain concrete specimens. Plain and reinforced concrete specimens were also used to study the mechanical properties of HSC and UHSC eccentrically loaded members. The reinforced concrete specimens were also used to study the ductility of HSC and UHSC columns subjected to eccentric loads.

The specimens were subjected to the action of two applied loads in order to maintain zero strain at a predetermined point during each test. The main variables were concrete strength, shape of the cross-section, and confinement steel (diameter, spacing and volumetric ratio). The study was limited to relatively low longitudinal and confinement reinforcement ratios.

Data from previous test series tested elsewhere were used together with the results of this experimental work in order to check the code design equations.

1.4 Thesis Arrangement

Chapter 2 of the thesis includes a literature review of tests conducted on C-shaped specimens. It also includes a review of HSC column tests and the analytical models that describe the behavior of HSC sections. Chapter 3 gives a description of the specimens, materials and procedures used in the experimental work. Chapter 4 gives details of strain measurements, behavior of specimens during the test and the different failure modes. Chapter 5 presents the flexural stress-strain curves prior to spalling of the concrete cover and the stress block parameters for different specimens. Chapter 6 presents stress-strain curves of the confined core. Chapter 7 discusses the ACI design equations and new equations are proposed for the rectangular stress block parameters. Chapter 8 investigates the reliability of different analytical models in predicting the behavior of the rectangular specimens. A modified model is proposed. Chapter 9 summarizes the work done in this investigation, states the main conclusions and gives recommendations for future study.

2- Literature Review

2.1 General

Hognestad et al. (1955) published a pioneering work on the flexural stress distribution in the compression zone of reinforced concrete members. The specimens of Hognestad et al. had a C-shape in elevation. That is, they consisted of a vertical test column with horizontal loading arms at each end. Loads were applied axially and at the ends of the arms. Since then many other researchers adopted the same testing method. A summary of different test series that included testing of C-shaped specimens is presented in Section 2.2. For each test series, brief details of dimensions of the specimens, the parameters studied, test set-ups, test procedures and test readings are given. Methods of analysis that were used in each investigation to calculate the stress-strain relationship and the rectangular stress block parameters of the specimens are discussed during the analysis presented in Chapters 5 and 6.

Numerous papers have been published describing the stress strain behavior of plain concrete with low, medium or high strength (among them are Wang et al. (1978), Carreria et al. (1985) and Carraquillo et al. (1981)). The effect of using spiral reinforcement on the stress-strain characteristics of low, medium or high strength concrete was studied by many researchers such as (Priestley et al. (1981), Martinez (1983) and Ahmad et al. (1982)). The effect of using rectilinear reinforcement on the stress-strain relationship of low and medium strength concrete was described by (Sargin et al. (1971), Valienas et al. (1977), Sheikh et al. (1982) and Park et al. (1982)). In the recent years, many researchers have extended this work to high strength concrete. In Section 2.3, a summary of published tests of rectilinearly confined high strength concrete, as well as the proposed analytical models are presented. The section includes also the work by Shah et al. (1983) that describes the stress-strain relationship of plain concrete. This model is used in the analysis in Chapter 8.

A summary of the current codes that do allow design for high strength concrete sections is presented in Chapter 7 of the analysis. Different theories that explain post peak behavior of concrete in compression are discussed in Section 4.3.5.

2.2 Tests of C-Shaped Specimens

2.2.1 Tests of Specimens with Plain Concrete Test Region

Hognestad et al. (1955) used C-shaped specimens as shown in Figure 2.1. By applying a major thrust P_1 by a testing machine and a minor thrust P_2 that could be varied independently of P_1 , the position of the neutral axis was kept constant at one face of the

central test region throughout the test. The total number of the specimens was 20. The cylinder strength f'_c ranged between 5 and 52.5 MPa. The testing ages were 7, 14, 28 and 90 days. The specimens were cast horizontally and tested vertically. The test region was plain concrete with cross-sectional dimensions of 5x8 in. (127x203 mm) and a height of 16 in. (406 mm). The end brackets had enough reinforcement to obtain failure in the central unreinforced test region. The specimens and their companion cylinders were tested dry.

The major load P_1 was applied through a 3/16 in. steel roller at a constant rate from zero to failure. The minor load P_2 was applied by a hydraulic jack through one or two tie rods and was measured by a calibrated electric strain gauges on the tie rods. By operating a hydraulic pump, the tie rod force was adjusted continuously so that the strain at the neutral face was maintained at zero within ± 5 microstrain. The relative position of the P_1 and P_2 as well as the stiffness of the tie rod by which P_2 was applied were chosen so that no uncontrolled release of strain energy would take place. Strains were measured by two 6 in. electric strain gauges at the neutral face, two similar gauges at the compression face and one similar gauge at mid depth of each of the two side faces. The deflection at mid height was measured by a dial gage so that the eccentricities of the thrust were known at any load level. The test duration was about 15 minutes.

Nedderman (1973) conducted an experimental program using C-shaped specimens similar in dimensions to those tested by Hognestad et al. The total number of the specimens was 13 with cylinder strength f'_c ranging between 79.2 and 97.5 MPa. In some cases, the load capacity of the cylinders exceeded that of the testing machine. In those cases, the load was held constant until the cylinder failed. However, it was felt that the cylinders were very close to failure when the maximum capacity of the testing machine was reached. The testing ages were 57 and 63 days. Due to problems during testing, only 9 specimens could be tested successfully. Because the end brackets had no reinforcement, large clamps made with 1/2 in. round steel bars and 3/4 in. thick plates were used as an auxiliary reinforcement in order to have failure in the test region. The specimens and their companion cylinders were tested dry.

The load P_1 was applied by a Tinius Olsen 400,000 lb capacity testing machine in increments that became smaller close to failure. The load from the testing machine was transmitted to the specimen by a ball and socket loading head attached to the testing machine and a bearing plate which rested on the top of the specimen. After troubles with this boundary condition during the first few tests, the major load P_1 was distributed from the ball and socket loading head to the specimen through a 3/8 in. thick masonite pad and 50 in.² aluminum plates. The load P_2 was applied by means of 60,000 lb hydraulic jack

through four 3/4 in. round steel rods and measured by means of a pressure dial gauge attached to the jack. Strains were measured using electrical strain gauges. The location and the gauge length of these gauges were identical to the test of Hognestad et al. Eccentricity of the load due to curvature of the specimen or poor end bearing generally resulted in a strain difference between the gauges on the neutral face of approximately 50 microstrain, however the average strain in that face was maintained at zero during the test. The test duration was between 30 to 45 minutes.

Kaar et al. (1978a) conducted an experimental program using C-shaped specimens similar in dimensions to those tested by Hognestad et al. The test series included 19 specimens made from normal weight aggregates with cylinder strength f'_c ranging from 44.8 to 102.4 MPa and 15 specimens made from light weight aggregates with cylinder strength f'_c ranging from 24.5 to 86.1 MPa. For each group of specimens, the controlled variables were concrete strength and type of coarse aggregates. The specimens were cast horizontally and tested vertically.

The major load P_1 was applied by a testing machine having 1-million-lb capacity through a system of bearing plates and rollers that accommodated rotation of the specimen during testing. The minor load P_2 was applied by a hydraulic ram through a system of rods, cross heads and rollers. During the test, the major load P_1 was increased at a constant rate and the minor load P_2 was controlled manually so that the strain at the neutral face was kept to zero. Strains were measured at mid height of the test section by 2.5 in. electrical strain gauges mounted in locations identical to those of Hognestad et al. A direct current differential transformer (DCDT) was used to monitor the deflection of the test section relative to the ends.

Swartz et al. (1985) tested 10 C-shaped specimens. One of the specimens had cross-sectional dimensions of 5x8 in. and nine had cross-sectional dimensions of 5x5 in. The cylinder strength f'_c of 3x6 in. cylinders ranged between 57.8 and 77.03 MPa. The testing ages were 47, 52 and 60 days. Specimens were cast in the horizontal position and tested vertically. The end brackets had enough reinforcement to obtain failure in the central unreinforced section. One of the specimens failed in tension while being placed in the machine and could not be tested, another specimen was cracked prior to testing. The specimens and their companion cylinders were tested dry.

The primary load P_1 was applied by 1.34 MN Emery-Tammall testing machine. The secondary load P_2 was applied using a hand-operated hydraulic jack. Because of the type of testing equipment used, and because of the complexity of the set-up, it was necessary to apply loads to failure in a load controlled manner. Strains were measured using 10 strain gauges for each specimen. Two of the strain gauges were mounted on the neutral face, six

gauges were mounted on the side faces and two gauges were mounted on the compression face. The strain gauges had a gauge length of 2.4 in. for two of the specimens, and 0.7 in. for the rest of the specimens. The testing procedure was to apply an increment of load P_1 , maintain this and apply load P_2 while monitoring the two strain gauges on the tension face. When they read zero on average, the load P_2 was maintained while the other strain readings were taken. The testing time was typically 30 min.

2.2.2 Tests of Specimens with Reinforcement in the Test Region

Soltman et al. (1967) tested 16 reinforced specimens. All of the specimens had cross-sectional dimensions of 4x6 in. except for two specimens that had cross-sectional dimensions of 3x6 and 5x6 in. respectively. The specimens had a prismatic shape with a total height of 52 in. and a central test region of 20 in. Two steel brackets fixed to the enlarged ends of the specimens were used to apply the minor load P_2 . Each bracket was composed of two 6 in. steel channel beams, each welded to 16x12x3/4 in. steel plate fixed to the test specimen using six 7/8 in. bolts. The specimens had no concrete cover except for two specimens. The main variables were spacing, size and type of transverse reinforcement, shape of the cross-section and thickness of the concrete cover. The concrete strength was not mentioned in the published paper.

The major load P_1 was applied by means of a 100 ton hollow-ram jack reacting against the laboratory floor. The load was measured by a 100 ton load cell placed against the cross-beam of a 60 ton test frame. The load was transferred to the concrete specimen through two parallel knife-edge supports to allow for freedom of rotation of the specimen in the plane of the applied moment. The minor load P_2 was applied to the brackets by jacking against a 7/8 in. diameter MacAlloy high-tensile steel bar. A 30 ton hollow-ram jack was used to apply the load and a 5 ton load cell to measure the load applied. The jack and the load cell were seated on two supporting units that allowed for unrestrained rotation of the tie-bar with respect to the brackets. The weight of the minor load arrangement was taken off the ends of the specimen by a counterweight connected to the brackets by steel cables passing over a set of pulleys.

Four 60 mm polyester-base electric strain gauges were used to determine the position of the neutral axis. Five mechanical demountable strain gauges were used to measure the strains along each side of the specimen. Two clinometers were placed on the top of the brackets to measure the total rotation of the specimen. Three deflection gauges 6 in. apart were used to measure the deflection at three points along the test region. The method of loading adopted was based upon maintaining the position of the neutral axis constant through the entire range of loading. The major load P_1 was applied in twelve

increments. The first four increments were made equal to 15% of the calculated load; the remaining increments were 5% each. Each increment was applied during a period of 15 min., about 4 min. for the application of the load and the rest for taking the instrument readings. After the first sign of crushing of the concrete, the applied load was controlled by increasing the strain at the central section by about 0.0007. Maximum strain values ranging from 0.012 to 0.02 were obtained.

Sargin et al. (1971) tested 63 specimens in four different sets. The specimens were 125x125x510 mm concrete prisms. No longitudinal reinforcement was used in any of them. Twenty two were plain, the remaining forty one contained lateral reinforcement. All but eight of the specimens were cast vertically. The test series included testing of 15 C-shaped specimens. The cylinder strength of the C-shaped specimens f'_c ranged between 20.6 to 32.3 MPa. Two steel brackets, consisting of 100 mm wide flange I beam attached to it's two ends by means of 22 mm diameter high-tensile steel bolts, were used to apply the secondary load P_2 . The specimens and their companion cylinders were tested dry.

The primary load P_1 was applied using a screw-type Riehle machine of 890 kN capacity. A spring system was used in parallel with the specimen to prevent any sudden release of energy from the testing machine. The specimen was loaded in both ends through cylindrical rollers and grooved end plates. The top roller was also used as a load cell for measuring the load applied on the test specimen. The secondary load P_2 was applied to the steel brackets by means of small hydraulic jack 45 kN capacity. A 90 kN load cell was used to measure this load.

Longitudinal strains were measured along 125 mm gauge length at the middle of two opposite faces (maximum and minimum strain faces). Sanborn Model 24 DCDT-900 displacement transducers were used for this purpose. The lateral deflection was measured by means of dial gauges. In some of the specimens, electrical resistance strain gauges were applied on some of the ties in order to measure the strain produced in them due to load application in the longitudinal direction. The specimens were loaded using the following procedures. The main load was increased in steps and, by manually operating a small hydraulic pump, the secondary load was adjusted so that the reading of the DCDT attached to the least strained face always remained zero. At about 60% of the expected maximum load, the spring system was connected to the upper cross-head and subsequent loading steps were based on deformation increments. Test duration varied from 45 to 90 min.

Keer et al. (1978b) performed tests on 17 specimens to evaluate the effects of rectangular ties as confinement reinforcement. Controlled variables included size and spacing of ties, amount of longitudinal reinforcement, concrete strength and size of the specimens. Two sizes of specimens were tested. The large specimens had cross-sectional

dimensions of 252x406 mm, height of the specimens was 2640 mm. The small specimens had cross-sectional dimensions of 127x203 mm, height of the specimens was 1320 mm. The concrete cover to the outside of the ties was 19 and 9.5 mm for the large and the small size specimens respectively. The cylinder strength f'_c ranged between 19.2 and 46.5 MPa. Reinforcement in the arms of the specimens was designed to resist the stresses in the end region during testing. The specimens and their companion cylinders were tested dry.

The specimens were subjected to a primary load P_1 , using a 4,448 kN capacity test machine. In addition, a secondary load, P_2 , was applied by a hydraulic ram through a system of rods, cross-heads and rollers. During each test, the secondary load was adjusted to maintain zero strain at the back face of the cross-section. Strains were measured on the neutral and compressive faces of the plain concrete specimens with electrical strain gauges. On confined specimens, direct-current differential transducers (DCDT's) were used to measure the distance between reference frames mounted transversely on the specimens. These measurements were used to determine strains in the plane of the neutral and compressive faces. For the large specimens, two pairs of frames were used over 406 and 762 mm. For the small specimens, 203 mm gauge length was used. An additional DCDT was used to measure horizontal displacement at midheight of the specimen. The test duration was not mentioned in the published report.

Schade (1992) tested 12 prismatic columns with cross-sectional dimensions of 150x150 mm and total height of 600 mm. Six columns had no reinforcement while the other six columns had 4 No.15 longitudinal bars with an average yield strength of 417 MPa and 5.7 mm dimpled ties spaced 150 mm apart with an average yield strength of 540 MPa. The average 102x204 mm cylinder strengths, f'_c , of the plain concrete and the reinforced columns were 105.9 and 109.6 MPa respectively. Two steel cantilever assemblies, each consisting of HS 76.2x90.8x4.78, were attached to the top and the bottom parts of the columns to apply the secondary load P_2 . Two transverse pieces of the same steel section were placed on the cantilevers in the location of the hydraulic jack of the P_2 load. The testing age was 10 days. The columns and the associated cylinders were allowed to dry for a period of 4 days before testing.

The primary load P_1 was applied to the columns by a servo-controlled closed loop MTS machine with a 200 kN capacity measured by the load cell of the machine. The load was transferred from the machine to the columns through a ball and socket arrangement. The secondary load P_2 was applied via a hand pump and measured with a load cell. Strains in the concrete were measured using 4 strain gauges that had a gauge length of 50 mm. One gauge was located on the center line of each face. Average steel strain on each longitudinal bar was measured using two strain gauges with a gauge length of 5 mm. All

testing was performed using stroke control. The stroke rate was 1.7×10^{-6} m/sec for the cylinders and 5.0×10^{-6} m/sec for the columns. The stroke was continuous and uninterrupted throughout each test. For the columns, while the MTS piston moved continuously it was possible to maintain zero strain within a range of ± 3 microstrain by applying an increased pressure through the hand pump. The average test period was 10 min. for columns and 5 min. for the cylinders.

2.3 Empirical Models for the Stress-Strain Curve for HSC

2.3.1 Model by Shah et al. (1983)

Shah et al. (1983) proposed stress-strain equations to represent the behavior of concrete sections. These equations can be used to describe the behavior of unconfined and spirally confined sections subjected to concentric compression loads. They were derived to match results of tests in which 3x6 in. cylinders were loaded axially in a closed loop testing machine. The average displacement between the top and the bottom platens of the machine was measured by LVDT's and was used for the feed back control. The model for spirally confined sections does not apply for the rectilinearly confined specimens tested in this test program. In the next Sections, only the expression for the unconfined concrete sections will be used in the analysis. Examples for the stress-strain curves of 60 and 120 MPa concrete are shown in Figure 2.2. For the unconfined section, the stress-strain equations of the ascending and descending parts respectively are in the form of

$$f = f_c' \left(1 - \left(1 - \frac{\epsilon}{\epsilon_c} \right)^A \right) \quad (2.1)$$

$$f = f_c' \exp(-K(\epsilon - \epsilon_c)^{1.15}) \quad (2.2)$$

where, f is the stress at a strain ϵ , f_c' and ϵ_c are the maximum stress and the corresponding strain and A and K are the parameters which determine the shape of the curve in the ascending and descending parts respectively. The values of the parameters A , K are determined by

$$A = E_c \frac{\epsilon_c}{f_c'} \quad (2.3)$$

$$K = 25 f_c' \quad (2.4)$$

where, E_c is the modulus of elasticity and is taken equal to $3320 \sqrt{f_c'} + 6900$ MPa.

2.3.2 Model by Mugaruma et al. (1983), (1989)

Mugaruma et al. (1983) tested square column specimens confined laterally by square high yield strength spiral reinforcement at intervals of 50 mm. Four plain concrete columns and 14 concentrically loaded reinforced concrete columns were tested to failure. The compressive strength of the concrete ranged from 34.9 to 89.2 MPa. The columns had cross-sectional dimensions of 147.4x147.4 mm and had no concrete cover. The volumetric ratio of the lateral reinforcement was 2.13%, except for two specimens that had 4.26%. All ties had a yield strength of 1390 MPa.

The authors concluded that, the brittle crushing behavior of HSC can be changed into ductile manner by using an adequate amount of high yield strength lateral reinforcement. An empirical stress-strain relationship was proposed. This empirical model was modified in 1989 by Mugaruma et al.

Mugaruma et al. (1989) tested 8 HSC columns confined by lateral reinforcement under reversed cyclic lateral loads. The columns were tested under constant axial compressive load levels ranged from 0.254 to 0.629 $f'_c b h$. The concrete compressive strengths were 85.7 and 115.8 MPa. The columns had cross-sectional dimensions of 200x200 mm and a concrete cover of 9 mm. The volumetric ratio of the lateral reinforcement was 1.61% with yield strengths of 328 and 792.3 MPa.

The authors concluded that the ductility enhancing efficiency of lateral reinforcement is reduced with the increase of concrete compressive strength. The use of high yield strength lateral reinforcement becomes indispensable for providing necessary flexural ductility in HSC columns. An empirical model was proposed based on the test results, and the Mugaruma et al. (1983) and modified Kent and Park (Park et al. (1982)) stress-strain models on confined concrete.

The proposed model consists of three parts (O-A, A-D, D-E) as shown in Figure 2.3. The parameters of the curve are; the peak stress/strain of the plain concrete (f'_c , ϵ_m); the peak stress/strain of the confined concrete (σ_m , ϵ_m); and the stress/strain at the ultimate strain (σ_m , ϵ_m). These parameters are defined by the following equations

$$\epsilon_m = (0.814K_m + 1.67)/1000 \quad K_m \leq 1.5 \quad (2.5.a)$$

$$\epsilon_m = 2.817/1000 \quad K_m > 1.5 \quad (2.5.b)$$

$$\sigma_m = (1 + 49c_r)f'_c \quad (2.6)$$

$$\epsilon_m = (1 + 34k_r)\epsilon_m \quad (2.7)$$

$$\epsilon_{cu} = (1 + 610c_c)\epsilon_m \quad (2.8)$$

$$\sigma_{cu} = \frac{2(\epsilon_c - \sigma_m \epsilon_m)}{\epsilon_m + \epsilon_{cu}} + \sigma_m \quad (2.9)$$

$$K_m = (f_c' / 55)(C/500)^2 (W/200) \quad (2.10)$$

$$c_c = 0.3194 P_v \frac{\sqrt{f_c'}}{f_c'} \left(1 - 0.5 \frac{s}{w}\right) \quad (2.11)$$

$$\epsilon_u = (-0.265K_m + 1.71)\epsilon_m \quad K_m \leq 1.5 \quad (2.12.a)$$

$$\epsilon_u = 1.31\epsilon_m \quad K_m > 1.5 \quad (2.12.b)$$

where; K_m is a parameter which represents the mix properties of fresh concrete. This parameter is defined by Equation (2.10); C is the unit cement content (kg/m^3); W is the unit water content (kg/m^3); c_c is the confinement factor that is defined by Equation (2.11); P_v is the volumetric ratio of confinement reinforcement; f_c' is the yield strength of confining reinforcement in MPa; s is the pitch of confinement reinforcement in mm; w is the minimum dimension of the confined concrete core in mm; σ_m is the area surrounded by the idealized stress strain curve of the confined concrete until the peak load in MPa; ϵ_m is the compressive strain at ultimate for plain concrete.

The ascending branch of the proposed model is given by Equations (2.13) and (2.14). The descending branch is given by Equation (2.15)

$$\sigma_c = E\epsilon_c + \left[(f_c' - E\epsilon_m)/\epsilon_m^2\right]\epsilon_c^2 \quad (\epsilon_c \leq \epsilon_m) \quad (2.13)$$

$$\sigma_c = \frac{(f_c' - \sigma_m)}{(\epsilon_m - \epsilon_m)}(\epsilon_c - \epsilon_m)^2 + \sigma_m \quad (\epsilon_m \leq \epsilon_c \leq \epsilon_{cu}) \quad (2.14)$$

$$\sigma_c = \frac{(\sigma_m - \sigma_{cu})}{(\epsilon_m - \epsilon_{cu})}(\epsilon_c - \epsilon_m) + \sigma_m \quad (\epsilon_{cu} < \epsilon_c) \quad (2.15)$$

where; σ_c is the compressive stress; ϵ_c is the compressive strain; $E_c = 4700\sqrt{f_c'}$ MPa.

For unconfined concrete the proposed model consists of two parts (OA, AB) as shown in Figure 2.3. The ascending part (OA) is the same as for confined concrete. The descending part (AB) is given by the following equation

$$\sigma_c = (\sigma_u - f_c')(\epsilon_c - \epsilon_u)/(\epsilon_u - \epsilon_m) + f_c' \quad (\epsilon_u < \epsilon_c) \quad (2.16)$$

where; σ_u, ϵ_u are the ultimate stress and strain and σ_u is defined by the following equation

$$\alpha_s = \frac{2(f_c - f_c' \epsilon_m)}{(\epsilon_u + \epsilon_m)} + f_c' \quad (2.17)$$

2.3.3 Model by Yong et al. (1988)

Yong et al. (1988) studied the behavior of laterally confined HSC columns under axial loads. Eighteen laterally and longitudinally reinforced columns and 6 plain concrete columns, all concentrically loaded, were tested to failure. The compressive strength of the concrete ranged from 83.6 to 93.5 MPa. The columns had cross-sectional dimensions of 152x152 mm and a concrete cover of 9.5 mm. The stress-strain behavior of these columns was studied with respect to the effects of the volumetric ratio and spacing of lateral ties, the concrete cover and the distribution of the longitudinal steel around the core perimeter.

The authors concluded that, the lateral confinement of HSC by lateral steel ties does improve the general behavior of concrete. Instead of collapsing in a very brittle and explosive fashion, the confined concrete specimens failed in more ductile and gradual way. The compressive strength, the strain at maximum stress and the strain values in the descending branch of the stress-strain curve of the concrete core all increased with an increase in the amount of lateral confinement. This increase in the lateral confinement results in a less than proportional increase in both the strength and the ductility of the confined concrete. The lateral confinement is less effective in enhancing the strength and the ductility of HSC than in the case of LSC. Increasing the number of longitudinal bars and distributing them around the core perimeter increases the effectiveness of the confinement of the concrete core. Spalling of the concrete cover does not seem to affect the percentage increase in the strength of the concrete core, but it does reduce the ductility of the core. The strain in the lateral steel did not reach its yield point at the level of the maximum core stress in some specimens. For this reason, the use of lateral steel with yield stress higher than 500 MPa is not recommended by Yong et al. For transverse steels with higher yield stresses, they recommend the use of a lower value of yield stress in the calculation of the confinement effect.

Based on the test results, an empirical model for the stress strain curve of the confined concrete is proposed. The model uses the formulae originally suggested by Sergin (1971) and modified by Valinas et al. (1977). A sketch of the proposed empirical model is shown in Figure 2.4. The parameters of the curve are: the peak stress/strain (f_c , ϵ_c); the inflection stress/strain on the descending branch (f_i , ϵ_i); and the stress/strain (f_u , ϵ_u) at an arbitrarily selected point on the descending branch.

By definition, the peak stress f_c is equal to $K f'_c$, where K and f'_c are the effective confinement and the concrete cylinder strength respectively. The expression of K suggested by Sargin (1971) and modified by Vallenat et al. (1977), is in the form

$$K = 1 + 0.0091 \left(1 - \frac{0.245s}{h'} \right) \left(p' + \frac{nd'}{8sd} p \right) \frac{f'_c}{\sqrt{f'_c}} \quad (2.18)$$

where; s = the center to center spacing of the lateral ties in inches; h' = length of one side of the rectangular ties in inches; n = number of longitudinal steel bars; d' = nominal diameter of lateral ties in inches; d = nominal diameter of longitudinal steel bars in inches; p' = volumetric ratio of lateral reinforcement; p = volumetric ratio of the longitudinal reinforcement and f'_c = yielding stress of the lateral steel in psi.

An expression, similar to Sargin's, (1971) was developed to predict the peak strain

$$\epsilon_c = 0.00265 + \frac{0.0035 \left(1 - \frac{0.734s}{h'} \right) (p' f'_c)^{3/2}}{\sqrt{f'_c}} \quad (2.19)$$

The remaining unknown values f_c , ϵ_c and f_{21} were calculated using the following equations obtained by linear regression:

$$f_c = f'_c \left[0.25 \left(\frac{f'_c}{f_c} \right) + 0.4 \right] \quad (2.20)$$

$$\epsilon_c = K \left[1.4 \left(\frac{\epsilon_c}{K} \right) + 0.0003 \right] \quad (2.21)$$

$$f_{21} = f'_c \left[0.025 \left(\frac{f_c}{1,000} \right) - 0.065 \right] \geq 0.3 f'_c \quad (2.22)$$

The empirical model consists of two polynomial equations, each similar in form to that originally proposed by Sargin (1971). For the ascending branch up to the peak stress and strain:

$$Y = \frac{AX + BX^2}{1 + (A-2)X + (B+1)X^2} \quad \epsilon_c \leq \epsilon_c \quad (2.23)$$

where; $Y = f_c/f'_c$; $X = \epsilon_c/\epsilon_c$; $A = E_c \epsilon_c / f'_c$; $B = [(A-1)^2 / 0.55] - 1$; $E_c = 7.55 w^{1.5} \sqrt{f'_c}$ and f_c and ϵ_c are the concrete stress and strain, respectively for the ascending branch.

A second order polynomial is proposed for the equation of the descending branch starts from the peak stress and strain:

$$Y = \frac{CX + DX^2}{1 + (C - 2)X + (D + 1)X^2} \quad \epsilon_c \geq \epsilon_c \quad (2.24)$$

where; $Y = f_c/f_o$; $X = \epsilon_c/\epsilon_o$; $C = \left\{ \frac{(\epsilon_{21} - \epsilon_c)}{\epsilon_o} \left[\frac{E_1 E_c}{(f_o - f_c)} \right] - \left[\frac{4\epsilon_c E_{21}}{(f_o - f_{21})} \right] \right\}$;
 $E_c = f_c/\epsilon_c$; $E_{21} = f_{21}/\epsilon_{21}$; $D = (\epsilon_c - \epsilon_{21}) \left\{ \frac{E_c}{(f_o - f_c)} \right\} - \left[\frac{4E_{21}}{(f_o - f_{21})} \right]$ and f_c and ϵ_c are the concrete stress and strain, respectively for the descending branch.

2.3.4 Model by Bjerkeli et al. (1990)

Bjerkeli et al. (1990) studied the deformation properties and ductility of HSC columns. The ductility of plain and confined normal and light weight concrete columns was investigated. The discussion in this chapter will only include normal weight (ND) columns. The test program consisted of four test series. The compressive strength of the concrete was measured by 100 mm cubes. All reinforcement steel, except for the 6 mm ties of the first, second and third series, had a yield strength ranging from 506 to 561 MPa. The 6 mm ties of the first, second and third series were deformed bars with a yield strength of 613 MPa. All the specimens were loaded at a constant rate of platen to platen displacements.

The first series consisted of 21 small scale circular columns with a diameter of 150 mm and height of 500 mm. The compressive strength of the concrete ranged from 62.5 to 99.6 MPa. The columns had no concrete cover and longitudinal reinforcement was not provided. The parameters in the tests were concrete strength, and the amount and distribution of the confining spiral reinforcement.

The second series consisted of 25 small scale square columns with cross-sectional dimensions of 150x150 mm and total height of 500 mm. The compressive strength of the concrete ranged between 90.9 and 108.7 MPa. The columns had four corner longitudinal bars of sizes 10 and 16. The parameters in these tests were the amount and distribution of the confinement ties, the influence of longitudinal reinforcement and the effect of reduced strain rate.

The third series consisted of 10 eccentrically loaded square columns with cross-sectional dimensions of 150x150 mm and total height of 1000 mm. The compressive strength of the concrete ranged between 86.7 and 88.5 MPa. The columns had four corner bars of size 16. The eccentricity and the confinement ratio were the parameters in this series in addition to the concrete mix design.

The fourth series consisted of 5 large scale rectangular columns with cross-sectional dimensions of 300x500 mm and total height of 2000 mm. The columns had 23 mm

concrete cover to the lateral reinforcement. In addition to the rectangular ties, each longitudinal bar was supported by straight bars anchored by friction welded plates. The compressive strength of the concrete ranged from 83.1 to 107.6 MPa.

The authors concluded that, confined HSC ND columns can develop a ductile behavior and sustain axial strains significantly larger than plain concrete. The effect of confinement and the ultimate strain are reduced by increasing the compressive strength. An increased compressive strength was observed in the case of strain gradients.

A theoretical model was developed to describe the stress-strain behavior of confined concrete. The model is based on modified expressions originally proposed by Martinez (1983). The empirical model consists of three parts as shown in Figure 2.5. The first part that describes the ascending branch is in the form

$$\sigma = \frac{E_c \epsilon}{1 + (E_c/E_s - 2) (\epsilon/\epsilon_u) + (\epsilon/\epsilon_u)^2} \quad (2.25)$$

where; σ is the concrete stress; ϵ is the concrete strain; $E_s = f_u/\epsilon_u$; and $E_c = 9500(f'_c)^{0.3}$

The second part is a straight line that describes the first portion of the descending branch with an equation in the form of

$$\sigma = f_u - z(\epsilon - \epsilon_u) \quad (2.26)$$

where, $z = 0.15 f_u / (\epsilon_{0.85} - \epsilon_u)$

The third part is a horizontal line at a stress value of f_{tr} which describes the second portion of the descending branch. The equation of f_{tr} is as follows

$$f_{tr} = 4.87 \frac{d_{co} A_{sh} f_y}{s_p A_c'} \quad (2.27)$$

The parameters of the curve are: the peak stress/strain (f_u , ϵ_u); the strain at 0.85 f_u in the descending part of the curve ($\epsilon_{0.85}$); and the horizontal part of the descending branch (f_{tr}).

These parameters are defined by the following equations

$$f_u = f_c + K_s 4.0 f_c \quad 45\text{MPa} < f'_c \leq 80\text{MPa} \quad (2.28.a)$$

$$f_u = f_c + K_s 3.0 f_c \quad 80\text{MPa} < f'_c \leq 90\text{MPa} \quad (2.28.b)$$

$$\epsilon_u = 0.0025 + K_s 0.050 (f_c/f'_c) \quad (2.29)$$

$$\epsilon_{0.85} = \epsilon_u' + K_s 0.050 (f_c/f'_c)/(1 - F) \quad (2.30)$$

$$f_{tr} = A_{sh} f_y / h' s_p \quad (2.31)$$

$$K_{s1} = [1 - a_t/d_{st}] \quad (2.32.a)$$

$$K_{s2} = \left(1 - \frac{n c^2}{5.5 A_c'}\right) \quad (2.32.b)$$

$$\varepsilon_{st} = 0.0025 \left((17.07/f_c')^2 + 1 \right) \quad (2.33)$$

$$F = \frac{1}{1 + (1/(f_c' K_s))^{1/4}} \quad (2.34)$$

where; d_{st} is the shorter out-to-out of ties in mm; a_t is the spacing between the ties; A_{st} is the total effective area of ties in direction under consideration; A_c' is the gross area of concrete section measured to center line of the outer ties; f_{st} is the yield stress of confining reinforcement in MPa; f_c' is the strength of the unconfined concrete; h' is the outer size of the confined section measured out-to-out of ties in the direction under consideration; n is the number of laterally supported longitudinal bars and c is the distance between the laterally supported longitudinal bars.

The confining pressure f_c' is calculated assuming equilibrium between forces from the confining reinforcement at yielding and the lateral stresses in the concrete as shown by Equation (2.31) and in Figure 2.6.c. The geometry of the confined concrete core is defined in terms of K_s , taken as the larger value of K_{s1} and K_{s2} . The factor K_{s1} is associated with the development of compression arches in vertical direction between the confinement reinforcement layers, shown in Figure 2.6.a. The expression used is originally developed by Shah et al. (1983) and is expressed by Equation (2.32.a). The factor K_{s2} is associated with the development of compression arches between laterally supported longitudinal reinforcement, shown in Figure 2.6.b. According to Sheikh et al. (1982), this factor is calculated from Equation (2.32.b).

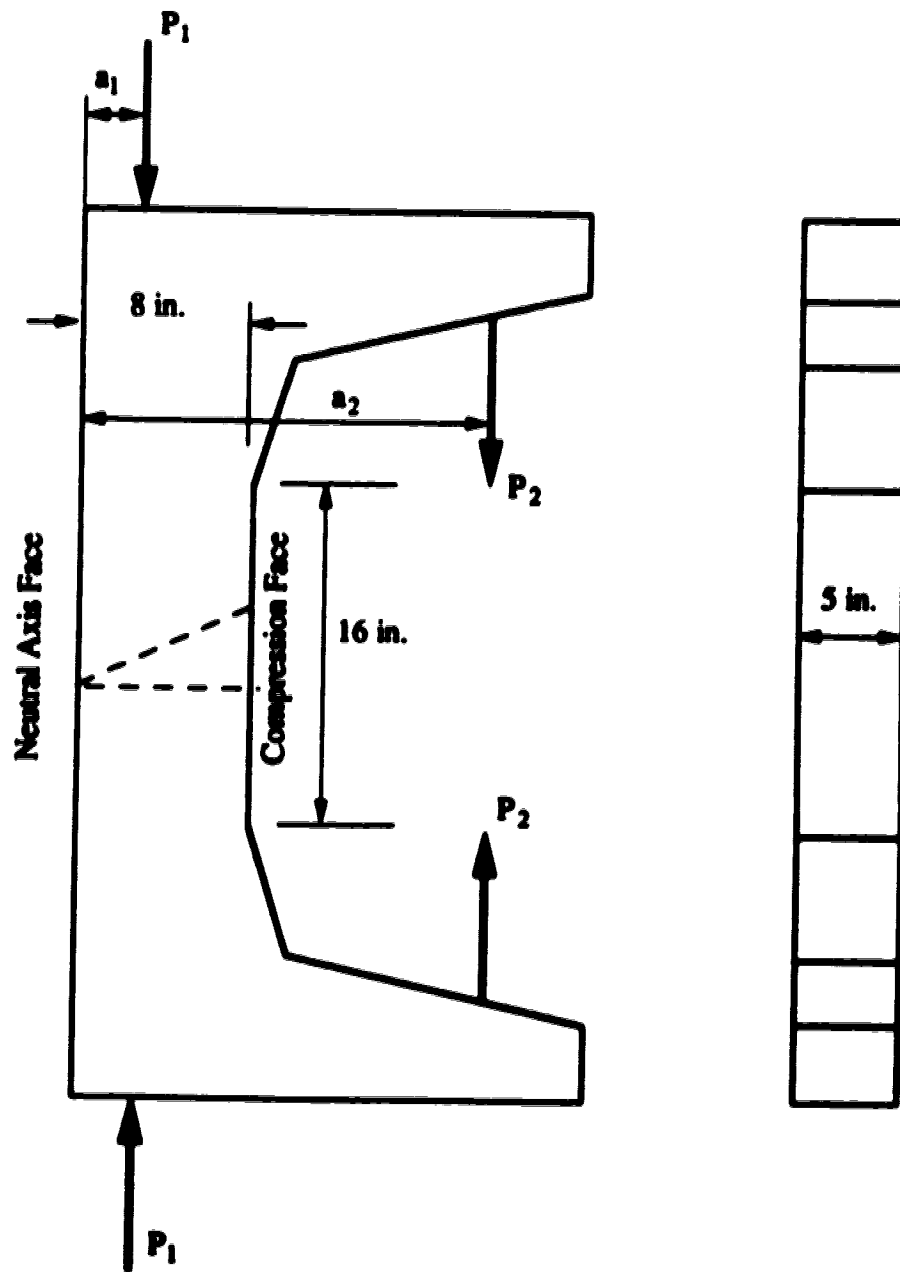


Figure 2.1 C-Shaped Specimen of Hognestad et al.

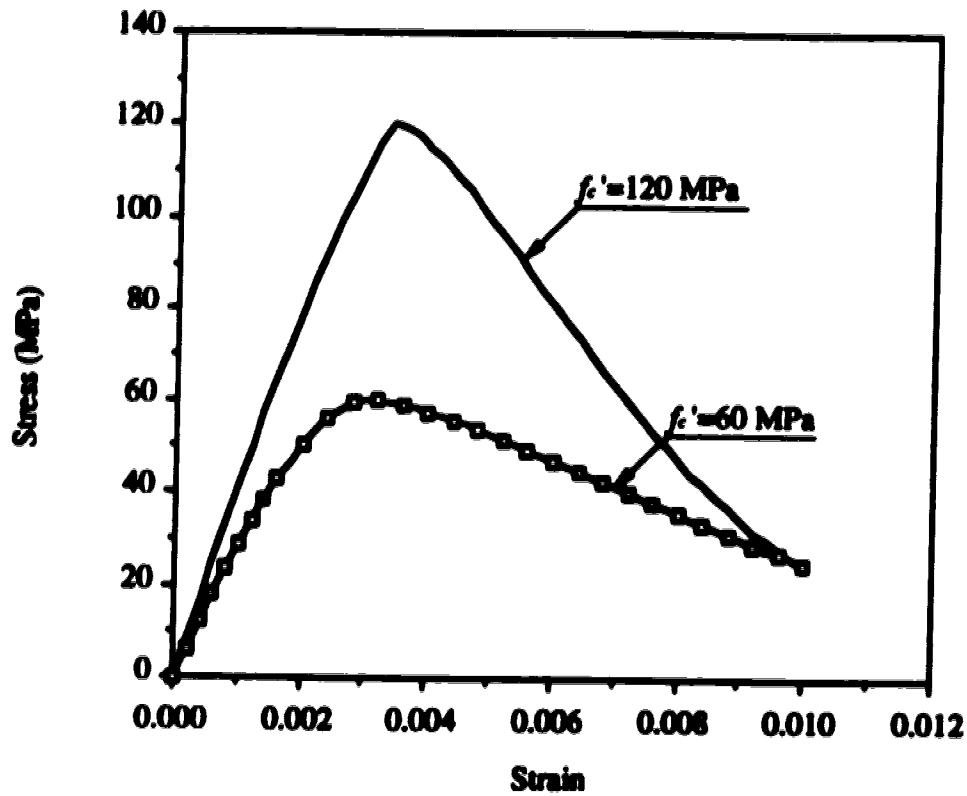


Figure 2.2 Stress-strain Curves for Plain Concrete by Shah et al. (1983)

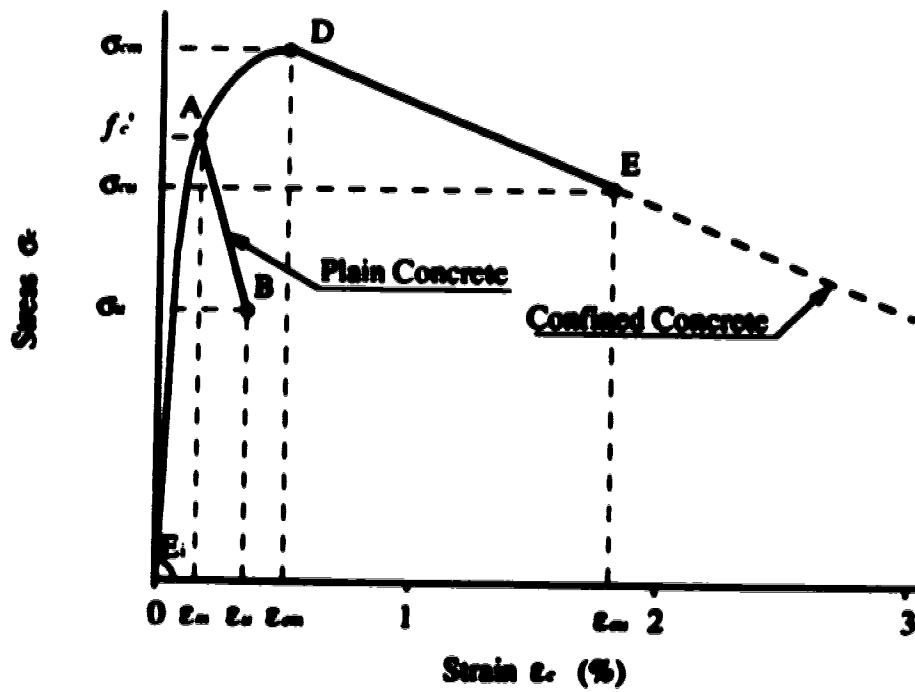


Figure 2.3 Idealized Stress Strain Curves by Meguruma et al. (1983), (1989)

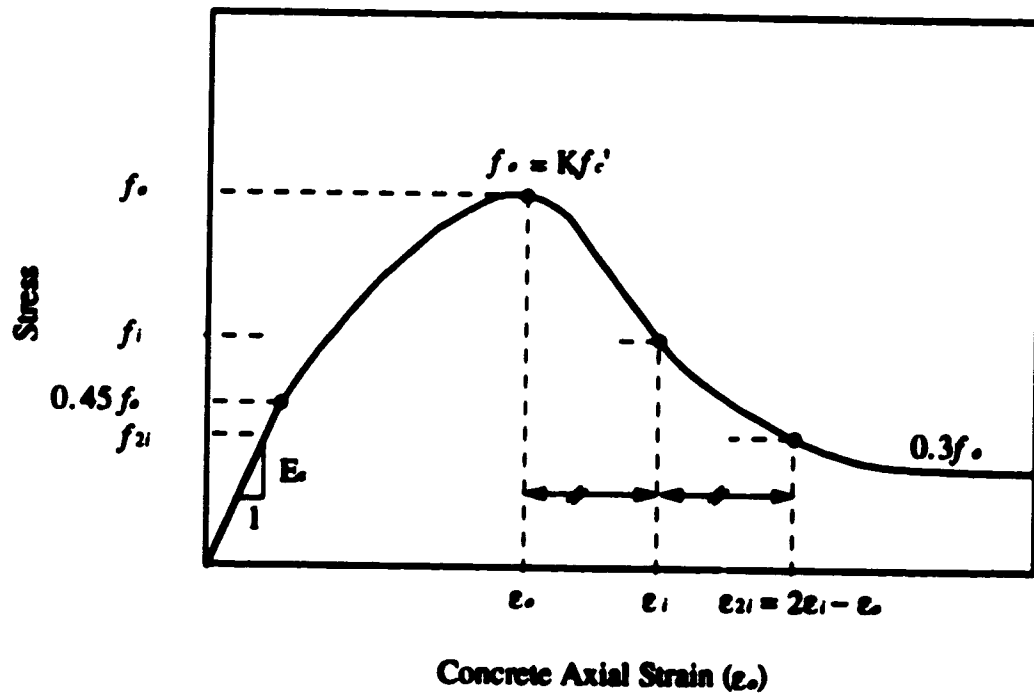


Figure 2.4 Empirical Model by Yong et al. (1988)

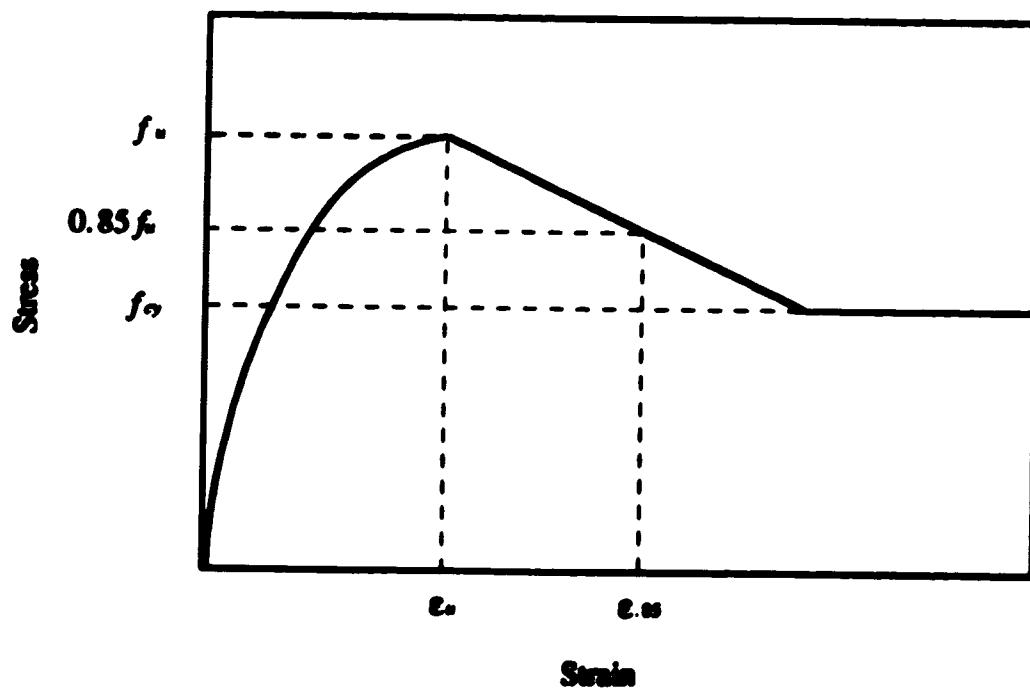


Figure 2.5 Empirical Model by Bjorkeli et al. (1990)

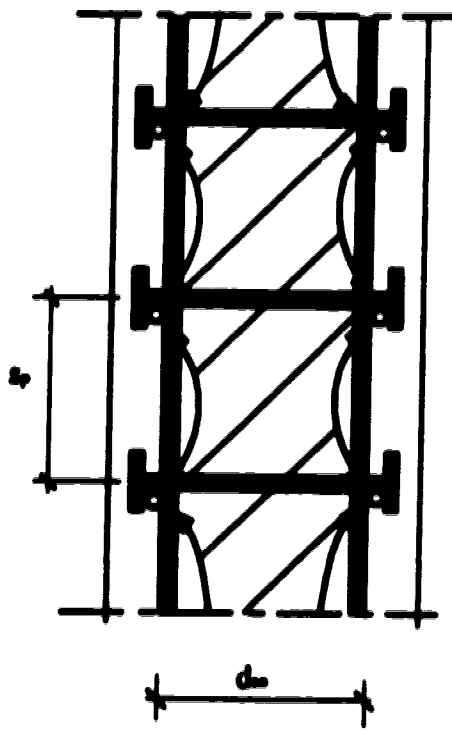


Figure 2.6.a Vertical section
Compressive arches between the
confinement reinforcement layers

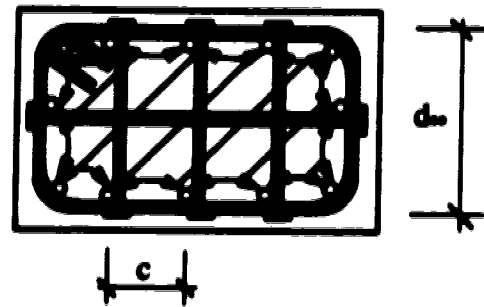


Figure 2.6.b Horizontal section
compressive arches
between longitudinal bars

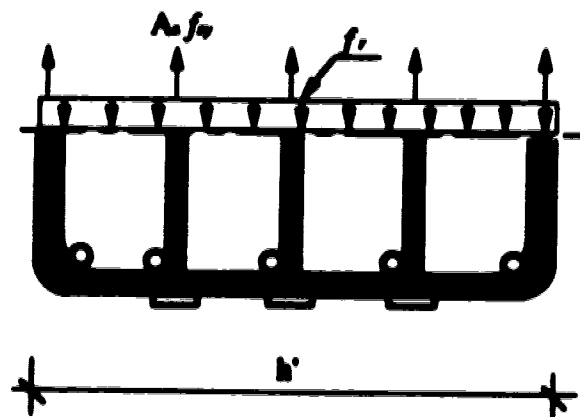


Figure 2.6.c Idealized "confining pressure" f_r

3- Experimental Program

3.1 General

The experimental program was designed to study the parameters defining the ACI rectangular compression stress block and the stress-strain relationship of eccentrically loaded high strength concrete columns. The program included two phases, the first phase consisted of tests of rectangular cross-section specimens, the second phase consisted of tests of triangular cross-section specimens. The triangular specimens gave information that is required to design rectangular cross-sections subjected to axial forces and biaxial moments and, more importantly, checked whether a full stress block could be developed after the tip reached high strain. A description of the specimens, materials and procedures during the experimental work is presented.

3.2 Test Specimens

3.2.1 Rectangular Specimens

The test series consisted of 15 C-shaped specimens shown in Figure 3.1. Three did not have reinforcement in the test region (column part) and 12 had vertical and horizontal reinforcement in this region. All the specimens had cross-sectional dimensions of 200x300 mm for the test region. The main parameters were concrete strength and confinement steel (diameter, spacing and volumetric ratio). Table 3.1 gives details of the concrete strength, reinforcement and testing method for each specimen. To assure that failure would occur in the test region, the end blocks were designed to have flexural and shear strengths well in excess of the loads applied in the test. Figure 3.2 gives details of the reinforcement in the test region and the end blocks. Table 3.2 gives the nominal dimensions and the tolerances of the nominal cross-sectional dimensions.

3.2.2 Triangular Specimens

The test specimens, shown in Figure 3.3, consisted of 6 C-shaped specimens; 2 without reinforcement in the test region and 4 with vertical and horizontal reinforcement. The section of the test region had a flat edge at the apex of the triangular giving a width of 20 mm in order to mount strain gauges in the most highly strained face. The main parameters were concrete strength and confinement steel (spacing and volumetric ratio). Table 3.3 gives details of strength, reinforcement and testing method for each specimen. Figure 3.4 gives details of the reinforcement in the test region and in the end blocks.

3.3 Materials

3.3.1 Concrete

The mixes used to cast the specimens were developed through extensive trial batching at University of Alberta and through previous work performed at University of Sherbrooke. The mixes were designed to develop cylinder strengths of 60, 90 and 120 MPa at 28 days. Since the 28 day period has no special significance, some of the specimens were tested at the age when the desired concrete strength was reached, others were delayed till the testing machine became available. The specimens were tested at ages ranging from 30 - 140 days.

3.3.1.1 Mix Constituents

3.3.1.1.1 Cement

Two different types of cement were used. Type 10 normal Portland cement was used for the 60 and 90 MPa mixes, while Type 30 high early strength was used for the 120 MPa mix. Both types of cement were supplied by Lafarge Canada Inc. Table 3.4 gives more information about the product.

3.3.1.1.2 Sand

The sand used was from a local pit. It consisted primarily of hard quartz rock types: orthoquartzite, quartzite hard sandstone and chert. Table 3.5 shows the percentage of each rock type. The sand had a fineness modulus of 2.70.

3.3.1.1.3 Coarse Aggregates

The coarse aggregates used were from a local pit. They are gravel primarily composed of orthoquartzite, quartzite and hard sandstone. Two different size distributions have been used, (20-5) mm blended coarse aggregates for the 60 MPa mix and (14-5) mm crushed coarse aggregates for the 90 and 120 MPa mixes. Table 3.6 shows the percentage of each rock type in each aggregate.

3.3.1.1.4 Silica Fume

Silica fume is an ultra-fine pozzolanic material. It can be used as a partial replacement for the Portland cement to produce a workable concrete with strength higher than 100 MPa. Silica fume was used to produce the 120 MPa mix. The product used was Force 10,000 supplied by W.R. Grace, Cambridge, Ma, which contains a condensed silica fume in a

water slurry (50% by weight). The product has a specific gravity of (1.36-1.39), the specific gravity of the silica fume is 2.2.

3.3.1.1.5 Super-plasticizer

Super-plasticizer is a powerful water reducing agent. It makes it possible to produce self-leveling concrete with only the water necessary to fully hydrate the cement particles. The product used was S.P.N which is a product of the Conchem Company. It has a polynaphthalene sulphate base.

3.3.1.2 Mix Proportions

Table 3.7 shows the proportions of concrete mix for the different target strengths. It should be noted that these mixes were based on the "air dried" conditions for aggregates (1.3% for sand and 1.6% for coarse aggregates). The amounts of water, sand and coarse aggregates were adjusted according to the actual moisture content of the aggregates measured at the time of casting. The super-plasticizer dose was based on having good workability without excessive bleeding. The percentage used ranged from 1.2% to 1.8% weight of solids in the S.P.N by weight of cement and silica fume content. Ten percent by weight of Portland cement was replaced by silica fume in mix No. 3.

3.3.1.3 Mechanical Properties

Tables 3.8 and 3.9 show the results of concrete material tests for each specimen. The meanings of moist cured and air cured in the tables are explained in Section 3.4. More details about the cylinder compression tests and the notched beam tests are presented in the next few sections.

3.3.1.3.1 Compression Tests of Cylinders

The stress-strain relationships in compression were obtained for each specimen using both 100x200 and 152x304 mm cylinders.

Portions of the descending branch of stress-strain curves for HSC show snap back behavior as shown in Figure 3.5. In order to obtain a complete stress-strain curve, a 2600 kN MTS rock testing machine was used with the control variable suggested by Rokugo et al. (1986). This method uses a feed back control signal utilizing both the load signal and the displacement signal instead of just the displacement signal as illustrated in Figure 3.5. By using this method the steep descending branch of high strength concrete cylinders could be obtained if θ is greater than α . An angle, θ , between 5-10 degrees and an average rate

of loading of 12 micro-strain/sec were chosen. The LABVIEW 2 testing program was used to write the commands required to operate the testing machine. The average strain of the cylinder was calculated by dividing the deformation of the cylinder by the total length of the cylinder. The deformation of the cylinder was calculated by subtracting the elastic deformation of the testing machine from the stroke readings. Figure 3.6 shows an example of the stress-strain curves obtained for 80 and 120 MPa cylinders.

The high strength concrete (HSC) cylinders exhibited a stress-strain curve similar to the low strength concrete (LSC) cylinders except that the ultimate load was reached at higher strain and the descending branch was steeper. Close to the maximum load carrying capacity, cracks appeared in the central zone of the cylinder and after reaching the ultimate load, these cracks propagated into the end zones. With the applied control system, it was possible to get a smooth and continuous descending branch.

The ultra high strength concrete (UHSC) cylinders developed two different failure mechanisms, an uncontrolled failure mechanism, that occurred suddenly at the maximum load carrying capacity in an explosive manner, where the cylinder was broken into small pieces. A controlled failure mechanism started with few cracks localized in a certain spot that appeared close to the maximum load carrying capacity. These cracks might appear in the central zone or near the end boundaries. At the maximum load carrying capacity, spalling of small pieces from the cracked zone occurred followed by dropping in the load being carried. The cylinder continued to carry the load with increases in the axial strain until another spalling and drop in the load being carried occurred. The descending branch was not smooth and was steeper than the descending branch of the HSC cylinder.

In all cases, the cracks passed through the coarse aggregates and a conical rupture, due to the end confinement, was observed.

3.3.1.3.2 Fracture Energy of Concrete

The fracture energy of concrete was determined for each specimen using a three point bending test on a notched beam. The dimensions of the beam and the test procedures were determined in accordance with RILEM draft recommendation (1985). Figure 3.7 shows the test set-up and an example of the fracture energy calculations.

3.3.2 Reinforcement

Different reinforcement sizes were used in the specimens. The properties of the reinforcement steel were determined only for the steel that was used in the test region. No.10 and No.15 deformed bars of Grade G30.12 M 400 were used for the longitudinal

reinforcement in the test region. The steel was supplied by Sherwood Steel in Edmonton, Alberta. For the transverse steel, two different sizes were also used, No.10 supplied by the same company and No.8 deformed bars which had a diameter of 8.7 mm. These were produced in Sweden. Although No.8 steel is not commercially available, it was used in many specimens because it was convenient for the size of the cross-section.

Tension tests were performed on 16 in. long specimens from each type of reinforcement, instrumented with a 2 in. gauge length Extensometer to measure the strain. Figures 3.8 to 3.10 show typical stress-strain curves for each type of reinforcement steel. The loading was stopped at two intervals during yield and one near the maximum load to get the static yield strength and the static ultimate tensile strength. All the steel from each type was from the same heat. Table 3.10 gives properties of reinforcement steel.

The characteristics of column steel were established by tension tests although the steel was exposed to compression in the specimens. Tests at University of Toronto by Seckin (see Sheikh et al. (1980)) showed that within the strain ranges under consideration, the tensile and compression stress-strain relationships are very similar.

3.4 Specimen Preparation

Forms were made of plywood and constructed in such a way to allow for easy stripping and reassembling. The specimens were cast vertically. The forms were oiled before inserting the steel reinforcement cage.

The reinforcement steel was assembled on the floor and tied together using steel wires to form a rigid cage as shown in Figure 3.11 for the triangular specimen T3. The steel cage was lifted using a crane and was adjusted in position inside the form using plastic chairs which were placed outside the tested region as shown in Figure 3.12 for the rectangular specimen V16.

After closing the form side, stiffeners consisting of steel pieces with a 2x4 in. hollow rectangular section and 1/2 in. threaded rods were clamped on the outsides of the form to prevent any lateral bulging during casting. The 1/4 in. rods required for attaching the rotation arms and the 1 in. rods used to attach the lateral support rods were installed inside the form (see Figures 3.13, 3.14 and 3.16).

Before casting, the moisture content of the aggregates was checked and the required amounts of sand, coarse aggregates and water were adjusted accordingly. Mixing was done in a 9 cubic foot mixer. After cleaning the mixer, the materials were charged in the order: sand, cement, silica fume (if any), water and super-plasticizers. These materials were mixed together for about 5 minutes before adding the coarse aggregates. Mixing time after adding the coarse aggregates was about 5-10 minutes.

The concrete was placed inside the form by the aid of a steel bucket. Six 152x304 mm cylinders; fifteen 100x200 mm cylinders and three 100x100x840 mm beams were made for each specimen. The size of the mixer was not enough to mix the amount of concrete required for the specimen in one batch. Three batches were required to produce a rectangular specimen and 5 batches were required to produce a triangular specimen. The test region, the cylinders and the beams were all cast from the same batch. The specimen and the beams were vibrated, while the cylinders were rodded.

Two hours after casting, the concrete surfaces of the specimen, the cylinders and the beams were covered with plastic sheets. Stripping was done 24 hours after casting. The cylinders and the beams were placed in a lime-water bath while the specimen was covered by plastic sheets for at least one week. Tables 3.8 and 3.9 list strengths for moist cured and air cured cylinders. The moist cured cylinders were cured as explained above. The dry cured cylinders were covered by plastic sheets after stripping to the time of testing.

The cylinders and the beams were taken out of the lime-water bath 1 to 2 weeks before testing and were placed on the floor covered by plastic sheets. The top and bottom faces of each cylinder were ground on a lathe to ensure that the two faces were perpendicular to the vertical axis of the cylinder. The cylinders and the beams were tested dry in the same conditions as the specimen.

The specimen surface was prepared to mount the strain gauges by sanding the surface and filling any small gaps using cold cure epoxy combined with cement and fine sand. The strain gauges were mounted using Armstrong adhesive produced by Armstrong Products Company. After placing the strain gauges, clamping forces were applied overnight using steel plates and C-clamps. The specimen were tested at least one week after mounting the strain gauges to allow for complete curing of the adhesive.

3.5 Test Set-Up

Each specimen was subjected to a primary load P_1 applied by a 6600 kN MTS machine and a secondary load P_2 applied by a hydraulic jack as illustrated in Figure 3.13. Since the spherical head of the MTS machine could not be counted on to accommodate the rotations of the end of the specimen and did not give a good measurement of the load position during the test, a system of curved plates and rollers that had a well defined center of rotation was used at the top and the bottom of the specimen as illustrated in Figure 3.14. The curved plates and rollers had a center of rotation in the tapered end of the specimen. A 1 in. rod through the column at this point served as the pivot point. Lateral supports were provided at the center of rotation of each system of end plates to prevent instability and to reduce the

lateral displacement at the center of rotation. As shown in Figure 3.13 the pivot rods and the line of action of the P_1 load could be offset from the axis of the specimen.

The secondary load P_2 was applied by 540 kN hydraulic jack, through a system of steel plates, pins, anchor rods and bolts attached at the top and bottom arms of the specimen. The loading system had enough stiffness to prevent sudden failure when the P_2 load dropped off during the test. Figure 3.14 shows details of test set-up.

A computer program was written to predict the maximum expected loads for each test. The program uses the stress strain relationship for HSC proposed by Shah et al. (1983) (Section 2.3.1). Using this program, the eccentricities of both of the loads were chosen in such a way to have enough capacities in both loading systems and to have failure occur before a compression force was developed in the P_2 hydraulic jack. Table 3.11 gives the chosen eccentricities of applied loads measured from the center line of each specimen.

3.6 Test Method

During each test, the stroke control system of the MTS machine was used to apply the load P_1 . As P_1 changed, the secondary load P_2 was adjusted accordingly to obtain zero strain at a predetermined point, generally on one face of the cross-section (the left hand side in Figures 3.13 and 3.14).

A feed back control system was used to control the change in P_2 load. When the MTS stroke changed, the reading in an LVDT mounted in the position of the neutral axis of the specimen would change to another reading. This change in the reading gave a new signal to the control system. The feed back control system corrected the error in the signal (error=current signal-initial signal) by moving the piston of the hydraulic jack. This movement changed the value of the P_2 load by the amount required to keep the neutral axis in position. The MTS 406 control unit was used for the feed back control.

When applying the loads in this way, the back face represented the neutral axis (axis of zero strain) of the compression zone. On the opposite side of the cross-section the extreme fibers were subjected to monotonically increasing compression strain. To reduce the fluctuation in P_1 and P_2 values during the test, a slow rate of loading was chosen and an LVDT with 1 mm full range was used for the feed back control system. All specimens except for V1 and V2 were tested using this procedure. Specimen V1 was tested using the feed back control with the axis of zero strain located 161.5 mm outside the specimen (to the left in Figures 3.13 and 3.14). Specimen V2 was tested with the P_1 load applied at a constant eccentricity and no P_2 load. The chosen eccentricity was 45 mm measured from the center line of specimen (to the right in Figures 3.13 and 3.14).

The slow rate of loading the columns involved increasing the strain in the compression face of the test region at a rate of 1000 microstrain / hour. Figure 3.15 shows a comparison between two cylinders tested by two different strain rates. The first cylinder was tested with a fast rate according to the CSA procedures for testing cylinders, while the second cylinder was tested with a slow rate similar to the rate that used in testing the specimens. The figure shows close agreement in the elastic part and slight change in the slope of the inelastic part. Based on the average of three tests at each rate, the cylinders tested using the slower rate were 4% lower in strength.

3.7 Test Arrangement

The lower curved plate and roller assembly was placed in the MTS machine and aligned. The specimen was then lifted by the crane, special care being taken so that no tensile cracks could occur in the test region. The specimen was lifted, aligned and leveled in the MTS machine. A thin layer of Plaster of Paris was used at the top and bottom surfaces of the specimen to insure vertical position and uniform bearing stresses. For the ultra high strength specimens, dental stone (Hydrocal 105) was used instead of Plaster of Paris.

The P_2 load set-up was aligned and bolted to the specimen and the lateral supports were attached. Temporary bearing supports were used to support the specimen between the time of aligning and testing.

3.8 Instrumentation

The MTS load cell was used to measure the primary load P_1 . A calibration test of the MTS load cell showed that it gave an error in readings ranging from 0% to 0.93% of the calibration load cell value in the 4000 kN load range. This error was not corrected during the analysis. A special dog bone load cell attached to the hydraulic jack was used to measure the load P_2 . Details about the P_2 load cell are provided in Section 4.2.4.

The deformations of the specimens were measured using both strain gauges and LVDT measurements. Rotation arms, made from 1 in. hollow square steel sections were mounted on 1/4 in. threaded rods embedded in the specimen as shown in Figure 3.13. Two sets of arms were used. The vertical distance between the inner rotation arms was equal to the cross-section depth. The location of the 1/4 in. rods is shown in Figures 3.1 and 3.3. The control LVDT was attached to the rotation arms at the position of the neutral axis. Two LVDT's were attached to the rotation arms 300 mm away from the zero strain face (300 mm to the right in Figure 3.13) to measure the average core deformation. Two other LVDT's were attached to the specimen through steel frames and bearing balls

mounted at the ends of the test region. These LVDT's were used to measure the average deformation over the entire tested part. A close up view of the location of the LVDT's is given in Figure 3.16. For specimen V2 the control LVDT was replaced by two LVDT's attached to the rotation arms 200 mm to the left in Figure 3.13 from the zero strain face.

One-inch gauge length electrical resistance strain gauges of the type SR-4, FAE-100N-12-50L and 4 in. gauge length strain gauges of the type SR-4, FAE-400N-12-50L, were mounted on different locations longitudinally and transversely. Details of different strain gauge configurations used during the test program are given in Chapter 4. The measurements of the surface strain were used during the test to check the neutral axis location and to determine the time of cover spalling.

Several LVDT's with different ranges 10-40 mm were connected to deflection bridges in order to measure the position of loads during the test and the lateral deflection of the specimen at different locations as illustrated in Figure 3.13. Figures 3.17 and 3.18 show pictures for the rectangular and triangular specimens before testing.

3.9 Test Procedure

The LVDT's were adjusted in position and the strain gauges were connected and checked. A small electrical vibrator was connected to the rotation arms to prevent the control LVDT from sticking. An elastic band was connected to the LVDT core to prevent it from jumping when a major loss of concrete cover occurred. The response of the feed back control was checked while the hydraulic pressure was off.

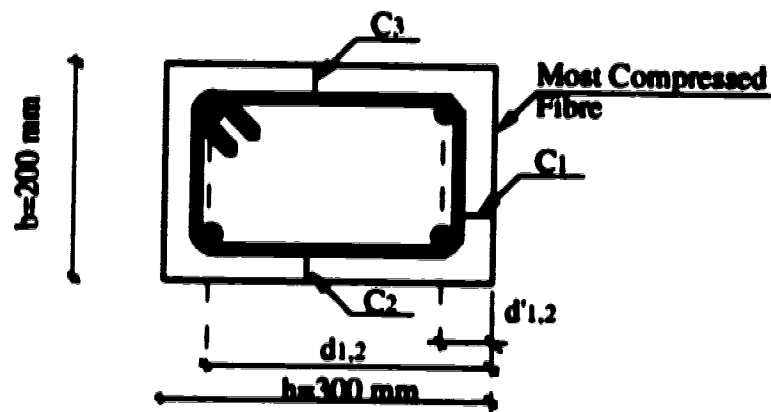
During installation of the specimen in the machine the rollers and curved end plates were bolted together. The rollers of the curved plates were released and the temporary bearings were removed. Zero readings were recorded and the test was started with the data acquisition system automatically recording readings at intervals. The MTS head was controlled to move down at a constant rate of about 2 mm/hr which is approximately equal to 0.33 micro-strain/ sec in the compression face of the tested part. During the test, any noticeable cracks or spalling were recorded. The duration of each test was between 3-7 hours. After spalling of concrete P_2 decreased in order to maintain zero strain. The tests were terminated when a complete destruction of the plain concrete specimens occurred or when the load P_2 reached zero for the reinforced concrete specimens. In two tests one of the hinges in the P_2 load set-up had been fixed and the test was continued till the P_2 loads reached 50 kN in compression.

After testing, the specimen was removed, the curved plates were cleaned and leveled for a new test. The cylinders and beams were tested as close as possible to the time of testing the specimen.

Table 3.1 Details of the Rectangular Specimens

Specimen	Compression Strength MPa (100 mm Cyl)	Longitudinal Reinf.	Lateral Reinf.				Test Method (Strain Gradient)	Steel Arrang
			Diameter (mm)	Spacing (mm)	Ties Outer Dimensions	Volumetric Ratio		
V1	70.7	4 No.15	10	200	178X278	0.01	Trapezoidal	
V2	82.8	4 No.15	8	100	172X272	0.01122	Constant Ecc	
V4	72.8	—	—	—	—	—	Triangular	Plain Concrete
V5	124.8	—	—	—	—	—	Triangular	
V6	98.8	—	—	—	—	—	Triangular	
V7	84.7	4 No.15	8	200	172X272	0.00561	Triangular	
V8	129.3	4 No.15	8	200	172X272	0.00561	Triangular	
V10	89.4	4 No.15	10	200	178X278	0.01	Triangular	
V11	127.5	4 No.15	10	200	178X278	0.01	Triangular	
V12	121.1	4 No.15	10	200	178X278	0.01	Triangular	
V13	72.5	4 No.15	8	100	172X272	0.01122	Triangular	
V14	124.7	4 No.15	8	100	172X272	0.01122	Triangular	
V15	124.8	4 No.15	8	100	172X272	0.01122	Triangular	
V16	59.26	8 No.10	8	50	172X272	0.0387	Triangular	
V17	127.7	8 No.10	8	50	172X272	0.0387	Triangular	

- Specimen V10 was cracked before testing

Table 3.2 Details of Cross-Section for the Reinforced Rectangular Specimens

Specimen	$d'1, d'2$	$d1, d2$	$C1$	$C2$	$C3$
V1	38, 38	270, 266	15	13	15
V2	48, 46	260, 260	14	16	12
V7	33, 34	265, 262	14	14	14
V8	38, 41	262, 266	13	14	14
V11	39, 39	260, 261	14	14	14
V12	41, 44	264, 262	14	14	14
V13	42, 42	265, 265	13	13	15
V14	36, 37	263, 262	16	14	14
V15	29, 29	262, 262	14	14	14
V16	38.5, 38.5	271.5, 271.5	14	14	14
V17	39.5, 39.5	262.5, 262.2	15	14	14

- All the hooks are standard 135-degree hooks with internal diameter $D=4d_b$ and minimum extended straight portion of length $6d_b$ (d_b =diameter of the bar)
- The nominal dimensions of the cross-section were used in the analysis
- The middle bars for specimens V16 and V17 were at $d=190$ mm

Tolerances of the nominal dimensions:

- (1) Overall concrete dimensions (± 2 mm)
- (2) Spacing of ties (± 3 mm)

Table 3.3 Details of the Triangular Specimens


Specimen	Compression Strength MPa (100 mm Cyl)	Longitudinal Reinf.	Lateral Reinf.				Test Method (Strain Gradient)	Steel Arrangement
			Diameter (mm)	Spacing (mm)	Ties Outer Dimensions	Volumetric Ratio		
T1	81.0	—	—	—	—	—	Triangular	
T2	89.4	3 No.15	8	100	206X360	0.012	Triangular	
T3	84.0	3 No.15	8	50	206X360	0.025	Triangular	
T4	129.1	—	—	—	—	—	Triangular	
T5	130.6	3 No.15	8	100	206X360	0.012	Triangular	
T6	117.8	3 No.15	8	50	206X360	0.025	Triangular	

Table 3.4 Cement Composition

	Normal Portland Cement Type (10)	High Early Strength Portland Cement Type (30)
Fineness: Blaine	418 m²/Kg	582 m²/Kg
Tricalcium Silicate (C₃S)	55.1 %	58.2 %
Dicalcium Silicate (C₂S)	18.2 %	15.5 %
Tricalcium Aluminate (C₃A)	6.4 %	6.5 %
Tetracalcium Aluminoferrite (C₄AF)	8.7 %	7.8 %

Table 3.5 Sand Composition

	Rock Type	%
Good	Orthoquartzite	21.7
	Quartzite	63.05
	Sand stone	4.9
	Trap- (Basalt)	1.5
	Granite	1.9
Fair	Chert	5.6
	Granite-weathered	0.2
Poor	Siliceous iron stone	0.1
	Sand stone- soft	1.0
Deletrious	Clay ironstone	0.05

Table 3.6 Coarse Aggregate Composition

	Rock Type	% Uncrushed (20-5) mm	% Crushed (14-5) mm
Good	Orthoquartzite	62.6	62.7
	Quartzite	14.1	13.8
	Sand stone- hard	10.6	10.6
	Trap- (Basalt)	5.6	5.7
	Rhyolite	4.0	4.1
	Granite	0.1	0.1
Fair	Orthoquartzite	1.5	1.5
	Quartzite	0.5	0.5
	Sand stone	0.1	0.15
Poor	Siliceous iron stone	0.3	0.3
	Sand stone- soft	0.011	0.0
Deletrious	Clay ironstone	0.99	0.55

Table 3.7 Mix Designs

Constituents	Mix Proportions (Kg/m ³)		
	Mix (1) Target Strength 60MPa	Mix (2) Target Strength 90MPa	Mix (3) Target Strength 120MPa
Cement	400 Type (10)	550 Type (10)	495 Type (30)
Water	128.4	137	113
Silica Fume	—	—	55
Sand	858	667	650
Coarse Aggregates	1000 Uncrushed (5-20) mm	1100 Crushed (14-5) mm	1110 Crushed (14-5) mm
S.P.N*	9.5 L	16.2 L	19.5 L
W/ (C+S)	0.3375	0.27	0.23
Specimens for Each Mix	V1, V4, V7, V10, V13, V16	V2, V6, T1, T2, T3	V5, V8, V11, V12, V14, V15, T4, T5, T6

- * S.P.N has 70% by weight water which was subtracted from the amount of water required
- All the mixes are based on 2% air content

Table 3.8 Results of Concrete Tests for the Rectangular Specimens

Specimen	Testing Age (Days)	Cylinders Compression Tests (MPa)			Splitting Tests f_{cs} (MPa) 152 mm (Moist Cured)	Fracture Energy G_F (N/m (J/m ²))
		100 mm (Moist Cured)	100 mm (Air Cured)	152 mm (Moist Cured)		
V1	87	70.7 (6)*	—	66.1 (3)	3.35 (3)	170 (3)
V2	42	82.8 (4)	—	—	—	—
V4	86	72.8 (5)	—	62.1 (3)	3.25 (3)	215 (2)
V5	108	124.8 (4)	115.7 (2)	110.0 (4)	5.07 (3)	195 (3)
V6	119	98.8 (8)	87.9 (6)	95.1 (3)	5.22 (3)	212 (2)
V7	126	84.7 (6)	—	78.4 (3)	4.78 (3)	197 (3)
V8	116	129.3 (3)	121.6 (2)	111.8 (3)	5.92 (3)	188 (2)
V10	140	89.4 (3)	—	84.0 (2)	3.86 (3)	166 (3)
V11	109	127.5 (5)	110.5 (2)	107.4 (3)	6.14 (3)	210 (2)
V12	32	121.5 (3)	—	117.1 (3)	—	193 (3)
V13	105	72.5 (10)	—	70.9 (3)	3.43 (3)	161 (2)
V14	112	124.7 (5)	112.2 (2)	107.4 (4)	5.65 (3)	184 (3)
V15	186	124.8 (7)	113.5 (2)	113.2 (3)	5.46 (4)	141 (3)
V16	87	59.3 (6)	—	59.1 (3)	3.55 (2)	166 (2)
V17	105	127.7 (4)	98.6 (2)	114.7 (3)	5.59 (3)	219 (3)

* The number in brackets refer to the number of tests carried out and averaged to get the value given

Table 3.9 Results of Concrete Tests for the Triangular Specimens

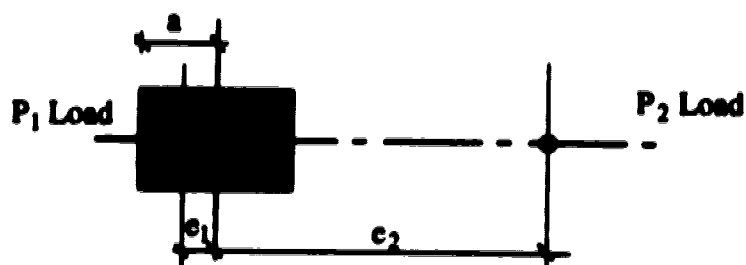
Specimen	Testing Age (Days)	Cylinders Compression Tests (MPa)			Splitting Tests f_{cs} (MPa) 152 mm (Moist Cured)	Fracture Energy G_F (N/m (Mm^{-2}))
		100 mm (Moist Cured)	100 mm (Air Cured)	152 mm (Moist Cured)		
T1	35	81.0 (4)*	77.2 (3)	69.3 (3)	4.64 (3)	203 (3)
T2	47	89.4 (3)	86.4 (2)	76.2 (3)	4.93 (3)	150 (3)
T3	48	84.0 (4)	78.0 (2)	72.2 (3)	4.34 (3)	195 (3)
T4	147	129.1 (4)	—	122.3 (3)	5.80 (3)	204 (2)
T5	158	130.6 (7)	—	121.3 (3)	6.00 (3)	199 (3)
T6	147	117.8 (4)	—	95.0 (3)	6.20 (3)	192 (2)

* The numbers in brackets refer to the number of tests carried out and averaged to get the value given

Table 3.10 Properties of Reinforcement Steel

Bar Size	Modulus of Elasticity E (MPa)	Static Yield Strength F_y (MPa)	Static Ultimate Strength F_u (MPa)
No.15	188200 (25)*	433.2 (25)	647.4 (9)
No.10	185000 (5)	423 (5)	669.8 (5)
No.8	216400 (3)	401 (3)	584.5 (2)

* The numbers in brackets refer to the number of tests carried out and averaged to get the value given

Table 3.11 Eccentricities of Applied Loads for Each Specimen

Specimen	Eccentricity of P_1 Load e_1 mm	Eccentricity of P_2 Load e_2 mm
V1, V4, V7, V10, V13, V16	0.0	700
V5, V6, V8, V11, V12, V14 V15, V17	30	700
T1, T2, T3, T4, T5, T6	13.83	600
V2	-45	—

- Measured eccentricities were within ± 1 mm of the values shown in the table
- Eccentricities e_1, e_2 were measured from the center line of the specimen
- $a = 150$ mm for the rectangular specimens
 $= 83.83$ mm for the triangular specimens

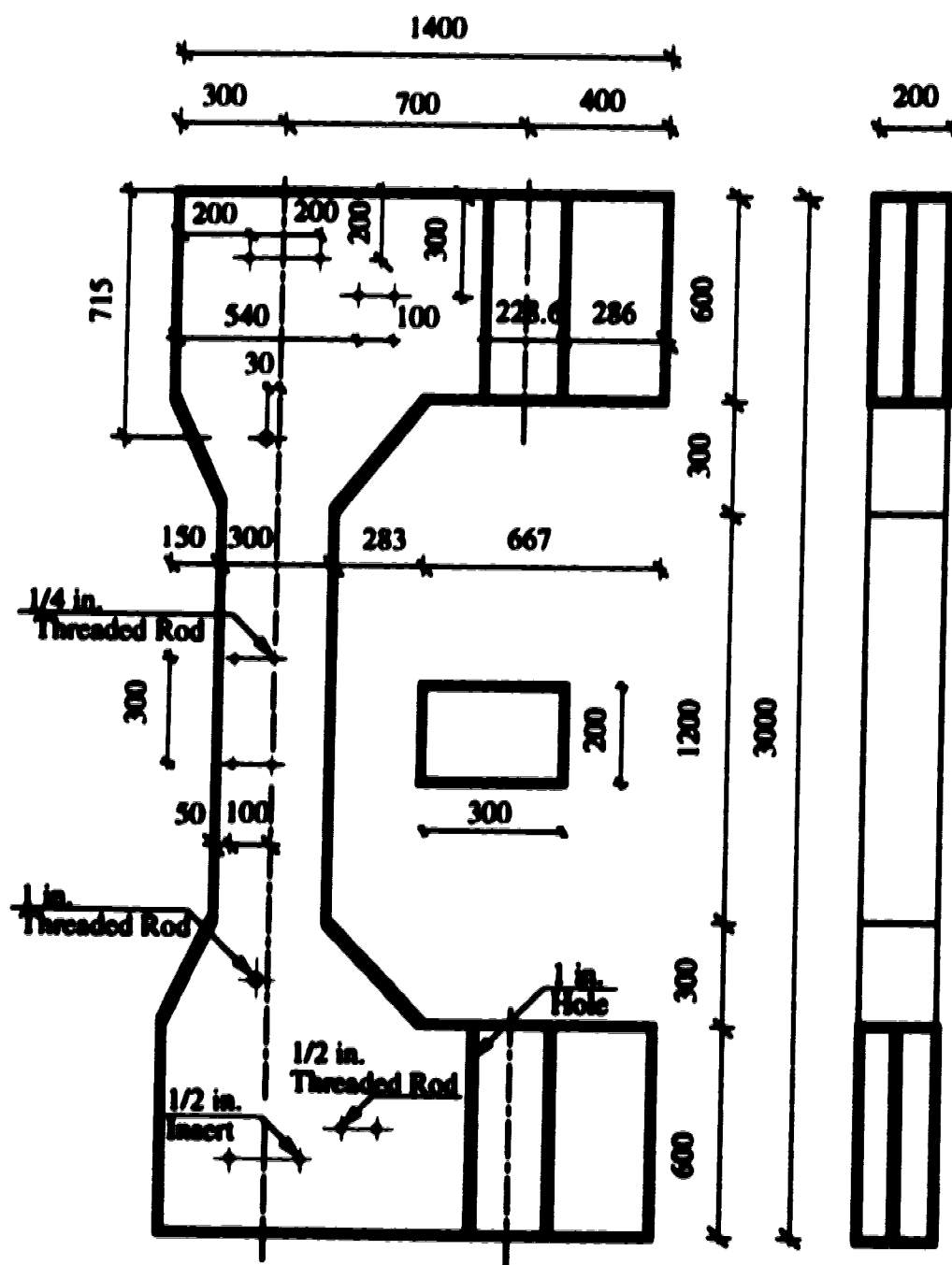


Figure 3.1 Concrete Dimensions for the Rectangular Specimens

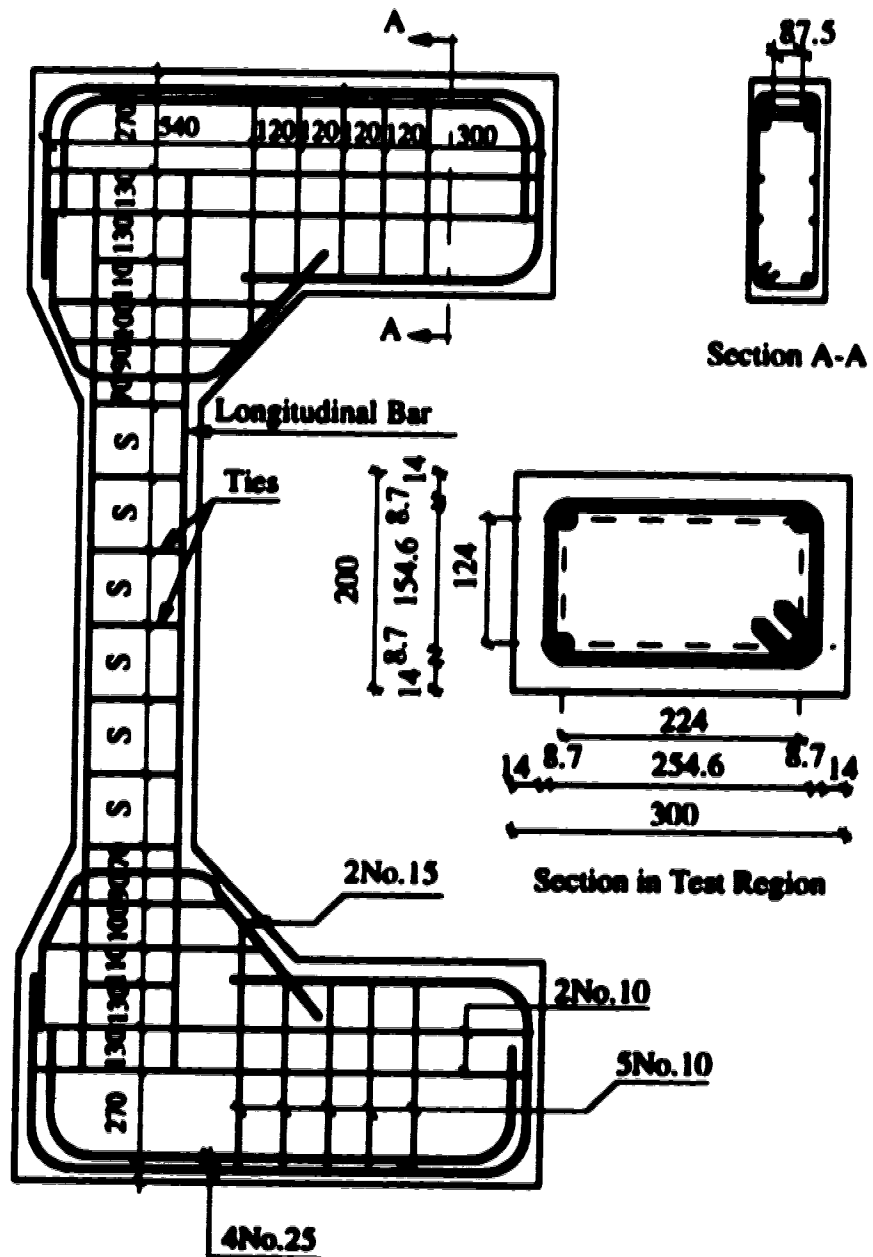


Figure 3.2 Details of Reinforcement for the Rectangular Specimens

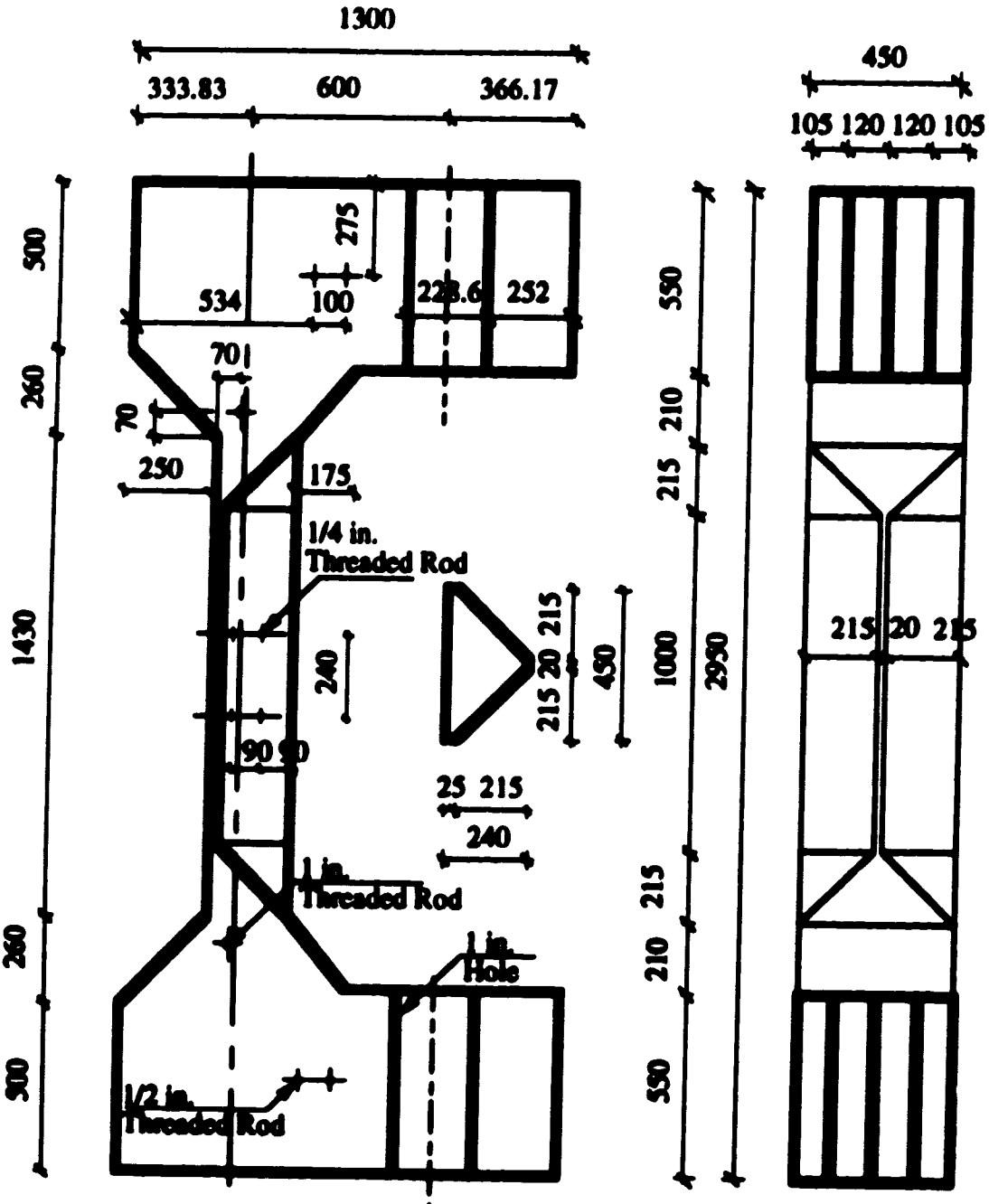


Figure 3.3 Concrete Dimensions for The Triangular Specimens

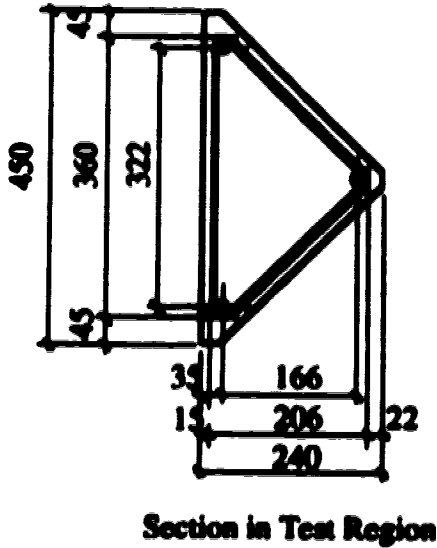


Figure 3.4 Details of Reinforcement for the Triangular Specimens

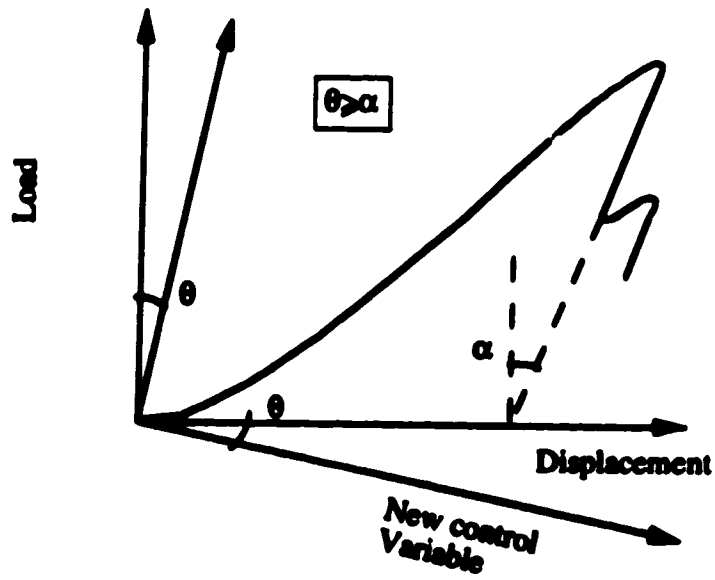


Figure 3.5 Cylinder Compression Test

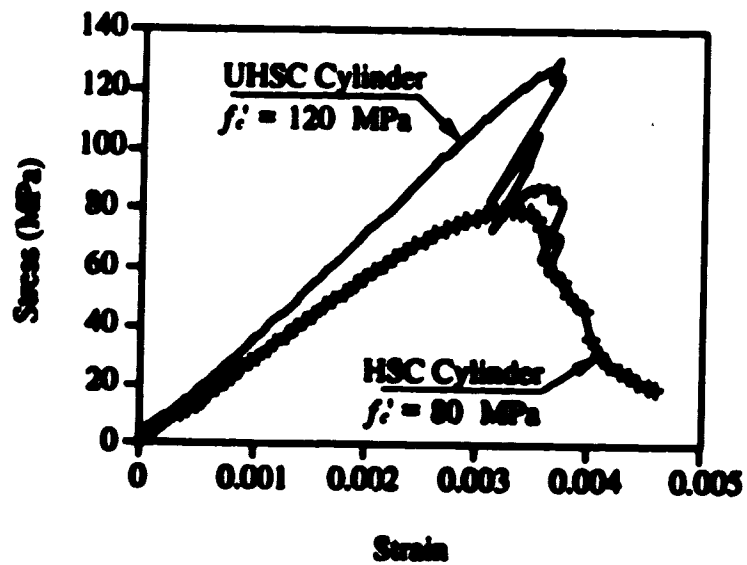
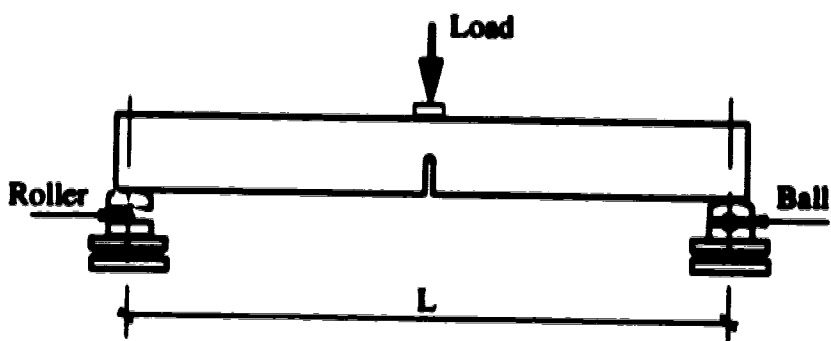


Figure 3.6 Stress-Strain Curves for 100 mm Cylinders



$$G_F = (W_0 + mg \delta_0) / A_{Lg} \text{ (N/m (J/m}^2\text{))}$$

m = Weight of the beam between supports (Kg)

A_{Lg} = The projection of the fracture zone on a plane perpendicular to the beam axis (m^2)

g = Acceleration due to gravity (9.81 m/s^2)

δ_0 = Deformation at the final failure of the beam (m)

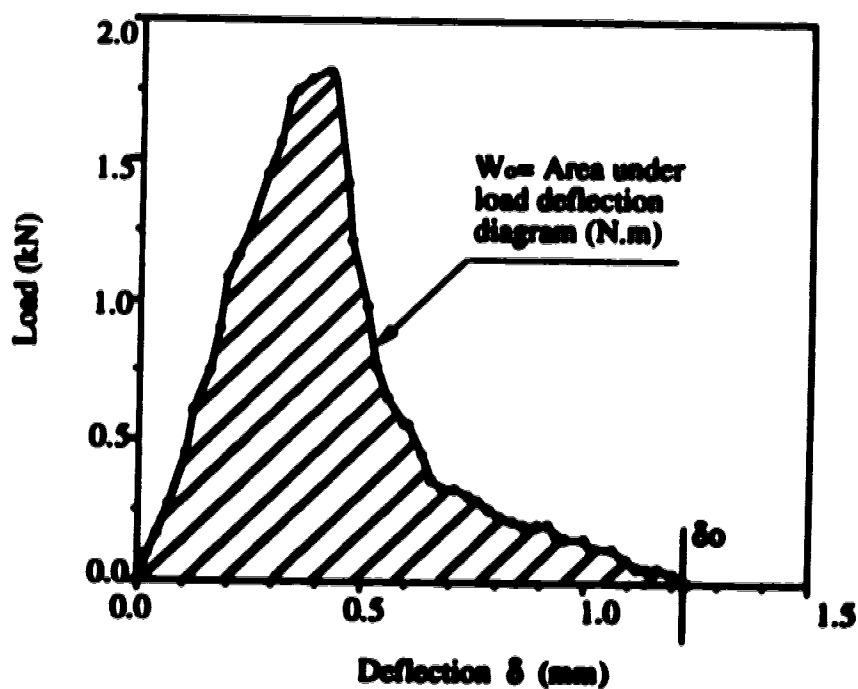


Figure 3.7 Details of Notched Beam Test

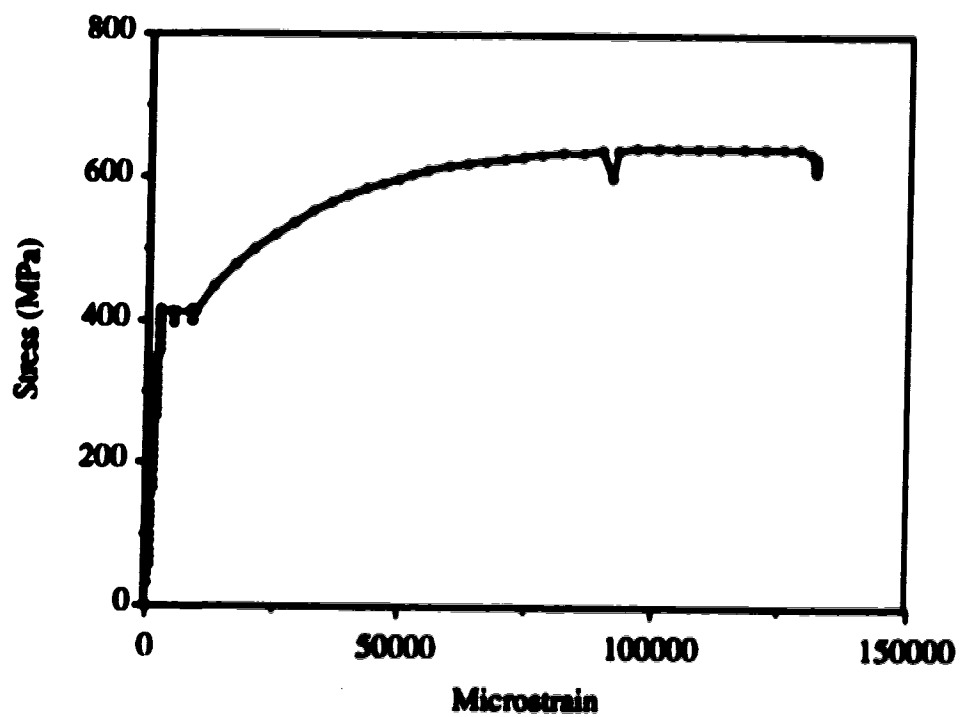


Figure 3.8 Stress Strain Curve for No.10 Bar

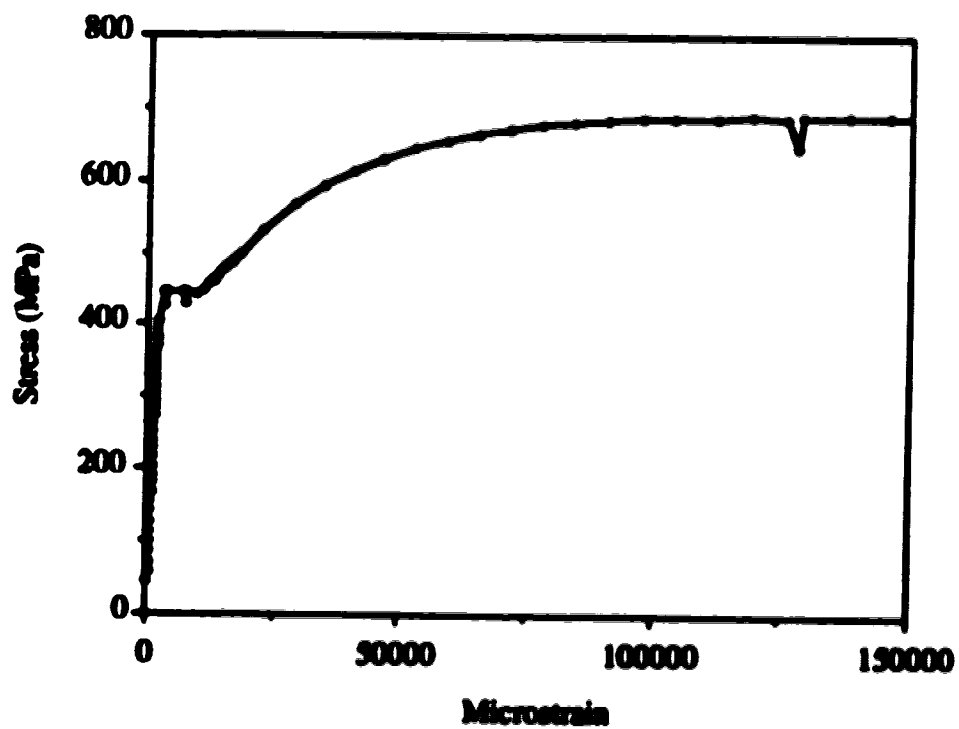


Figure 3.9 Stress strain Curve for No.15 Bar

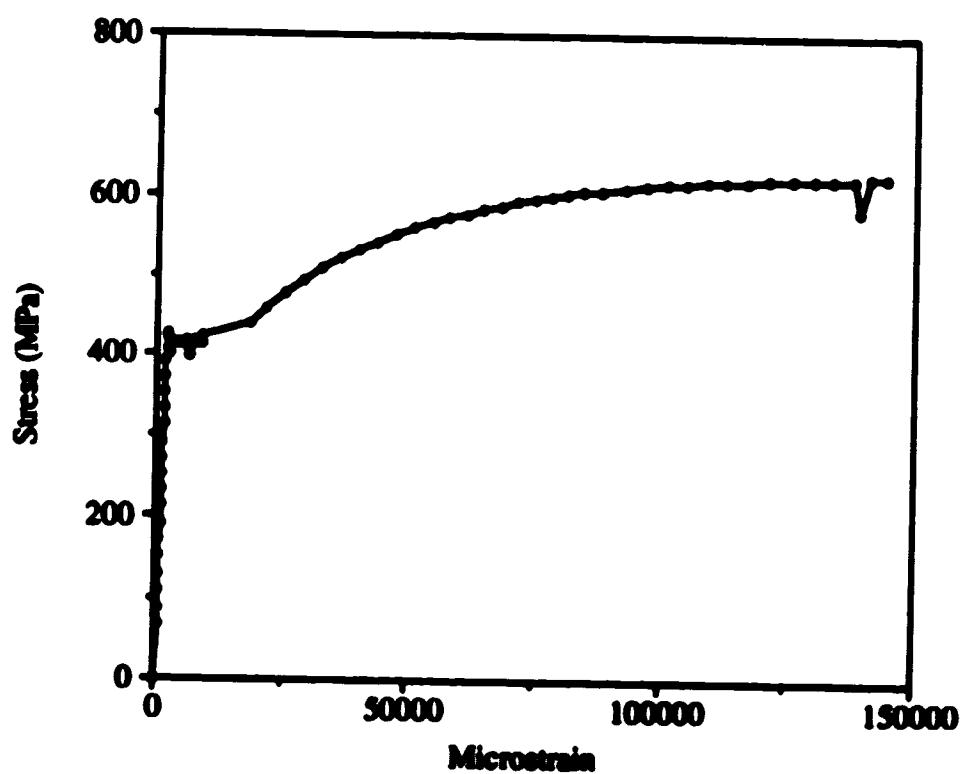


Figure 3.10 Stress Strain Curve for No.8 Bar

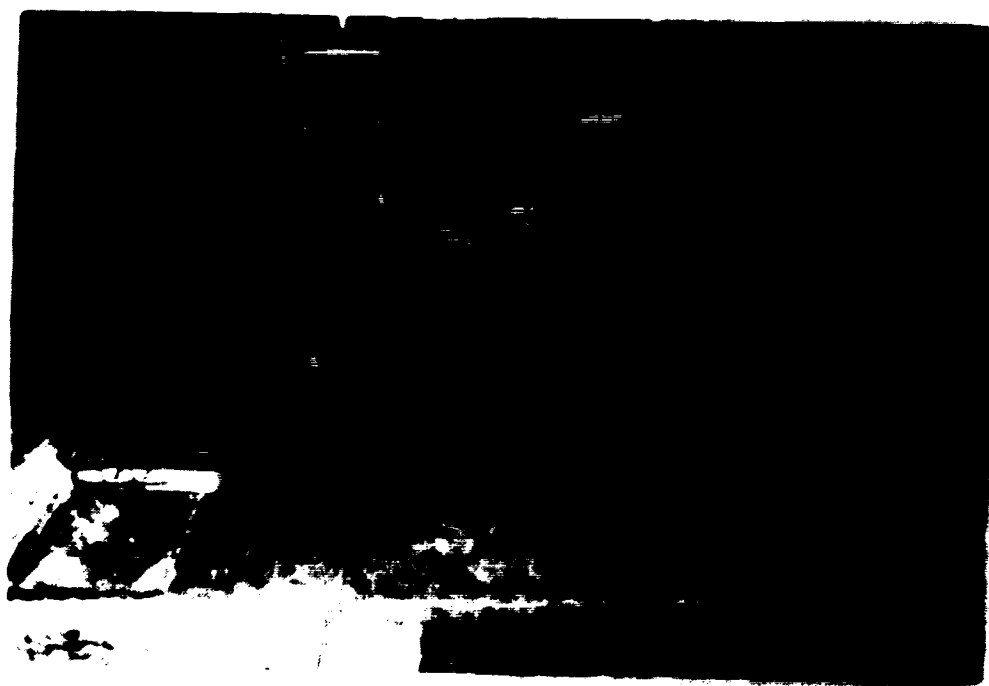


Figure 3.11 Assembling of the Steel Cage for Specimen T3 on the Floor



Figure 3.12 Placing of the Steel Cage of Specimen V16 inside the Form

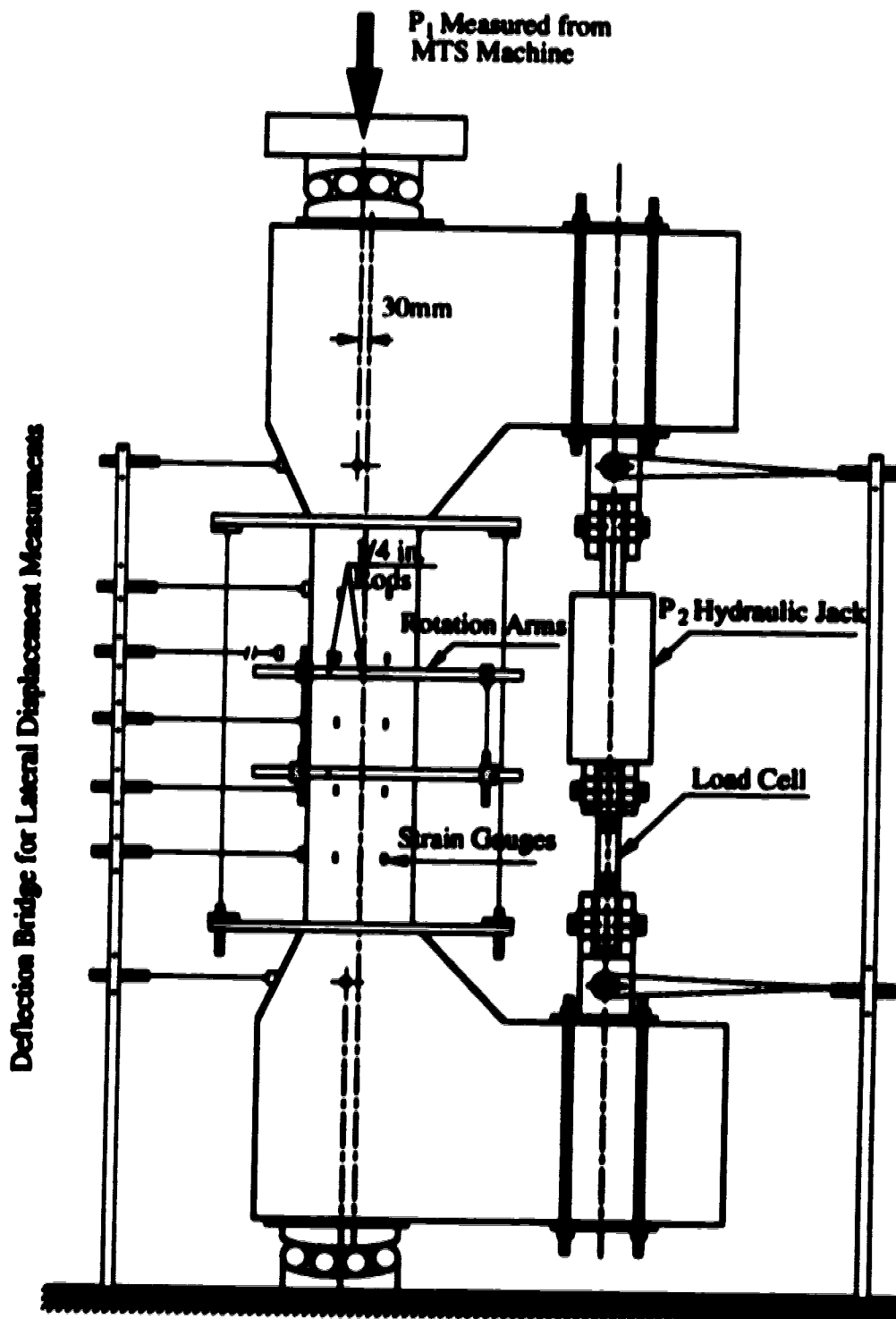


Figure 3.13 Details of Test Measurements

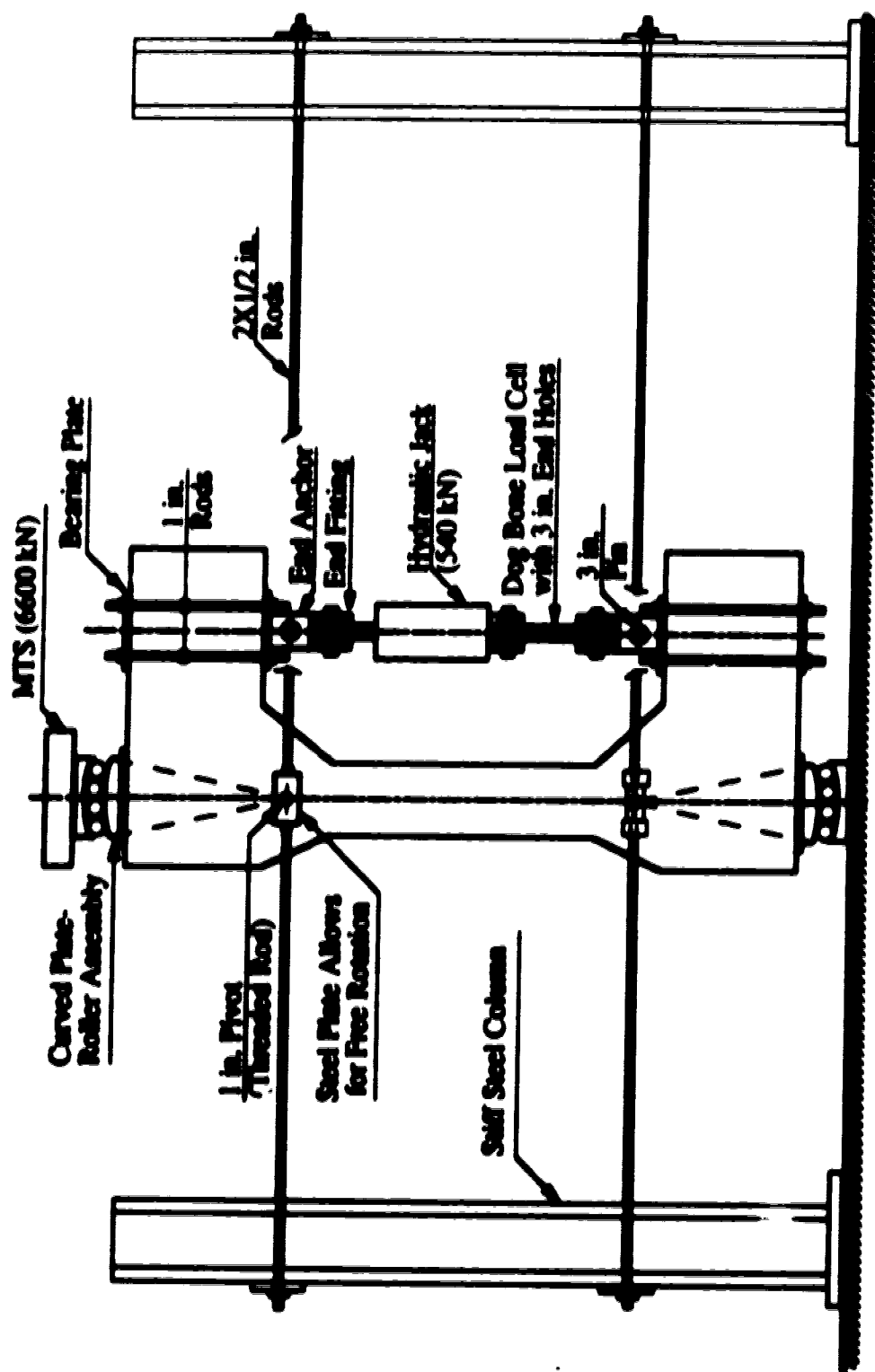


Figure 3.14 Details of Test Set-up

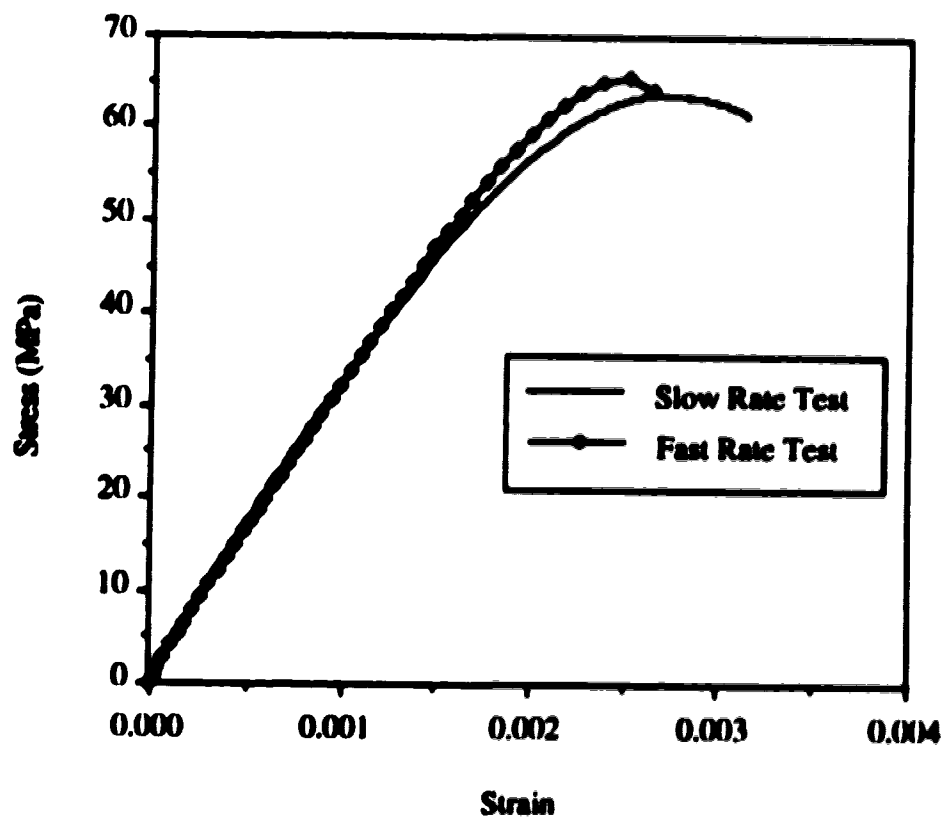


Figure 3.15 Cylinder Compression Tests with Different Rate of Loading

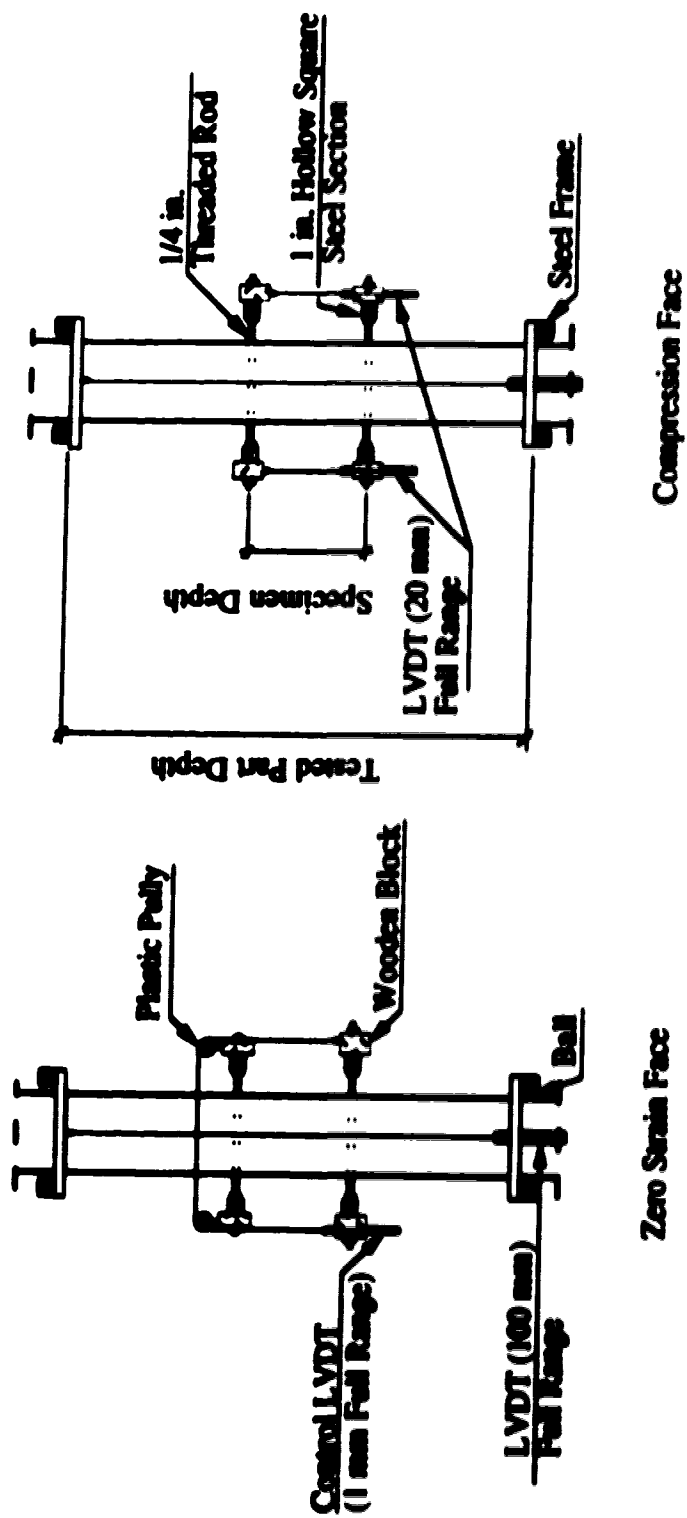


Figure 3.16 Details of LVDT Locations

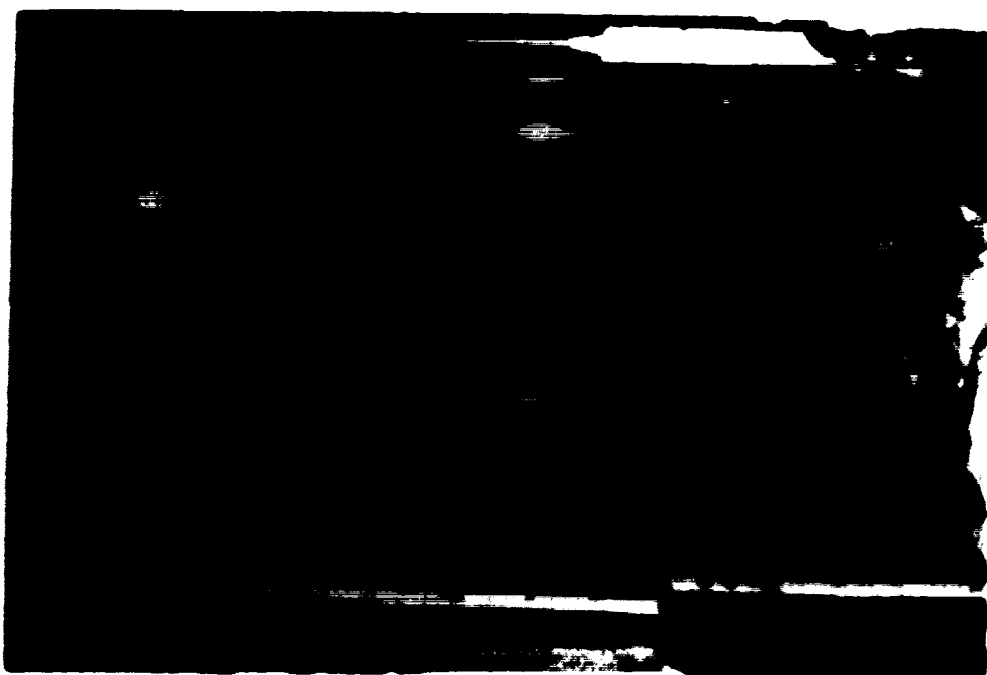


Figure 3.17 Test Set-up for Rectangular Specimens



Figure 3.18 Test Set-up for Triangular Specimens

4- Analysis of Test Results

4.1 General

Several problems were encountered during the test program and one of the specimens was damaged in the process. The plain concrete specimens were gauged in several different configurations in order to investigate the behavior of high strength concrete specimens in flexure. The reinforced specimens showed different behavior according to the concrete strength and lateral reinforcement arrangement.

Details of testing problems, strain measurements, behavior of specimens during the test and different failure modes are presented. The stress strain relationships obtained from the specimens are included in the discussion of this chapter. The methods that were used to obtain these graphs are explained in Chapter 5.

4.2 Problems Encountered in Testing

4.2.1 The Actual Position of the Neutral Axis

During each test, the neutral axis was maintained at a predetermined point, generally on the back face of the specimen as illustrated in Section 3.6. Several strain gauges were mounted in the back face of the specimen to measure the actual strain in that face. Figure 4.1 shows the strain gauge configuration.

In the first test (specimen V10), both loads were applied from the start using the stroke control system explained in Section 3.6. An external signal from an LVDT that was mounted on the center line of the test region was used to control the P_1 load instead of the MTS stroke control system. After applying 400 kN of the axial load P_1 and 30 kN of the eccentric load P_2 , the MTS head moved upward due to an error in the control signal. The axial load dropped to zero while the eccentric load was still applied to the specimen. Several tension cracks were observed in the back face (zero strain face) of the specimen. These tension cracks caused damage to the strain gauges mounted in that face. The P_1 load was adjusted after that and the test was continued. The results from this test showed lower capacity than any other test. Specimen V10 is not used in the analysis due to pre-cracking.

In the remaining tests, the procedures were changed to avoid another accident. The MTS stroke control system was used to control the P_1 load to prevent the dependency of the P_1 load on the stroke control system of the P_2 load. The P_1 load was applied first to maintain some compression stresses in the cross-section of the test part prior to applying hydraulic pressure in the P_2 load jack. The change in the reading of the LVDT was recorded. The initial P_2 load was then applied manually so that the readings of the LVDT

and the strain gauges of zero strain face indicate that the neutral axis was in the required position. The test started from this stage using the control system described in Section 3.6.

In all tests, the readings of the control LVDT did not show any significant change in the required position of the neutral axis. In most tests, no significant strains were measured by the strain gauges mounted on the back face of the specimens. Before spalling of the cover, these readings were in the range of ± 100 microstrain. During the tests of specimens V1 and T1, the readings of the strain gauges were significantly higher than the expected values.

To investigate the actual position of the neutral axis, the readings of the strain gauges on the back face were plotted versus the average strain at the compression face obtained from the LVDT's on the rotation arms, as illustrated in Figure 4.2 for specimen T1. This figure indicates that, despite the scatter in the strain gauge readings, significant compression strains were measured in the back face of the specimen. These readings suggest that the neutral axis was located outside of the specimen which gave a greater depth to the neutral axis. The same conclusion was reached by comparing the slope of the axial force-bending moment curve of the specimen with the curves of similar strength specimens. This comparison indicates that the specimen was subjected to loads with smaller eccentricity than that assumed in the original design of the experiment. The readings of the strain gauges appear to be correct. The scatter between their readings at different locations could be related to the non homogeneity of the concrete surface. The neutral axis was probably dislocated at the beginning of the test when the strain readings were very small and any error in the measurement could cause significant change in the neutral axis position. This error may have happened because the rotation arms that carried the control LVDT suffered from restriction of movement, so the control LVDT gave incorrect response.

The shift in the position of the neutral axis does not affect the analysis of the specimens as long as the actual position can be determined with reasonable accuracy. The actual position of the neutral axis was estimated using the average strain readings of gauges No.3 and No.4, shown in Figure 4.1 and the average strain readings obtained from the LVDT's of the rotation arms. These gauges were chosen in the analysis because they were located at the center line of the specimen where the desired position of the neutral axis was controlled. Using the average of the two readings eliminated the effect of any loading eccentricity.

Figure 4.3 shows the calculated depth to the neutral axis of specimen V8 during the test. The specimen had an overall depth of 300 mm. From Figure 4.3 the neutral axis depth used in the analysis was taken as 302 mm. Table 4.1 gives the average neutral axis

depths of all the specimens. These will be used in the analysis. For each specimen the neutral axis depth represents the average compression depth during the test with an error of $\pm 1\%$. The neutral axis depth was averaged over the range of compression face strain from 1000 microstrain to the failure strain of the plain concrete specimen or to the spalling strain of the concrete cover of the reinforced specimens. For strains that were lower than 1000 microstrain, the fluctuation in the readings of the strain gauges had a big effect in the calculated neutral axis depth and furthermore errors in the value of the neutral axis depth at this stage are not significant in the analysis. For strains higher than the spalling strain, the readings of the strain gauges were not useful. The drop in the P_2 load resulting from spalling of the concrete cover, did not occur fast enough, causing tension cracks in the back face. At this stage, the readings of the control LVDT showed good control of the position of the neutral axis while the readings of the strain gauges gave unreliable values. These readings were dependent on the location of the gauge and the crack patterns. A gauge adjacent to a tension cracks measured high tensile strains while a gauge located far from the tension cracks measured high compression strains.

For specimens V1 and T1 regression equations were used to express the compression depth, as illustrated in Figures 4.4 and 4.5. These equations were used to define the neutral axis position during the analysis. Figure 4.6 shows the calculated compression depth for Specimen V2. The specimen was tested under constant eccentricity without any control to the position of the neutral axis. Four LVDT's mounted on the rotation arms were used along with gauges No.3 and No.4 to calculate the position of the neutral axis for the specimen during the test.

4.2.2 Effects of Cracking on the Control System

The sudden and brittle spalling of the concrete cover for the UHSC specimens V5, V8, V14 and V17 caused vibrations in the rotation arms supporting the control LVDT. Because of these vibrations, the core of the control LVDT jumped out and the P_2 load dropped down to zero, while the P_1 load did not change. For specimen V8 which had few stirrups, no post peak behavior was expected and the test was terminated at that point. Specimen V14 failed during the attempt to reapply the P_2 load while the P_1 load was still in place. The results from this test are useful for the stress block analysis, but not for the ductility analysis. Specimen V15 was tested to duplicate the results of specimen V14.

Following the loss of the cover specimen V17 was unloaded and the test was started from the beginning. The same procedure was attempted for the plain concrete specimen V5. This specimen lost big pieces along the edges of the compression face of the test region, that caused the hydraulics to shut down, without having complete failure. The

specimen failed under much lower loads during the attempt to reapply the load. During the remaining tests, an elastic band was connected to the core of the LVDT to prevent any sudden movement.

4.2.3 Concrete Cylinder Compression Tests

As illustrated in Tables 3.8 and 3.9, compression tests were carried out in both 100x200 mm and 152x304 mm cylinders. The ratio between the compression strength of the 100x200 mm air cured cylinders to the compression strength of the 100x200 mm moist cured cylinders ranged between 0.87 to 0.97 with a mean value of 0.92. This ratio was 0.77 for the cylinders of specimen V17. The ratio between the compression strength of the 100x200 mm cylinders to the compression strength of the 152x304 mm cylinders ranged between 1.0 to 1.24 with a mean value of 1.10. An average ratio of 1.11 between the compression strength of 100x200 mm cylinders to 152x304 mm cylinders was suggested by Carrasquillo et al. (1981). Previous work by Leesaard et al. (1993) showed a mean value of 1.05.

During the test series, both types of cylinders were cast from the same concrete batches and had the same type of curing. The maximum size of the coarse aggregates (14 to 20 mm) was small compared to the size of the cylinder and should not cause any size effects on the compression tests. The variation in the strength between the two types of cylinders could be because of fabrication or testing procedures. Both types of cylinders were ground on a lathe to give planar end surfaces before testing and were tested using the same machine (2.6MN MTS rock mechanics machine) with the same bearing blocks. These blocks had a spherical seat with a radius (62 mm) that does not meet the requirements of ASTM Standard C39-83b, for testing 152 mm diameter cylinders. The axial stiffness of the load frame of the testing machine is 10.5×10^9 N/m and is not expected to affect the breaking load of the cylinders. It can only affect the descending branch of the load deformation relationship. However, Cole (1967), showed that the lateral rigidity of the testing machine is usually related to the longitudinal rigidity and the lateral instability has a marked effect upon the mode of failure of brittle test specimens.

The results of the 100x200 mm moist cured cylinders were chosen to represent the concrete strength. The fabrication and testing procedures seemed to be more adequate for that size. Because the strengths of the 100x200 mm cylinders exceeded those from 152x304 mm cylinders the results would thus be on the conservative side. The air cured cylinders did not follow the code procedures for curing control cylinders. The reason for testing air cured cylinders was to compare the stress strain curve of the cylinders with that obtained from the specimens, since the same curing procedures were applied in both cases.

4.2.4 P_2 Load Cell

Two load cells were used during the test program. The first load cell had a maximum capacity of 350 kN. The response of this load cell was linear for loads not higher than 250 kN. The load cell had a sensitivity of 2 kN within that range. This load cell was used to test the first six rectangular specimens where the P_2 load did not exceed 200 kN. During the test of specimen V16, the P_2 load dropped to zero without the specimen failing. The test was continued after fixing one of the hinges so that the loading system would be stable when compression load was applied. A sudden drop in the P_2 load caused buckling of the load cell. The load cell was replaced during the next tests. The second load cell had a maximum capacity of 550 kN. The response of the load cell was not linear and the loading part was different than the unloading part. A third order polynomial equation was used to express the relation between the voltage readings and the applied loads as shown in Figure 4.7. The calibration was carried out both at the beginning and the end of the test program.

4.3 Plain Concrete Specimens

4.3.1 Strain Gauge Configurations

During the test program, three plain concrete specimens with rectangular cross-section, V4, V5 and V6, and two plain concrete specimens with triangular cross-section, T1 and T4, were tested. Different strain gauge configurations were used for each specimen, as illustrated in Figures 4.8 to 4.11. The strain gauge configuration in the back face was as shown in Figure 4.1.

4.3.2 Strain Measurements

4.3.2.1 Assumption of Linear Strain Distribution

Figures 4.12 to 4.14 show the strain distributions at various loading stages for specimens V4, V6 and T4 respectively. The graphs indicate that the assumption of linear strain distribution in compression zones is true even for strain values that are close to failure. The strain values were calculated at four different locations. The average of two strain gauges were used to get each strain value. For the compression face more than two strain gauges were normally used to get the average value. Four inch strain gauges were used for specimen V4, while one inch strain gauges were used for specimens V6 and T4. The last reading for specimen V4 shows a low value of the strain at the compression face due to cracking at the position of the gauges.

4.3.2.2 Poisson's Ratio

Experimental data on Poisson's ratio for high strength concrete (HSC) are limited. Ahmad et al. (1987) conclude that Poisson's ratio for HSC in the elastic range seems compatible to the expected range of values for low strength concrete (LSC) (0.18-0.24) depending on the stress level. Poisson's ratio is expected to be lower in the inelastic range because of the smaller relative increase in lateral strains for HSC due to less microcracking, especially in the post peak region.

The transverse strains in the compression face and the side faces were measured using one inch strain gauges. For each strain gauge Poisson's ratio was obtained by dividing the reading of the gauge by the average compression strain reading calculated from the LVDT's of the rotation arms at the center line of the gauge. This method gives approximate values for Poisson's ratio. In order to have more accurate values, special strain gauges that measured the strains in two perpendicular directions should be used. The scatter in the calculated values of Poisson's ratio is illustrated in Figure 4.15. The figure shows the values obtained from different gauges for specimen V5 plotted versus the strain in the compression face. The scatter between different gauges readings was less in the elastic range and increased rapidly close to failure.

Figure 4.16 shows the average values of Poisson's ratio calculated from the gauges of the compression face for specimens V4, V5 and V6. These values are plotted versus the relative compression strains at that face, where ϵ_{max} is the strain at the maximum stress of the stress-strain curve of the specimen. The figure shows good agreement between the three specimens in the elastic and inelastic ranges. The average values of Poisson's ratio in the elastic range varied between 0.16-0.22. The value at peak stress was 0.40 for specimens V4 and V5, and 0.30 for specimen V6. In the post peak range, specimen V4 showed much higher values for Poisson's ratio. Specimens V5 and V6 had no post peak behavior. The strength of V4, V5 and V6 were 72.8, 124.8 and 98.8 MPa respectively. Specimens V5 and V6 had similar mix design but V5 had 10% replacement of the cement content by silica fume. The existence of silica fume in the concrete mix seemed to have no effect in the values of Poisson's ratio.

4.3.2.3 Longitudinal Strain Distribution

Figures 4.17 and 4.18 show the longitudinal strain distribution at the compression face of specimen V4 using 4 in. and 1 in. gauges respectively. The graph of the 4 in. gauges shows more uniform strain distribution than the graph of the 1 in. gauges which indicates that the 4 in. gauge length measures average strain values while the 1 in. gauge length

measures localized strain values. These localized strain values are highly affected by the surface condition and the maximum aggregate size which was 20 mm for some specimens and 14 mm for the others. The last two readings for the 4 in. strain gauges at the center line and at 200 mm above the center line of the test region showed lower strain values than the previous readings, while some of the 1 in. strain gauges in the same horizontal level showed unloading in the last readings. This decrease in the strain readings was due to loss of contact between the gauges and the concrete section because of spread of cracks prior to failure. The stress-strain curve obtained from specimen V4 showed that the peak stress occurred at strain value of 2800 microstrain. All the strain gauges on the compression face measured higher strain values than that value.

Figure 4.19 shows the longitudinal strain distribution in the back face of plain concrete specimen V4 using the 4 in. strain gauges. From the strain distribution in both faces shown in Figures 4.18 and 4.19, it can be concluded that, up to a compression face strain of about 2200 microstrain the strain distribution was almost identical at any horizontal section of the test region. For average strain higher than 3100 microstrain, the strain readings in the middle zone of the test region at the compression face increased rapidly while the strain readings in the same zone of the test region at the back face were still close to zero. The strain gauges in the top and bottom zones of the test region showed less increase in the strain readings at the compression face and a rapid increase in the strain readings at the back face. This change in the behavior indicates that a localized softening zone was forming in the middle of the test region where the neutral axis was controlled. The formation of this softening zone was accompanied with gradual reduction in the eccentricity of the total applied loads (eccentricity of $(P_1 + P_2)$). This reduction in the eccentricity of the applied loads caused trapezoidal strain distribution at sections away from the failure zone.

For the rest of the plain concrete specimens the strain distribution in the back face and the compression face was close to uniform to the end of the tests.

4.3.2.4 Transverse Strain Distribution on Compression Face

Figures 4.20 and 4.21 show the transverse strain distributions in the compression face of specimen V5 along two different axes as shown in Figure 4.9. The figures show that up to about 2500 microstrain of compression strain, the distribution of transverse strain was close to uniform along the member and across the member. At higher values of compression strain, the transverse strain readings in some gauges started to increase significantly, while the other gauges did not show any significant increase. This non uniform distribution of the transverse strain was noticed both longitudinally and

transversely. Close to failure the readings of the right side gauges showed significantly higher strain readings than the readings of the left side gauges.

The increase in the strain readings of some gauges reflected the existence of longitudinal cracks close to the locations of these gauges. The right corner of the compression face spalled off from the center line to the top of the test part just before the failure. The pattern of these cracks was compatible with the transverse strain profile close to failure. The same behavior was noticed in the readings for specimen V6. The highest strain reading was at the right top gauge, where the first spalling was observed.

4.3.2.5 Transverse Strain Distribution on Side Faces

Figures 4.22 to 4.24 show the transverse strain readings measured from the strain gauges on the side faces of specimen V5. These readings were plotted versus the transverse strain measured by the strain gauges in the compression face. Each strain reading of the side faces, is the average of the readings of the two strain gauges that were mounted in the same location in the opposite faces of the specimen. Each strain reading in the compression face is the average of the readings of the strain gauges that were mounted in the same horizontal plane with the gauges on the side faces.

The figures show that the transverse strain readings of the side face were much lower than the transverse strain readings of the compression face. In the elastic part, the transverse strain readings at the side faces were increasing linearly with the increase in the transverse strain readings at the compression face. In general there was a good agreement between the readings of different gauges. In the inelastic part, the behavior was different, the increase in the readings of the strain gauges of the side face was less than the increase in the readings of the strain gauges of the compression face. Figure 4.25 shows the transverse strain distribution at loading stage near failure in longitudinal sections of the side faces of specimen V5. At this loading stage the strain gauges in the middle zone of the test region showed less increase in the strain readings compared to the strain readings of the gauges far from the middle zone as illustrated in the figure. These lower readings of the strain in the middle zone were due to the deflected shape of the specimen. The deflected shape generated radial compression forces, as explained by Kotsavos (1982). From the strain readings of different gauges, the maximum difference between the readings of gauges at the middle region and gauges at top and bottom regions was 200 microstrain. According to the stress-strain curve of this specimen, the maximum value of the radial compression stresses was in the order of 5% of f'_c .

4.3.3 General Behavior and Failure Modes

The first sign of failure was the large increase in the readings of some strain gauges at the compression face of the test region. This increase was not proportion to the increase in the applied loads. This was followed by the first visible vertical small cracks which usually developed at the junction of the top of the compression face of the test region and the top end block. These cracks, which developed long before failure, were probably due to the stress concentrations at the transition zones. The next observation was the appearance of small vertical cracks along the edges of the compression face of the test region. These cracks usually started along one of the edges, followed by spalling of small pieces from that edge and more cracks along the other edge. At the same time some of the strain gauges at the locations of these cracks started to give meaningless numbers because of losing contact with the concrete section.

For specimen V4, the spalling was accompanied with unloading in the P_2 load while for specimens V5 and V6 the P_2 load did not show any unloading prior to failure. The P_1 load did not show any unloading prior to failure in any of the tests. The failure occurred suddenly in an explosive manner. The specimens failed by crushing in the most compressed fibers near the compression face with large pieces of the concrete thrown away from the test region. The failure surfaces were smooth, passing through the coarse aggregates and making an angle between sixty to ninety degrees with the horizontal. Several tensile cracks were observed on the pieces that were thrown from the back face of the test region. These cracks were generated at the failure moment due to the fast failure of the highly strained fibers while the eccentric load P_2 was still applied. Figures 4.26 and 4.27 show pictures for specimen V5 and V6 after testing.

For the triangular specimens, specimen T1 had the best controlled failure in all of the plain concrete specimens of the test series. The gradual cracking and spalling of the most compressed fibers near the apex of the triangular section did not affect the section capacity very much, since the major portion of the triangular section was subjected to relatively lower strains. This gradual loss of the section was accompanied by a decrease in the P_2 load. By controlling the movement of the MTS head, each time spalling occurred, the failure was controlled and the P_2 jack had enough time to respond decreasing the P_2 load value without having sudden failure. The test was terminated when the P_2 load dropped down to zero. The specimen was completely cracked but no explosive failure occurred. Specimen T4 had an explosive failure similar to the rectangular specimens. Before failure, some vertical cracks and spalling of concrete were noticed at the apex of the triangular section.

In general the HSC specimens showed more cracks prior to failure while the UHSC specimens failed in more explosive way with few visible cracks. The triangular HSC

specimen T1 showed more ductile behavior than the HSC rectangular specimens while the UHSC specimen T4 showed similar behavior to the UHSC rectangular specimens. The ultimate strain for the three plain rectangular specimens was close regardless of the strength of the specimen or the shape of the stress strain curve. The rectangular specimens failed at an average strain values ranging between 3800 to 4000 microstrain measured from the rotation arms. The triangular specimens failed at higher strain values than the rectangular specimens. Specimen T1 failed at an average strain value of 4200 microstrain, while specimen T4 failed at an average strain value of 4500 microstrain measured from the rotation arms. The values of 4200 and 4500 microstrain for specimens T1 and T4 respectively represents the strains at the first major loss of concrete from the apex of the triangular section, the test continued after that to an average strain of 5200 microstrain calculated at the apex of the cross section. This increase in the ultimate strain for the triangular sections was explained by Rüsch (1960).

4.3.4 Moment about the Neutral Axis

Moments about the neutral axis were normalized relative to the maximum moment measured during the test. Figure 4.28 shows the normalized moment about the neutral axis plotted versus the average compression strain at the compression face obtained from the rotation arms for the rectangular specimens. Specimen V4 showed higher relative moment with a short descending branch. The maximum moment was reached at a strain value that is higher than the strain value at maximum strength obtained from the stress strain curve of the specimen (presented in Chapter 5). Specimens V5 and V6 did not show any descending behavior in either the stress strain relationship or the moment strain relationship.

Figure 4.29 shows the moment about the neutral axis plotted against the compression face strain for the triangular specimens. The neutral axis for specimen T1 did not remain at a given location as explained in Section 4.2.1. The figure shows a brittle descending branch for specimen T1 and no descending behavior for specimen T4. The descending branch for the moment strain curve was formed by the consecutive loss of the most compressed fibers of the specimen as explained in Section 4.3.3.

4.3.5 Discussion of Post Peak Behavior of Concrete

By applying different boundary conditions on uniaxial tests of concrete cylinder and prism, Kotsavos (1983) concluded that, the descending branch of any stress-strain relationship is structure dependent. The descending branch obtained in uniaxial compression test is due to

the restraint of the deformation of the specimen by the testing device. If this restraint is eliminated, the specimen will suffer a complete and immediate loss of load carrying capacity as soon as the ultimate strength is exceeded. Kotsavos (1982) reached the same conclusion on beam tests that showed longitudinal compressive strains on the compression face in excess of 0.0035. Strain gauges were mounted in the compression face and the side faces. The strain readings of these gauges showed the following observations. The deflected shape of the beam caused radial compression forces in the side faces of the beam while the transverse strain distribution in the compression face was not uniform showing higher strains at the top of the flexural cracks of the beam. This non uniform distribution generated significant restraint forces at the highly strained regions. Kotsavos concluded that this ductile behavior and the observed high ultimate strain in the compression zone of a beam were caused by a complex multiaxial compressive state of stress below ultimate strength rather than post ultimate material characteristics.

In the test series reported here, the readings of the strain gauges indicate the existence of radial compression stresses due to the deflected shape. These stresses were estimated in Section 4.3.2.5 to be less than 5% of f'_c . Figures 4.20 and 4.21 of Section 4.3.2.4 showed non uniform transverse strain distribution at high longitudinal strains similar to the observation in Kotsavos beam tests. In the tests of specimen V5 and V6, the flexural cracks that occur on beam tests did not exist. Furthermore, using two rows of gauges instead of one row showed that this non uniform distribution of the transverse strain occurred in both directions depending on the location of the longitudinal cracks that developed in the compression face of the specimens.

van Mier (1986) conducted uniaxial compression tests in concrete prisms. He reached the conclusion that the descending branch of the stress-strain curve is a structural response rather than a material response. Localized strain softening is the reason for that behavior. After the peak load, localized fracture in uniaxial compression causes strain softening in part of the specimen referred to as the fracture zone while unloading is observed elsewhere. van Mier reached this conclusion by measuring the surface strain using electrical strain gauges. By testing different prism sizes, he showed that the post peak deformations of the fracture zone are not dependent on the specimen size. The part of the specimen outside the fracture zone unloaded. As a result the specimen size affects the descending branch. With increasing specimen height the descending branch becomes more brittle. van Mier predicted that Kotsavos could not measure the strain softening in his beam tests because of the relatively small size of the compression zone.

Hillerborg (1988) extended van Mier's work to flexural members. He treated the compression zone of a concrete beam as a uniaxially compressed specimen which means

that the deformations have to be described by means of a stress-strain curve for the ascending part and a stress-deformation curve for the descending part. This assumption lead to the conclusion that the stress-strain curve in a concrete beam and accordingly the rotational capacity should be inversely proportional to the beam depth. He supported his conclusion by using test data of Corley (1966).

In the test series reported here, the longitudinal strain distribution did not show any unloading after the peak stress was reached in the compression face as illustrated in Figures 4.17 and 4.18. Some of the gauges showed lower values very close to failure because of losing contact with the concrete section due to cracking. The size of the compression zone and the gauge length of the used strain gauges were quite suitable to measure this behavior if it did exist. The behavior of a uniaxially compressed specimen is different from the behavior of an eccentrically compressed specimen in the descending branch of loading history because of the different loading and boundary conditions. This suggests that Hillerborg's assumption that the compression zone of a beam behaves as a uniaxially compressed specimen is not true. Tests of HSC beams conducted by Alca et al. (1993) showed that the rotational capacity of beams subjected to pure flexure is not size dependent.

Bažant et al. (1991) showed that for uniaxial compression tests the softening must localize right after the peak stress state. Bažant predicted that softening of beams would happen when the moment decreases at increasing rotation. In most design cases this is unlikely to occur since the sections are well under reinforced in order to allow for the generation of the plastic hinges in all the structure before having failure. In some sections subjected to moment and high axial loads such as prestressed beams, columns or beams in frames, a pronounced softening is seen. In such a case Bažant predicted that the rotation stability would be size dependent.

Specimen V4 showed softening behavior, in a small part, with a decrease in the moment capacity with increases in the curvature as explained in Sections 4.3.2.3 and 4.3.4. The failure occurred because the softening became unstable because the energy released from the loading frame and the end blocks of the specimen, which were much less stressed, was higher than the energy that could be absorbed by the softening zone. The UHSC specimens V5 and V6 did not show any softening, the failure happened at the peak moment which corresponded to the peak stress too. By testing specimens made from brittle material like HSC, a complete softening branch, if it exists, is unlikely to be obtained by using a stroke controlled loading system. A more complicated test arrangement like the one used for cylinder tests is needed. The significance of obtaining the softening branch of plain concrete specimens is not clear since any real structure has a minimum amount of reinforcement which changes the behavior completely.

4.4 Reinforced Concrete Specimens

4.4.1 Average Longitudinal Strain

Three different measurement devices were used to estimate the longitudinal deformations of the specimens. Details of these measurement devices are given in Section 3.8 and Figure 3.16. The LVDT's between the rotation arms measured the average deformations of the concrete column over a gauge length equal to the depth of the cross-section of the test region, while the LVDT's between the steel frames at the end of the test region measured the average deformations over the entire test region. The strain gauges measured the surface strains in different locations along the test region. The strain gauge readings were highly affected by the surface condition and ceased to function after the spalling of the concrete cover. Using average values obtained from the readings of several strain gauges reduces the scatter in these readings and gives a reasonable estimate of the surface strain. The average strain at the compression face and at the back face of the test region could be calculated using the three independent measurement devices mentioned before.

Figure 4.30 shows the average strain at the compression face calculated by the three independent readings for specimens VII plotted versus the average strain from the rotation arms. The figure shows good agreement between the average readings of the strain gauges and the rotation arms at low strain. In all tests the differences between the two strain measurements were within 200 microstrain. This agreement indicates that at low strain, the concrete core and the concrete cover behaved in similar manners. In some practical cases, because of the low workability of the concrete mix, the quality of the concrete in the cover becomes lower than the quality of the concrete in the core of the column. At higher strain, close to the ultimate strain of the plain concrete specimens, the average readings of the strain gauges showed lower values than the average readings of the rotation arms. This change in the behavior was due to the separation of the cover from the core. The separation occurred because the concrete core was restrained from expansion by the ties and the concrete cover was free to expand laterally. At this stage the confinement reinforcement started to show some effect on the behavior of the specimen. The strain gauges showed unloading till the time of spalling where the concrete cover spalled off a portion of the compression face. In most of the UHSC specimen tests, the stage between separation and spalling of the concrete cover was quite short and was not noticeable.

Figure 4.30 also shows that at low strain readings, the readings from the gauges between the steel frames were in good agreement with the readings of the rotation arms. In all tests, the maximum differences between the two strain measurements were 400 microstrain for the rectangular specimens and 800 microstrain for the triangular specimens.

In all tests, the readings of the steel frame were lower than the readings of the rotation arms. These differences between the two strain readings were probably due to the deflected shape of the specimen during the test. The second order effect due to the deflected shape of the specimen caused higher applied moments in the middle zone of the test region than those applied in the upper and lower zones of the test region. At higher strain, close to and after spalling, the readings from the gauges between the steel frames show much lower values than the readings of the rotation arms. This observation was true in all tests.

Figure 4.31 shows the average strain in the back face of specimen V11, measured from the steel frame, the average of the strain gauges and the control LVDT. The figure shows good agreement between the readings of the control LVDT and the average readings of the strain gauges at low strain readings. After spalling of the concrete cover, the average readings of the strain gauges increased rapidly while the readings of the control LVDT did not show any significant change. The readings from the gauges between the steel frames show an increasing compression strain from the start of the test. In all tests, the maximum differences between the readings of the steel frame and the average of the strain gauges were within 500 microstrain.

The strain measurements shown in both figures indicate that before spalling of the cover the strain distribution in the test region was close to triangular at any horizontal section. After spalling of the cover, the average strain in the back face increased rapidly, while the average strains in the compression face increased slightly. The average strain distribution in the test region changed to trapezoidal, while the strain distribution in the middle zone of the test region where the neutral axis position was controlled was still triangular. The change in the behavior of the specimen after spalling was due to the uneven spalling of the cover. The cracks in the concrete cover were more concentrated in the middle zone and part of the top zone of the test region. As a result of that, the lower and part of the upper zones of the test region were subjected to less eccentricity of the applied loads. This decrease in the eccentricity of the applied loads caused an increase in the neutral axis depth which lead to the trapezoidal strain distribution in parts of the test region far from the middle zone. As the average strain in the test region increased, the vertical cracks continued to spread and widened causing more spalling in the middle zone and the longitudinal bars, which had already yielded, started to buckle, causing more damage in that region. Figures 4.32 and 4.33 show pictures of specimens V11 and V17 after testing. The pictures show that most of the damage happened in the middle zone of the test region.

The readings of the rotation arms give the best continuous measurement for the average longitudinal strain. Having the average strain calculated from two LVDT's

mounted in two different sets of arms, eliminates the effect of any small eccentricity of the loads in the direction of the minor axis. It also decreases the error if one of the LVDT's was not properly aligned due to the spread of cracks during the test. The readings of the two LVDT's were compared to each other in every test. In all tests, except for the tests of the plain concrete specimens V4 and T1, the readings of each of the two LVDT's over the average of the two readings were between 0.92 and 1.08. This ratio ranged from 0.96 to 1.04 at any loading stage before spalling of the cover. The uneven loss of the cover in the compression face and the side faces produced some moment about the minor axis of the cross-section. This moment caused an increase in the difference between the two readings of the LVDT's after spalling of the cover. For the plain concrete specimens V4 and T1, this ratio mentioned before ranged from 0.86 to 1.14 and 0.83 to 1.17 respectively. The readings of the strain gauges obtained from the two opposite faces of these two specimens did not show any noticeable eccentricity of the loads in the minor axis during the tests. The most probable reason for these differences is poor alignment of one of the LVDT's. However, for these two specimens, the average of the readings of the strain gauges versus the average of the readings of the rotation arms were compatible and this was used in data reduction.

The average strain obtained from the LVDT's on the rotation arms will be used to represent the longitudinal strain during the analysis of the specimens. The term, average compression face strain refers to the strain calculated at the compression face of the specimen based on the gross cross sectional dimensions even after spalling of the cover. The computation of the axial load carried by the longitudinal bars is based on their load-strain characteristics obtained from tension tests. The strains in the steel bars are estimated using the readings of the rotation arms calculated at the center line of the bars. It is assumed that no bond slip and no buckling of the longitudinal bars took place during testing, although inelastic buckling of the longitudinal bars occurred after spalling of the cover in many cases.

4.4.2 General Behavior and Failure Modes

Since the specimens were tested under the action of two loads with the position of the neutral axis controlled, the behavior of the specimen can be expressed in terms of axial loads and moments about the neutral axis (Figures 4.42 and 4.43 of Section 4.4.3 show the normalized neutral axis moment plotted versus the average compression face strain for the rectangular and triangular specimens).

During each test, the ascending part of loading history of the reinforcement specimens was the same as that for the plain concrete specimens which indicates that the

confinement had no effect on that part of the loading history. This observation was verified in Section 4.4.1 by the good agreement between the strain readings of the rotation arms and the average readings of the strain gauges on the compression face. The first peak of the moment about the neutral axis during the test was generally associated with the separation of the concrete cover. At this stage the confinement became effective due to the large increase in the transverse strain. The concrete cover gradually spalled off while the confined concrete core started to gain strength. The cover first spalled off in the compression face. At a later stage, the spalling of the cover extended to the side faces and to the ineffectively confined area close to the outer perimeter of the core. The longitudinal bars located near the compression face yielded long before spalling of the cover. The strain at which the longitudinal steel exhibited inelastic buckling was highly dependent on the confinement steel, especially on tie spacing.

Spalling of the cover caused a drop in the moment capacity which was indicated by a drop in the two applied loads. With further movement of the MTS head, the moment started to change. For well confined specimens, the moment reached a second peak. The absolute maximum was highly dependent on the lateral confinement and compression strength. For poorly confined specimens, the small increase in the capacity of the confined core could not balance the loss in the cross-section due to spalling of the cover. These specimens did not show a second peak and some of them had no descending behavior.

In all tests, the first visible vertical cracks developed at the junction of the top of the compression face of the test region and the top end block due to stress concentrations. These cracks were followed by other vertical cracks along the edges of the compression face of the test region. Later these extended towards the vertical center line of the compression face. When this occurred the strain gauges started to unload reflecting the separation of the cover. The spread of the vertical cracks in the compression face before spalling of the cover was more gradual for the HSC specimens than for the UHSC specimens in which the spalling happened suddenly with big pieces thrown away. The cover first spalled off from part of the compression face at an average compression strain between 4000 to 4500 microstrain for the rectangular specimens and between 4500 to 5000 microstrain for the triangular specimens. In some tests, significant horizontal tension cracks were noticed at the back face of the test region after the cover had spalled off. These cracks developed with the first spalling that occurred in the compression face because the P_2 load did not decrease fast enough, to account for the loss of the section, applying tensile strains to the less strained face (similar to the plain concrete specimens at failure).

Specimens V7, V8, V11 and V12 had single rectangular ties spaced 200 mm apart and four corner longitudinal bars. Except for specimen V11 these columns showed no

descending behavior. The increase in the capacity of the confined core was not enough to compensate for the loss of the concrete cover. The spalling that happened in an uneven manner at different spots on the compression face, was followed by buckling of the longitudinal bars at failure. Figures 4.34 and 4.35 show pictures for specimens V7 and V12 after testing. Figure 4.34 shows that compression failure occurred also in the back face at the bottom part of the test region of specimen V7 (not in the same level with the spalling in the compression face). This compression failure occurred suddenly at the end of the test and was notified by buckling of the longitudinal bars adjacent to that face.

Specimen V11 showed behavior similar to specimens V13 and V15, which had single rectangular ties spaced 100 mm apart and four corner longitudinal bars. At the first peak, each specimen showed a sudden decrease in the P_2 load and a minor decrease in the P_1 load. The test continued with the P_1 load maintained at almost the same value while the P_2 load continued to decrease. The drop in the P_2 load was more gradual for the HSC specimen while for the UHSC the drop in the load was sharp and sudden. Each drop in the P_2 load was followed by a less steep unloading part. This behavior reflected the gradual loss of the cover for the HSC specimen and the more brittle and sudden loss of the cover for the UHSC specimen. The test was ended when the P_2 load dropped to zero, without having complete failure, at an average strain at the location of the compression face between 5500 to 6000 microstrain. Figures 4.36 and 4.37 show pictures for specimen V15 after testing showing that the cracks of the compression face extended to the side faces. The pictures also show the tension cracks that happened prior to failure and the spalling of the cover that happened at failure at the back face of the test region in the same level with the spalling in the compression face.

Specimens V16 and V17 which had a double tie configuration spaced 50 mm apart and eight longitudinal bars, showed no decrease in the P_1 load after the first peak. The load continued to increase with less steep slope while the P_2 load showed a gradual decrease in magnitude. Each test continued to high strain values without failure. The average compression strain at failure at the location of the compression face was 1100 microstrain and 18000 microstrain for specimens V16 and V17 respectively. The test was ended when the P_2 load had dropped to zero. Figures 4.38 and 4.39 show specimen V16 after testing with cracks extended in the four faces of the specimen.

The triangular specimens showed more ductile behavior than the rectangular specimens. The cover spalled off in a more gradual and less brittle manner. Specimens T2 and T5 which had three longitudinal bars and lateral reinforcement similar to specimens V13 and V15, showed an increase in the P_1 load and a more gradual decrease in the P_2 load after the first peak. Each test was ended without having a complete failure when the P_2

load had dropped to zero. Specimens T3 and T6, with less lateral reinforcement than specimens V16 and V17, showed similar ductile behavior. Figures 4.40 and 4.41 show specimen T5 after testing.

4.4.3 Moment about the Neutral Axis

For each specimen, the moments about the neutral axis were normalized with respect to the moment value at the first peak before spalling of the concrete cover and plotted versus the average compression face strains. In order to study the effect of each variable on the behavior of the specimens, the normalized curves are compared in Figures 4.42 to 4.48 with respect to each of the following variables: compression strength, volumetric ratio of the ties, tie spacing, testing method, position of the neutral axis and section geometry. The results of this study is summarized as follows:

The effect of confinement on the behavior of the rectangular specimens was small or did not exist, except for specimens V16 and V17 as shown in Figure 4.42. Specimen V7 and V8, which had single rectangular ties (8 mm in diameter) spaced 200 mm apart and four corner longitudinal bars, showed similar behavior to the plain concrete specimens V4 and V5. The HSC specimens V4 and V7 had small descending branch while the UHSC specimens V5 and V8 showed no descending behavior. Specimens V13 and V15, which had single rectangular ties (8 mm in diameter) spaced 100 mm apart and four corner longitudinal bars, showed a sharp decrease in the moment capacity after the first peak. Each specimen had a short and steep descending branch and the moment did not reach a second peak. Specimens V16 and V17, with sufficient amount of lateral reinforcement to confine the core, exhibited ductile behavior. Specimen V16 did not show any reduction in the moment capacity after the first peak, the moment increased gradually till it reached the second peak at higher strain. The second peak was 10% higher than the first peak. The test was ended shortly after the second peak because the P_2 load dropped down to zero. Specimen V17 with the same steel configuration and higher strength concrete, showed reduction in the moment capacity after the first peak, where the test was stopped and the specimen was loaded from the beginning. In Figure 4.42 the first loading path of specimen V17 is denoting by V17(1) while the second loading path is denoting by V17(2). The second peak was 6% lower than the first peak and was followed by a very gradual decrease in the moment capacity. The increase in ductility for specimens V16 and V17 was due to interaction between the different variables that affecting the ductility of confined concrete.

Figure 4.43 shows the normalized neutral axis moment for the triangular specimens plotted versus the average strain at the compression face. The HSC plain concrete specimen T1 showed a steep descending branch while the UHSC plain concrete specimen

T4 showed no descending behavior. Specimens T2 and T5, which had ties (8 mm in diameter) spaced 100 mm apart and longitudinal bars in the columns, did not show reduction in the moment capacity after the first peak. The second peak for specimen T2 was 2% higher than the first peak followed by relatively short part with a gradual decrease in the moment capacity. This amount of lateral reinforcement introduced a significant improvement in the behavior of specimens T2 and T5 compared to the plain concrete specimens T1 and T4. Specimens T3 and T6, which had ties (8 mm in diameter) spaced 50 mm apart and longitudinal bars in the columns, exhibited ductile behavior. The specimens showed a second peak load that is from 3 to 9 % higher than the first peak followed by a long horizontal plateau.

The rectangular specimens showed that the effectiveness of lateral confinement on the capacity after spalling was reduced by increasing the concrete strength, while the triangular specimens showed a slight improvement in the ductility of the UHSC specimens compared to the HSC specimens. Thus, there is agreement between these tests of the rectangular specimens and previous tests about the reduction in the effectiveness of ductility by increasing the strength. The only difference between the test procedures for the HSC and UHSC triangular specimens was the age of testing. The HSC specimens were tested at ages of 5 to 7 weeks, while the UHSC specimens were tested at ages of 21 to 22 weeks.

Figure 4.44 shows that increasing the volumetric reinforcement ratio from 0.5% to 1.0% did not show any significant increase in the ductility of the UHSC specimens. Specimen V8 which had 0.5% volumetric reinforcement ratio, showed no descending behavior, while one of two specimens that had a 1% volumetric reinforcement ratio showed the same behavior. The other specimen showed a short and brittle descending branch of the moment strain curve. The insignificant change in the behavior could be related to the large spacing of the ties (200 mm) and the relatively low volumetric reinforcement ratio in both cases. Bjerkeli et al. (1990) showed significant increase in the strength and ductility of columns tested with 3.1% lateral reinforcement ratio compared to columns that had 1.1% lateral reinforcement ratio.

Decreasing the spacing of the ties from 200 mm to 100 mm with the same volumetric ratio, led to marginally better performance without much increase in the ductility as illustrated in Figure 4.45. One of the specimens with 200 mm tie spacing, failed at the moment of spalling, while the specimens with 100 mm spacing ties exhibited a short and brittle descending behavior.

The constant eccentricity specimen V2 reached the first peak at higher strain than the corresponding specimen with controlled neutral axis position V13. The different slope of the ascending part, shown in Figure 4.46, could be related to the larger eccentricity of the

applied load during the constant eccentricity test especially close to the end of the test. The constant eccentricity specimen failed after the first peak with almost no descending branch while the specimens that tested with constant position of the neutral axis exhibited a short and brittle descending behavior.

Specimen V1 with trapezoidal strain profile resulting from the loads being applied with smaller eccentricity showed a slightly earlier spalling of the cover than comparable specimens V11 and V13. The descending branch behavior of this specimen was not significantly different from that of specimen V13 as shown in Figure 4.47.

The section geometry had a significant influence on the behavior of the specimens. The triangular specimens showed higher strain at the first peak and exhibited more ductile behavior after that. Figure 4.48 compares the behavior of rectangular and triangular specimens that had similar lateral reinforcement.

4.4.4 Lateral Steel Requirements by the Code

The reinforcement of the rectangular specimens was chosen to satisfy the minimum requirements of Clause 7.6.5 of the Canadian Code CAN3-A23.3-M84 for the design of tied columns. The specimens did not satisfy the requirement of the Code for the minimum thickness of the concrete cover of 40 mm. Some of the specimens did not satisfy the minimum diameter size of 10 mm for the lateral reinforcement recommended by Clause 7.10.5 of the ACI 318-89. Clause 21.4.4 of the Canadian Code and Clause 21.4.4 of the ACI Code for design of columns in seismic regions required an amount of lateral reinforcement that is higher than the actual amount of reinforcement of any of the specimens. Specimen V16 satisfied the requirements of the codes for minimum volumetric ratio but for the tie arrangement of this specimen, if the tie size remains the same, the tie spacing should be reduced from 50 mm to 37.5 mm to satisfy the code spacing requirements. Specimen V17 with the same reinforcement and higher compressive strength, required a volumetric ratio of 0.055 and spacing of 18 mm for the ties to satisfy the code requirements.

The test results suggested that, the code recommendations for maximum tie spacing of tied columns, which is 200 mm for the size of test specimens, is not conservative and should be decreased to avoid sudden failure with the spalling of the cover. Although specimens V16 and V17 did not satisfy the requirements for design according to the seismic design rules, they showed relatively good ductility under monotonically increasing loads especially for the HSC specimen, V16. The close spacing of the ties observed here suggests that the code requirements may be difficult to achieve for high strength concretes without using very high yield strength ties.

Table 4.1 Neutral Axis Depth of Different Specimens

Specimen No.	Design Neutral Axis Depth (mm)	Average Actual Depth (mm)	Remarks
V1	461.5	—	See Figure 4.4
V2	was not controlled	—	See Figure 4.6
V4	303	302	2% maximum error
V5	303	294	
V6	303	298	
V7	303	303	
V8	303	302	1.5% maximum error
V11	303	302	
V12	303	300	
V13	303	295	
V14	303	296	
V15	303	305	
V16	303	298	
V17	303	296	
T1	242	—	See Figure 4.5
T2	242	234	
T3	242	242	
T4	242	240	
T5	242	235	
T6	242	240	

Specimen	Strain Gauges
V1, V4, V5 V7, V8, V11 V13, V14 V16, V17	4 in. Gauge Length
V2, V6, V12 V15, T1, T2 T3, T4, T5 T6	1 in. Gauge Length

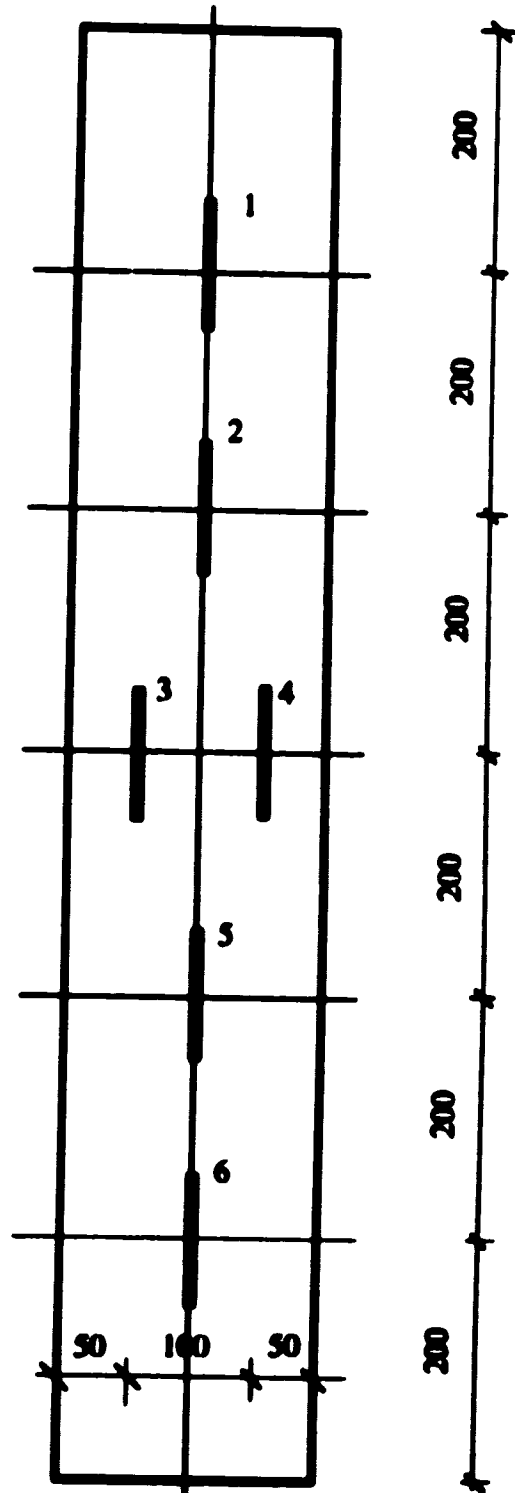


Figure 4.1 Strain Gauge Configuration on the Back Face of the Specimens

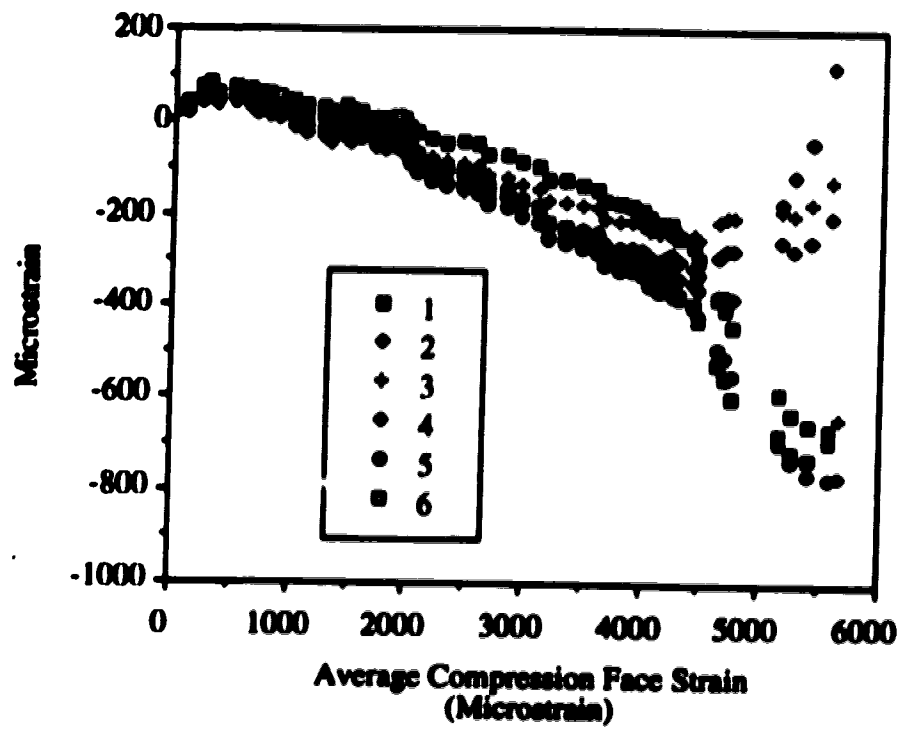


Figure 4.2 Readings of the Strain Gauges on the Back Face of Specimen T1

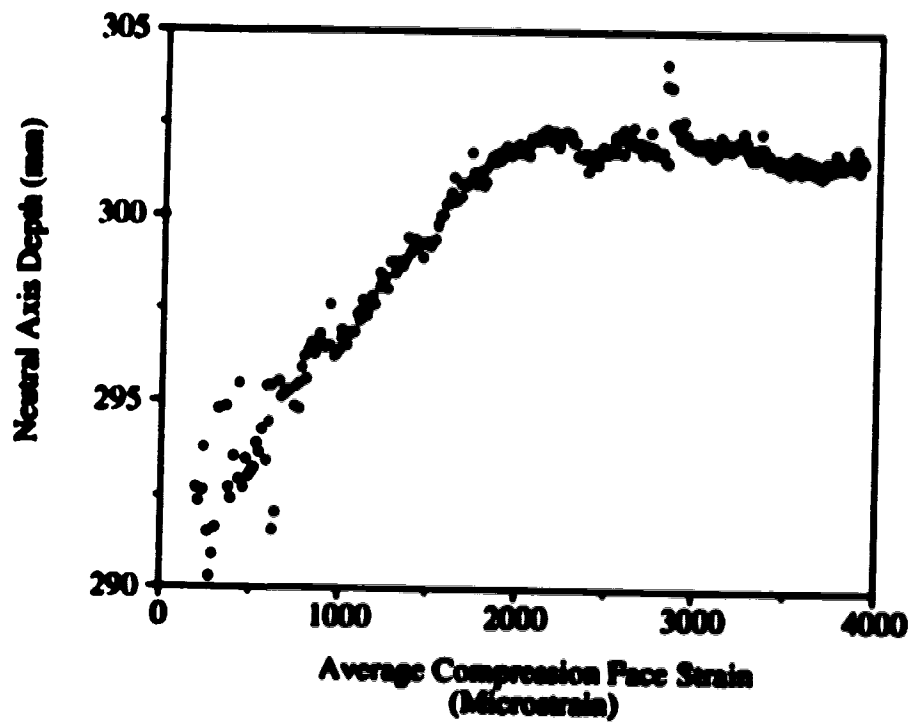


Figure 4.3 Neutral Axis Depth of Specimen V8

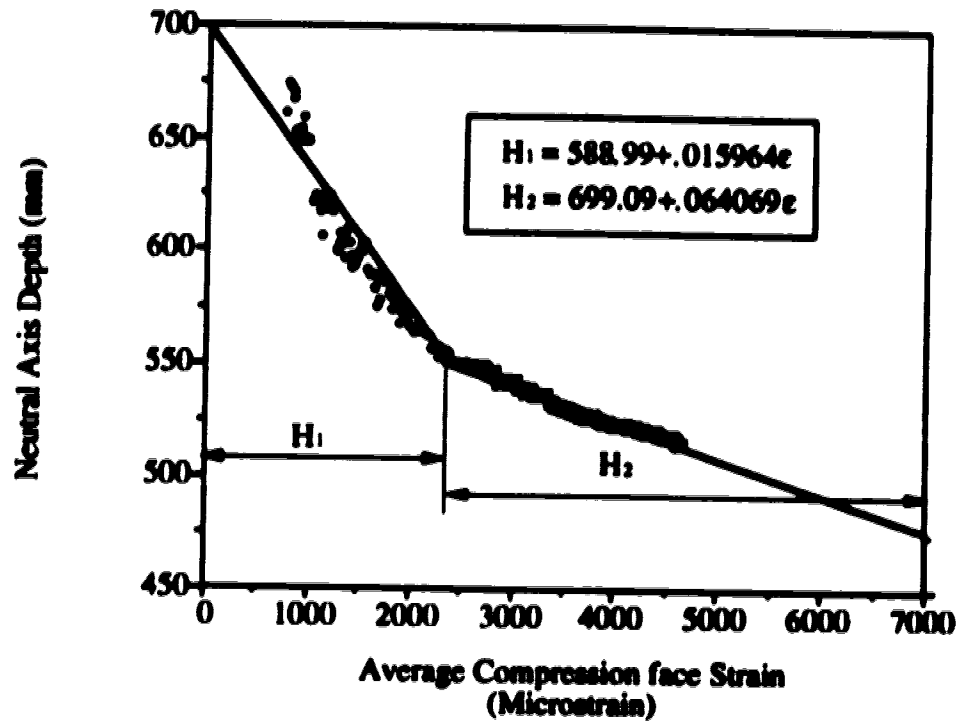


Figure 4.4 Neutral Axis Depth of Specimen V1

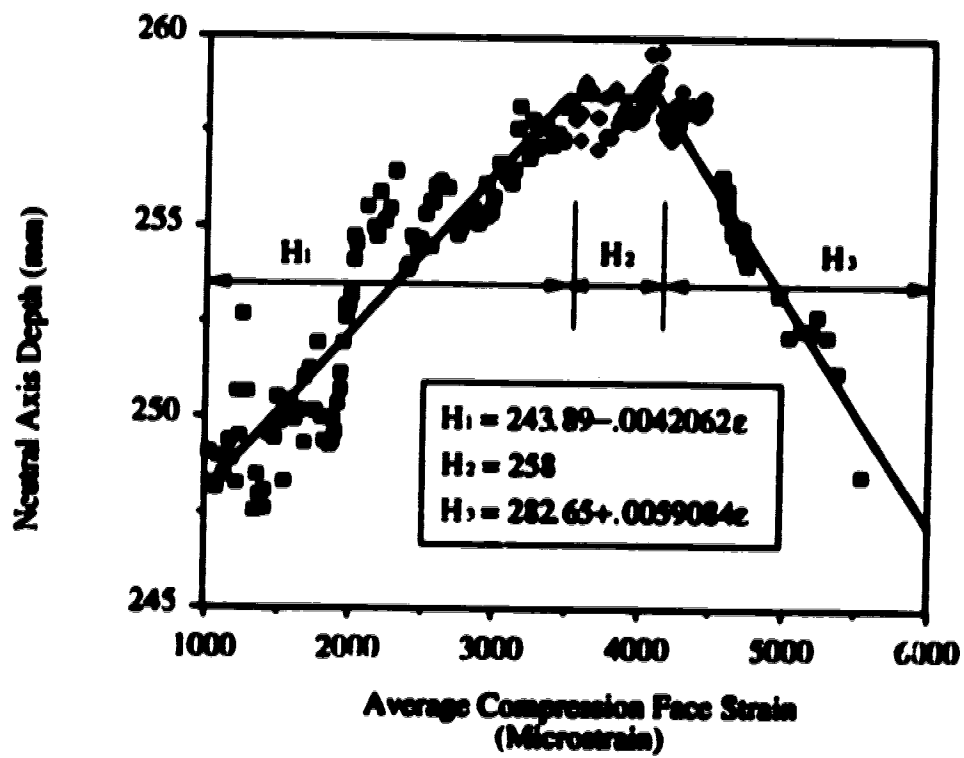


Figure 4.5 Neutral Axis Depth of Specimen T1

100

PRECISION™ RESOLUTION TARGETS

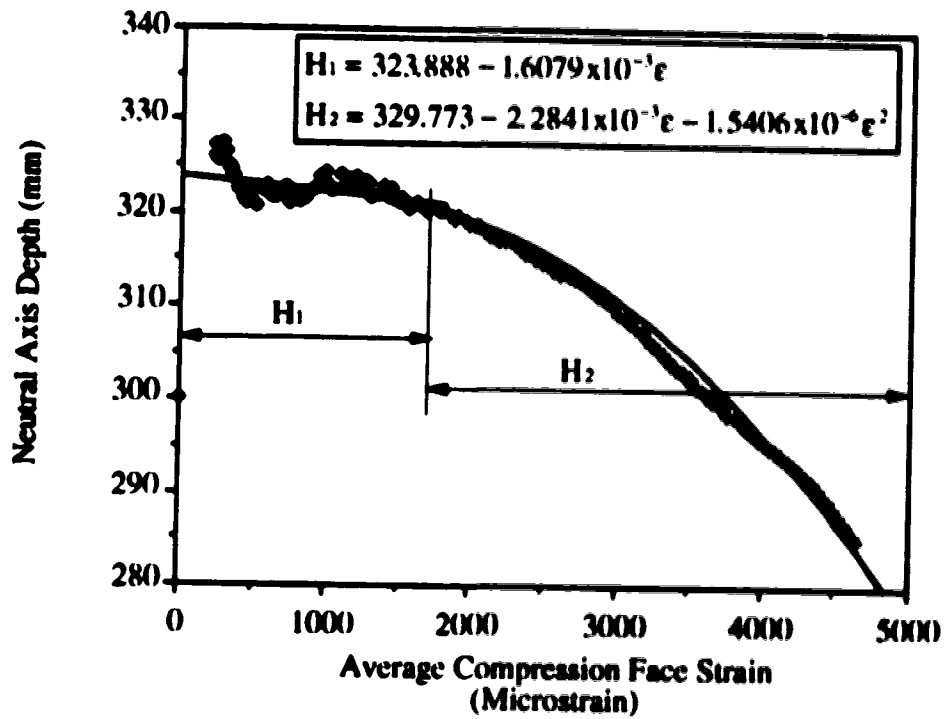


Figure 4.6 Neutral Axis Depth of Specimen V2

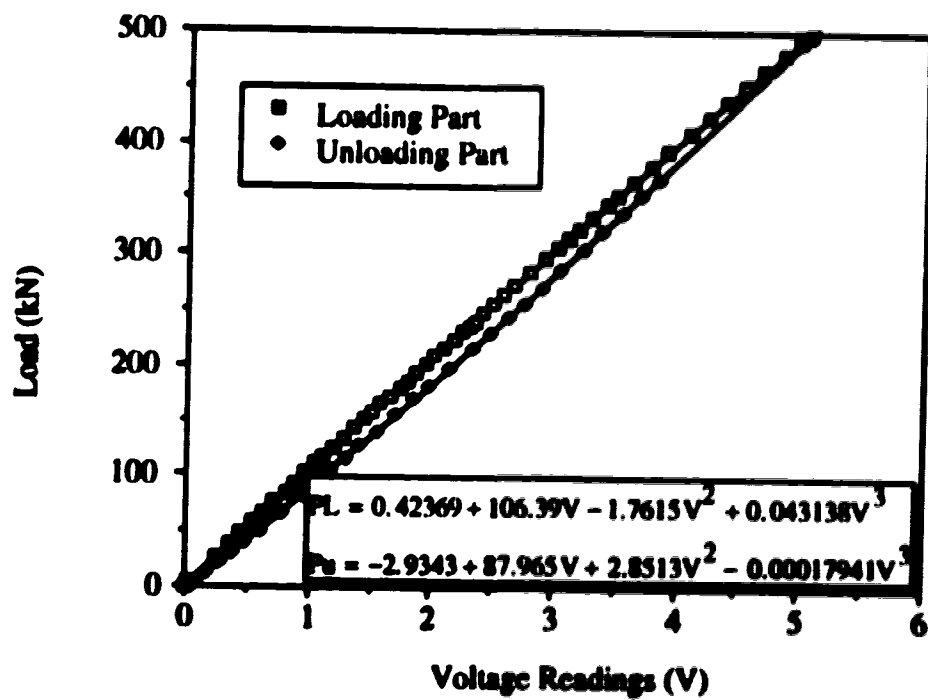


Figure 4.7 Calibration Equations for P₂ Load Cell

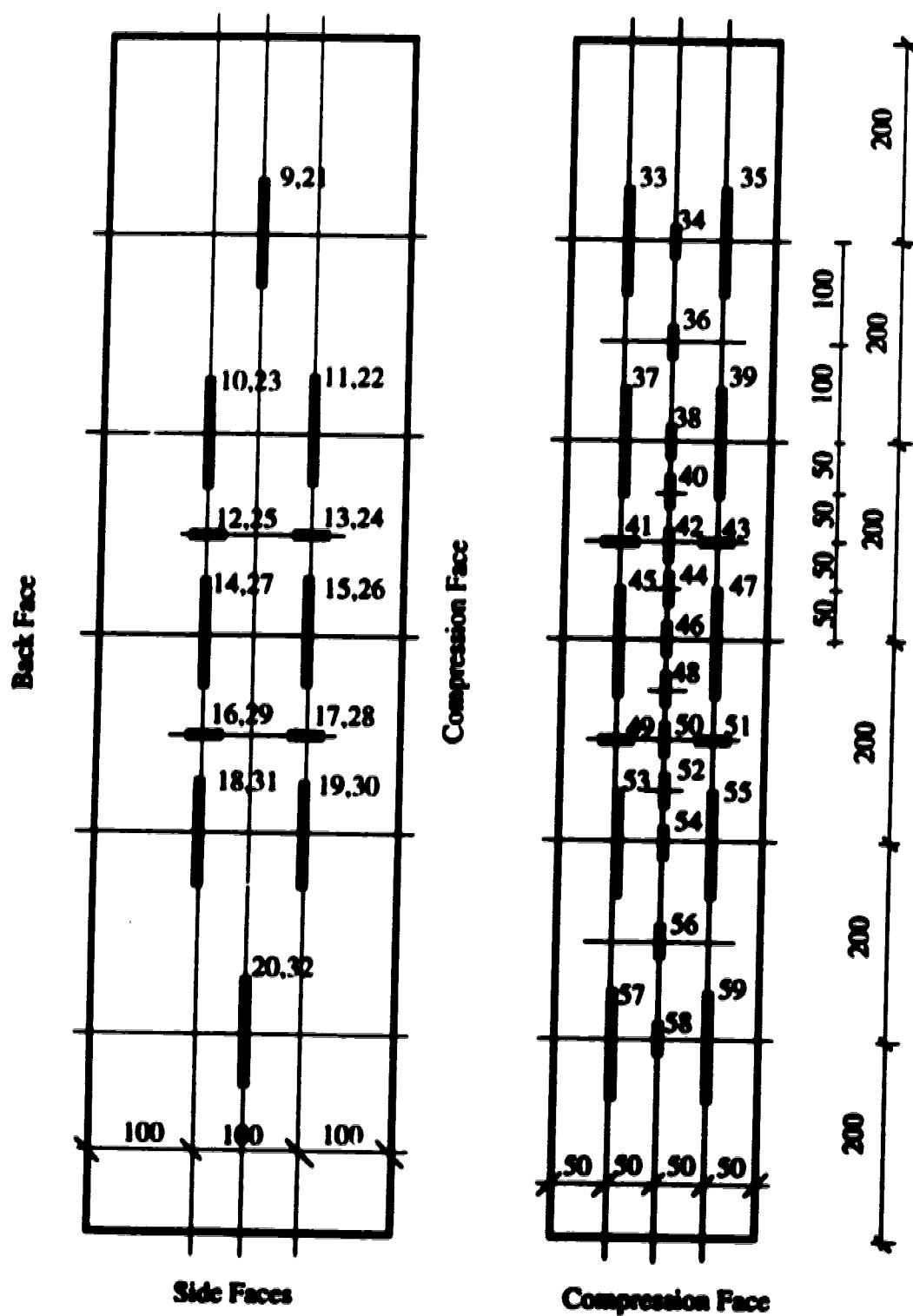


Figure 4.8 Strain Gauge Configurations for Specimen V4

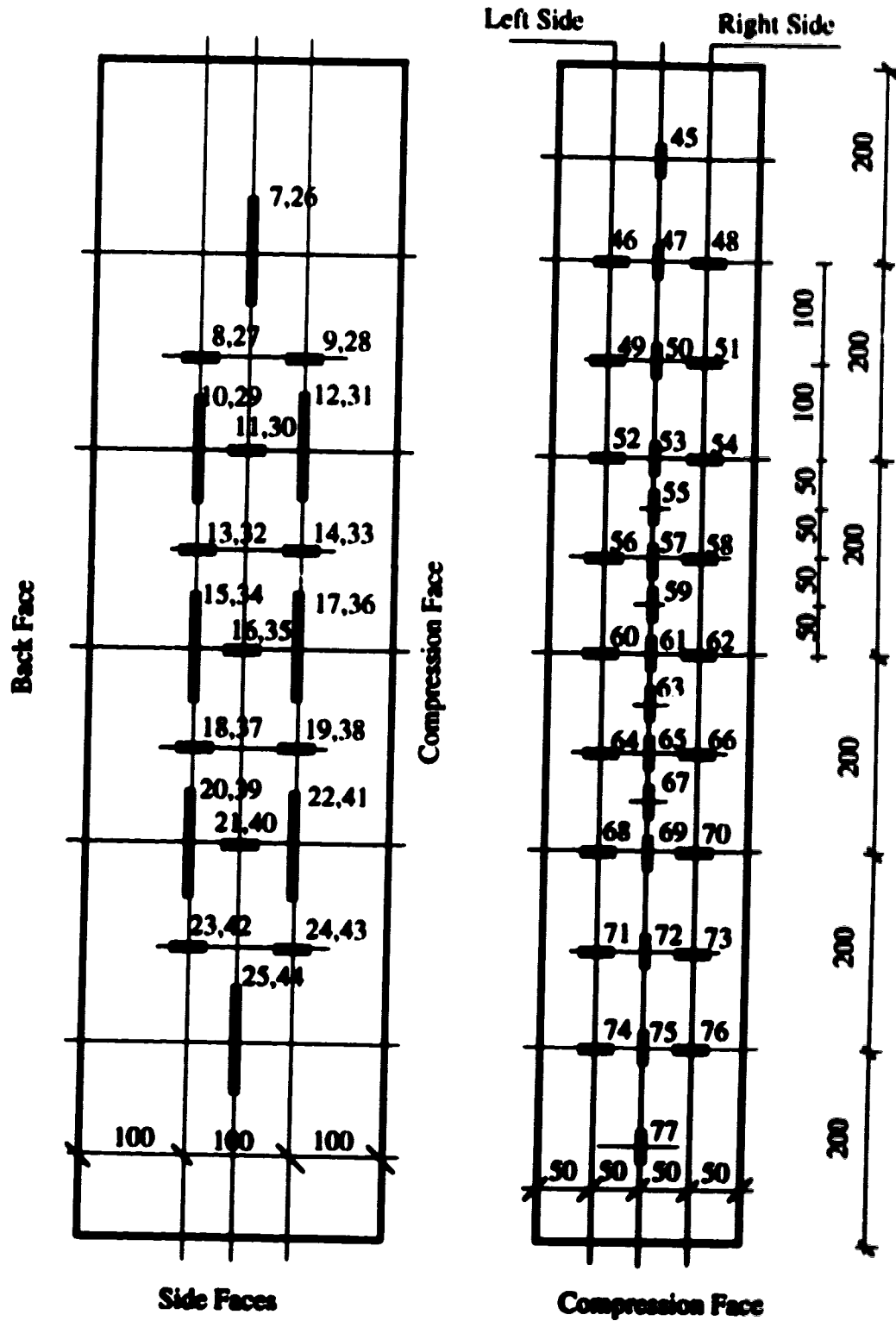


Figure 4.9 Strain Gauge Configurations for Specimen V5

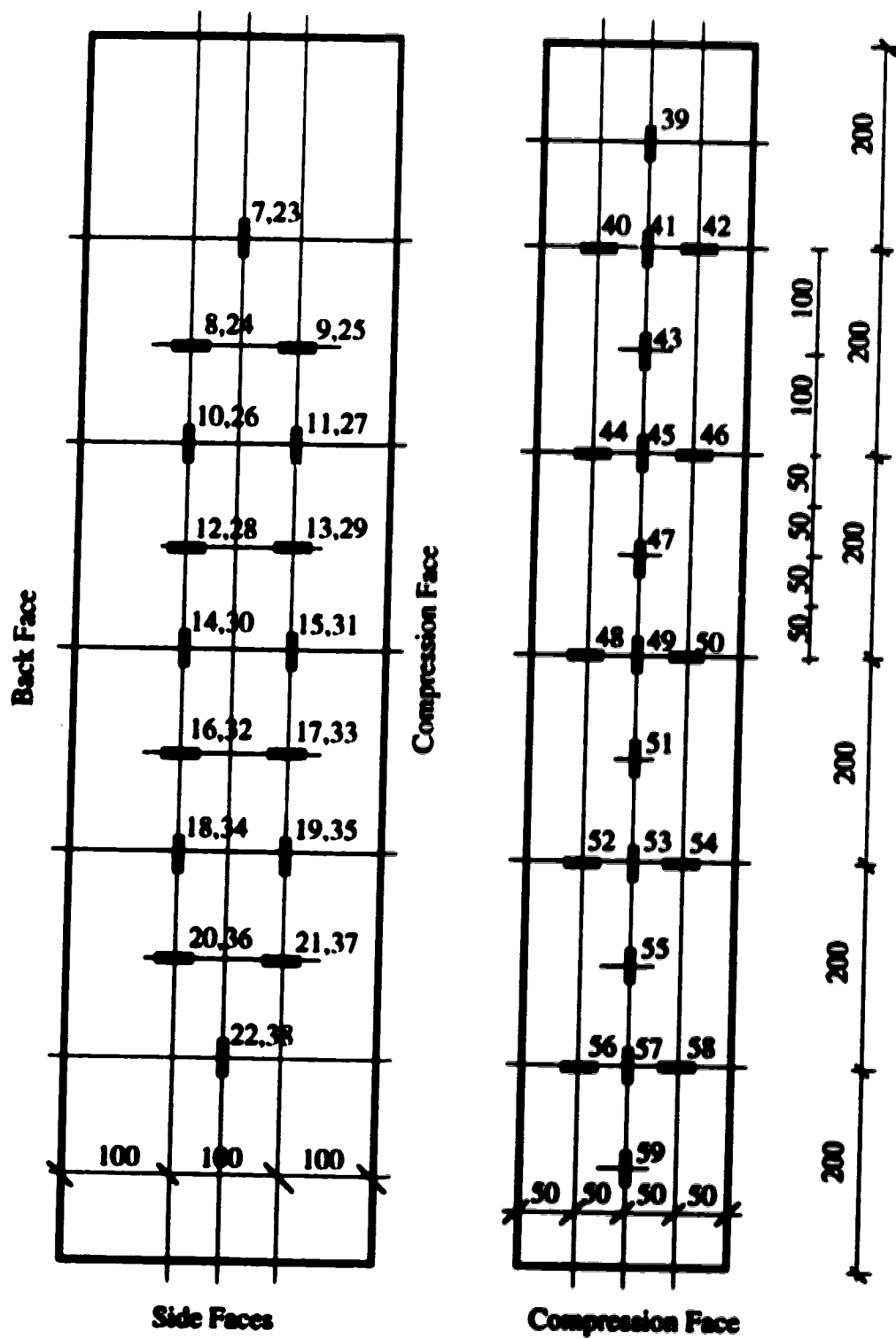


Figure 4.10 Strain Gauge Configurations for Specimen V6

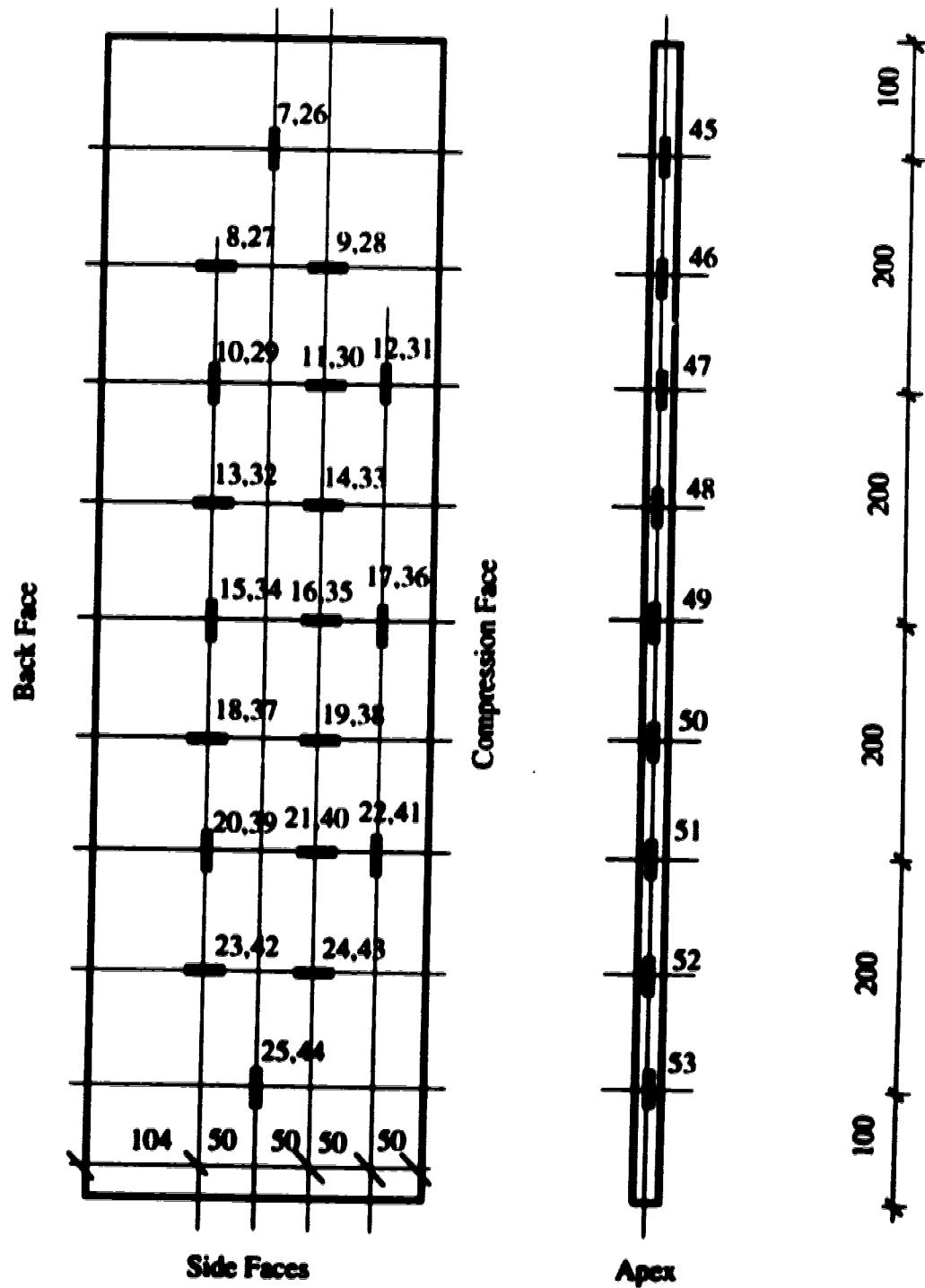


Figure 4.11 Strain Gauge Configurations for Specimens T1 and T4

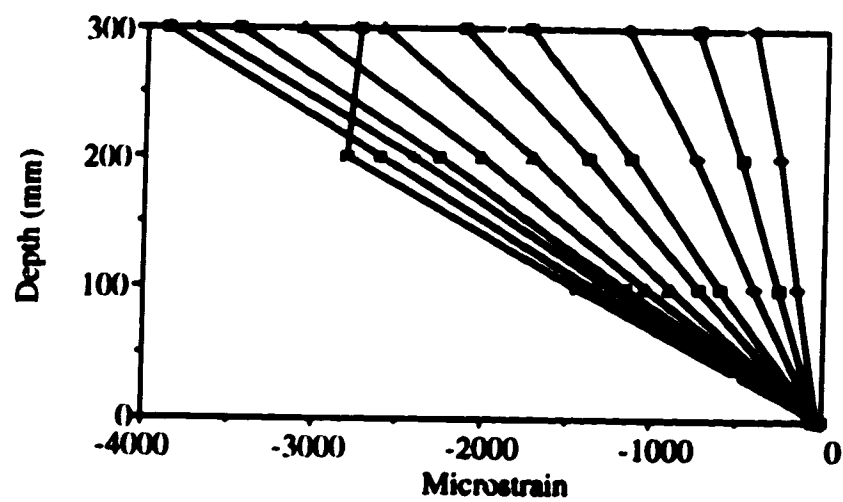


Figure 4.12 Strain Distribution for Specimen V4

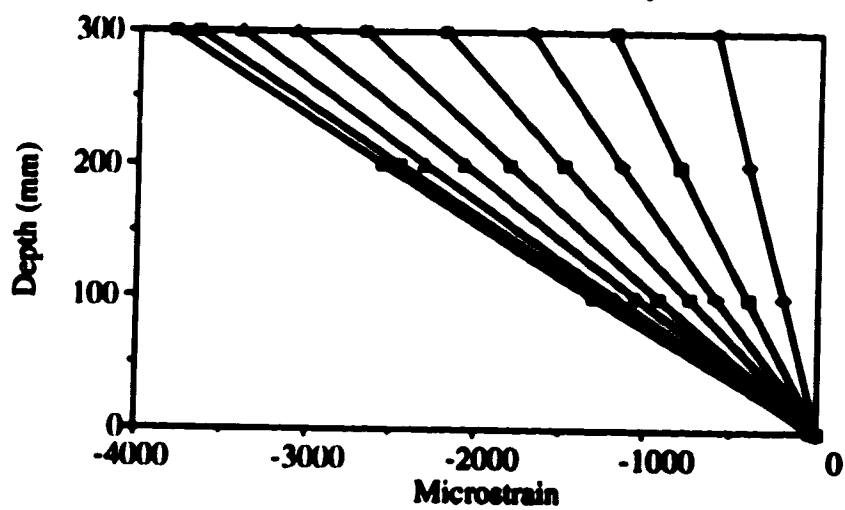


Figure 4.13 Strain Distribution for Specimen V6

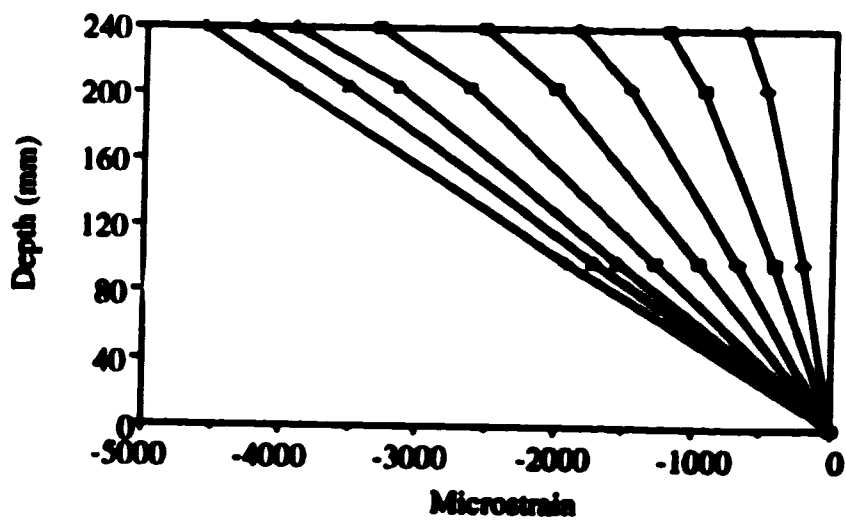


Figure 4.14 Strain Distribution for Specimen T4

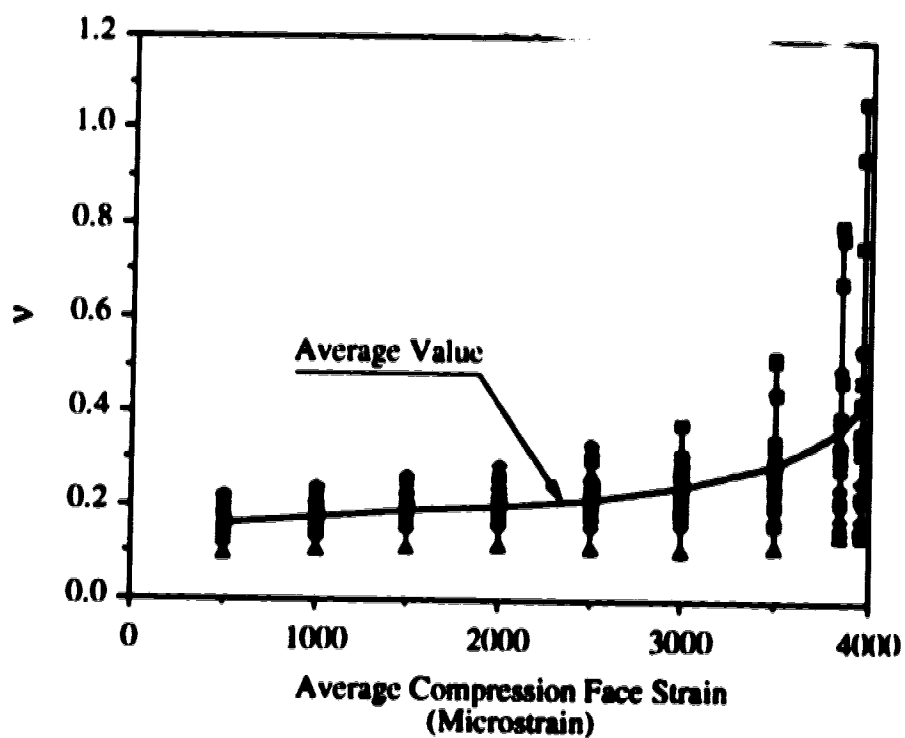


Figure 4.15 Poisson's Ratio Calculated at Different Locations for Specimen V5

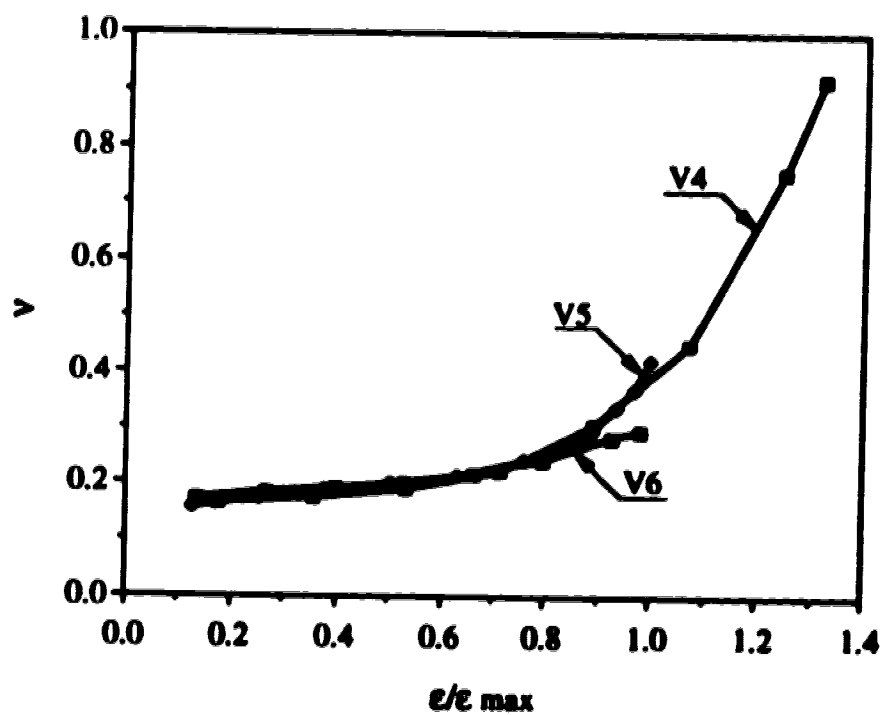


Figure 4.16 Average Poisson's Ratio

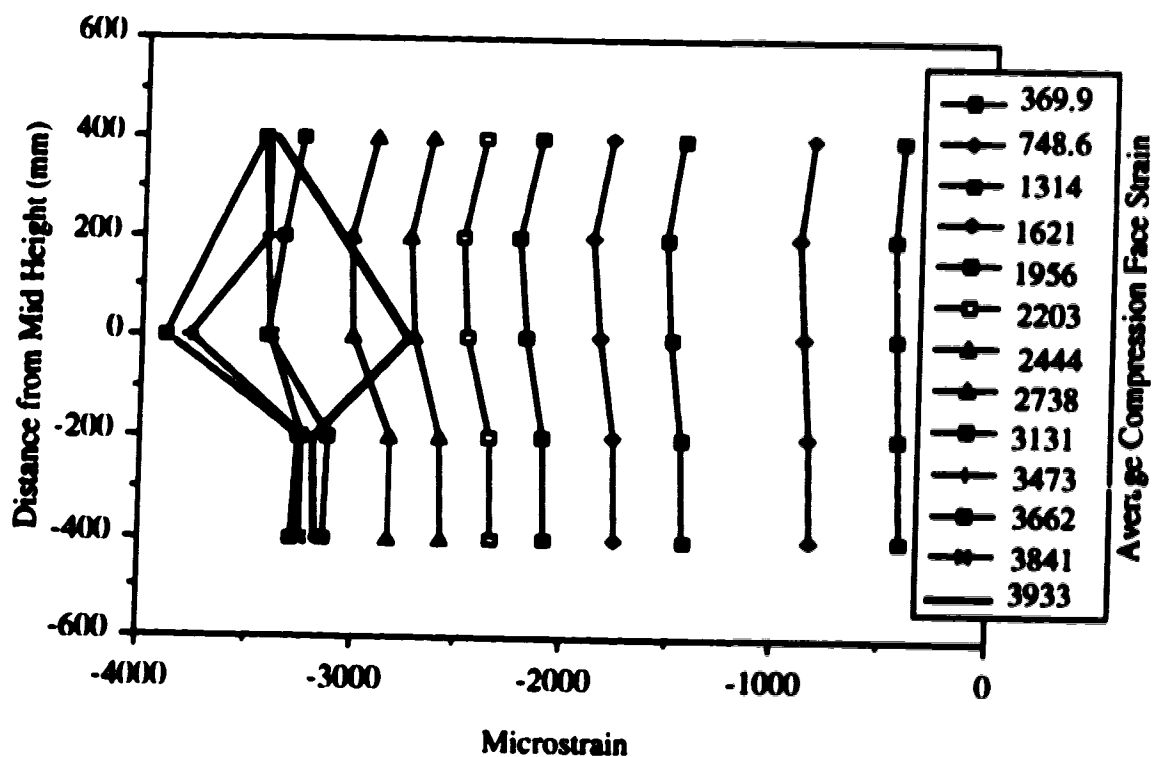


Figure 4.17 Longitudinal Strain Distribution at the Compression Face of Specimen V4 Using the 4 in. Gauges

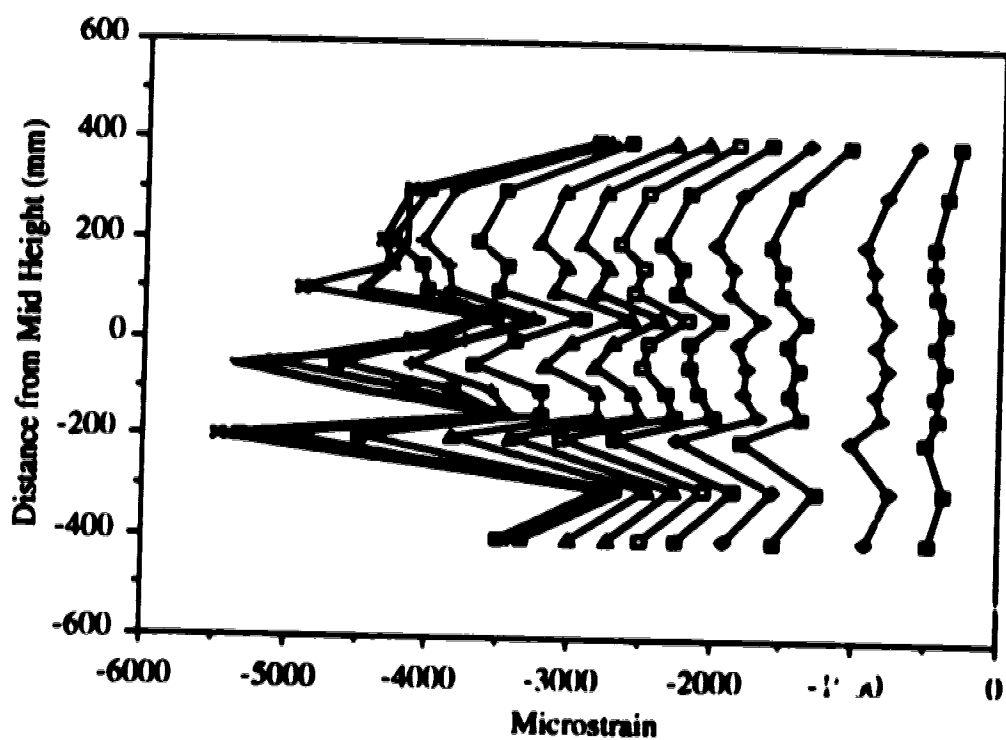


Figure 4.18 Longitudinal Strain Distribution at the Compression Face of Specimen V4 Using the 1 in. Gauges

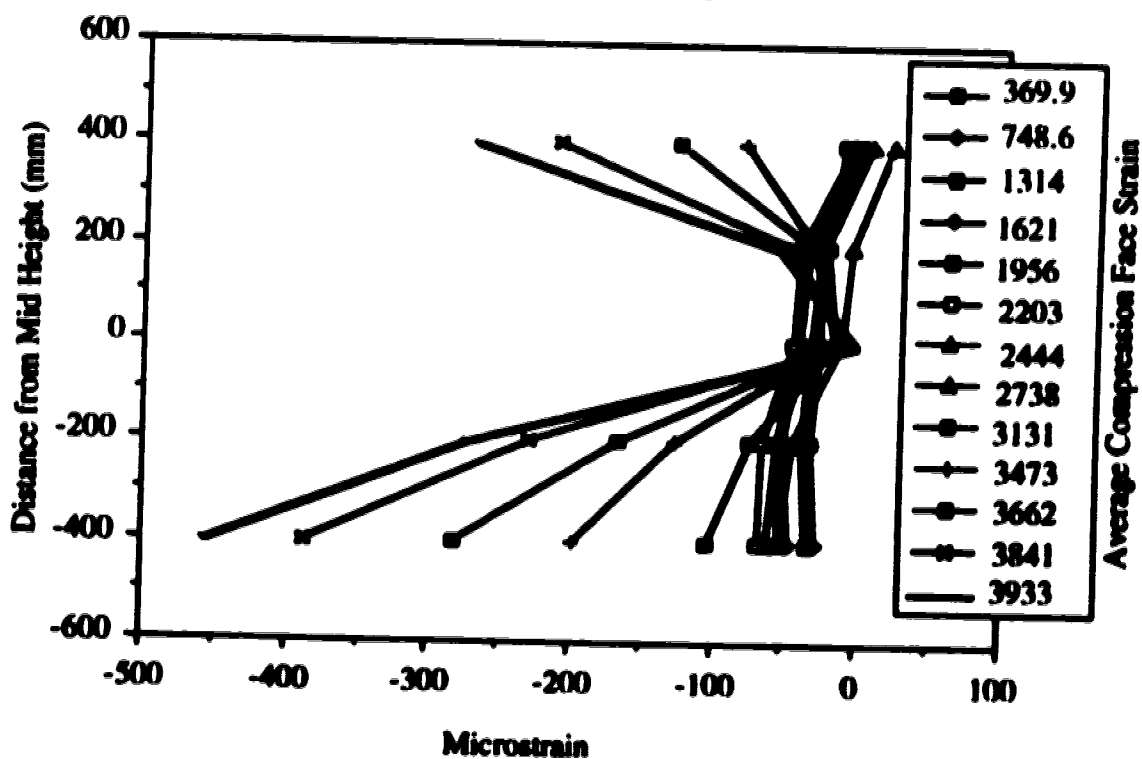


Figure 4.19 Longitudinal Strain Distribution at the Back Face of Specimen V4

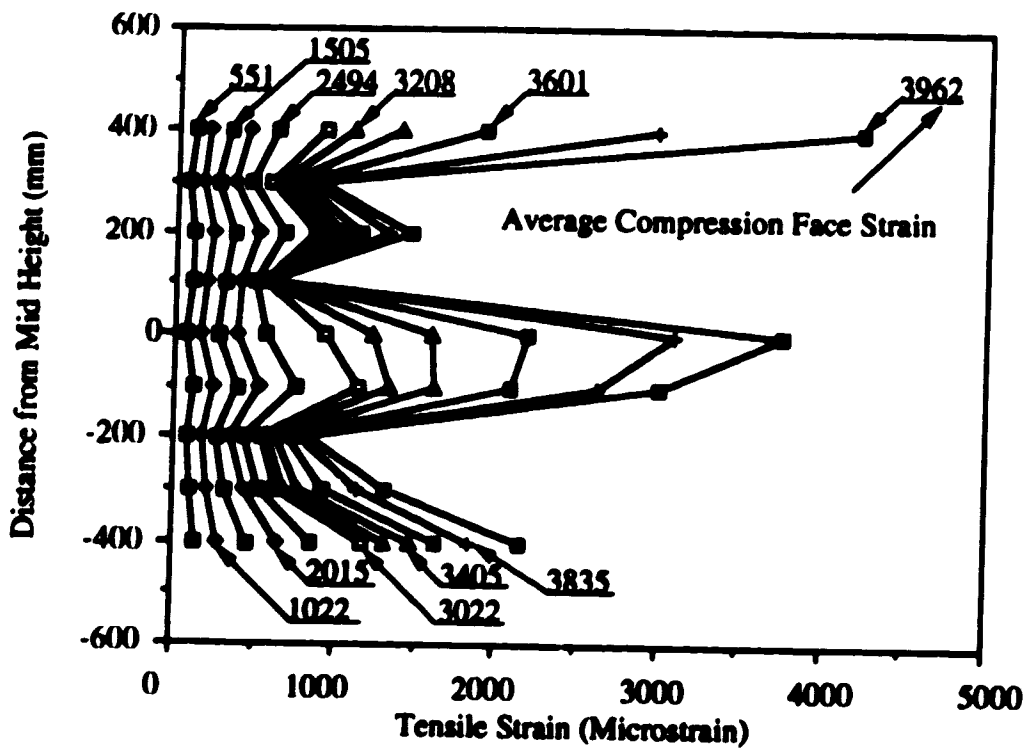


Figure 4.20 Transverse Strain Distribution at the Right Side of the Compression Face of Specimen V5

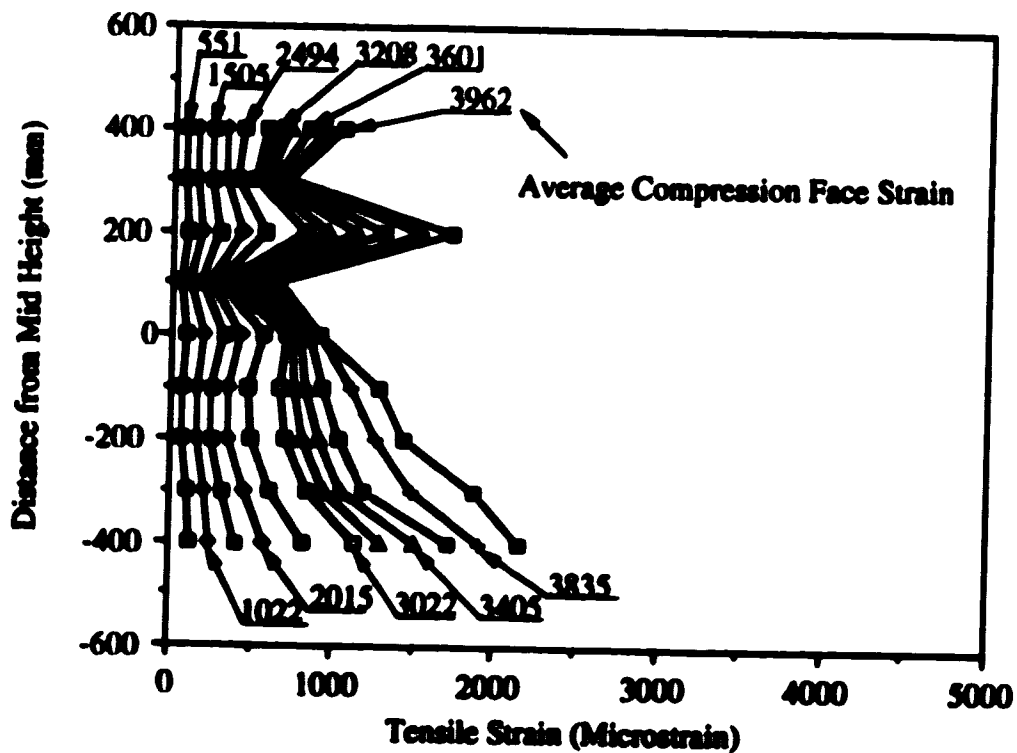


Figure 4.21 Transverse Strain Distribution at the Left Side of the Compression Face of Specimen V5

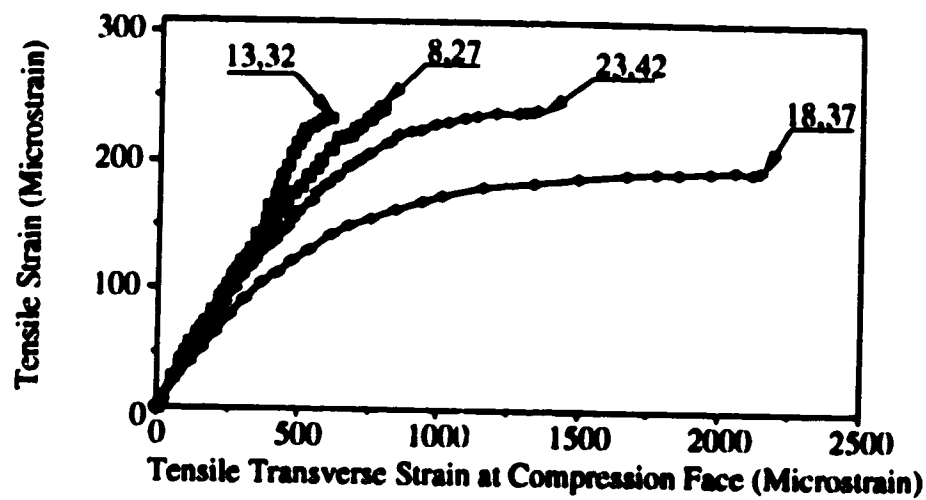


Figure 4.22 Transverse Strain at 100 mm From the Back Face of Specimen V5

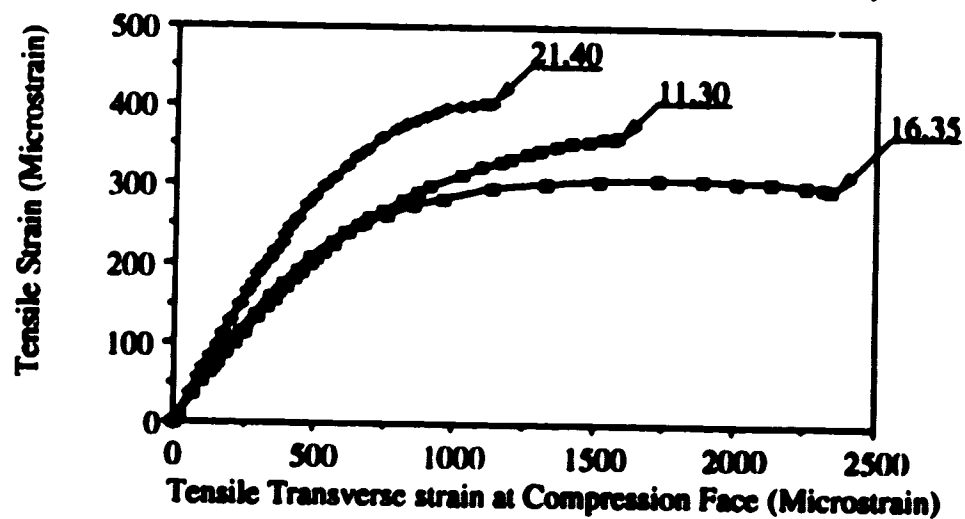


Figure 4.23 Transverse Strain at 150 mm From the Back Face of Specimen V5

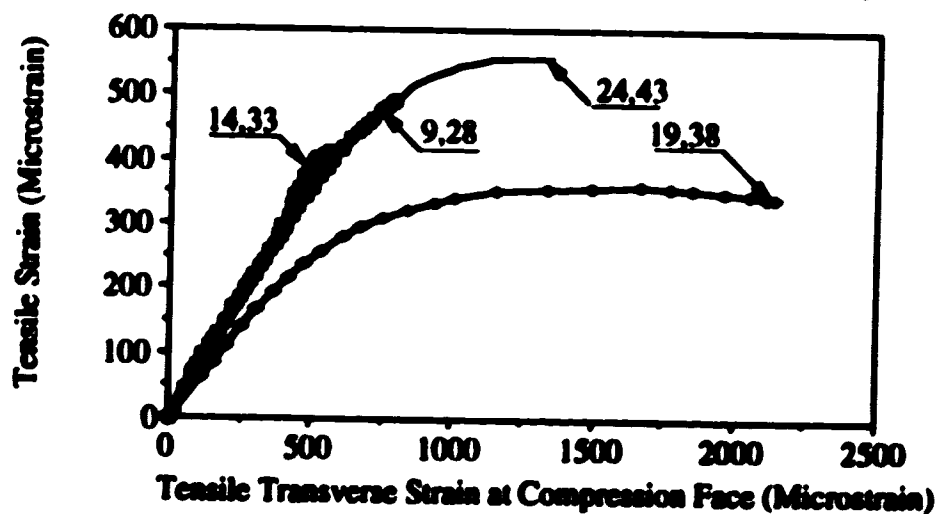


Figure 4.24 Transverse Strain at 200 mm From the Back Face of Specimen V5

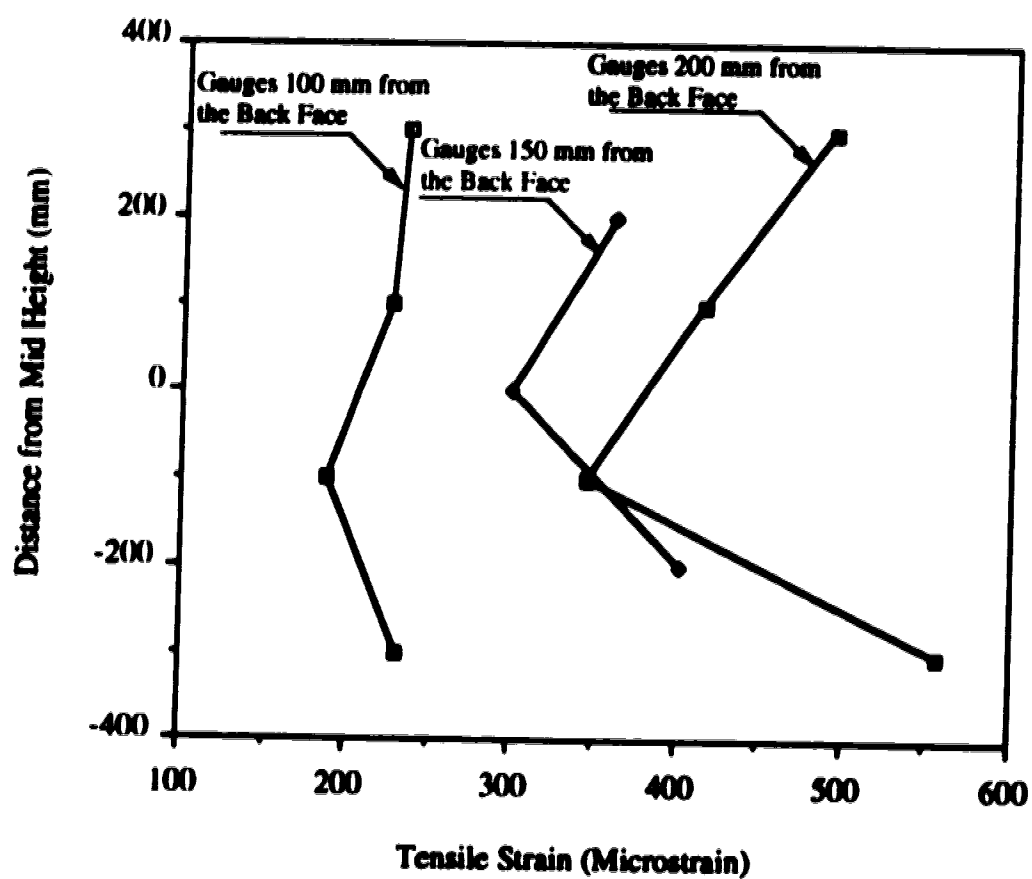


Figure 4.25 Transverse Strain Distribution on the Side Faces of Specimen V5 near Failure

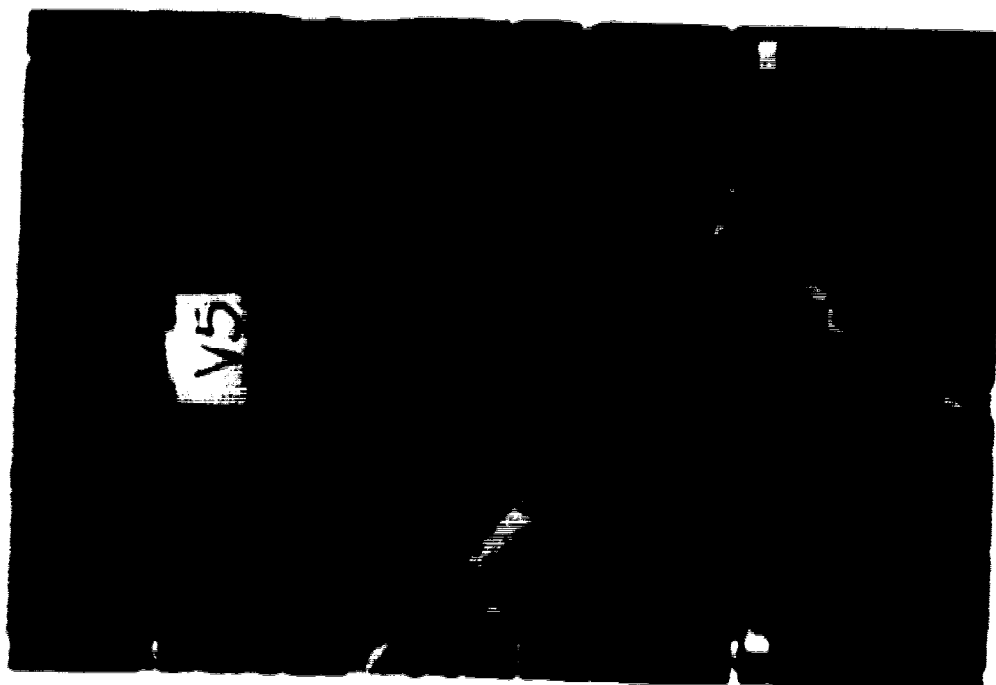


Figure 4.26 Side Face of Specimen V5 after Testing



Figure 4.27 Compression Face of Specimen V6 after Testing

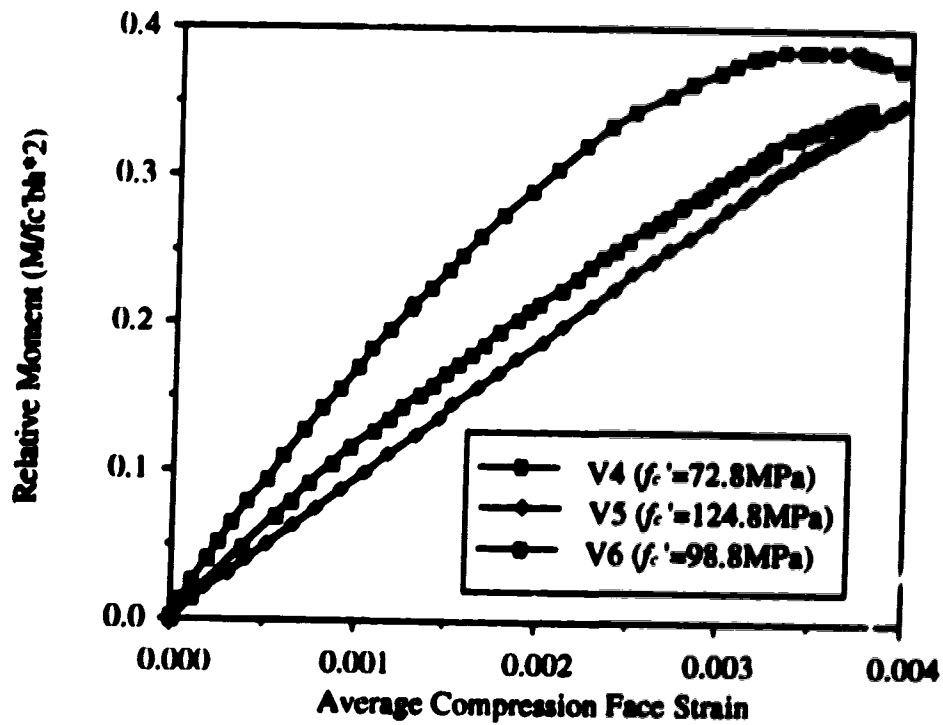


Figure 4.28 Normalized Moment about the Neutral Axis for the Rectangular Specimens

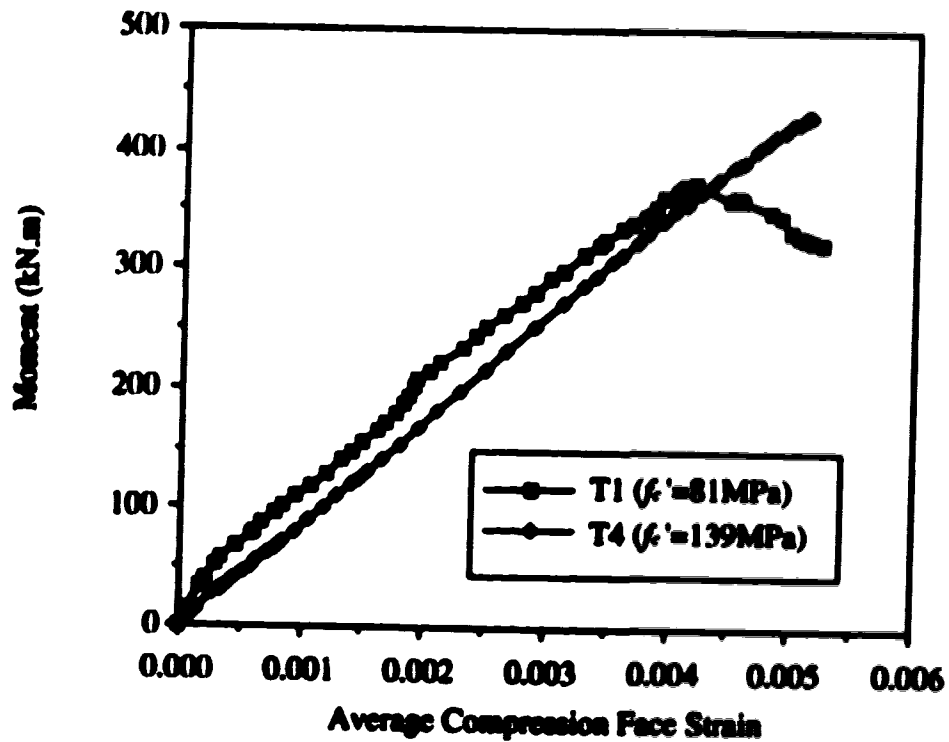


Figure 4.29 Moment about the Neutral Axis for the Triangular Specimens

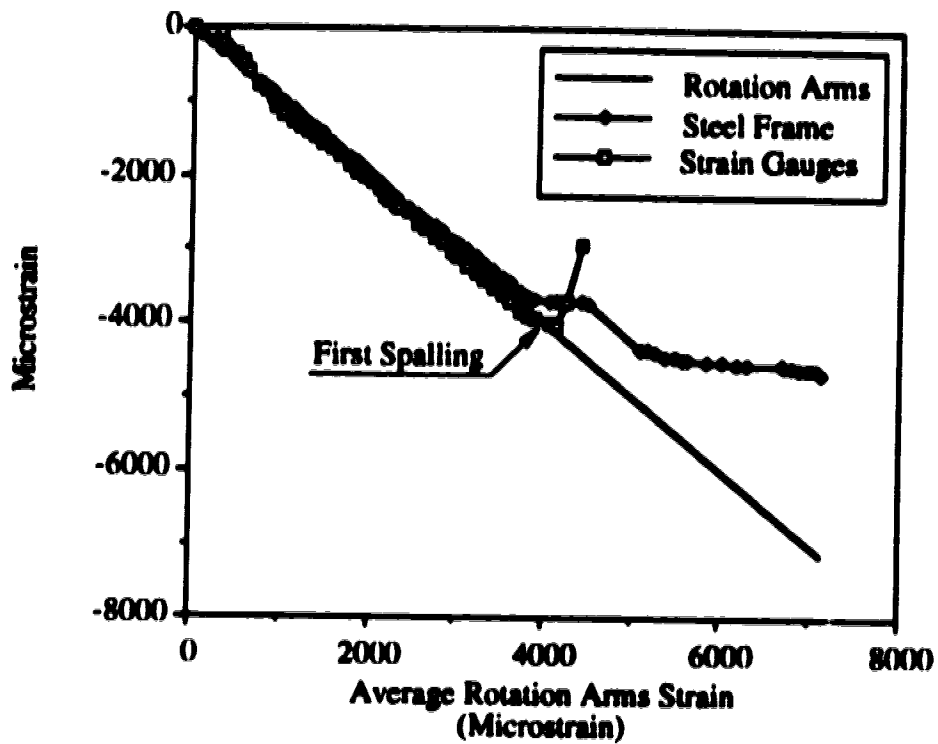


Figure 4.30 Average Longitudinal Strain at the Compression Face of Specimen V11

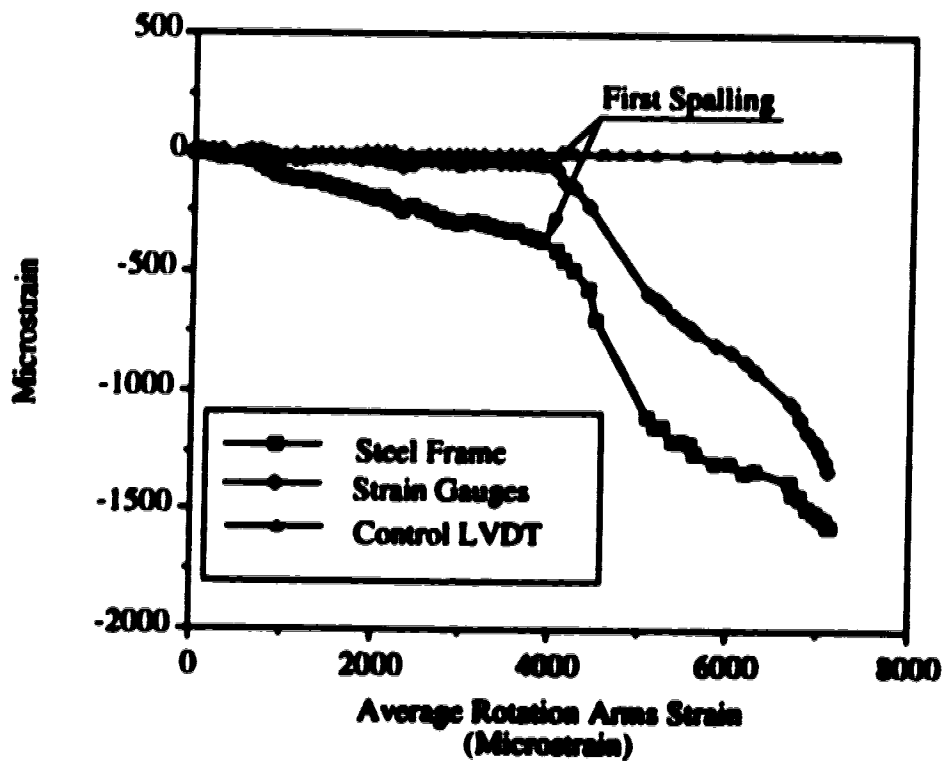
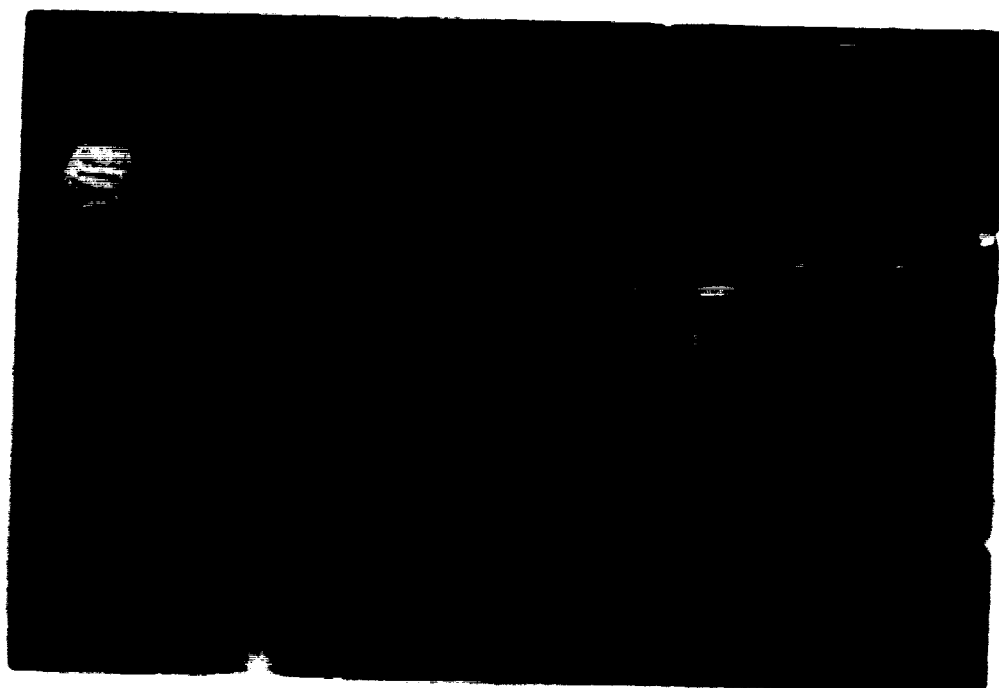


Figure 4.31 Average Longitudinal Strain at the Back Face of Specimen V11



**Figure 4.39 Compression Face of Specimen V17
after Testing**



**Figure 4.38 Compression Face of Specimen V11
after Testing**

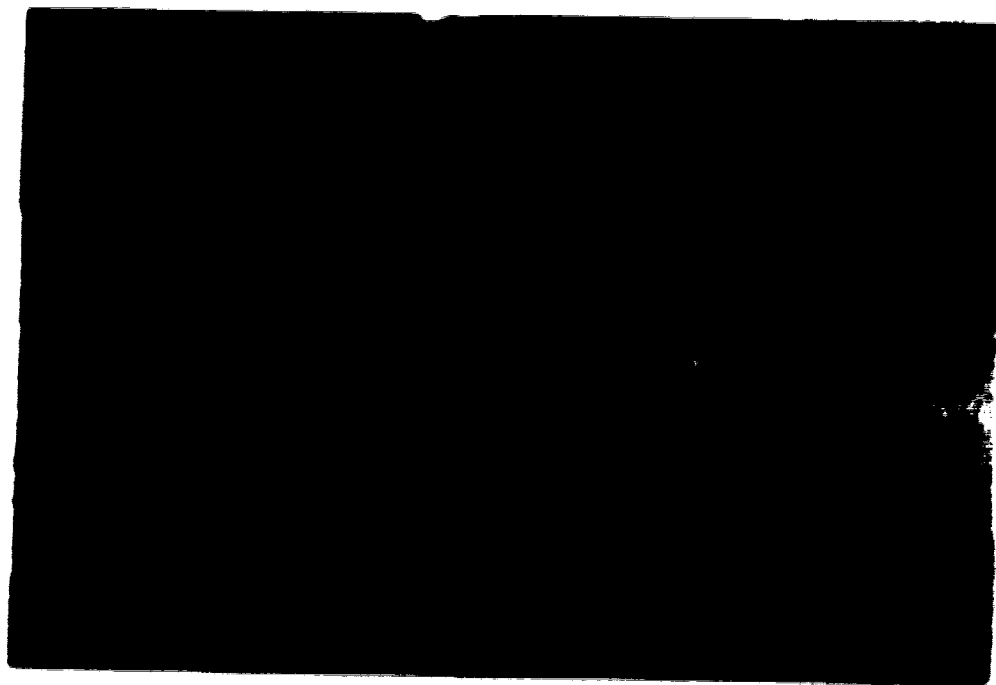


**Figure 4.34 Compression and Side Faces of Specimen V7
after Testing**

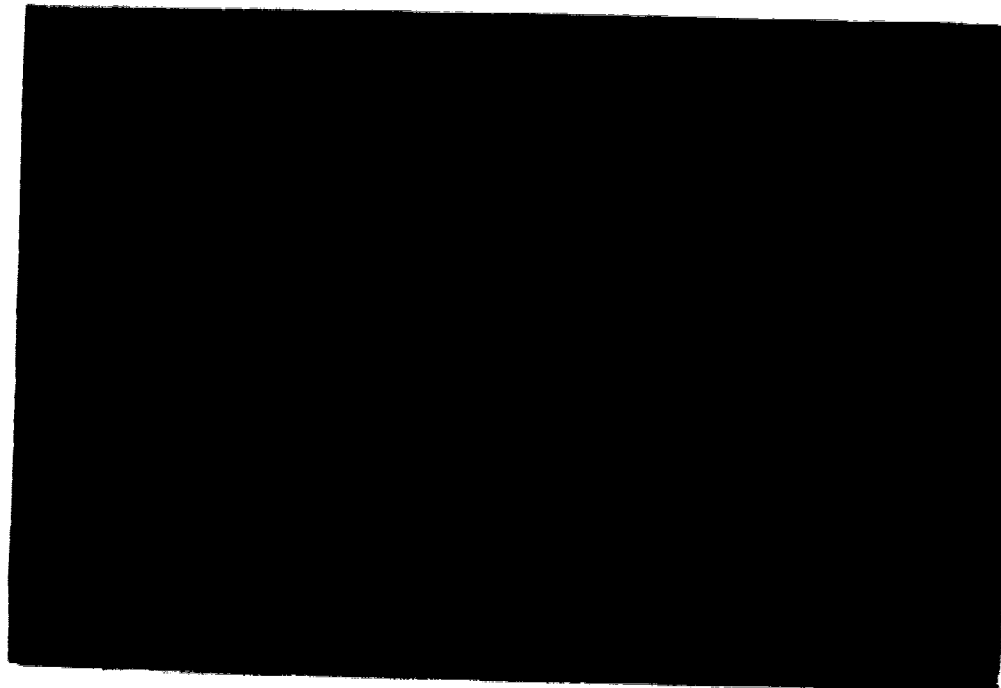


**Figure 4.35 Compression and Side Faces of Specimen V12
after Testing**



**Figure 4.36 Compression and Side Faces of Specimen V15
after Testing**

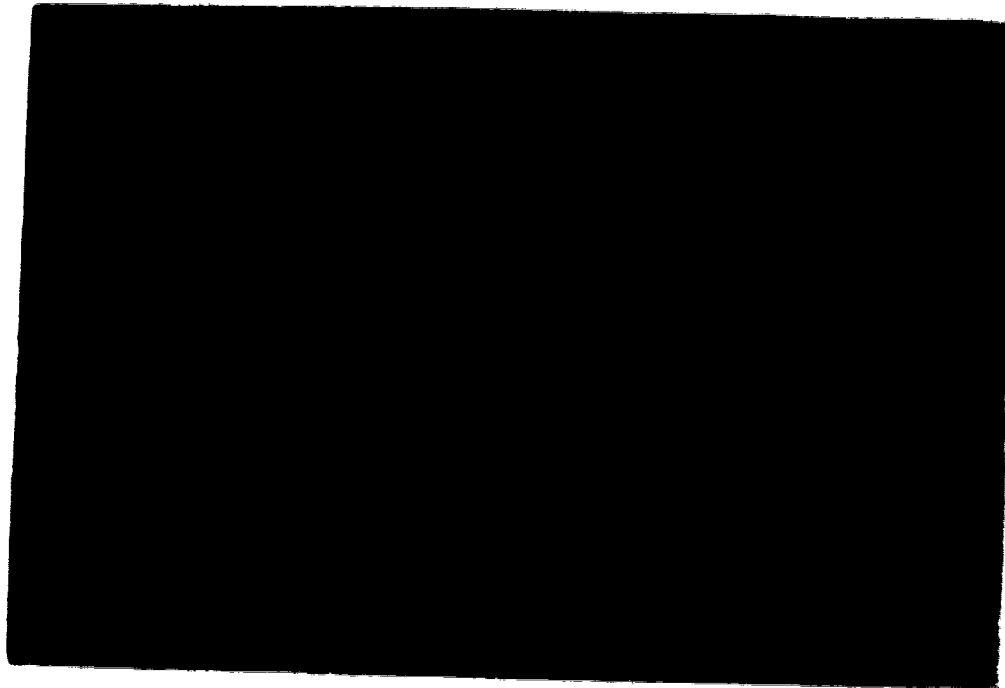


**Figure 4.37 Tension Cracks and Spalling of the Cover at
the Back Face of Specimen V15**

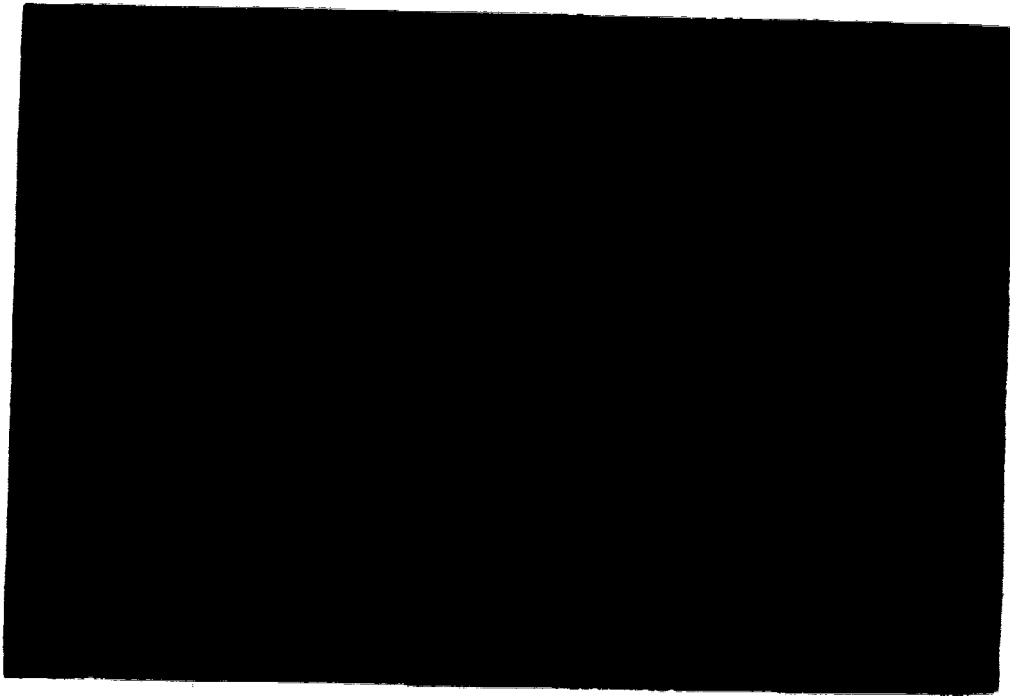


**Figure 4.38 Compression and Side Faces of Specimen V16
after Testing**



**Figure 4.39 Cracks Appear in the Side and Back Faces
of Specimen V16**



**Figure 4.41 Side View of Specimen T5
after Testing**



**Figure 4.40 View from the Tip of Specimen T5
after Testing**

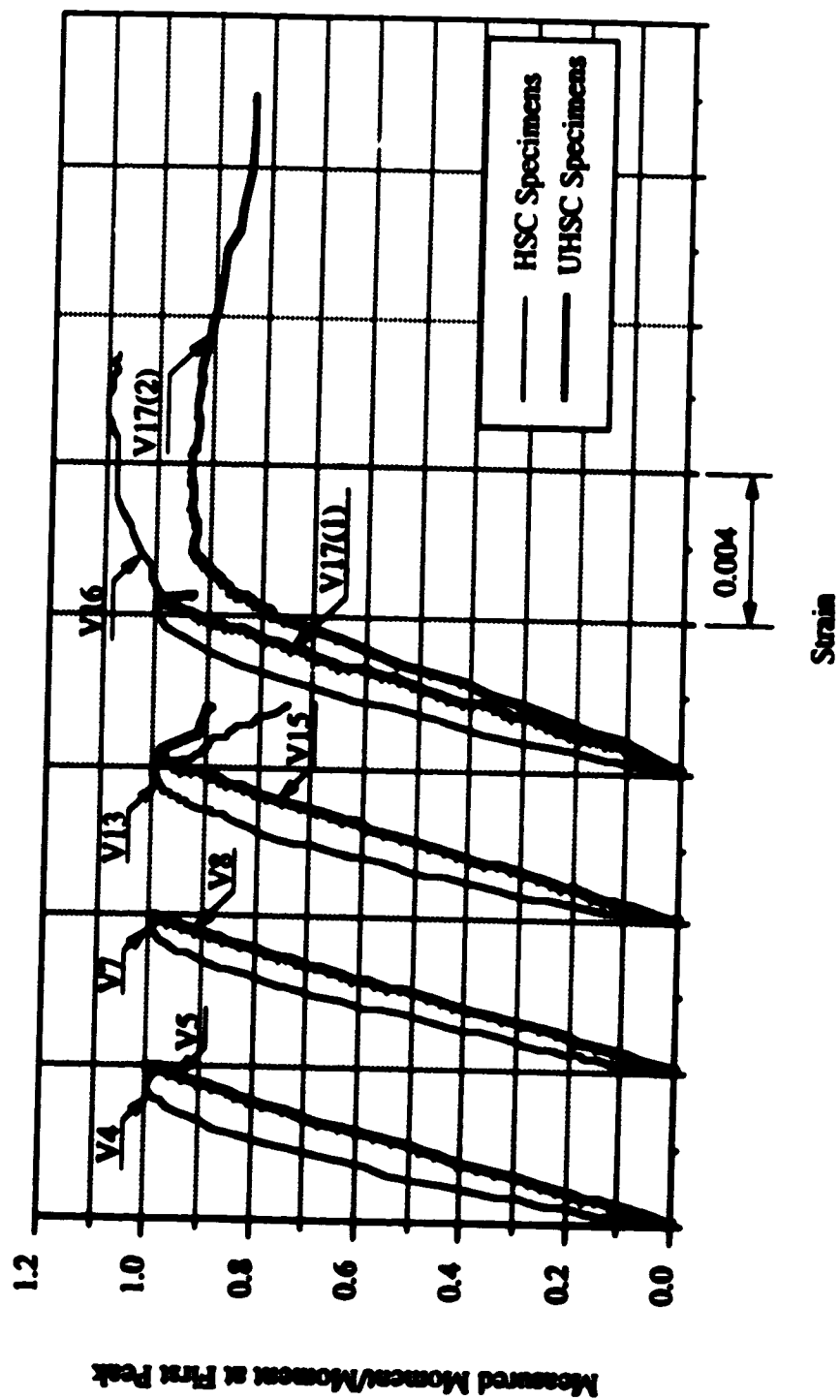


Figure 4.42 Normalized Moment about the Neutral Axis for the Rectangular Specimens

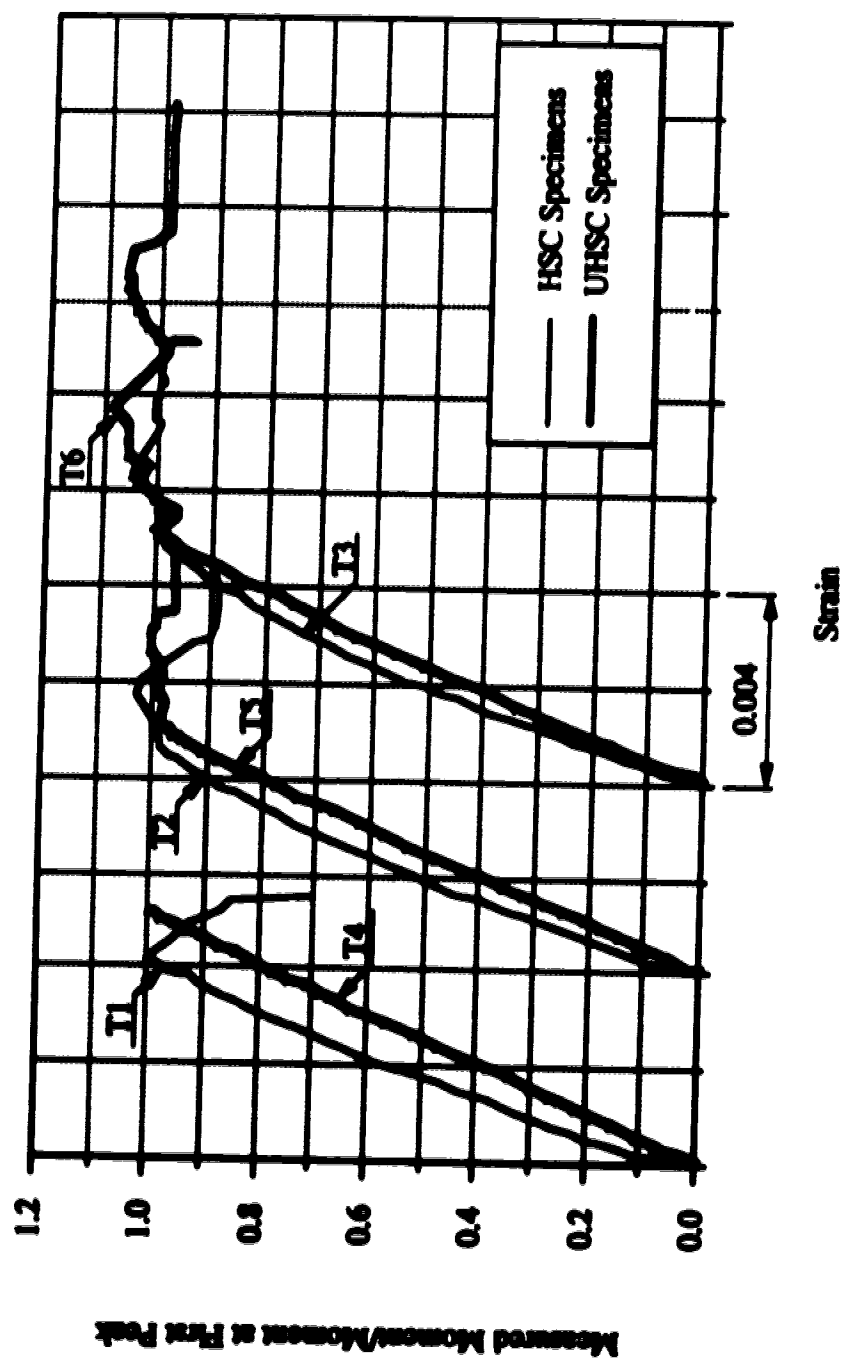


Figure 4.43 Normalized Moment about the Neutral Axis for the Triangular Specimens

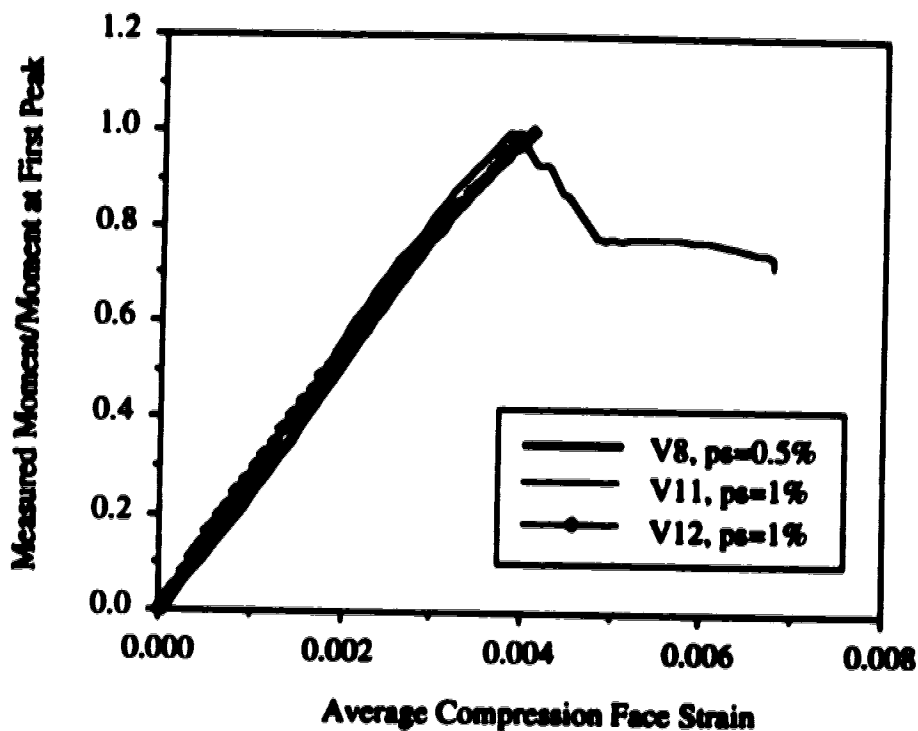


Figure 4.44 Effect of Increasing the Volumetric Ratio of Confinement Reinforcement

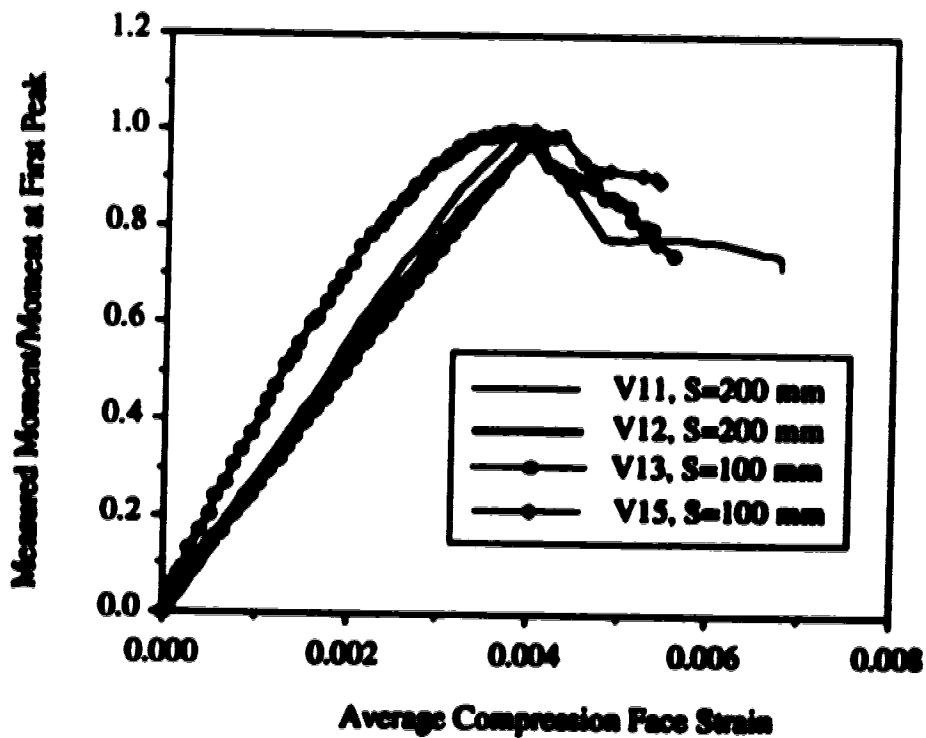


Figure 4.46 Effect of Tie Spacing on the Normalized Moment

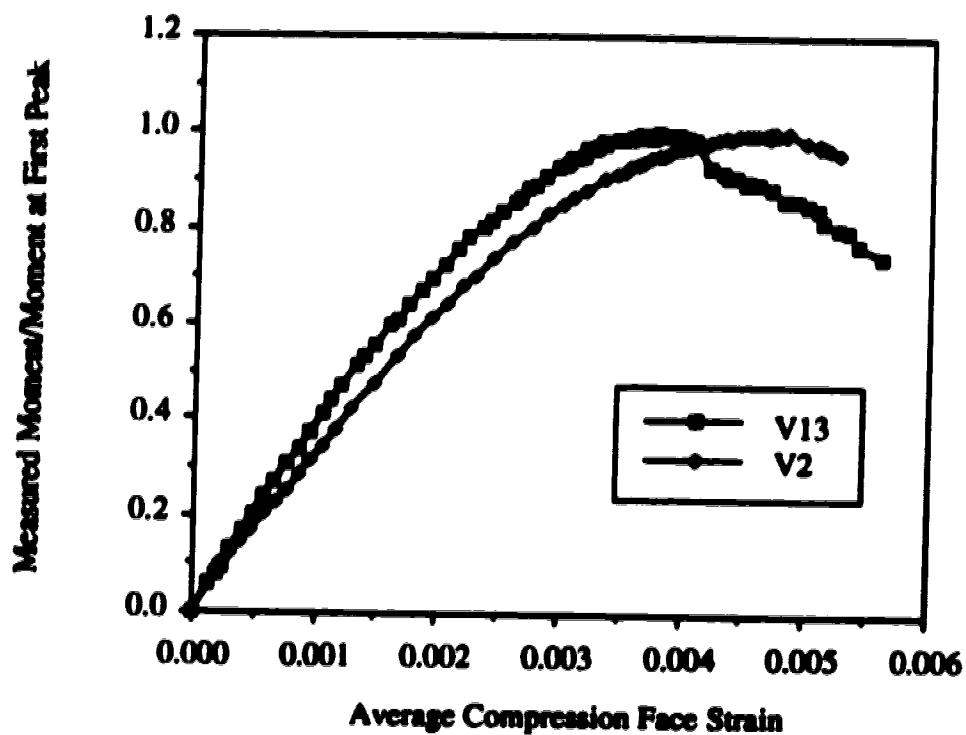


Figure 4.46 Effect of Testing Method

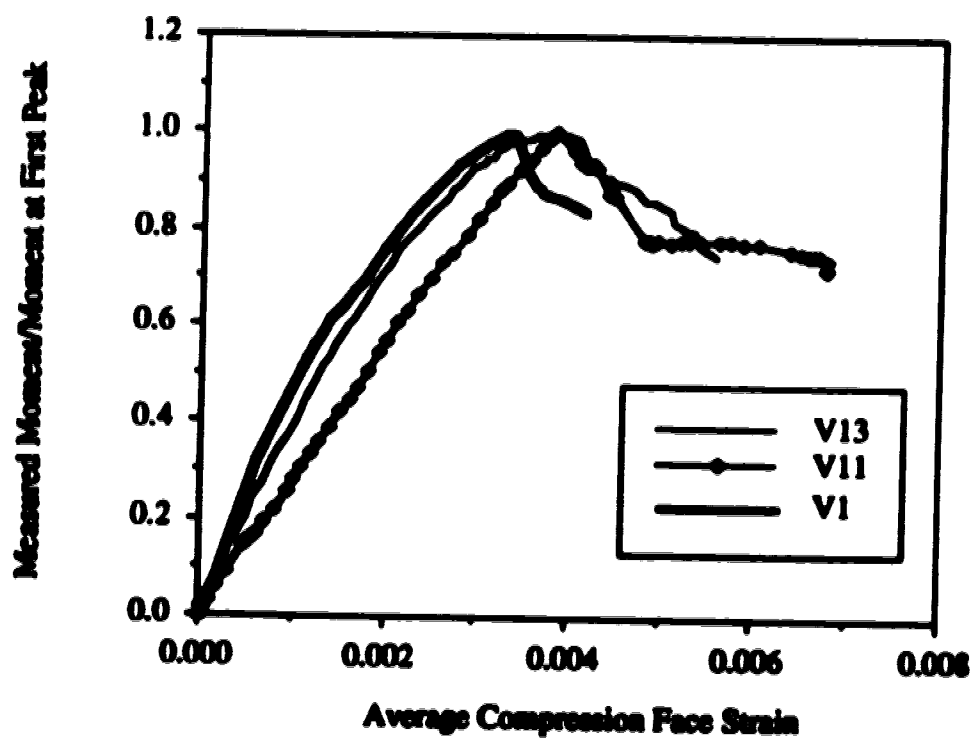


Figure 4.47 Effect of Changing Neutral Axis Position

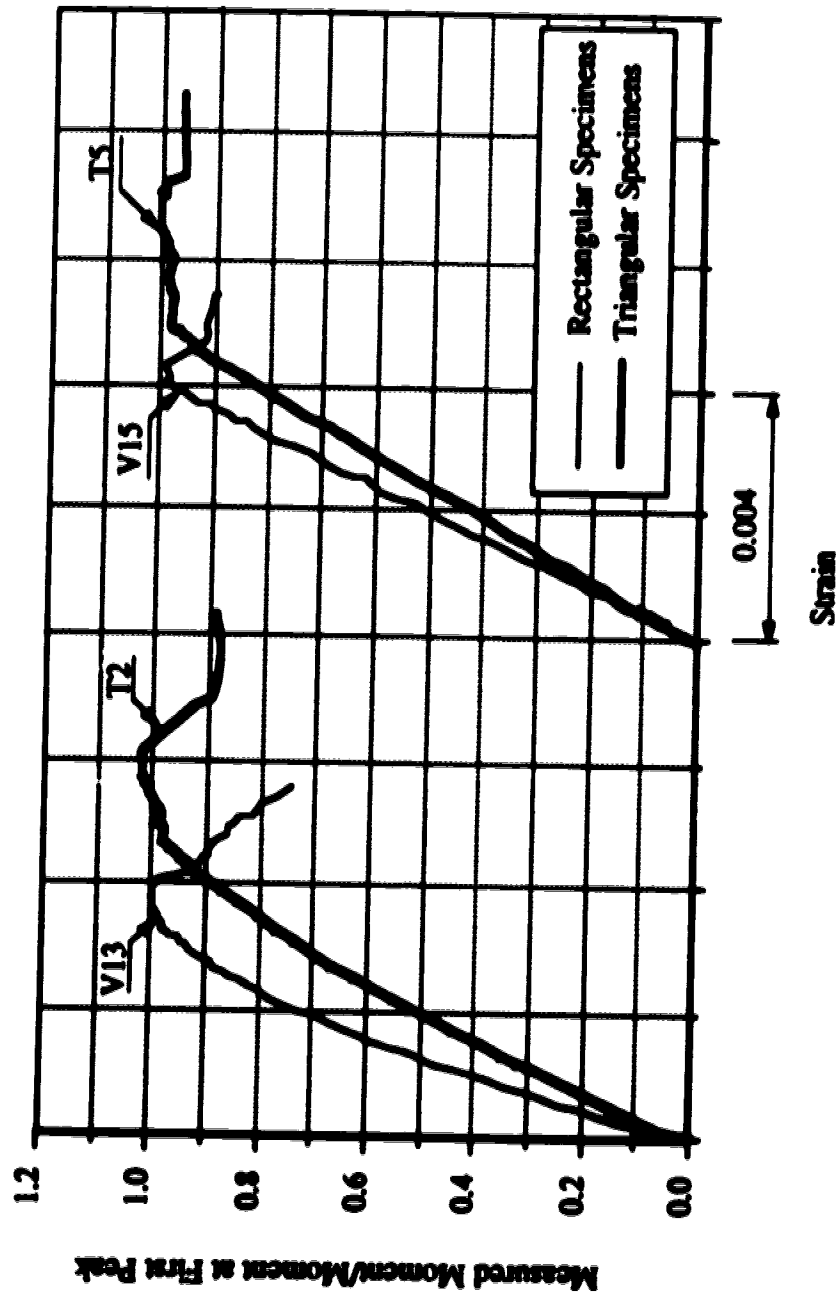


Figure 4.48 Effect of Section Geometry

5- Design Parameters

5.1 General

The experimental program was designed to study the stress block parameters. These parameters can be determined from the applied loads and moments. The stress-strain curves for the specimens prior to the spalling of the concrete cover are important for many reasons. These curves provide a check on the accuracy of the test measurements. The maximum stress for the stress-strain curves for concrete in flexure are required to separate the design parameters. It is important to check whether the stress-strain curves for concrete in flexure differ much from the stress-strain curve for concentrically loaded cylinder since for design purposes they are assumed to be identical.

The flexural stress-strain curves prior to spalling of the concrete cover are presented with a brief discussion about the mathematical approach used to derive these curves. The stress block parameters for different specimens are also given.

5.2 Stress-Strain Relationship in Flexure

5.2.1 Mathematical Approach

The first attempt to determine the stress-strain relationship in flexure was by Prentis (1951), by applying numerical differentiation to beam test data. The basic assumptions that Prentis used to derive these equations were:-

- 1- Linear strain distribution over the cross-section
- 2- Concrete compressive stress is a function of strain only, effects of time and strain gradient are neglected
- 3- Concrete does not resist tension

In order to eliminate the complications resulting from tensile stresses and cracks in concrete, Hognestad et al. (1955), used C-shaped specimens with a triangular strain distribution as shown in Figure 2.1 to calculate the flexural stress-strain relationship of rectangular cross sections. Using the same assumptions as Prentis, Hognestad derived equations for the concrete stress f_c as a function of the continuously measured strain at the most compressed fibers ϵ_c and the measured quantities f_o and m_o . From the equilibrium of external and internal applied loads and moments, the following equations are obtained

$$C = P_1 + P_2 = f_o b h = \frac{bh}{\epsilon_c} \int_0^{\epsilon_c} f(\epsilon_x) d\epsilon_x \quad (5.1)$$

$$M = P_1 a_1 + P_2 a_2 = m_o b h^2 = \frac{b h^2 \epsilon_c}{\epsilon_c^2} \int_0^{\epsilon_c} f(\epsilon_x) \epsilon_x d\epsilon_x \quad (5.2)$$

where; $f_o = \frac{P_1 + P_2}{bh}$, $m_o = \frac{P_1 a_1 + P_2 a_2}{bh^2}$, b is the width of the cross-section, h is the depth of the cross-section, C is the total applied load, (P_1 and P_2) are the individual applied loads, M is the total applied moment and (a_1 and a_2) are the eccentricities of the two applied loads measured from the neutral axis position taking into consideration the second order effect due to the deflected shape of the specimen during testing. The two independent equations, written in terms of loads and moments, allow a possibility to check the accuracy of the test data since several experimental sources of error affect the two equations differently.

By differentiating the third and fourth terms of Equations (5.1) and (5.2) with respect to ϵ_c and rearranging, the following equations are obtained

$$f_c = f_o + \frac{df_o}{d\epsilon_c} \epsilon_c \quad (5.3)$$

$$f_c = 2m_o + \frac{dm_o}{d\epsilon_c} \epsilon_c \quad (5.4)$$

Soliman et al. (1967) extended these equations for reinforced concrete sections. The stress was still assumed to be a function of the strain only which means that, in case of a concrete cover, the concrete cover and the concrete core were assumed to have the same stress-strain relationship. The resulting stress-strain relationship represents the average behavior of the cross-section. The expressions for f_o and m_o were modified to account for the part of the loads and moments that are carried by the reinforcement

$$f_o = \frac{C_c}{bh} = \frac{P_1 + P_2 - \sum (A_{si} f_{si})}{bh} \quad (5.5)$$

$$m_o = \frac{M_c}{bh^2} = \frac{P_1 a_1 + P_2 a_2 - \sum (A_{si} f_{si} a_{si})}{bh^2} \quad (5.6)$$

where; A_{si} is the area of each reinforcement steel bar, f_{si} is the stress carried by each bar and a_{si} is the horizontal distance from the position of the neutral axis to the vertical center line of each bar.

In the case of trapezoidal strain diagram, the stress-strain equation for the most compressed fibers is represented by f_c and the stress-strain equation for the less strained

fibers is represented by f_a . The differentiation of Equations (5.1) and (5.2) leads to the equations

$$f_c - \left(\frac{a}{h}\right) f_a = f_o + \frac{df_o}{de_c} e_c \quad (5.7)$$

$$f_c - \left(\frac{a}{h}\right)^2 f_a = 2m_o + \frac{dm_o}{de_c} e_c \quad (5.8)$$

where; a is the distance from the position of the neutral axis to the less strained fibers of the cross-section and h is the neutral axis depth. By assuming a form for the stress-strain relationship that is a function of the strain only, the f_a part can be expressed in terms of f_c , leading to two independent equations for f_c .

Similar equations for the triangular cross-sections, tested in the test series reported here, can be derived using the same basic assumptions for the rectangular cross-sections. This leads to the following equations

$$f_c = \frac{A}{b_o h} \left(f_o + \frac{df_o}{de_c} e_c \right) - \frac{2h}{b_o e_c^3} \int_0^{e_c} f(e_x) e_x dx \quad (5.9)$$

$$f_c = \frac{A}{b_o h} \left(2m_o + \frac{dm_o}{de_c} e_c \right) - \frac{2h}{b_o e_c^3} \int_0^{e_c} f(e_x) e_x' dx \quad (5.10)$$

where; $f_o = \frac{P_1 + P_2}{A}$, $m_o = \frac{P_1 a_1 + P_2 a_2}{A h}$, A is the area of the cross-section, b_o is the width of the cross-section at the apex of the tested triangular section and h is the neutral axis depth. The full derivation of these equations are given in Appendix A. In case of a reinforced section, the definition of f_o and m_o should be modified as shown in Equations (5.5) and (5.6).

Two different approaches can be used to calculate the stress-strain relationship from the test data. The first approach uses the differential Equations (5.3) and (5.4). By having the quantities f_o and m_o measured over small increments of strains, the differential parts may be closely approximated by finite differences $\Delta f_o / \Delta e_c$ and $\Delta m_o / \Delta e_c$. These finite difference parts are very sensitive to any slight error in the test data and a very large scatter in the calculated value of f_c occurs if the results obtained from the test are applied directly in these equations. Different methods can be used to smooth the test data before calculating the finite difference parts, (Soliman et al. (1967), Neddorman (1973), and Kaar et al. (1978a, 1978b)). Swartz et al. (1985) used a different approximation by fitting the quantities f_o and m_o into a third degree parabola. In that case there is no need to

approximate the differential parts by finite differences since these differentials can be evaluated and a smooth curve can be obtained.

The second approach uses the integration of Equations (5.1) and (5.2). This method requires assuming a certain shape of the stress-strain relationship first in order to be able to evaluate the integration parts of these equations. The unknown coefficients of these equations are determined by minimizing the least squares. This approach was used by Smith et al. (1969) and Pastor (1985) assuming a polynomial expression for the stress-strain relationship. Schade (1992) used the same approach with a stress-strain relationship suggested by Loov (1991).

Using a polynomial equation for the stress-strain relationship is the easiest way to calculate the stress-strain relationship. The disadvantage of using a polynomial equation is that it can not adequately express a curve that has an ascending branch and a steep descending branch which is expected in HSC tests. This problem did not show up in the test series reported here since the descending branch of the plain concrete specimens was short. For the reinforced concrete specimens, the analysis in this chapter is limited to the part of the test prior to the spalling of the concrete cover. In the next part of this chapter the approach of Swartz et al. will be used to obtain the stress-strain relationship but the regression equations will not be restricted to third order polynomials. The order of the polynomial equations will be chosen to give the best fit to the tests data.

At any loading stage, the force carried by each reinforcing steel bar is taken equal to the force calculated from the force-strain relationship of the bar minus the force that could be carried if the same area of the bar was occupied by concrete. This analysis required three steps. First the stress-strain equation for the specimen was estimated using the force in the bar equal to the force calculated from the force-strain relationship of the bar only. Then the force in the bar is modified using the calculated stress-strain equation of the specimen as mentioned before. The first step is then repeated with the modified force in each bar.

The procedures that were used in this Chapter to obtain the stress-strain curves of the rectangular specimens are described in Appendix B.

5.2.2 Accuracy of the Analysis

The stress-strain curves from both the load and moment equations (Equations 5.3 and 5.4) showed a good agreement. For the rectangular specimens, the two stress-strain curves usually differed by less than 2% with the maximum difference being 3.5% for specimens V15 and V17. These differences, which are compatible with the errors reported by Hognestad et al. (1955), reflect the accuracy of the test measurements. For the triangular

specimens, the differences between the two stress-strain curves were less than 4% for specimens T1, T3, T4 and T6. Specimens T2 and T5 showed maximum difference of 15% close to the peak of the stress-strain curve. This significant difference between the two stress-strain curves is probably due to the triangular shape of the cross-section. For the triangular section most of the compression zone area is located closer to the less strained fibers which means that the most strained fibers carried a small portion of the applied loads. This distribution of the forces in the cross-section makes the calculation of the portion of the stress-strain curve that it is close to the peak stress more sensitive to the errors in the test data and to the approximations used in the analysis.

For each specimen, the average of the curves obtained from the two equations is used to represent the stress-strain curve of the specimen. In order to check the accuracy of the analysis, this average stress-strain equation for each specimen was used to calculate the applied loads and moments during the test of the specimen. Figures 5.1 and 5.2 show a comparison between the measured and calculated loads and moments at different loading stages of the tests of specimens V1 and V16. Specimen V1 showed the least agreement between the measured and calculated loads and moments while specimen V16 expressed the typical behavior of the rest of the rectangular specimens. The measured and calculated loads and moments for specimens T1 and T5 are shown in Figure 5.3 and 5.4. Specimen T1 showed the least agreement for the triangular specimens. Specimen T5 showed good agreement between the measured and calculated loads, despite the significant difference between the two calculated stress-strain equations for the specimen which reached 15% close to the peak of the curve. This was because the most highly strained area was a small part of the cross-section and had little effect on the load and moment.

5.2.3 Comparison between different Stress-strain Curves

Figure 5.5 shows the stress strain curves for the plain concrete specimen V6 and for two cylinders that had different curing procedures as explained in Section 3.4. The curves of the two cylinders showed identical behavior in the linear part of the ascending branch. At higher stress levels the air cured cylinder started to show higher strains at the same stress level. The maximum strength of the air cured cylinder was less than the maximum strength of the moist cured cylinder, as was generally the case in all of the cylinder tests as shown in Tables (3.8 and 3.9) and Section 4.2.3. The descending branch of the stress-strain curves from both types showed close agreement with a larger drop in stress immediately after the peak for the moist cured cylinder (see Figures 5.5 to 5.10). The strength of the concrete in the columns has been taken as the moist cured 100x200 mm cylinder strength as explained in Section 4.2.3.

Figure 5.5 shows that specimen V6 had a stress-strain curve with an ascending branch that is very similar to the air cured cylinder and no descending branch. The very steep descending branch for the cylinders explains why it was not possible to obtain that part in the column specimen tests with the stroke control system used in the tests. The effect of rate of loading and strain gradient seem to have very little effect in the ascending branch of the stress-strain relationship. Figure 3.15 (Section 3.6) shows that the rate of loading of the cylinder tests did not have significant effect on the stress-strain curve of the cylinders. The reinforced concrete specimen V14 showed the same behavior with a small flat portion at the top of the stress-strain curve as illustrated in Figure 5.6. The ratio between the maximum stress of the flexural stress-strain curve to the cylinder stress-strain curves, referred to as K_3 , is given in Tables 5.1 and 5.2 for different specimens.

The plain concrete HSC triangular specimen T1 showed good agreement between the stress-strain curve obtained from the specimen and that from the moist cured cylinder as illustrated in Figure 5.7. Figure 5.8 shows that for the plain concrete UHSC specimen T4, the stress-strain curve of the column specimen had higher maximum stress and strain than the corresponding cylinder. The same observation is shown in Figure 5.9 for the reinforced HSC specimen T2, while the reinforced UHSC specimen T6 showed higher strain with lower stress than the corresponding cylinder as illustrated in Figure 5.10.

In general, the stress-strain curves of the rectangular specimens and the cylinders tended to show agreement. The stress-strain curves of the triangular specimens did not show that. This probably is due to the shape of the cross-section and the assumptions used in the analysis that assumed the stress to be a function of the strain only, ignoring the effect of the shape of the cross-section and the confinement. However the flexural stress-strain curves obtained from the triangular specimens gave an accurate prediction of the applied loads and moments. This suggests that these curves adequately represent the structural behavior of the triangular specimens.

5.2.4 Summary of the Stress-Strain Curves of the Specimens

Figure 5.11 shows the stress strain curves for most of the HSC rectangular specimens. The figure shows that, except for the highly confined specimen V16, the reinforced specimens showed similar behavior to the plain concrete specimen V4 in the ascending and descending branches prior to spalling of the concrete cover. For the UHSC rectangular specimens similar behavior was achieved as illustrated in Figure 5.12. Specimen V5 was plain concrete.

Figure 5.13 shows the stress-strain curves for the triangular specimens. The figure shows close agreement between different specimens except for the plain concrete HSC specimen T1 which showed a long descending branch.

The stress-strain curves of all the specimens in this test series showed higher strain values at the peak stress than the reported maximum strain values from previous test series of HSC columns. This observation may be due to the local aggregates that was used to produce these specimens. The aggregates were adequate to produce concrete with the target strengths but these aggregates may have had a lower modulus of elasticity than the aggregates used to produce specimens in previous column tests.

5.3 Stress Block Parameters K_1 , K_2 , K_3 and ϵ_u

5.3.1 Rectangular Specimens

The stress block parameters K_1 , K_2 and K_3 can be determined for each specimen using the applied loads and moments. Figure 5.14 shows a sketch of the stress block parameters for a rectangular compression zone. From the figure, the parameter K_1 is defined as the ratio of the average compressive stress to the maximum compressive stress. The parameter K_2 is the ratio of distance between the extreme fiber and the resultant of compressive stress to distance between the extreme fiber and the neutral axis. The parameter K_3 is the ratio of the maximum compressive stress to the cylinder strength. The design values of the stress block parameters are determined at the strain value ϵ_u that corresponds to the maximum moment about the neutral axis during each test.

The ACI 318-89 and the CAN3-A23.3-M84 codes use a simplified set of stress block parameters based on an assumed rectangular stress block. By keeping the resultant of the forces in the middle of the assumed rectangular stress block, the rectangular stress block by the code, as shown in Figure 5.14, is defined by two parameters only, α_1 and β_1 , where α_1 is equivalent to K_3 , β_1 is equivalent to K_1 and K_2 is equal to $\beta_1/2$. The codes assume a constant value of 0.003 for the limiting strain ϵ_u .

For each of the plain rectangular specimens, the parameters K_1K_3 were determined from the equilibrium of the external and internal loads as follows:

$$C = P_1 + P_2 = K_1K_3f'_c bh \quad (5.11)$$

by rearranging and substituting for $\frac{P_1 + P_2}{bh}$ by f_c , the following equation was used to determine K_1K_3 :

$$K_1 K_3 = \frac{P_1 + P_2}{f_c' b h} = \frac{f_o}{f_c'} \quad (5.12)$$

The parameter K_3 was obtained for each plain specimen by dividing the maximum compressive stress of the stress-strain curve of the specimen by the average strength of the cylinders of this specimen.

The parameter K_2 was determined from the equilibrium of the external and internal moments as follows:

$$M = (P_1 a_1 + P_2 a_2) = (P_1 + P_2) \times (1 - K_2) h \quad (5.13)$$

by rearranging the following equation was used to determine the parameter K_2

$$K_2 = 1 - \left(\frac{(P_1 a_1 + P_2 a_2)}{(P_1 + P_2) h} \right) = 1 - \frac{m_o}{f_o} \quad (5.14)$$

In the case of reinforced concrete specimens, the quantities f_o , m_o were modified as explained in Equations (5.5) and (5.6) and Section 5.2.1.

Table 5.1 gives a summary of the design parameters for the rectangular specimens. The mean value of K_3 for the HSC and the UHSC specimens were 0.932 and 0.919 respectively. These values are higher than the code value of 0.85 for α_1 . The mean values of the parameters $K_1 K_3$ and K_2 of the HSC specimens were 0.624 and 0.373 respectively. These values are comparable with the values obtained from a stress-strain curves that have a shape of a second order parabola with a maximum stress of f_c' at the ultimate strain. The values of the parameters $K_1 K_3$ and K_2 in that case are 0.667 and 0.375 respectively. For the UHSC specimens, where the shape of the flexural stress-strain curves were close to triangular, the mean values of the parameters $K_1 K_3$ and K_2 were 0.524 and 0.347 respectively. For a triangular stress-strain curves with maximum stress of f_c' , these parameters are 0.5 and 0.333 respectively. The ACI values of $\alpha_1 \beta_1$ and $\beta_1/2$, for any concrete strength higher than 55 MPa, are 0.5525 and 0.325 respectively. The discussion about the validity of the code procedures is given in Chapter 7. The strains at the maximum moments before spalling of the concrete cover for all of the specimens were higher than the code limiting value of 0.003. The UHSC specimens had higher ultimate strain values than the HSC specimens.

5.3.2 Triangular Specimens

Figure 5.15 shows a sketch of the stress block parameters for a triangular compression zone. The figure also shows the ACI assumed stress block. The ACI code uses the same values of α_1 , β_1 and ϵ_u as recommended for the rectangular sections. In the analysis of the

triangular sections, the parameter K_1 is defined as the depth of an assumed compression block, as shown in the figure, in order to keep the values of the parameter in comparable with the values of the ACI parameter β_1 . Therefore the design parameters for the plain concrete triangular specimens were determined as follows:

$$C = P_1 + P_2 = K_1^2 K_3 f_c' b h / 2 \quad (5.15)$$

$$M = P_1 a_1 + P_2 a_2 = (P_1 + P_2) \times (1 - K_2) h \quad (5.16)$$

these two equations were simplified, similar to the equations of the rectangular cross-sections, leading to the following equations:

$$K_1^2 K_3 = \frac{f_o}{f_c'} \quad (5.17)$$

$$K_2 = 1 - \frac{m_o}{f_o} \quad (5.18)$$

Figure 5.16 shows the actual cross-section of the test specimens and the triangular cross-section that had the same base and apex. The differences between the area and the center of gravity of the two cross-sections were very small, as illustrated in the figure, and were neglected in the analysis. The parameter K_2 was the only parameter that could have significant error if it was taken as the test value. The modified value of K_2 was calculated, assuming the same position for the resultant force in both cross-sections as follows:

$$k_2 h = K_{2t} h_t + 10 \quad (5.19)$$

where; K_{2t} is the value obtained from the test, h is equal to 250 mm and h_t is equal to 240 mm.

Table 5.2 gives a summary of the design parameters for the triangular specimens. The mean values of the parameters $K_1^2 K_3$ and K_2 of the HSC specimens were 0.528 and 0.544 while the same values for the UHSC specimens were 0.411 and 0.534. The ACI values of $\alpha_1 \beta_1^2$ and $0.667 \beta_1$, for any concrete strength higher than 55 MPa, are 0.399 and 0.433 respectively. The results of the test are compared with the code procedures in Chapter 7. The ultimate strain for the triangular specimens were much higher than the code limiting value of 0.003 as illustrated in the table.

Table 5.1 Stress Block Parameters for the Rectangular Specimens

Specimen	f_c' (MPa)	ϵ_s Strain at Maximum	Design Parameters		K_1	K_3	Remarks
			$K_1 K_3$	K_2			
V1*	70.7	0.00331	0.460	0.264	0.50	0.920	
V2	82.8	0.00458	0.619	0.352	0.644	0.973	Constant Ecc. Test
V4	72.8	0.00348	0.637	0.393	0.709	0.898	
V6	98.8	0.00378	0.561	0.374	0.629	0.892	
V7	84.7	0.00369	0.583	0.360	0.669	0.872	
V13	72.5	0.00372	0.619	0.388	0.712	0.87	
V16	59.3	0.00363	0.727	0.370	0.671	1.084	
Mean	78.5	0.00366	0.624	0.373	0.672	0.932	Excluding Specimen V1 and Strain ϵ_s of Specimen V2
σ	12.3	0.0001	0.053	0.0144	0.031	0.076	
V5	124.8	0.00396	0.539	0.344	0.585	0.922	
V8	128.5	0.00391	0.547	0.347	0.550	0.995	
V11	127.5	0.00389	0.468	0.345	0.572	0.819	
V12	121.5	0.00408	0.523	0.353	0.575	0.909	
V14	124.7	0.00398	0.507	0.341	0.576	0.881	
V15	124.8	0.0040	0.557	0.343	0.566	0.984	
V17	127.7	0.00433	0.527	0.356	0.572	0.921	
Mean	125.6	0.00402	0.524	0.347	0.57	0.919	
σ	2.24	0.00014	0.027	0.0051	0.010	0.055	

* The neutral axis depth was equal to 1.719h at the maximum moment about the neutral axis (h is the depth of the cross-section)

Table 5.2 Stress Block Parameters for the Triangular Specimens

Specimen	f_c' (MPa)	ϵ_s Strain at Maximum	Design Parameters		K_1	K_3	Remarks
			$K_1^2 K_3$	K_2			
T1 *	81.0	0.0042	0.507	0.530	0.71	1.006	
T2	89.4	0.0047	0.523	0.548	0.70	1.066	
T3	84.0	0.0049	0.555	0.554	0.74	1.013	
Mean	84.8	0.0046	0.528	0.544	0.717	1.028	
σ	3.47	0.0003	0.02	0.010	0.017	0.027	
T4	129.1	0.0051	0.448	0.516	0.641	1.089	
T5	130.6	0.005	0.409	0.501	0.643	0.989	
T6	117.8	0.005	0.411	0.534	0.670	0.915	
Mean	125.8	0.005	0.423	0.517	0.651	0.998	
σ	5.71	0.00005	0.018	0.0135	0.013	0.071	

* The neutral axis depth was equal to 1.072h at the maximum moment about the neutral axis (h is the depth of the cross-section)

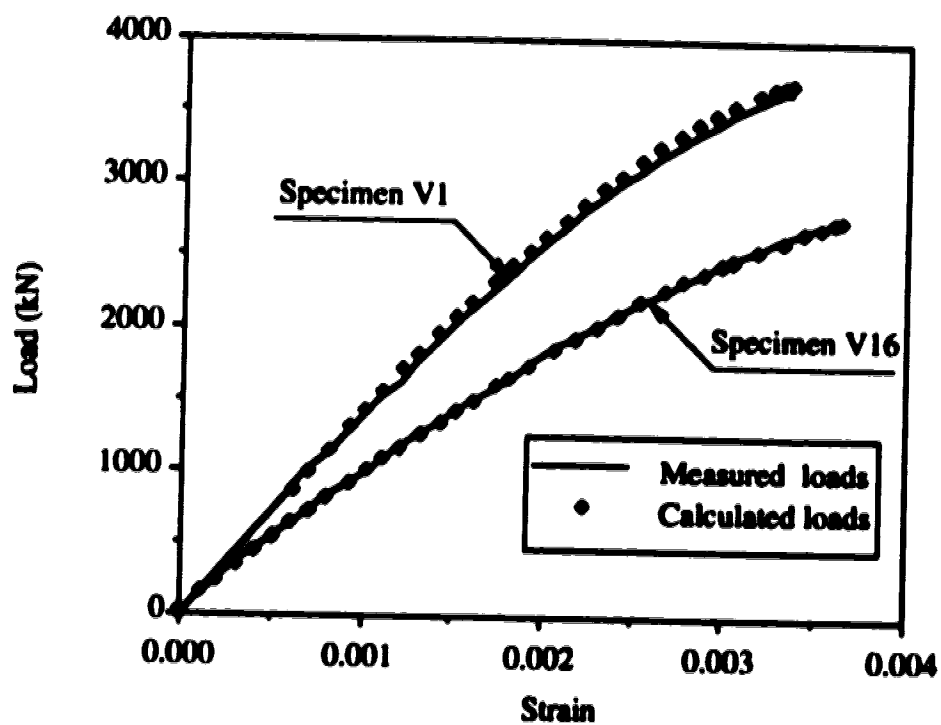


Figure 5.1 Measured and Calculated Loads for Specimen V1 and V16

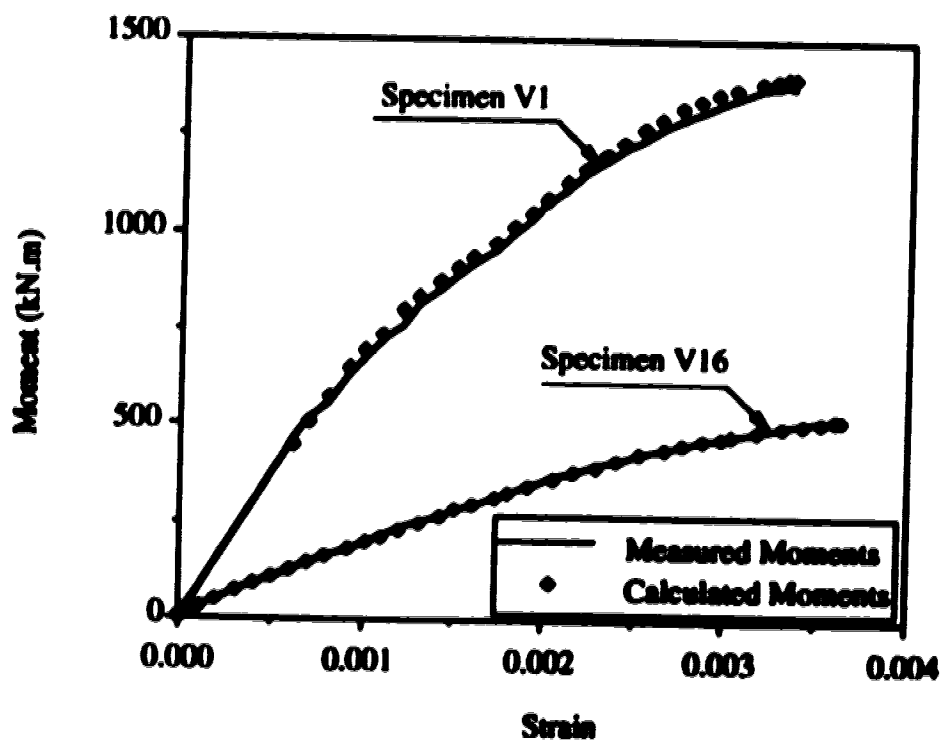


Figure 5.2 Measured and Calculated Moments for Specimen V1 and V16

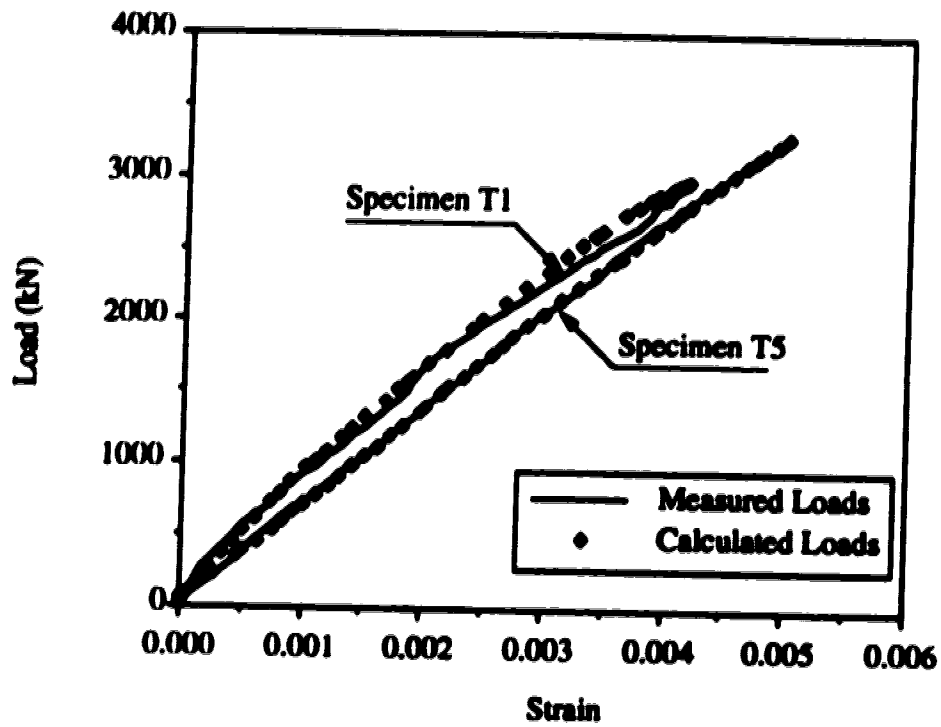


Figure 5.3 Measured and Calculated Loads for Specimen T1 and T5

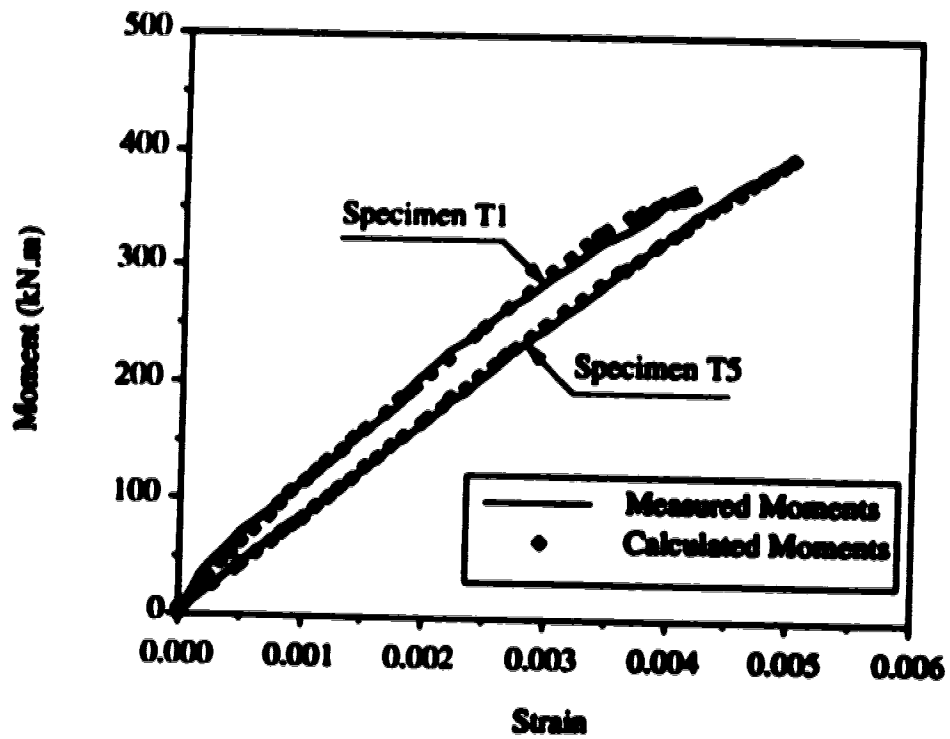


Figure 5.4 Measured and Calculated Moments for Specimen T1 and T5

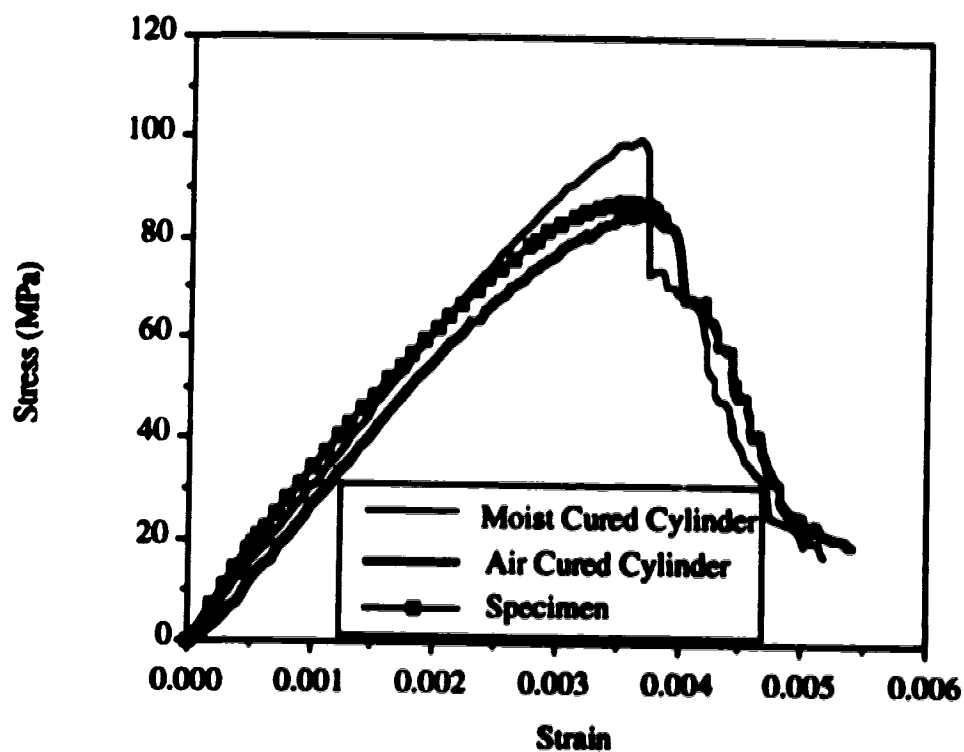


Figure 5.5 Stress-Strain Curves for Specimen V6

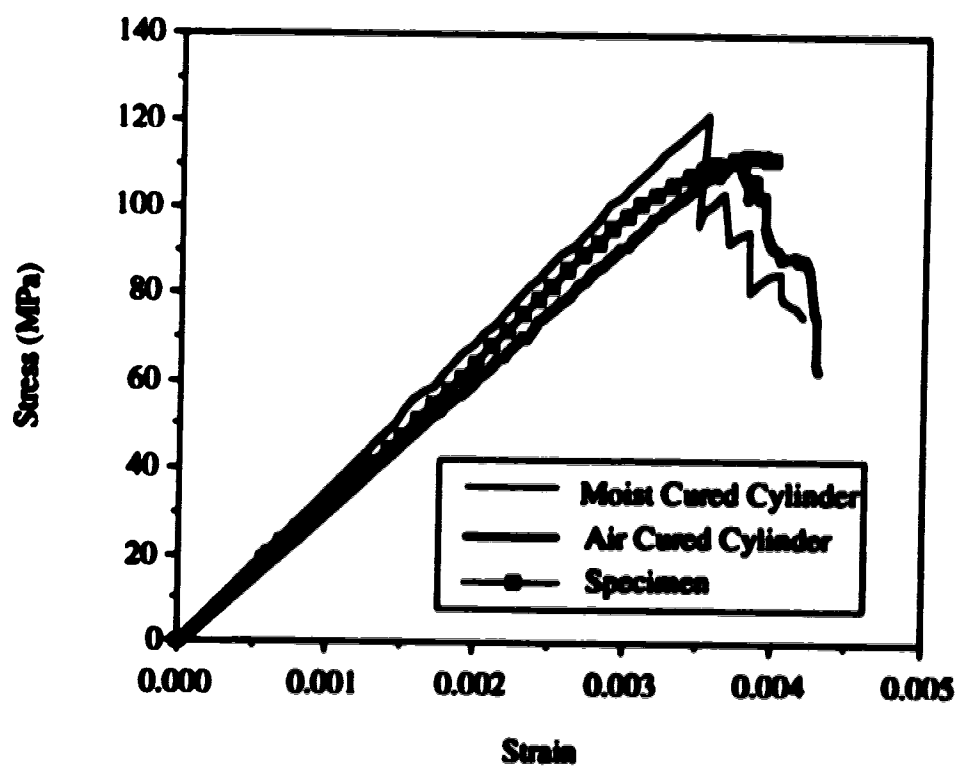


Figure 5.6 Stress-Strain Curves for Specimen V14

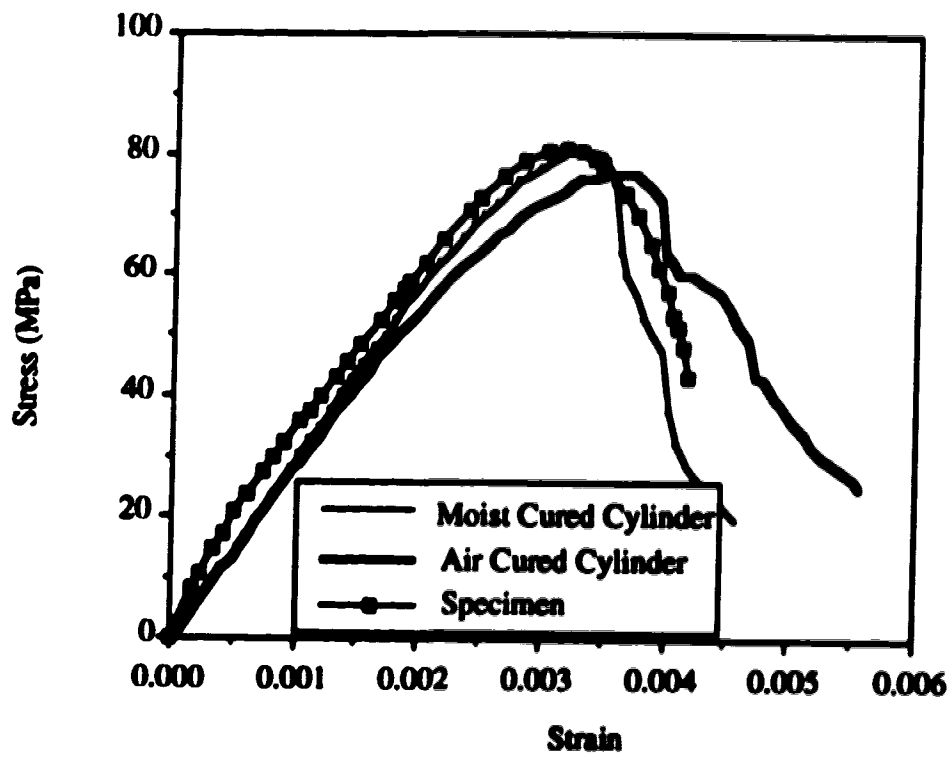


Figure 5.7 Stress-Strain Curves for Specimen T1

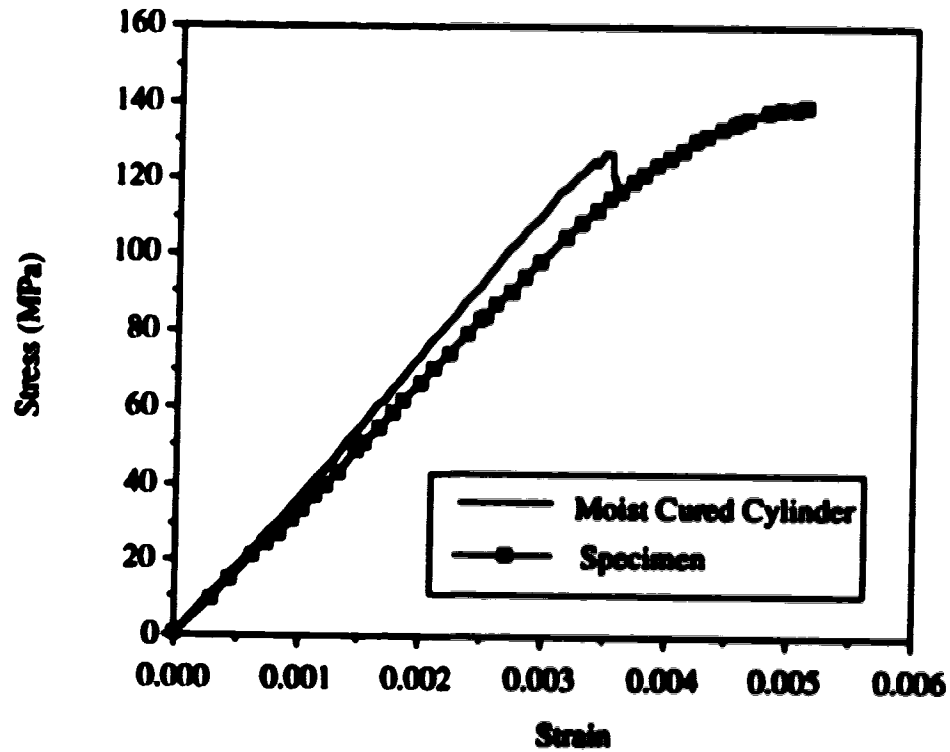


Figure 5.8 Stress-Strain Curves for Specimen T4

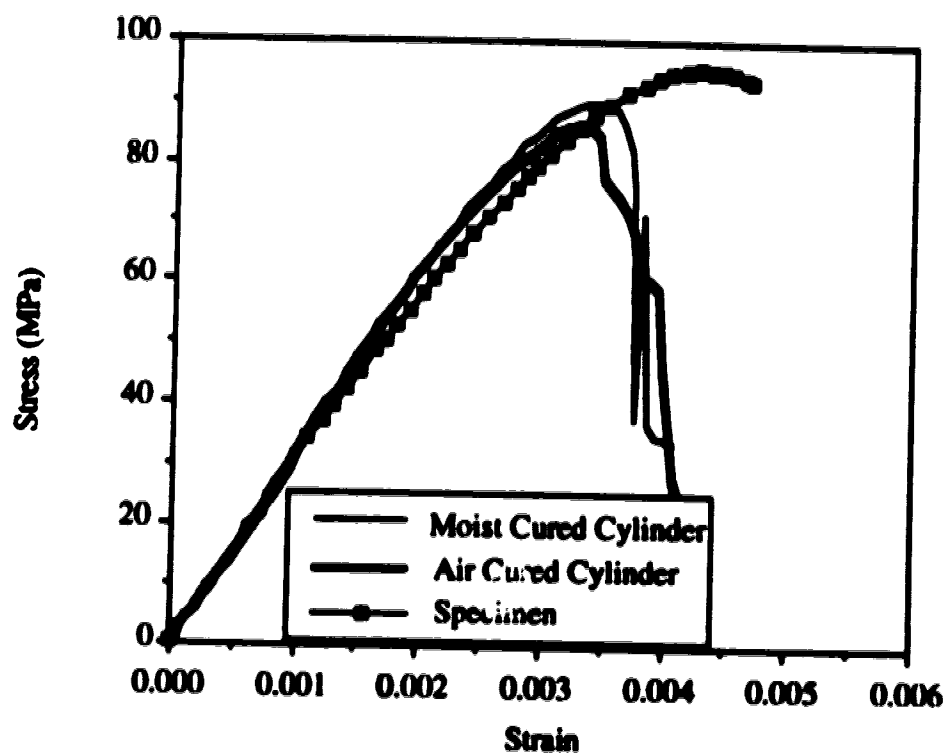


Figure 5.9 Stress-Strain Curves for Specimen T2

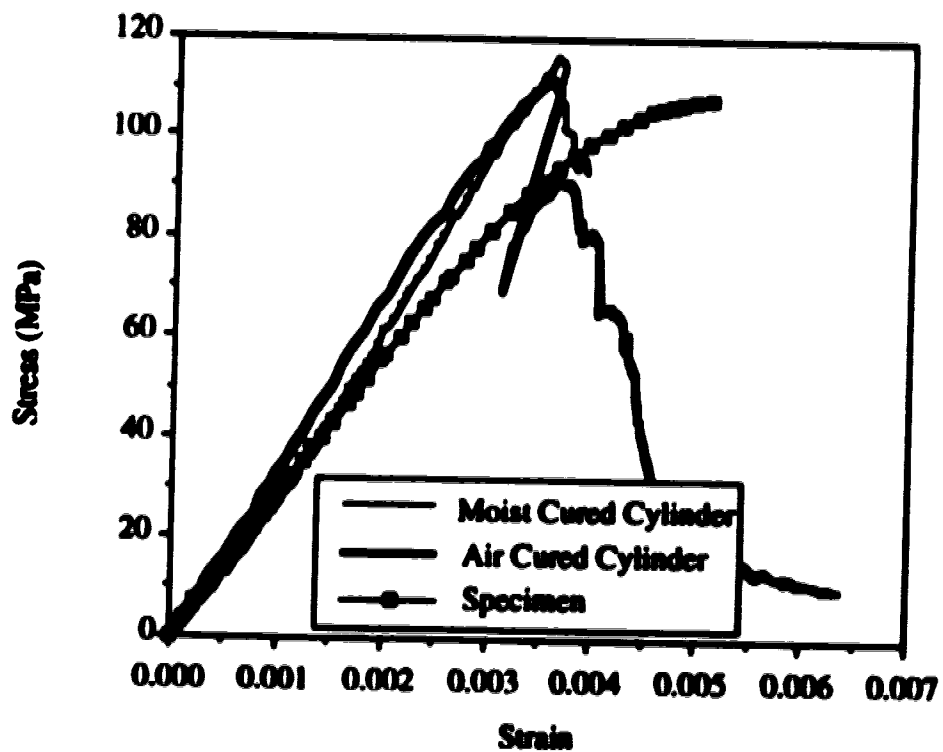


Figure 5.10 Stress-Strain Curves for Specimen T6

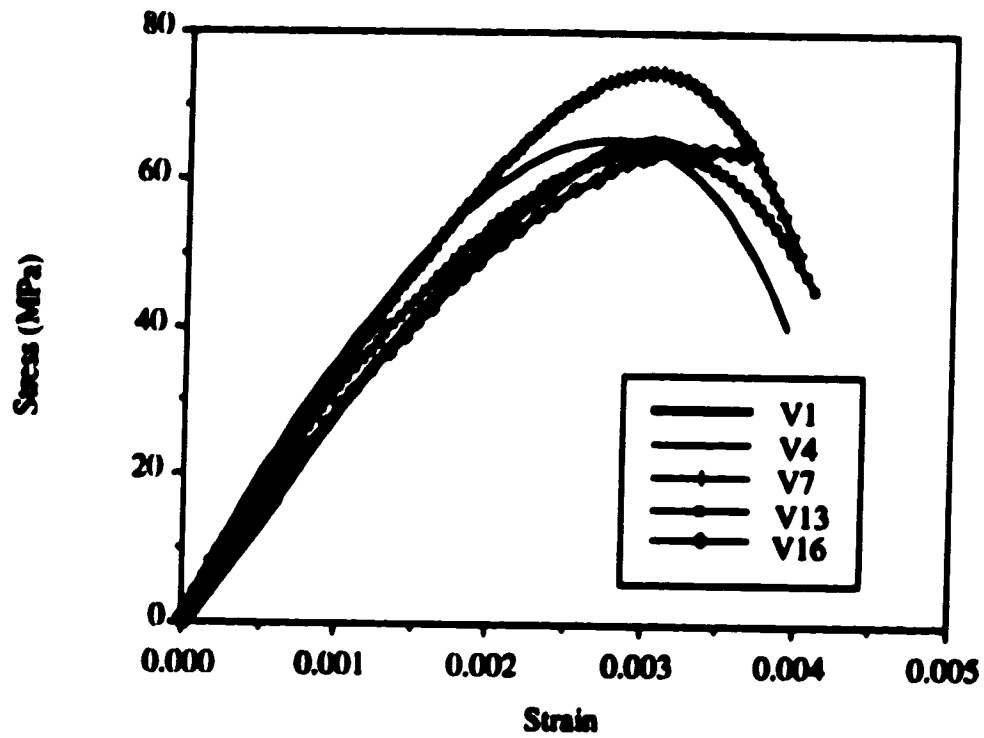


Figure 5.11 Stress-Strain Curves for the HSC Rectangular Specimens

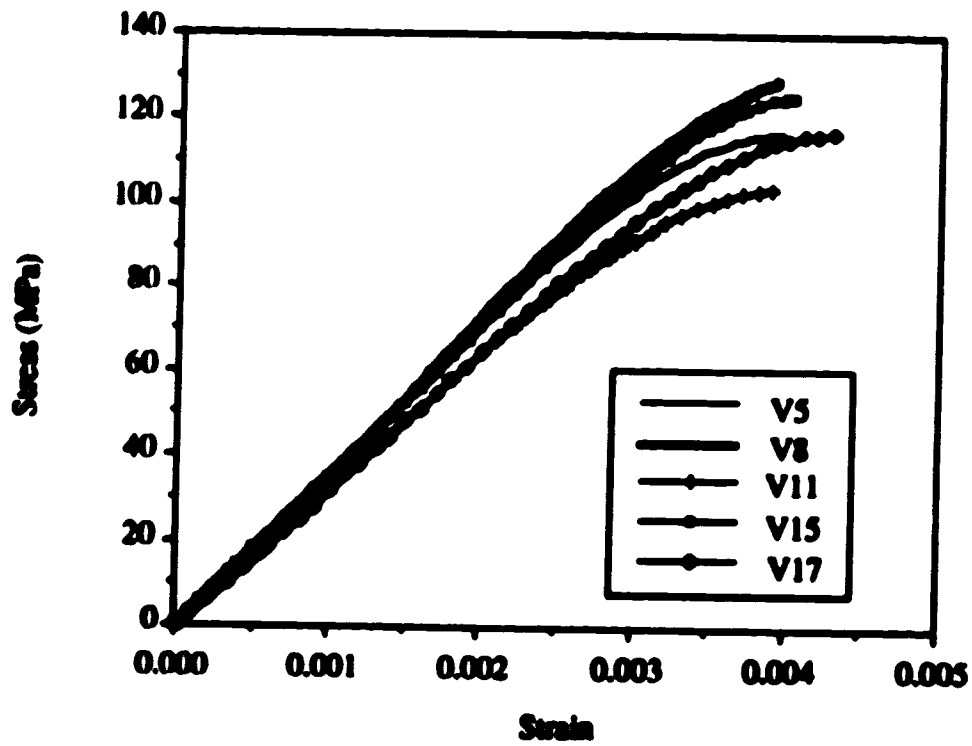


Figure 5.12 Stress-Strain Curves for the UHSC Rectangular Specimens

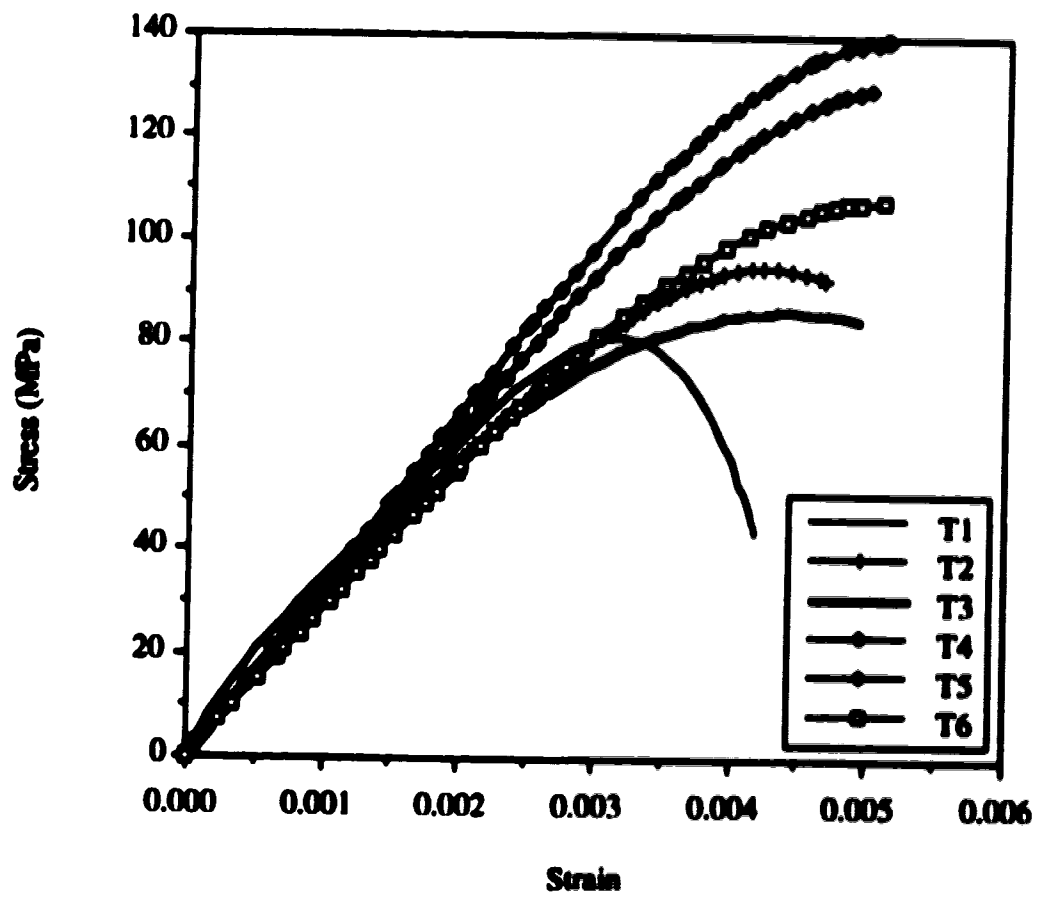


Figure 5.13 Stress-Strain Curves for the Triangular Specimens

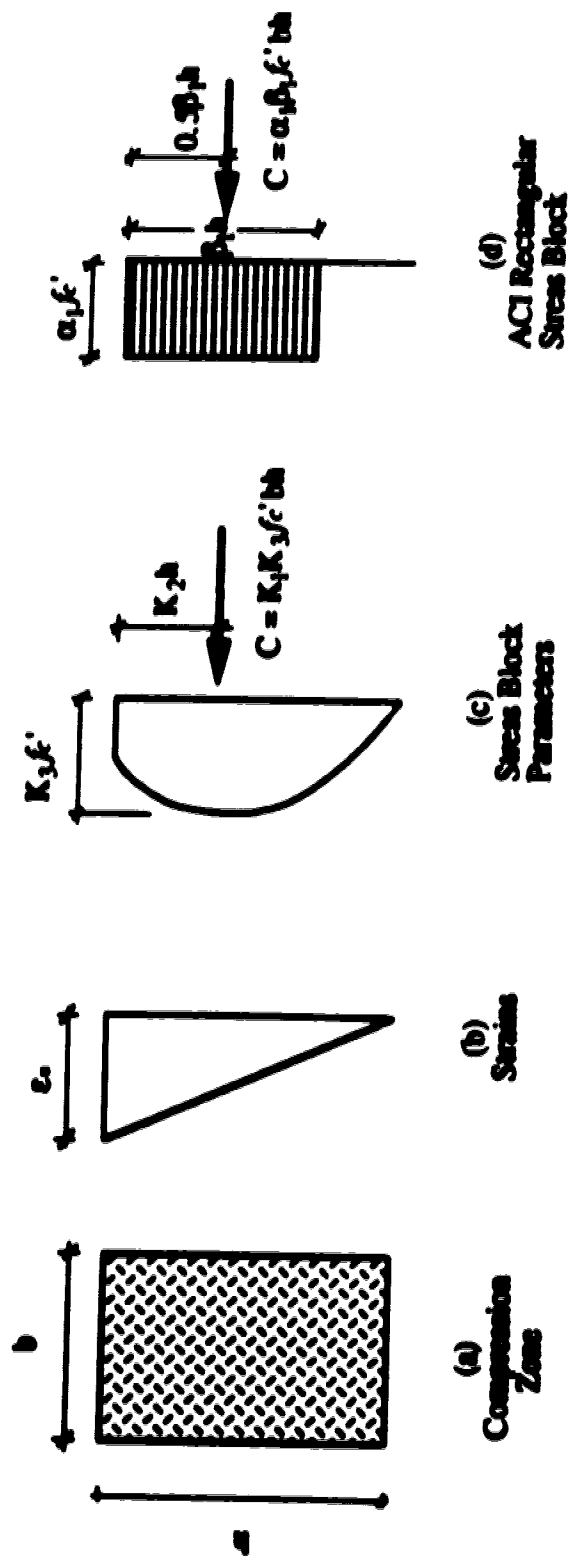


Figure 5.14 Stress Block Parameters for the Rectangular Sections

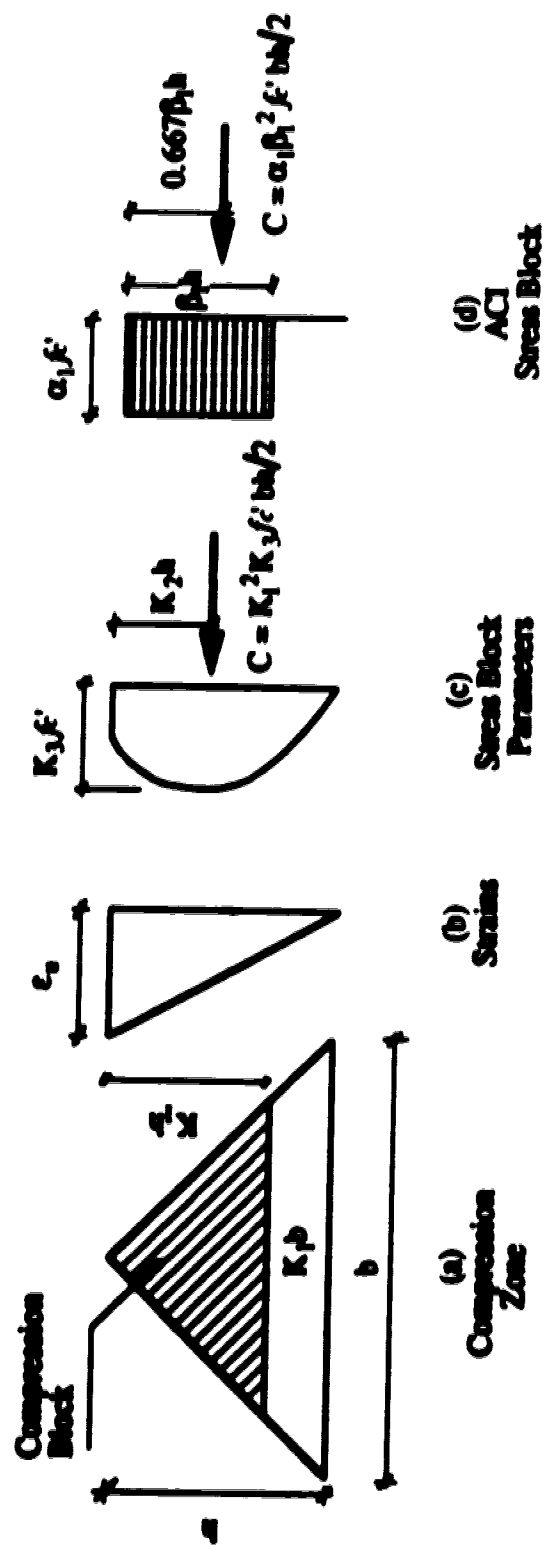


Figure S.15 Stress Block Parameters for the Triangular Specimens

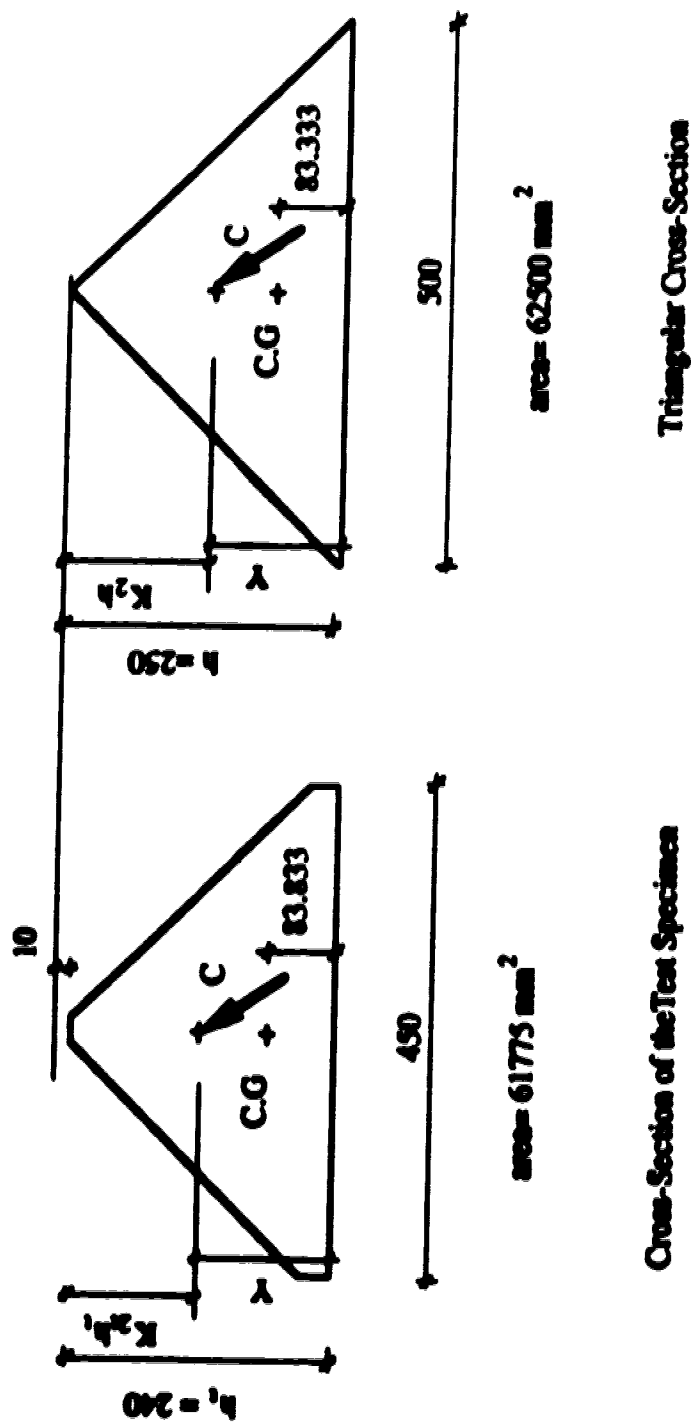


Figure S.16 Details of the Cross-section of the Triangular Specimens

6- Flexural Stress-Strain Curves of the Confined Core

6.1 General

The flexural stress-strain curves of the specimens, presented in Chapter 5, were based on the gross cross-sectional dimensions. In order to get the flexural stress-strain curves of the confined core, the laterally reinforcement specimens are treated as composite members consisting of concrete core and concrete cover. For every specimen the behavior of the concrete cover during the test was established using the readings of the strain gauges and the LVDT's of the rotation arms. Because of the complexity of the behavior of the concrete cover, assumptions are used in order to estimate the contribution of the concrete cover to the load and moment at each loading step.

In this Chapter the flexural stress-strain curves of the confined core are presented with a discussion about the behavior of the concrete cover, the mathematical approach and the assumptions used in order to obtain these curves.

6.2 Behavior of the Concrete Cover

6.2.1 Previous Work

In the literature, there are three pioneering test series that dealt with the flexural stress-strain curves of confined specimens tested in a similar manner to the specimens in the current test series. Soliman et al. (1967) tested rectangular specimens with longitudinal and lateral reinforcement. Most of the specimens had no concrete cover. The method of analysis for plain concrete specimens was applied to these specimens. Kaar et al. (1978b) tested a series of rectangular specimens with longitudinal and lateral reinforcement. The gross cross-section was used in the analysis. The influence of the concrete cover loss was not discussed in the published report.

Sargin et al. (1971) tested a series of rectangular specimens with longitudinal and lateral reinforcement. The load carrying capacity of the concrete cover was taken less than that of the plain concrete specimens made from the same concrete mix. Sargin considered the concrete cover to be weaker than the concrete in identical plain concrete specimens for the following reasons:

(a) The ties interrupt the continuity of concrete. Because of the lateral confinement of the core, the lateral tensile strains in the core are smaller than those in the cover. This causes separation between the cover and the core. When the separation starts, the slender cover is more vulnerable to instability effects and local defects on the surface than the solid unconfined plain concrete specimens.

(b) In practice, the existence of ties may result in inadequate compaction of, and air and water concentrations in the cover concrete, and so the cover concrete is inherently of a lower strength than the core concrete or the concrete in a plain specimen.

A parameter, K_{3c} , that represents the ratio of the maximum stress in the cover to the stress in a plain concrete was used in Sargin's analysis. The stress-strain relationships in both cases were assumed to be identical up to a certain level of strain, ϵ_{cs} , at which the maximum stress in the concrete cover is reached. The two curves were assumed to be different after that. The parameter K_{3c} was calculated by trial and error. An initial value of the parameter K_{3c} was assumed and hence the strain at the maximum stress ϵ_{cs} was calculated. After establishing a stress-strain relationship for the concrete cover using the values of K_{3c} and ϵ_{cs} , the load and moment carried by the cover were calculated by integrating stresses over the cover area. By subtracting the above from the total measured load and moment, the load and moment carried by the core were calculated. The method of analysis for eccentrically loaded homogeneous specimens was then applied to the core to obtain the stress-strain curve.

Sargin then checked the stress-strain curve of the confined core with the stress-strain curve of an identical plain concrete specimen. The two curves should coincide up to the level of strain ϵ_{cs} . If there was a significant difference between the two curves, a different value of K_{3c} was assumed and the procedures were repeated.

6.2.2 Observed Behavior of the Concrete Cover

As described in Section 4.4.1, the longitudinal deformations of the specimen were measured using three different devices. These readings showed that at low strain values, the concrete cover and the concrete core behaved similarly. The separation between the concrete cover and the concrete core occurred at strain values very close to the spalling strain. The strains at this stage were close to the ultimate strain of similar plain concrete specimens. After spalling of the concrete cover, the average strain distribution in the test region was trapezoidal, although the strain distribution in the middle zone of the test region, where the neutral axis was controlled, was still triangular.

In order to explain the behavior of the concrete cover during each test, the readings of the strain gauges were plotted versus the average strain from the rotation arms. Figures 6.1 and 6.2 show the readings of the strain gauges at the compression face of specimen V13. Figure 6.3 shows the readings of the strain gauges at the side faces of specimen V13, 200 mm from the zero strain face. The strain gauge configurations were as shown in Figure 4.8. Specimen V13 showed the first major spalling of the concrete cover in the compression face at an average strain value of 4000 microstrain.

Figures 6.1 and 6.2 show close agreement between the readings of the strain gauges and the average strain from the rotation arms up to an average strain value of 3500 microstrain. At higher average strains, the readings of the strain gauges on the top half of the compression face No. (33, 35, 37, 39, 47) showed sharp unloading. At the same time other gauges on the compression face showed slight decrease in their readings. Following that strain gauges No. (37, 39) gave meaningless numbers, not plotted in the figure, indicating that spalling of the concrete cover occurred in their locations. Strain gauges No. (33, 35, 47) showed more drop in their readings indicating that the separation between the concrete cover and the concrete core continued in the locations of these gauges. Strain gauges No. (45, 53, 55, 57, 59) showed a gradual decrease in their readings. These observations indicate that separation between the cover and the core started in the top zone and extended to the middle zone of the compression face.

Figure 6.3 shows that the separation between the concrete core and the concrete cover at the location of gauges No. (11, 15, 22, 26) on the side faces, occurred at lower values of strain than that for the gauges on the compression face. Gauges No. (11, 22), that were in the same horizontal level with the part that first spalled off in the compression face, showed a sudden drop in the strain readings at an average strain value of the rotation arms close to 4500 microstrain (about 3000 microstrain in the location of the gauges). Gauges No. (15, 26) in the middle of the test region showed the first sign of separation between the cover and the core at an average strain of the rotation arms close to 5000 microstrain (about 3400 microstrain in the location of the gauges). Gauges No. (19, 30), located 200 mm below the center line of the test region, showed change in the strain distribution after the first spalling occurred in the compression face. This change in the behavior was because, at the same horizontal level of these gauges, the concrete cover in the compression face was still integral with the concrete core. As a result of that the strain distribution at this section changed from triangular to trapezoidal (see Section 4.4.1).

The behavior of the concrete cover during each test can be explained by the following. The concrete cover behaved in a similar manner to the concrete core until the time of separation. The strain values at the first separation were very close to the spalling strain which was close to the ultimate strain of similar plain concrete specimens. The spalling occurred over part of the compression face. It normally started at part of the top zone of the test region and continued to include the middle zone. The spalling of the cover in these zones did not include the whole section. Some of the gauges showed readings which might indicate that part of the concrete cover was still in contact with the concrete core. In most cases the concrete cover of the bottom zone of the compression face did not spall off. No explanation is given for this. The specimens were cast in the vertical

direction. The top, as cast was at the top in the test. The readings of the strain gauges in the bottom zone of the compression face showed a decrease in the strain values. In most cases, the spalling of the concrete cover in the side faces occurred only in the zone where the spalling occurred in the compression face. It started at strains that were smaller than those at spalling of the concrete cover in the compression face.

6.2.3 Simplified Assumptions for the Behavior of the Cover

The cross-section of the specimen is treated as a composite section consisting of the concrete cover and the concrete core. The center line of the stirrups is assumed to define the boundaries between the cover and the core, as shown in Figure 6.4. To simplify the analysis the central part of the cover on the zero strain face is considered as a part of the concrete core as shown in the figure. Table 3.2 gives details of the cross-sectional dimensions for each specimen. Figure 6.5 defines the boundary between the concrete cover and the concrete core for the triangular specimens. The figure also gives the dimensions of the concrete core used in the analysis of all of the specimens.

The concrete cover of each specimen is assumed to follow the stress-strain curve for that specimen as reported in Chapter 5. This stress-strain curve represents the gross cross-section behavior before spalling of the cover. The ultimate strain in this curve represents the strain value at the first major spalling in the compression face of the specimen. If part of the concrete cover is subjected to higher strains than the ultimate strain, the load carrying capacity of this part of the cover is taken equal to zero in the analysis.

6.3 Mathematical Approach

The method of analysis for homogenous sections as described in Section 5.2.1 was applied to the concrete core to obtain the stress-strain relationship. The load and the moment carried by the concrete cover were calculated by integrating stresses over the cover area. By subtracting these from the total measured load and moment, the load and moment carried by the core are calculated.

In the analysis in Chapter 5, the quantities f_c and m_c were smoothed by fitting the test data into polynomial equations. Equations 5.3 and 5.4 were then applied to the fitted data. This procedure is not suitable for getting the stress-strain relationship of the core because of the limitations of polynomial equations as explained in Section 5.2.1.

In this Chapter different procedures are used to smooth the test data. The number of the data points is first reduced. This procedure decreases the error that occurred in

calculating the differential parts. The data points at increments close to 100 microstrain in the ascending part of loading, and 200 microstrain in the descending part of loading are kept. Each data point is smoothed separately using the least square fit of a third order polynomial equation. Nine data points are used in the regression analysis of each point (four points from each side and the data point). Equations 5.3 and 5.4 are then applied to the fitted data with the differential parts of the equations approximated by finite differences. For some specimens the transition zone between the first part of the curve prior to spalling and the second part of the curve after spalling was not smooth. In this case, two points were eliminated and the transition zone of the curve was represented by straight line.

6.4 Stress-Strain Curves of the Rectangular Specimens

Prior to spalling of the cover the stress-strain curves from both the load and moment equations showed good agreement with the stress-strain curves of the gross cross-section. This indicates that the assumptions used for the behavior of the concrete cover in the ascending part of loading were close to the actual behavior. After the concrete cover started to spall off, the stress-strain curves from the load and moment equations showed differences. In all tests the maximum difference between the two curves was 12%. These differences between the two curves were due to the simplified assumptions used in the analysis instead of the actual complicated behavior of the concrete cover. These assumptions affected the load and moment equations in different ways leading to different stress-strain curves for the same specimen. An average stress-strain curve from both equations is considered the most representative of the actual behavior for each specimen.

Figure 6.6 shows the stress-strain curves of the confined core of the HSC specimens V1, V13 and V16 and the plain concrete specimen V4. Details of reinforcement are given in Table 3.1. The figure shows that, except for the highly confined specimen V16, the reinforced specimens did not show any significant increase in the ductility of the confined core. Specimen V1, with trapezoidal strain distribution, showed a shorter descending branch for the curve of the confined core than the curve of the plain concrete specimen V4. The stress-strain curve of the core of specimen V13 had a long and steep descending branch. Specimen V16 showed an increase in the maximum core stresses after the cover spalled off. The peak stress was attained at a strain value of about 6000 microstrain. The ratio between the peak stress to the cylinder strength was about 1.5. After the peak stress, the stress-strain curve showed a long plateau with an average stress of 85 MPa to a strain value of about 9000 microstrain. For higher strain values, the curve had a ductile descending branch to the end of the test.

Figure 6.7 shows the stress-strain curves of the confined core of the UHSC specimens V11, V15 and V17 and the plain concrete specimen V5. The stress strain curve of the plain concrete specimen V5 had no descending branch. The confined core of specimens V11 and V15 showed a very steep descending branches. Specimen V17, with a tie configuration similar to specimen V16, showed a ductile behavior. The stress-strain curve of the confined core of the specimen reached it's peak at the time of spalling of the concrete cover. After that the curve had a long plateau, with a stress value close to 90% of the peak, to a strain value of about 10000 microstrain. For higher strain values, the curve had a long descending branch to the end of the test.

6.5 Stress-Strain Curves of the Triangular Specimens

At low strain values the stress-strain curves from the load and moment equations showed good agreement with the stress-strain curves of the gross cross-section. Close to the spalling strain, the curves of the load equation showed significant scatter from the stress-strain curves of the gross cross-section while the curves of the moment equation continued to show very good agreement with these curves. After spalling of the concrete cover the differences between the stress-strain curves from the load and moment equations were much higher. In some cases, the stress-strain curve of the load equation showed an increase in the slope of the curve with an increase in the strain. These observations suggested that the simplified assumptions for the behavior of the concrete cover had a significant effect in the accuracy of load equation while they did not affect the accuracy of the moment equation to the same degree. For this reason the moment equation was used to obtain the stress-strain curves of the confined cores of the triangular specimens.

Figure 6.8 shows the stress-strain curves of the confined core of the HSC specimens T2 and T3 and the plain concrete specimen T1. Details of reinforcement are given in Table 3.3. The figure shows an improvement in the slope of the descending branch with an increase in the lateral reinforcement. The figure also shows no increase in the stresses after spalling of the concrete cover. The ultimate strain for the confined specimens were much higher than the ultimate strain of the plain concrete specimen.

Figure 6.9 shows the stress-strain curves of the confined core of the UHSC specimens T5 and T6 and the plain concrete specimen T4. The stress-strain curve of the plain concrete specimen T4 had no descending branch. The stress-strain curve of the confined core of specimen T5 had a long and steep descending branch. Specimen T6 showed a ductile behavior. After spalling of the concrete cover the stresses dropped gradually to about 70% of the maximum stress at a strain value of 9000 microstrain. The curve continued to the end of the test with almost the same level of stress.

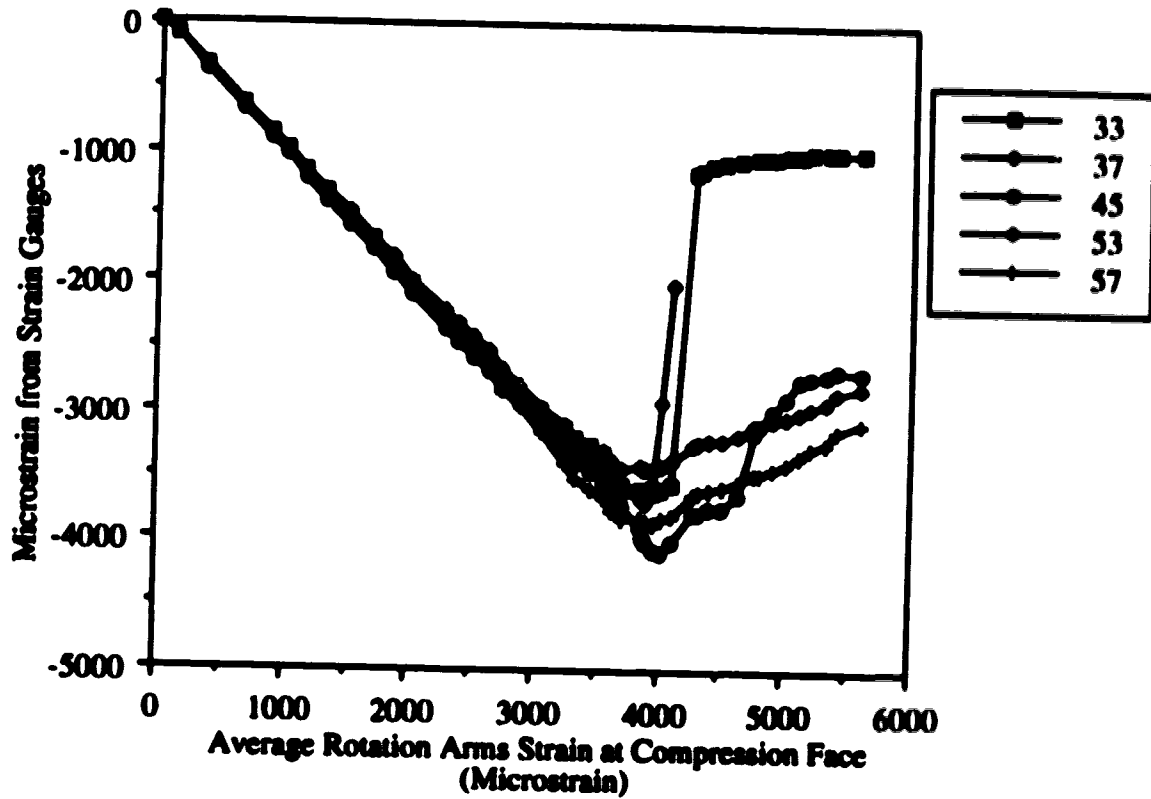


Figure 6.1 Strain Gauges at the Left Side of the Compression Face of V13

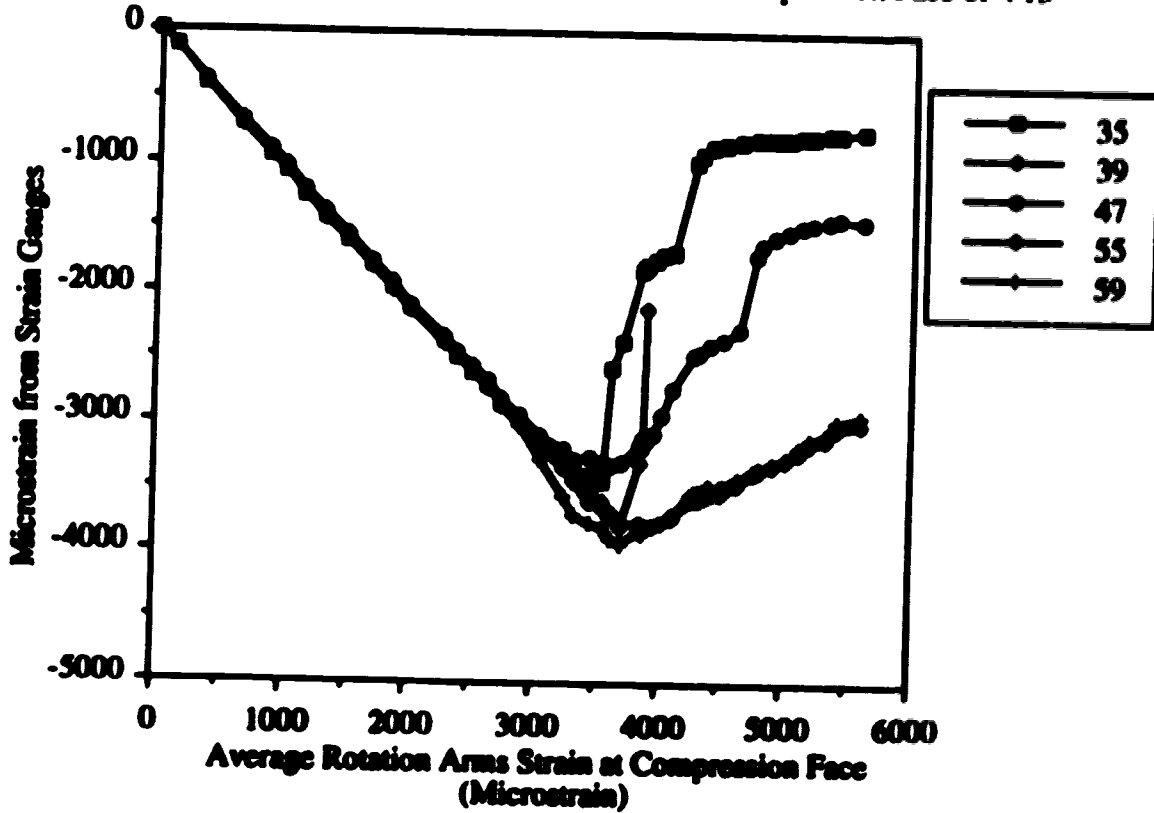


Figure 6.2 Strain Gauges at the Right Side of the Compression Face of V13

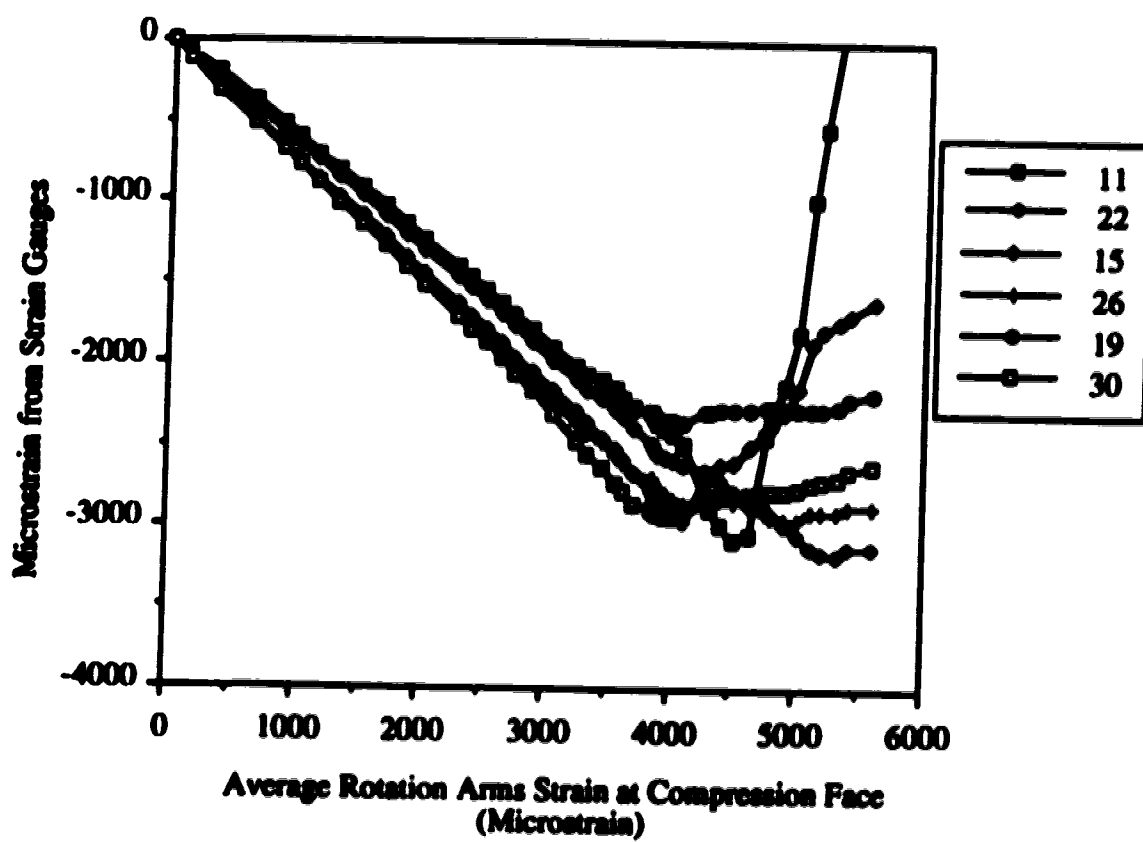


Figure 6.3 Strain Gauges at 200 mm from the Zero Strain Face of V13

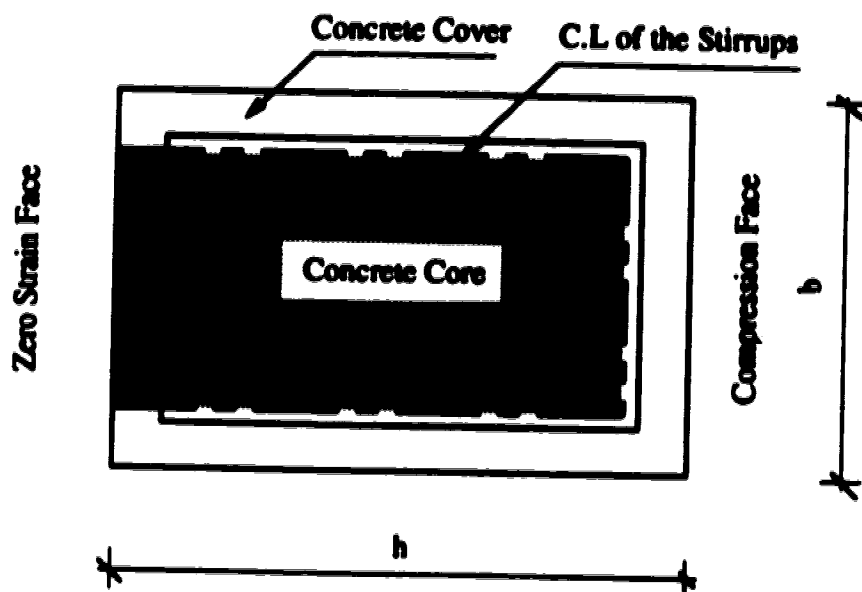


Figure 6.4 Boundaries between Concrete Cover and Concrete Core for the Rectangular Specimens

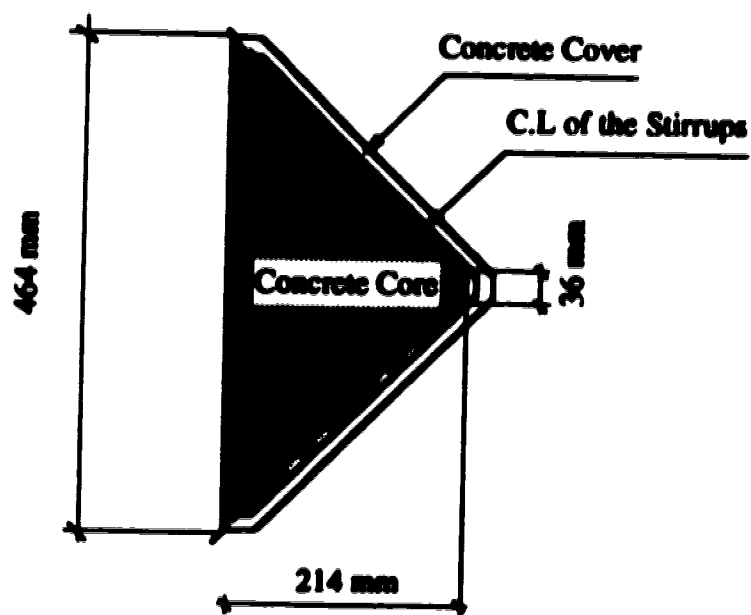


Figure 6.5 Boundaries between Concrete Cover and Concrete Core for the Triangular Specimens

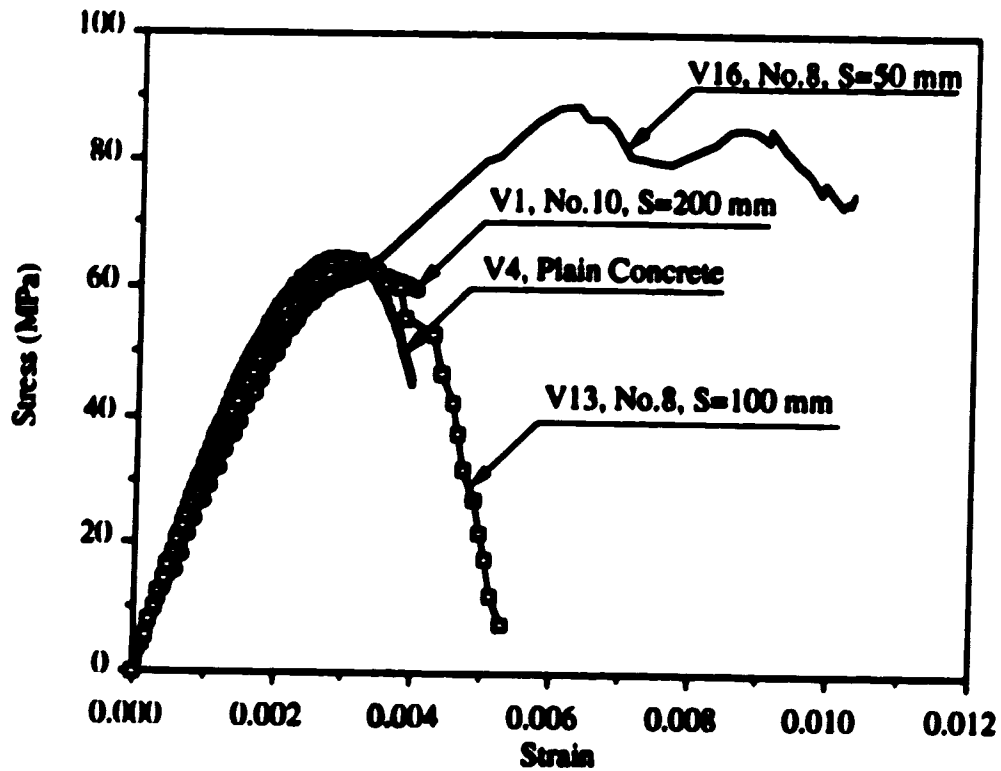


Figure 6.6 Stress-Strain Curves of the Confined Core of the HSC Rectangular Specimens

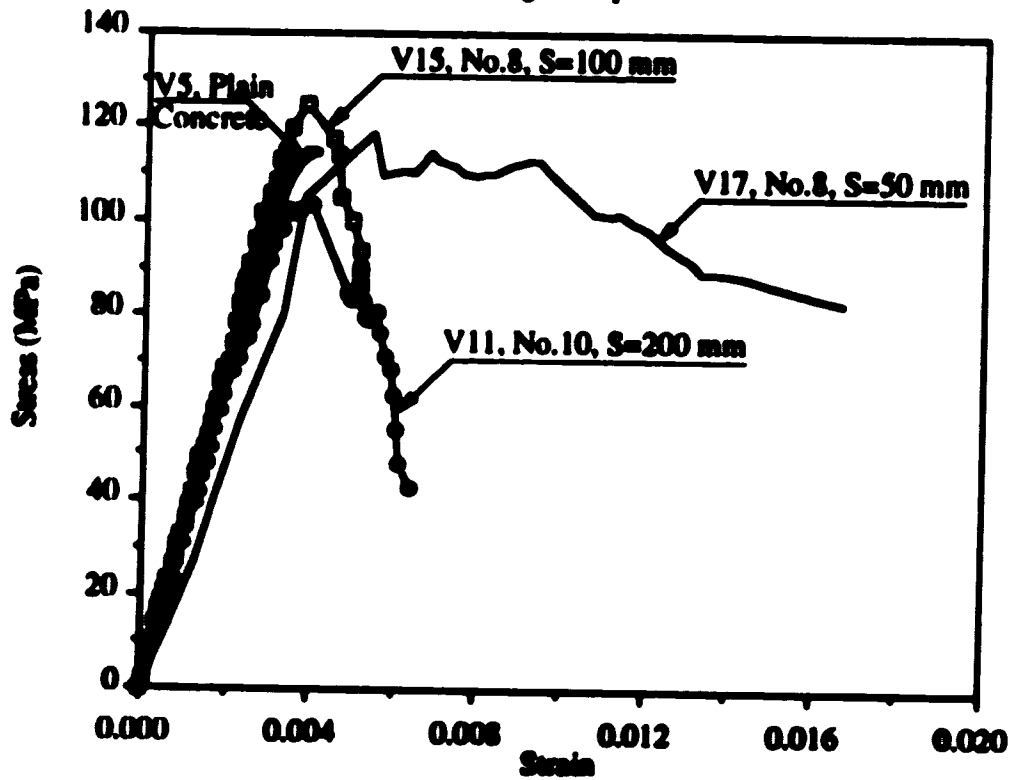


Figure 6.7 Stress-Strain Curves of the Confined Core of the UHSC Rectangular Specimens

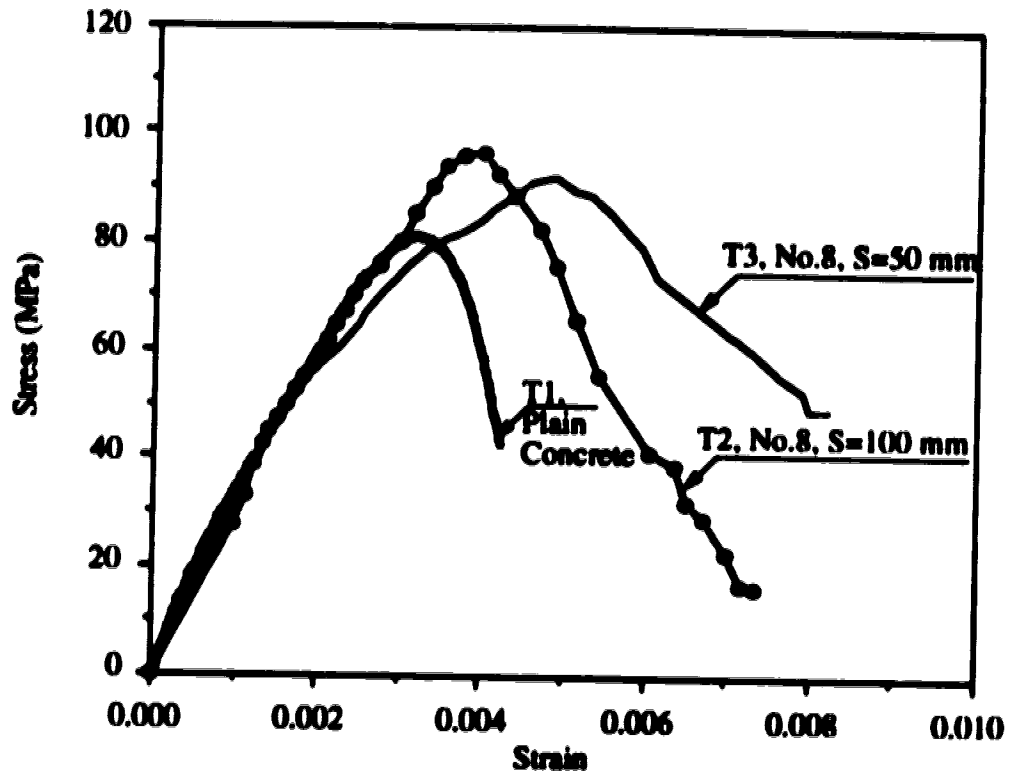


Figure 6.8 Stress-Strain Curves of the Confined Core of the HSC Triangular Specimens

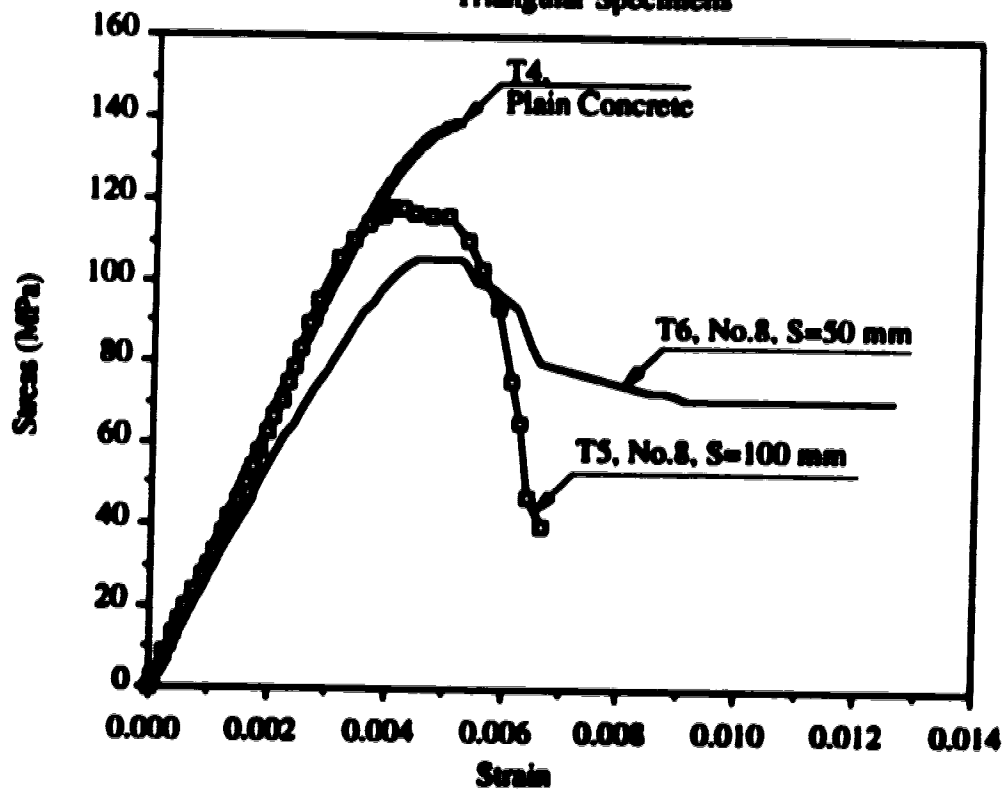


Figure 6.9 Stress-Strain Curves of the Confined Core of the UHSC Triangular Specimens

7- Design Equations

7.1 General

Most concrete codes do not cover concrete with strengths above 50-60 MPa. A summary of some of the current codes that do allow design for HSC sections is presented. Details are given for the ACI and the Norwegian codes which do consider some aspects of design of HSC. Researchers have suggested that the ACI rectangular stress block is unconservative by up to 12% for HSC column sections. New equations are proposed for the rectangular stress block parameters.

7.2 Stress-Strain Relationships in Different Design Codes

7.2.1 US Code ACI 318-89 and Canadian Code CAN3-A23.3-M84

The ACI code specifies the concrete compression strength using 152/304 mm cylinders. Although there is no limitation to the concrete strength in general, the maximum strength to be considered for the contribution to the shear strength is 70 MPa. In the ACI code, rectangular, trapezoidal, parabolic or other stress blocks may be assumed provided the relationship between concrete compressive strength distribution and the resulting concrete strain is in agreement with the test data. The ACI rectangular stress block that is recommended for design is defined by the parameters α_1 , β_1 and ϵ_u (see Section 5.3). The parameter α_1 is assumed to have a constant value of 0.85. The parameter β_1 is equal to 0.85 for concrete strengths, f_c' up to 30 MPa and is reduced continuously at a rate of 0.08 for each 10 MPa of strength in excess of 30 MPa. The parameter β_1 is not taken less than 0.65. The limiting compressive strain ϵ_u is assumed to have a constant value of 0.003.

7.2.2 Norwegian Code NS 3473-1989

The highest grade for normal density concrete based on tests of 100/100/100 mm cubes is 105 MPa (C105). The conversion factor to a 152/304 mm cylinder is 0.8 up to grade C55 and the cube strength minus 11 MPa for higher grades. The Norwegian code assumes an effective K_1 value which decreases with increasing strength, going from 0.84 for cylinder strength of 20 MPa to 0.66 for cylinder strength of 94 MPa. The strain values at the peak stress, ϵ_{m1} , change from 0.00197 to 0.00215 and the strain values at ultimate strain, ϵ_{m2} , change from 0.00384 to 0.00268 with a change in the cylinder strength from 20 to 94 MPa. Figure 7.1 gives the recommended stress strain relationship for different concrete grades. The symbol f_m in the figure represents the strength of the concrete in the

structure. The moment and the normal force capacity of rectangular sections can be calculated by direct use of the magnitude of the resultant force (R), which is equivalent to K_1 and the position of the resultant (C), which is equivalent to K_2 . Table 7.1 (taken from Thorenfeldt et al. (1987)) gives the values of f_{cm} , R and C for different concrete strengths.

7.2.3 Finnish Code Rak MK4 1989

The highest grade concrete defined using 150/150/150 mm cubes is 100 MPa (K100). The conversion factor to a 152/304 mm cylinder is taken as the cube strength minus 8 MPa. The Finnish code assumes a constant value of K_3 equal to 0.70. Figure 7.2 shows the stress-strain relationship recommended by the code. The symbol f_{ek} in the figure represents the concrete strength in the structure.

7.2.4 CEB/FIP Model MC90

The highest grade concrete defined using the uniaxial compression strength of cylinder 150/300 mm is 80 MPa (C80) for normal density concretes. The stress-strain diagrams are generally of the form shown schematically in Figure 7.3. The value of ϵ_{ci} is set to -.0022. Values of E_c , E_{ci} , ϵ_{cu} change with changes in the concrete grade as shown in Table 7.2.

7.3 Interaction Diagrams for Concrete Columns

Almost all compression members in concrete structures are subjected to moments in addition to axial loads. In order to design a concrete member that is subjected to different cases of loading, an interaction diagram is generated for the cross-section. This could be done using a strain compatibility solution where a series of strain distributions are assumed each corresponding to particular point on the interaction diagram, and computing the corresponding values of P and M . Once enough points have been computed, the results are summarized in an interaction diagram. Details of the procedures of generating the interaction diagram are given by MacGregor (1992).

To generate an interaction diagram for a concrete section, any stress-strain relationship for concrete in compression can be used. For design purposes, a stress-strain relationship that is recommended by one of the design codes with the appropriate design factors is normally used. Using different stress-strain equations can lead to substantial differences in the obtained interaction diagrams. Figure 7.4 shows interaction diagrams for two square sections with cylinder compressive strengths of 60 and 120 MPa. The interaction diagrams were generated using both the ACI rectangular stress block and the Norwegian code design stress-strain curve. Since the highest grade for the Norwegian

code is C105 (cylinder strength f'_c of 94 MPa), the coefficients of the stress-strain curve of 94 MPa concrete were used with $f'_c = 120$ MPa to generate the stress-strain curve of the 120 MPa section. The resistance factors were taken equal to 1.0. Details of the dimensions and the reinforcement of the cross-section are given in the figure.

Figure 7.4 shows that the Norwegian code is conservative compared to the ACI code. The difference between the two interaction diagrams was significant for the part of the diagram where the axial load is high (when the section is subjected to axial forces with small eccentricities). For the pure moment case (beam section) the effect of using a different design equation or changing the concrete strength is negligible.

7.4 Derivation of Factors for Use in the ACI Design Procedures

(factors derived based on measured load from column tests and measured load and moment from eccentrically loaded column tests at the first peak before spalling of the cover)

7.4.1 Structure to Cylinder Compression Strength Ratio, K_3

The parameter K_3 is the ratio between the strength of the concrete in columns compared with concrete of the same mix in standard compression test cylinders. This parameter can be determined from tests on concentrically loaded columns by dividing the part of the maximum load carried by the concrete section by the gross cross-section area multiplied by the cylinder compression strength. It can also be determined from tests on eccentrically loaded columns. In this case the parameter K_3 can not be obtained from the equilibrium of the external and internal loads since the column strength is related to the cylinder strength by the parameters K_1K_3 . It is necessary to compute the stress-strain relationship of the cross-section with certain assumptions to calculate K_3 , as described in Chapter 5.

The report of the ACI Committee 363 (1984) on HSC recommends the use of a constant value of K_3 equal to 0.85. This recommendation was based on the results of an experimental program on concentrically loaded plain concrete high strength cylinders with different sizes, conducted by Martinez et al. (1982). The FIP/CEB (1990) state of the art report on HSC included results from two test series on concentrically loaded reinforced HSC columns with strengths ranging from 75 to 100 MPa conducted by Høiseth et al. (1983) and Bjorkeli et al. (1990). The average value of K_3 was 0.82 in the first test series and a value that ranged between 0.94 to 0.96 in the second test series.

Figure 7.5 shows K_3 values obtained from different eccentrically loaded columns. All of the specimens were tested under a triangular strain distribution. The test series by Karr et al. (1978a) and Swartz et al. (1985) were on plain concrete specimens. The test

series by Schade (1992) and the current research included both plain and reinforced concrete specimens. The figure indicates that despite the scatter in the test results, the ACI value of 0.85 is conservative with respect to the values of K_3 obtained from eccentrically loaded tests. This conclusion does not mean that the ACI code is conservative in predicting the applied loads on eccentrically loaded sections since the force in the cross-section is related to the cylinder strength by the multiple of the parameters $K_1 K_3$ as discussed before. Although not evident from the figure there were no significant differences between the K_3 values of the plain concrete specimens and the reinforced concrete specimens.

Figure 7.6 shows the values of K_3 obtained from tests conducted on concentrically loaded columns. The columns used in preparing Figure 7.6 had a wide range of amounts of lateral reinforcement ranging from columns without any reinforcement, to columns that had more reinforcement than required by the ACI code for seismic regions. The values of K_3 obtained from the test series conducted by Sheikh et al. (1980) were calculated using the gross cross-sectional area at the peak loads that might occur after spalling of the cover. The peak load was higher than the load values before spalling because of the confinement effects. For the other tests the K_3 value was calculated at the first peak which occurred at or before spalling of the cover. The values of K_3 from the test of Richart et al. (1929,1934,1947) were taken from the reference Martinez (1983).

Figure 7.6 shows that the ACI value of 0.85 is not conservative. All the test results of Cusson et al. (1992) were lower than the code value. The figure also shows more scatter between the results of different HSC column test series than that of different LSC column test series but it does not show a strong trend for K_3 to become lower as the concrete strength increases. Some test series of HSC columns showed high values of K_3 and others showed quite low values of K_3 . High values of K_3 were also reported in the FIP/CEB (1990) report on HSC, as discussed before. Other tests that were conducted in University of Toronto (not plotted in Figure 7.6) showed values of K_3 as low as 70% of the value given by the ACI code. These tests included eccentrically loaded columns made with 60 MPa concrete tested by Sundararaj (1991) and concentrically loaded columns made with 66 MPa concrete tested by Polat (1992). Tests on concentrically loaded spirally reinforced cylinders made with 63 MPa concrete that were conducted by Martinez (1983) (not plotted in Figure 7.6) showed an average value of K_3 equal to 0.8. The lower strength concrete specimens of the same test series showed an average value of K_3 equal to 0.98.

The lower values of K_3 reported in some of the HSC column tests were explained in different ways. Martinez (1983) claimed that the quality of the concrete in the protective cover of the spiral columns was inferior to that of the concrete inside their cores. This difference in quality occurred because of inadequate compaction of the concrete in the cover

caused by the low workability of the HSC mixes. The low failure loads of University of Toronto tests were explained by the early spalling of the concrete cover. This early spalling of the concrete cover were caused by the formation of splitting cracks in the plane of the longitudinal reinforcing bars. Due to the very low permeability of the most high strength concrete only the outermost shell of the column will dry out causing restrained shrinkage stresses in the outer shell. Cusson et al. (1992) explained the low capacity of their columns by the existence of longitudinal weakness planes in the columns due to the high density of steel reinforcement.

More tests on concentrically loaded HSC columns are required to provide better understanding of the behavior of these columns. The design codes should provide a conservative value of K_3 compared with the available test data.

7.4.2 ACI Design Parameters of the Rectangular Stress Block

The stress block parameters K_1 , K_2 and K_3 obtained from previous tests are used in the following analysis in order to check the ACI design procedures. The experimental data are tabulated in Appendix C. These previous tests had a wide range of variables (not listed in Appendix B) including rate of loading, size of the specimen, concrete mix design, type of aggregates, amount of reinforcement and test procedures. The data points from Hognestad et al. (1955) and Rüsch (1955) were obtained from enlarged graphs from the reference Abeles et al. (1956).

The ACI rectangular stress block parameters were used to generate a normalized interaction diagram for plain concrete sections as shown in Figure 7.7. The interaction diagram was normalized with respect to f'_c and the cross-section dimensions. For reinforced concrete sections, this normalized interaction diagram represents the contribution of the concrete section in the loads and the moments carried by the section after excluding the part of the loads and the moments that were carried by the reinforcement steel in the manner explained in Section 5.2.1. In the normalized interaction diagram each test can be represented by one point (R_1), as illustrated in Figure 7.7. This point represents the maximum capacity of the specimen obtained during the test. The coordinates of this point (m_1 , m_2) are function of the stress block parameters K_1 , K_2 , K_3 and the relative position of the neutral axis depth ζ_1 ($\zeta_1 = c/h$). For each test these coordinates were determined using the following equations:

$$\text{Normal Force} = C = K_1 K_3 b c f'_c = \zeta_1 K_1 K_3 b h f'_c \quad (7.1)$$

$$\text{Bending Moment} = M = C \times (0.5h - K_2 c) = Ch \times (0.5 - \zeta_1 K_2) \quad (7.2)$$

$$n = \frac{C}{bh\zeta f'_c} = \zeta_1 K_1 K_3 \quad (7.3)$$

$$m = \frac{M}{bh^2 \zeta f'_c} = \zeta_1 K_1 K_3 \times (0.5 - \zeta_1 K_2) \quad (7.4)$$

To generate the normalized interaction diagram corresponding to the code values of α_1 and β_1 , a series of points in that diagram are calculated. Each point in the diagram has the coordinates (n, m) defined by the following equations:

$$n = \zeta \alpha_1 \beta_1 \quad (7.3a)$$

$$m = 0.5 \zeta \alpha_1 \beta_1 \times (1 - \zeta \beta_1) \quad (7.4a)$$

These equations are identical to Equations (7.3) and (7.4) of (n, m) of the test point with the use of the code stress block parameters α_1 and β_1 instead of the stress block parameters obtained from the test. By changing the value of ζ , different points are calculated and the normalized interaction diagram shown in the figure can be generated.

Figure 7.7 also shows that any data point can be defined by the radial distance from the origin ($0-R_c$) and the slope θ . The relative position of the neutral axis depth ζ_c for the point in the interaction diagram that has the same slope θ , R_c , can be calculated from the equation of $\tan \theta$, as follows:

$$\tan \theta = \frac{1}{0.5 - \zeta_1 K_2} = \frac{1}{0.5 - \zeta_c \beta_1 / 2} \quad (7.5)$$

From the value of ζ_c the radial distance ($0-R_c$) can be calculated. The percentage ratio δ , defined in the Figure 7.7 indicates how far the test point is from the ACI interaction diagram. A positive value of δ for a particular test point means that the code is conservative while a negative value of δ means that the code is not conservative in predicting the maximum capacity of the tested specimen.

The percentage ratio δ was calculated for a total of 94 tests. All of the specimens, except for those by Rüsch, were of the C-shaped specimens. Figure 7.8 shows the percentage ratio δ of these tests plotted versus the concrete strength. The figure indicates that the ACI code is not conservative for most concrete strengths, especially for HSC and UHSC sections. Most of the test points were between $\pm 20\%$ from the code prediction. About 55% of the test points had lower strengths than the code prediction. The mean value of δ for all the tests was -0.1% (test/calculated capacity of concrete = 0.999) with a standard deviation of 9.91% (coefficient of variation of 0.0992). For structural grade concretes with f'_c greater than 30 MPa the average δ drops to -1.76% . Figure 7.9 shows the mean value of δ in each cell plotted versus the concrete strength. The figure shows that

the mean value of δ decreased from about +12% for LSC test points to about -12% for UHSC test points. Figure 7.8 and 7.9 suggests that the ACI rectangular stress block parameters need to be modified. The new design parameters should provide more conservative prediction to the capacity of the HSC and UHSC sections.

7.4.3 Proposed Parameters for the Rectangular Stress Block

The first step of the analysis to modify the ACI parameters was to find a more accurate equation to represent the position of the resultant force. The position of the resultant force is represented by the parameter K_2 obtained from test results or $\beta_1/2$ as suggested by the ACI code. Figure 7.10 shows the experimental data of K_2 , the proposed equation and the current ACI equation for $\beta_1/2$ plotted versus the compression strength. The ACI value of $\beta_1/2$ falls below the data showing that it is too small. If $\beta_1/2$ is too small, the internal lever arm is too big and the moment capacity will be overestimated. The proposed equation plotted in Figure 7.10 has been chosen to pass through the center of the data and is conservative compared to the current equation for any concrete strength. The expression for β_1 is represented by the equation:

$$\beta_1 = (0.95 - 0.0025f'_c) \geq 0.70 \quad (7.6)$$

The second step of the analysis was to choose the parameter α_1 . This parameter should provide a conservative lower bound for the experimental data of K_2 obtained from concentrically loaded columns. It also should provide conservative design for eccentric sections when combined with the parameter β_1 . Several trials were made to choose a suitable equation for α_1 . For each trial, figures similar to Figures 7.6 and 7.8 were used to check the validity of this equation for design. These trials showed that the use of a constant value for α_1 could provide a safe design for HSC and UHSC sections but the value of α_1 is much lower than 0.85 in that case and will give very conservative design for the LSC sections. The parameter α_1 is best represented by an equation that decreases with an increase in the concrete strength. The following equation was chosen to represent the parameter α_1

$$\alpha_1 = (0.85 - 0.00125f'_c) \geq 0.725 \quad (7.7)$$

For concrete strength greater than 100 MPa α_1 and β_1 are both taken constant and are equal to 0.725, 0.7 respectively. The shape of the stress-strain curve in that case is very close to triangular. The stress block parameters $\alpha_1\beta_1$ and $\beta_1/2$ for a triangular stress-strain curve with $f_c = f'_c$ are 0.5 and 0.33 respectively. The same stress block parameters using the proposed equations are 0.5075 and 0.35 respectively. Figure 7.11 shows the

experimental data for K_3 obtained from concentrically loaded columns and the α_1 equation for different codes. The figure shows that the ACI value of 0.85 is not conservative, the Norwegian code is very conservative while the proposed equation provides a lower bound for most of the data points. Figure 7.12 shows the experimental data, the current and proposed design parameters $\alpha_1\beta_1$ plotted versus the concrete strength. The figure shows that the proposed parameters give higher resultant forces for LSC and HSC sections than the ACI equations while they give lower resultant forces for UHSC sections.

Figure 7.13 shows the percentage ratio δ for different tests calculated with respect to the normalized interaction diagram of the proposed design parameters. The figure shows that only 16% of the experimental data points had lower capacity than the predicted capacity, four of which were lower than 5%. Figure 7.14 shows that the mean value of δ in that case is greater than zero for all concrete strengths. The mean value of δ for all of the 94 tests was 10.8% (test/calculated capacity of concrete = 1.108) with a standard deviation of 9.93% (coefficient of variation of 0.0896).

Figures 7.15 and 7.16 show the interaction diagrams generated using the ACI code, the Norwegian code (using f'_c of 129.3 and 72.5 MPa respectively) and the proposed parameters for two different specimens that were tested during this test program. The ACI interaction diagrams overestimate the capacity of these specimens. The interaction diagrams of the Norwegian code provide a very conservative estimate to the capacity of these specimens. The proposed parameters provide a safe design for these specimens.

7.4.4 Design of Triangular Compression Zones

The ACI design parameters and the proposed parameters were used to estimate the maximum strength of the triangular specimens. The estimated strengths of these specimens were compared with the measured maximum strength during each test. This analysis followed the same procedures described in Section 7.4.2 for rectangular specimens. Figure 7.17 shows the normalized interaction diagram for a triangular cross-section using the ACI parameters. The coordinates of each data point (m , m_1) were calculated as follows:

$$\text{Normal Force} = C = K_1^2 K_3 b' c f'_c / 2 = \zeta^2 K_1^2 K_3 b h f'_c / 2 \quad (7.8)$$

$$\text{Bending Moment} = M = C \times \left(\frac{2}{3} h - K_2 c \right) = C h \times \left(\frac{2}{3} - \zeta K_2 \right) \quad (7.9)$$

$$m = \frac{2C}{b h f'_c} = \zeta^2 K_1^2 K_3 \quad (7.10)$$

$$m_i = \frac{2M}{bh^2 f_c} = \zeta_1^2 K_1^2 K_3 \times \left(\frac{2}{3} - \zeta_1 K_2 \right) \quad (7.11)$$

To generate the ACI interaction diagram, a series of points in that diagram were calculated. Each point had a coordinates similar to those of Equations 7.10 and 7.11 based on the ACI design parameters β_1 , $2/3\beta_1$ and α_1 instead of K_1 , K_2 and K_3 . The resulting equations and the expression for $\tan \theta$ of the test point were as follows:

$$n = \zeta^2 \beta_1^2 \alpha_1 \quad (7.10a)$$

$$m = \frac{2}{3} \zeta^2 \beta_1^2 \alpha_1 \times (1 - \zeta \beta_1) \quad (7.11a)$$

$$\tan \theta = \frac{1}{\frac{2}{3} - \zeta K_2} = \frac{1}{\frac{2}{3}(1 - \zeta \beta_1)} \quad (7.12)$$

Figure 7.18 shows the results from the analysis of the six triangular specimens that were tested in this experimental program. All six specimens had lower capacity than that predicted by the ACI code. The mean value of δ using the ACI design procedures was -11.8% (test/calculated capacity of concrete = 0.882) with a standard deviation of 6.29% (coefficient of variation of 0.071). Only one specimen had lower capacity than that predicted by the proposed parameters. This specimen showed a considerably lower cylinder strength than the design strength. The mean value of δ using the proposed equations was 2.0% (test/calculated capacity of concrete = 1.02) and a standard deviation of 6.21% (coefficient of variation of 0.0609).

Figure 7.18 also indicates that the mean value of δ drops with the increase in the concrete strength. The mean value of δ for the HSC specimens, using the proposed equations, was 6.59% and for the UHSC specimens, excluding T6, was 1.425%. This figure has only six data points, all from U of A test program. The results from U of A test program for the rectangular specimens showed the same trend. The mean value of δ for the HSC specimens was 12.54% and for the UHSC specimens was 4.18%. More data points are needed for triangular compression zones in order to have more confidence in the design procedures of these sections.

7.4.5 Limiting Strain

Values of the maximum strain ϵ_u , obtained in this test series were considerably higher than the limiting strain value of 0.003, as shown in Tables 5.1 and 5.2. The UHSC specimens showed even higher values for the maximum strain compared with the HSC specimens. The specimens tested in the test series reported here showed higher strain values at the peak

stress than the reported maximum strain values from previous test series of HSC columns. Despite that, based on the reported values of maximum strain in previous tests of C-shaped specimens, the value of 0.003 for the ultimate strain as suggested by the ACI code seems appropriate as a conservative lower bound of experimental data.

7.5 Conclusions and Design Recommendations

1- The rectangular stress block can be used to design HSC and UHSC sections with some modification to the parameters used to define the stress block.

2- The constant value of 0.85 for the parameter α_1 is unconservative for high strength concrete. The proposed equation for α_1 is

$$\alpha_1 = (0.85 - 0.00125 f'_c) \geq 0.725 \quad (7.7)$$

3- The parameter β_1 leads to an overestimation of the lever arm. The proposed equation for β_1 is

$$\beta_1 = (0.95 - 0.0025 f'_c) \geq 0.70 \quad (7.6)$$

4- The 0.003 value for ultimate strain seems to be suitable for use in design.

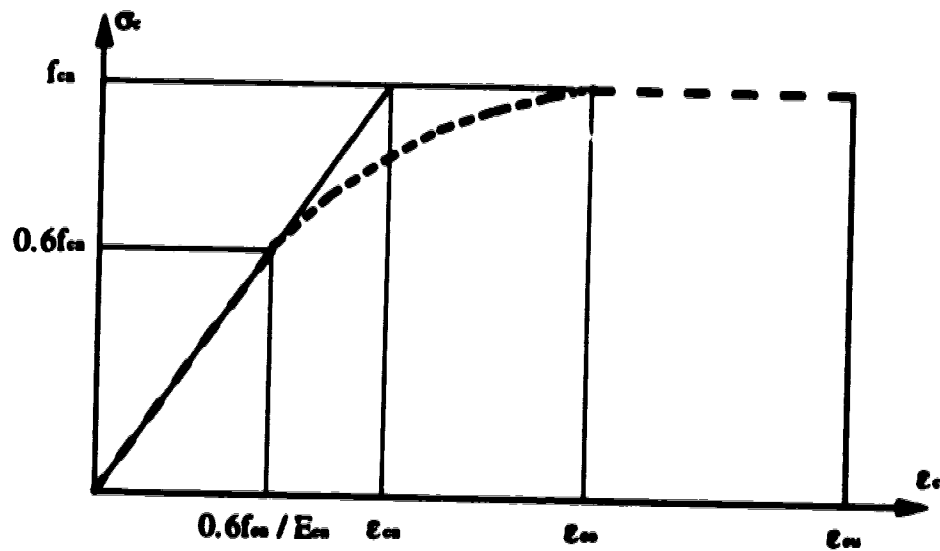
5- For design purposes, the lateral confinement of the cross-section seems to have no effect on the maximum capacity of the section prior to spalling of the cover. This conclusion is based on the results of the rectangular and triangular specimens tested in the test series reported here.

Table 7.1 The Stress Block Parameters of the Norwegian Code NS 3473-1989

f_c' (cylinder)	20	28	36	44	54	64	74	94
f_{ca} (Structural)	16.8	22.4	28.0	33.6	39.2	44.8	50.4	61.6
R (Resultant)	0.877	0.829	0.804	0.778	0.751	0.722	0.66	
C (Position)	0.445	0.424	0.413	0.403	0.392	0.382	0.361	

Table 7.2 Data Required to Generate the Stress-Strain Diagram of the CEB/FIP Model MC90

Concrete Grade	C12	C20	C30	C40	C50	C60	C70	C80
E_c (10^3 N/mm^2)	27.0	30.5	33.5	36.5	38.5	41.0	42.5	44.5
E_{ci} (10^3 N/mm^2)	9.0	12.5	17.5	22.0	26.5	31.0	35.5	40.5
ϵ_{cu} (10^3)	-5.0	-4.3	-3.6	-3.3	-3.0	-2.8	-2.6	-2.4



$$0 \leq \varepsilon \leq 0.6f_{cs}/E_{cs}: \quad \sigma = \varepsilon E_{cs}$$

$$0.6f_{cs}/E_{cs} \leq \varepsilon \leq \varepsilon_{m0}: \quad \sigma = \varepsilon E_{cs} - (m-1)f_{cs}[(\varepsilon E_{cs} - 0.6f_{cs})/((m-0.6)f_{cs})]^{(m-0.6)/(m-1)} \lambda^{m-1}$$

$$\varepsilon_{m0} \leq \varepsilon \leq \varepsilon_{m1}: \quad \sigma = f_{cs}$$

where;

$$E_{cs} = 10^4 (f_{cs})^{0.3}, \quad \varepsilon_{cs} = f_{cs}/E_{cs}, \quad m = \varepsilon_{m1}/\varepsilon_{m0}$$

$$\varepsilon_{m0} = (0.004f_{cs} + 1.9)10^{-3} \geq (0.015f_{cs} + 1.17)10^{-3}$$

$$\varepsilon_{m1} = (2.5m - 1.5)\varepsilon_{m0}$$

**Figure 7.1 Schematic Stress-Strain Diagram for the Norwegian Code
NS 3473-1989**

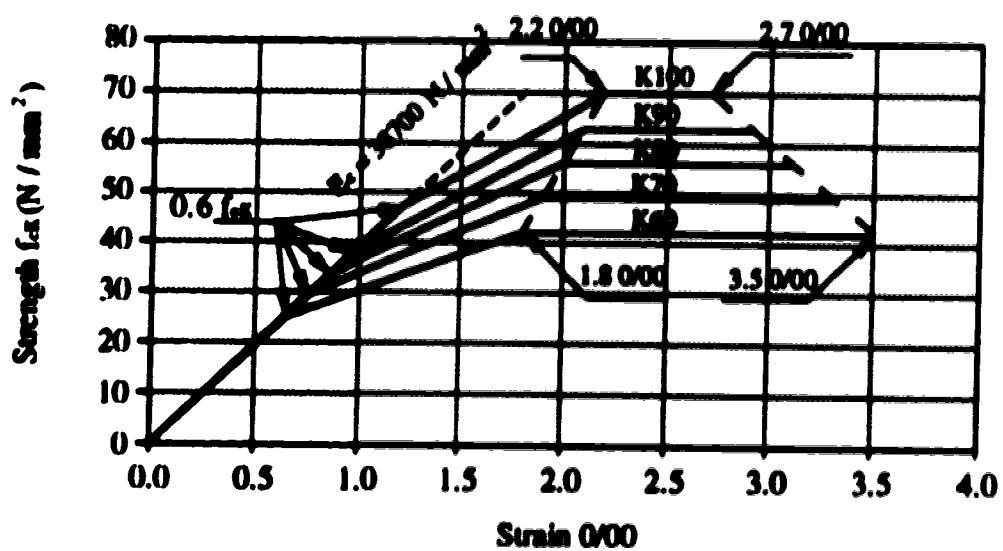


Figure 7.2 Stress-Strain Diagram for the Finnish Code Rak MK4 1989

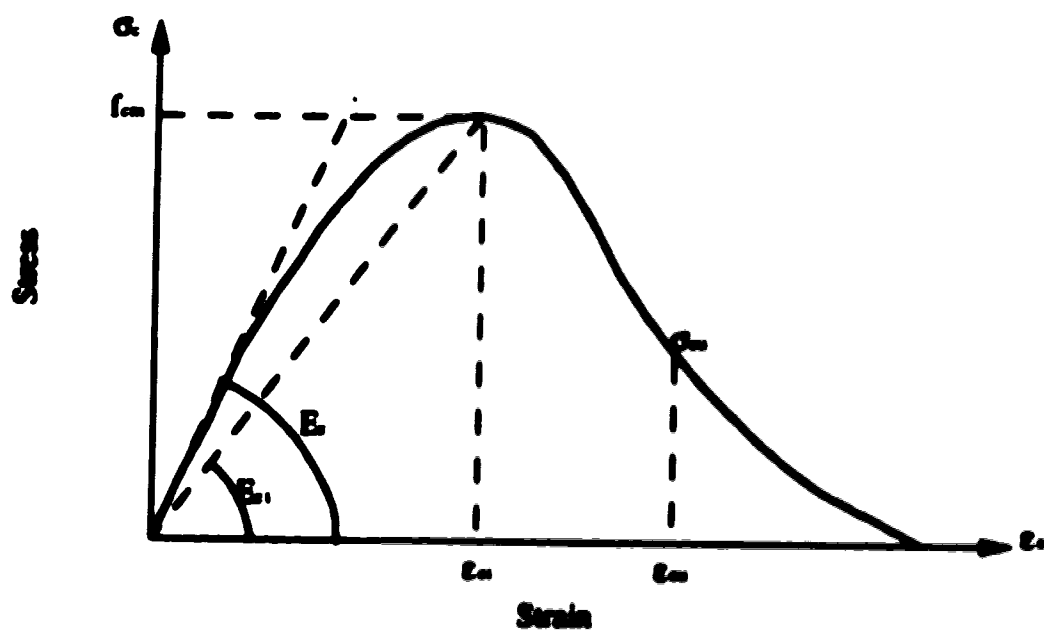


Figure 7.3 Stress-Strain Diagram for Uniaxial Compression MC90

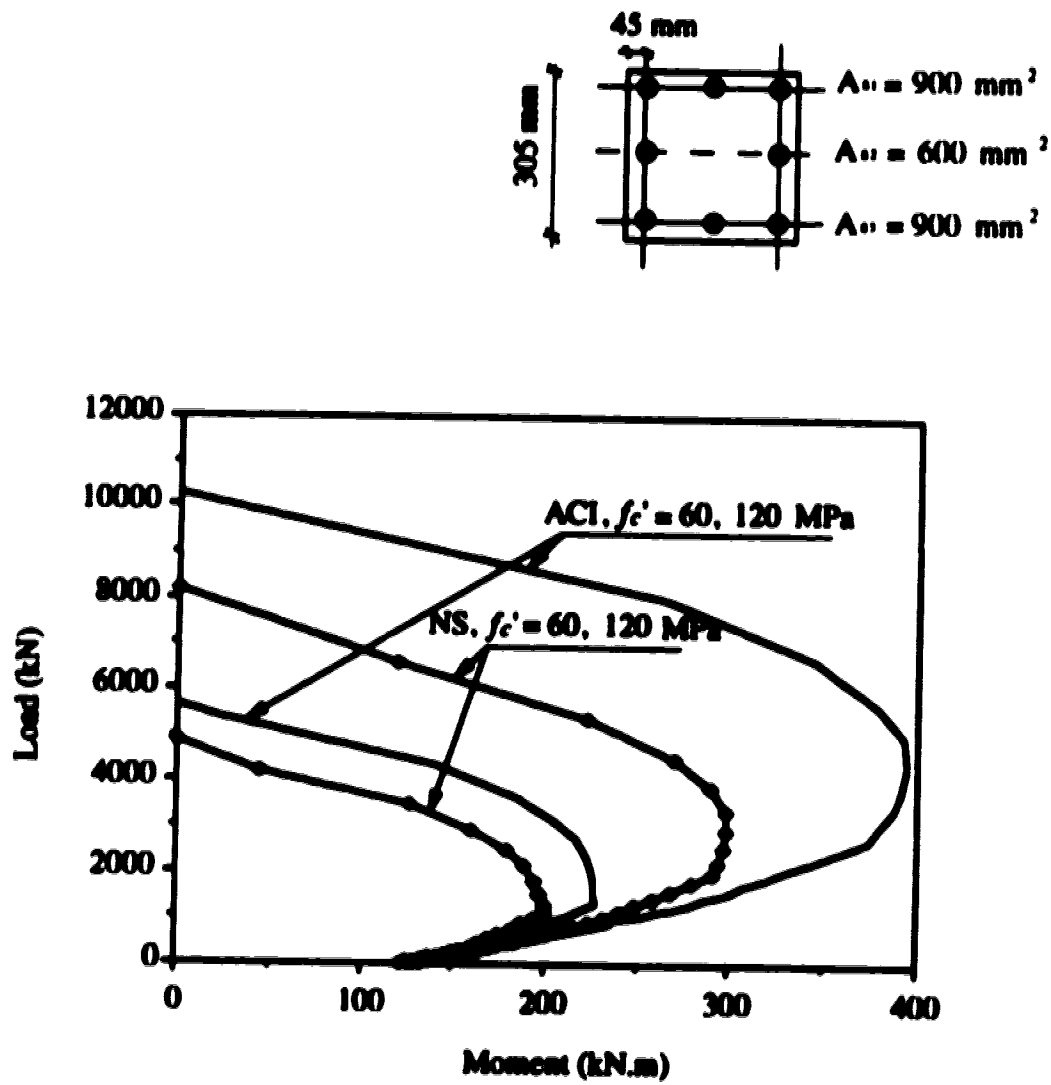


Figure 7.4 Interaction Diagrams of Different Design Codes

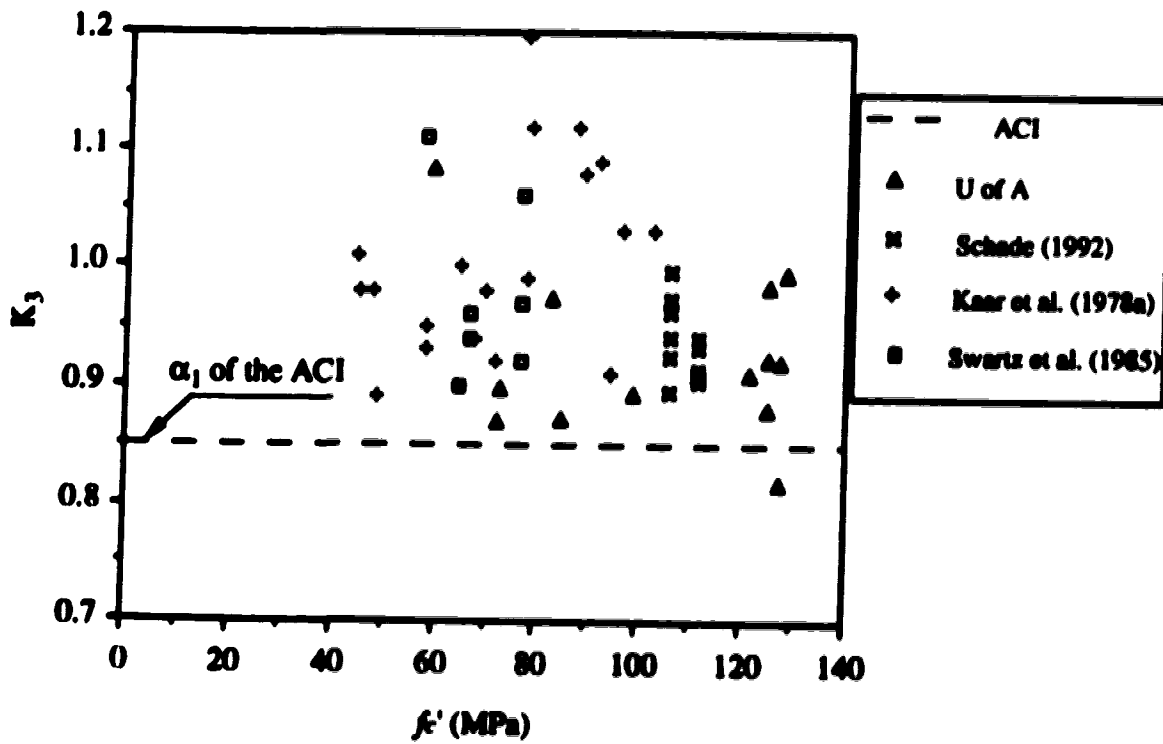


Figure 7.5 Values of K_3 from Tests of C-Shaped Specimens

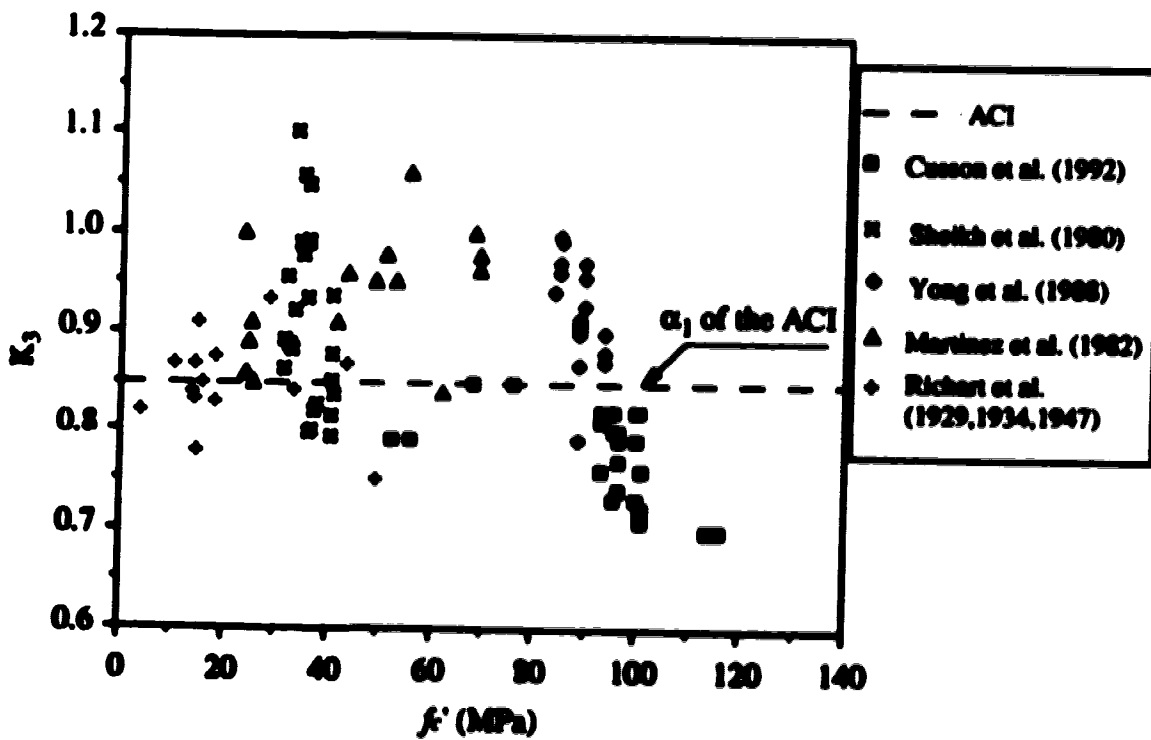


Figure 7.6 Values of K_3 from Tests of Concentrically Loaded Columns

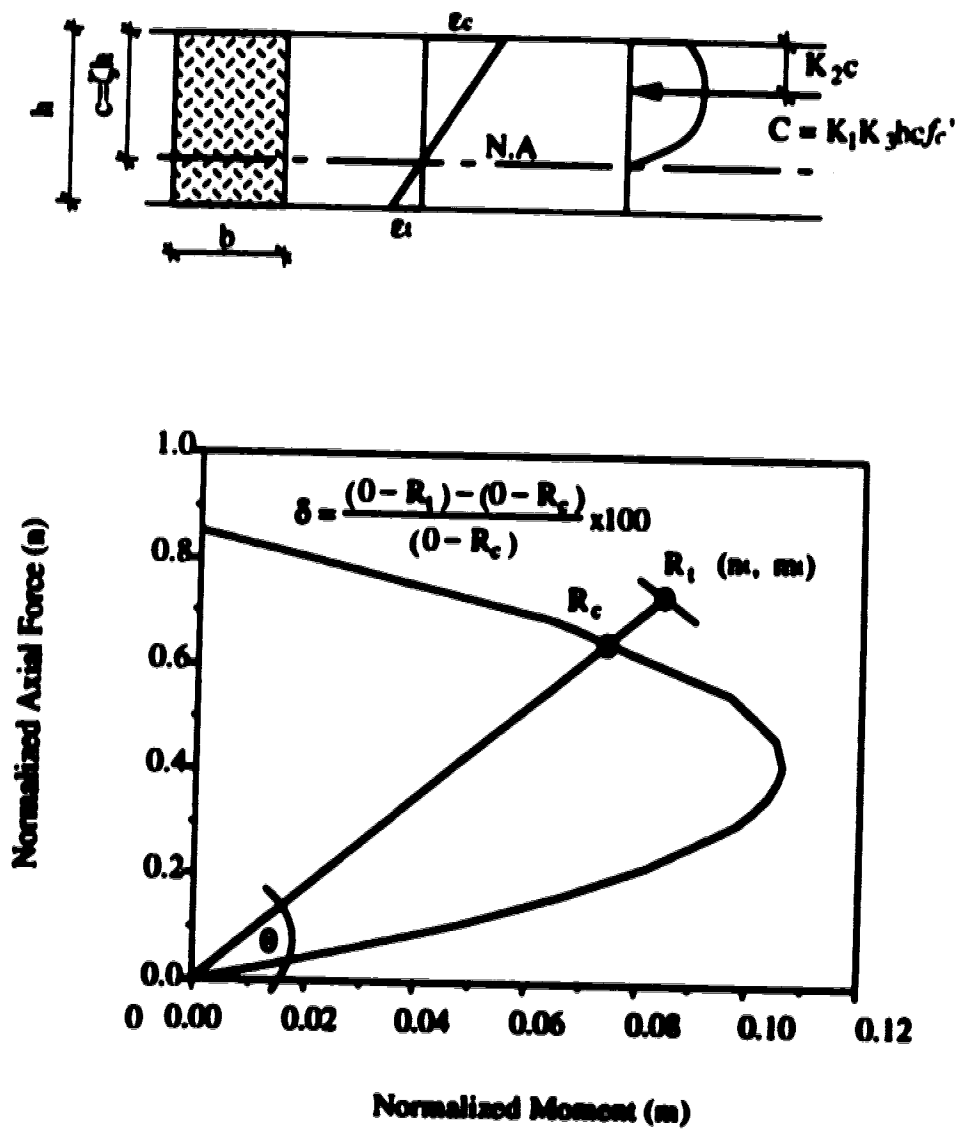


Figure 7.7 ACI Normalized Interaction Diagram for Rectangular Plain Concrete Sections

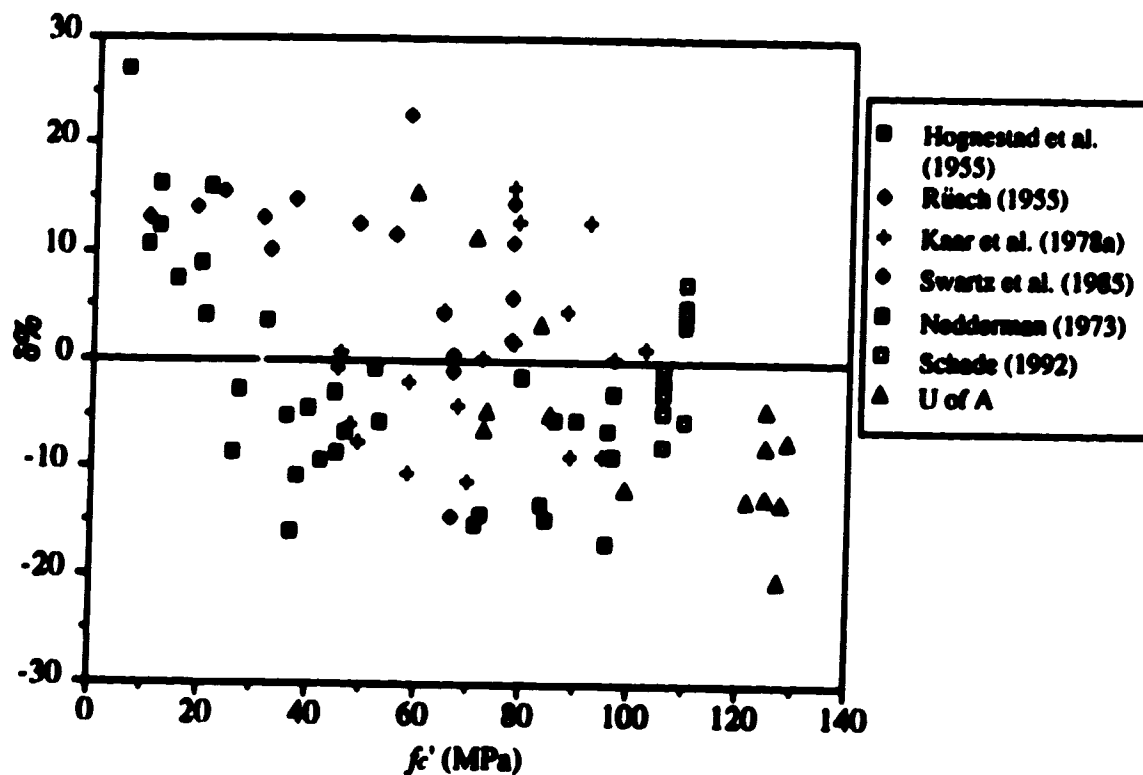


Figure 7.8 Tests of Eccentrically Loaded Columns Compared with the ACI Code

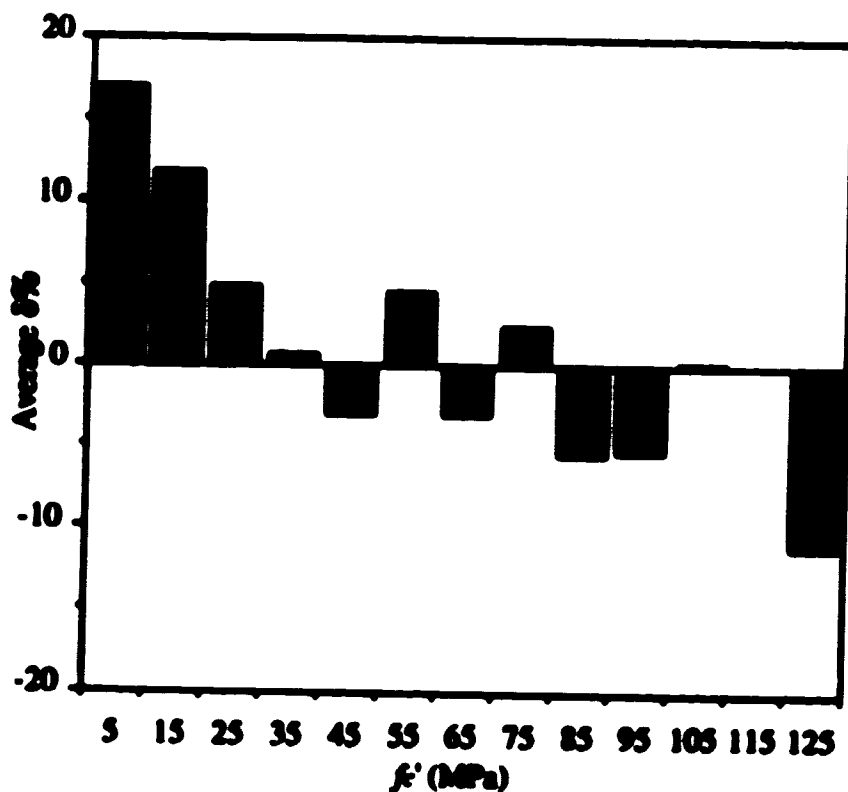


Figure 7.9 Mean Values of δ versus the Concrete Strength

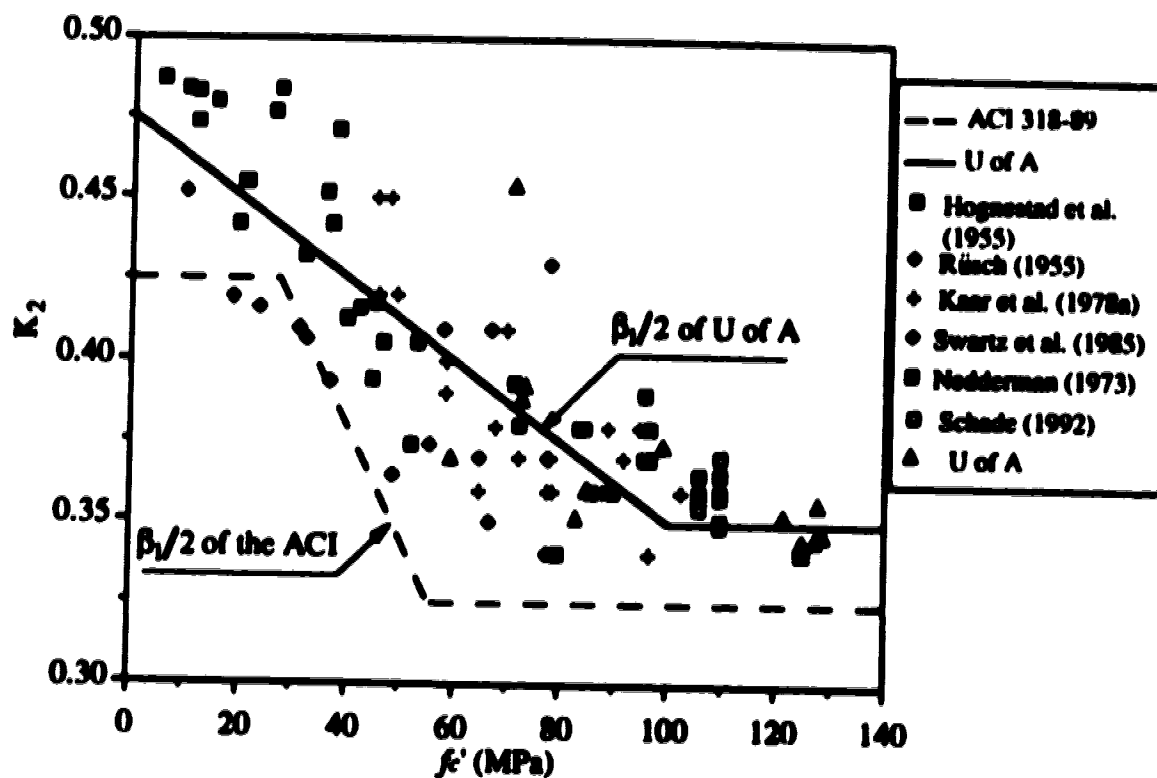


Figure 7.10 Proposed Equation for $\beta_1/2$ Compared to Tests of Eccentrically Loaded Columns

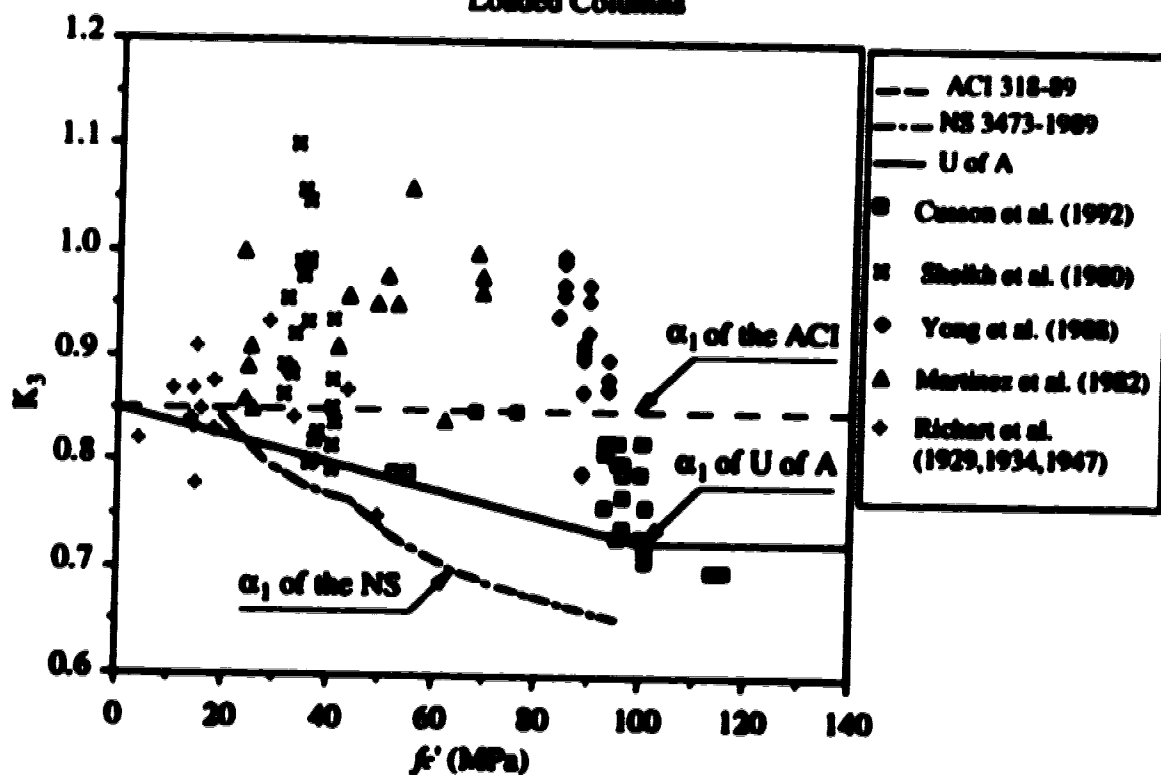


Figure 7.11 Proposed Equation for α_1 Compared to Tests of Concentrically Loaded Columns

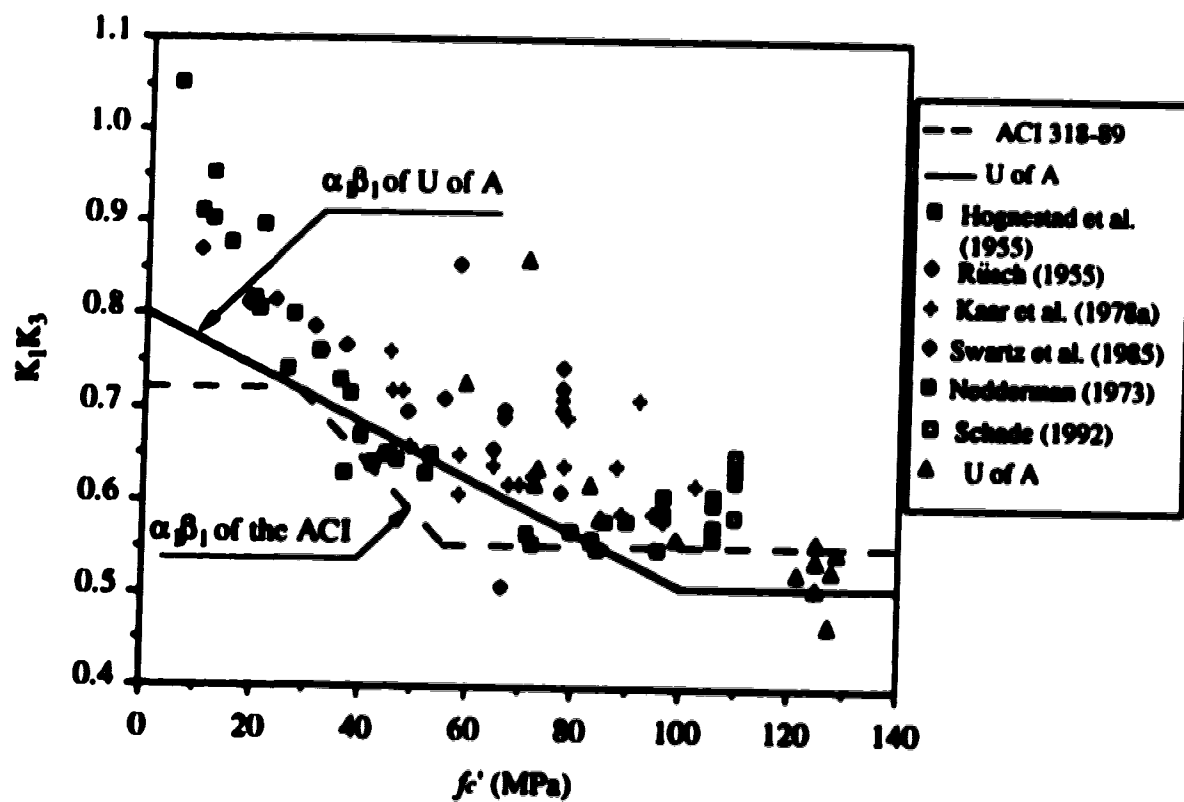


Figure 7.12 Equations for $\alpha\beta_1$ Compared to Tests of Eccentrically Loaded Columns

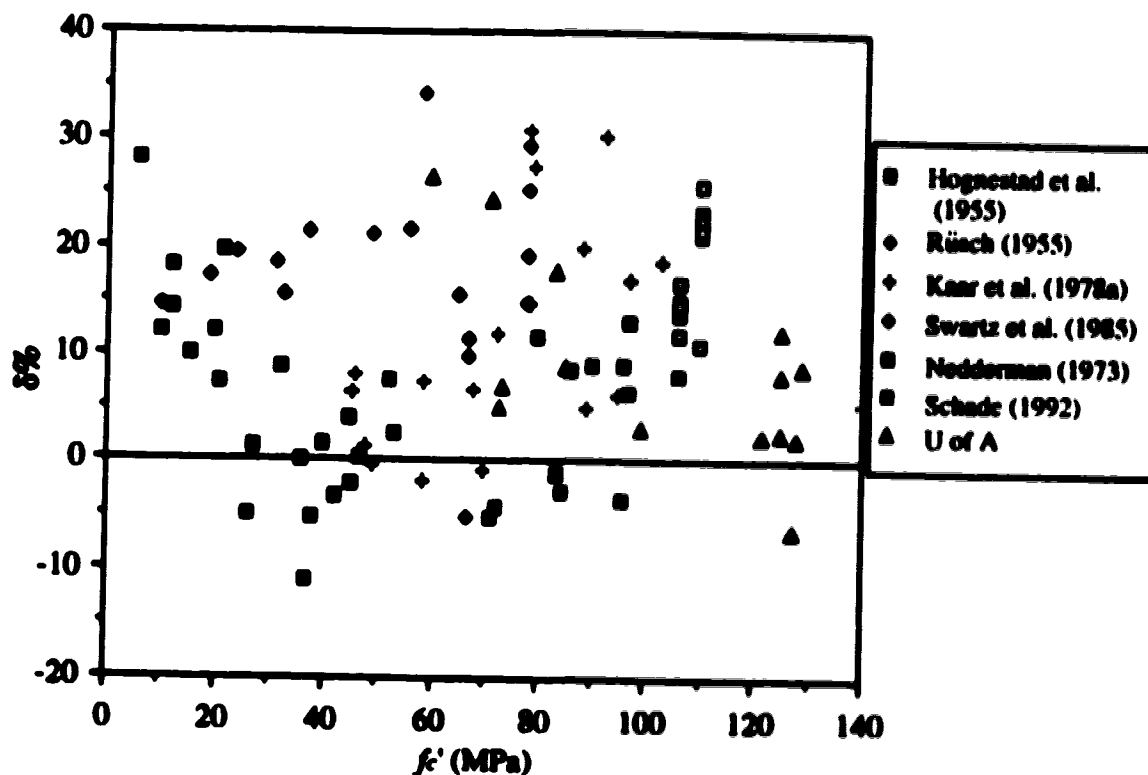


Figure 7.13 Tests of Eccentrically Loaded Columns Compared with U of A

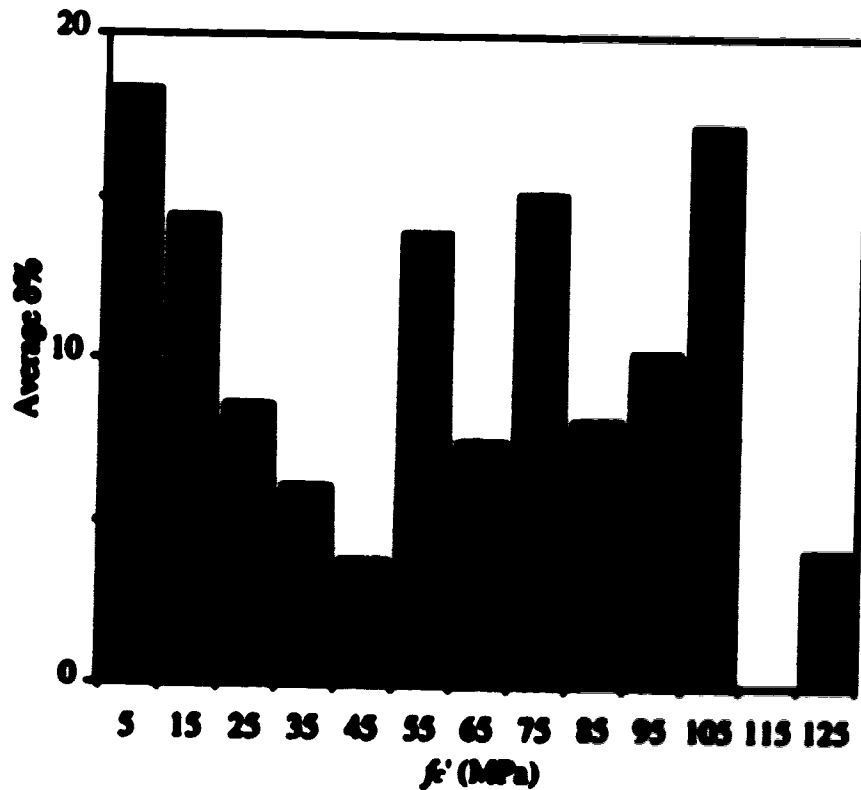


Figure 7.14 Mean Values of δ versus the Compression Strength

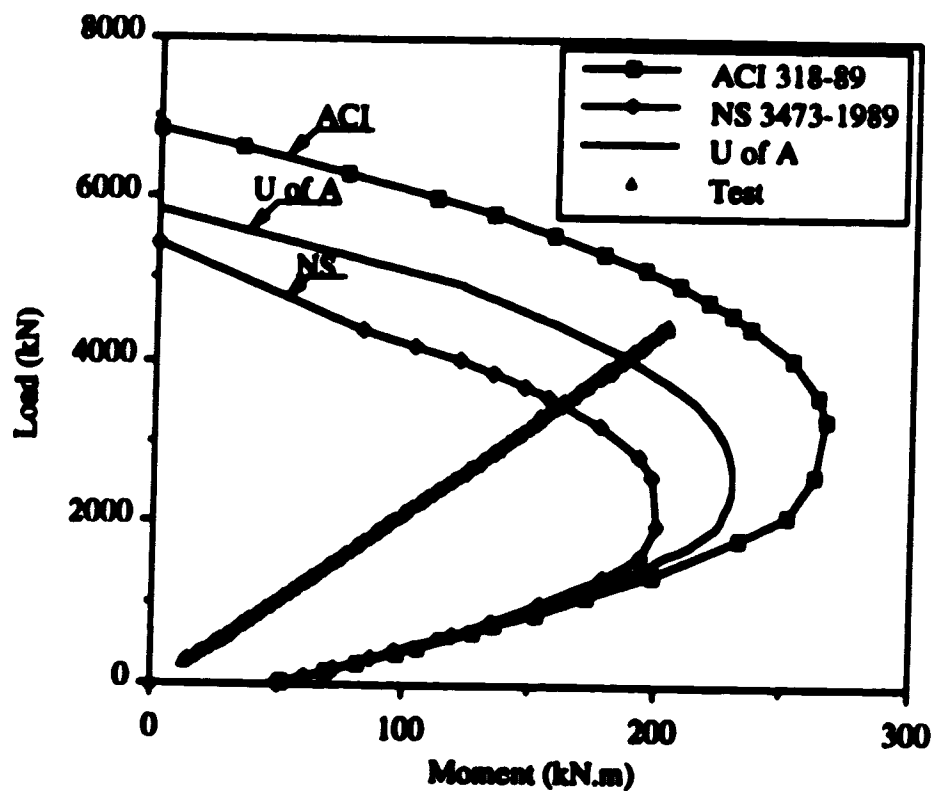


Figure 7.15 Tests of Specimen V8 with Compressive Strength of 129.3MPa

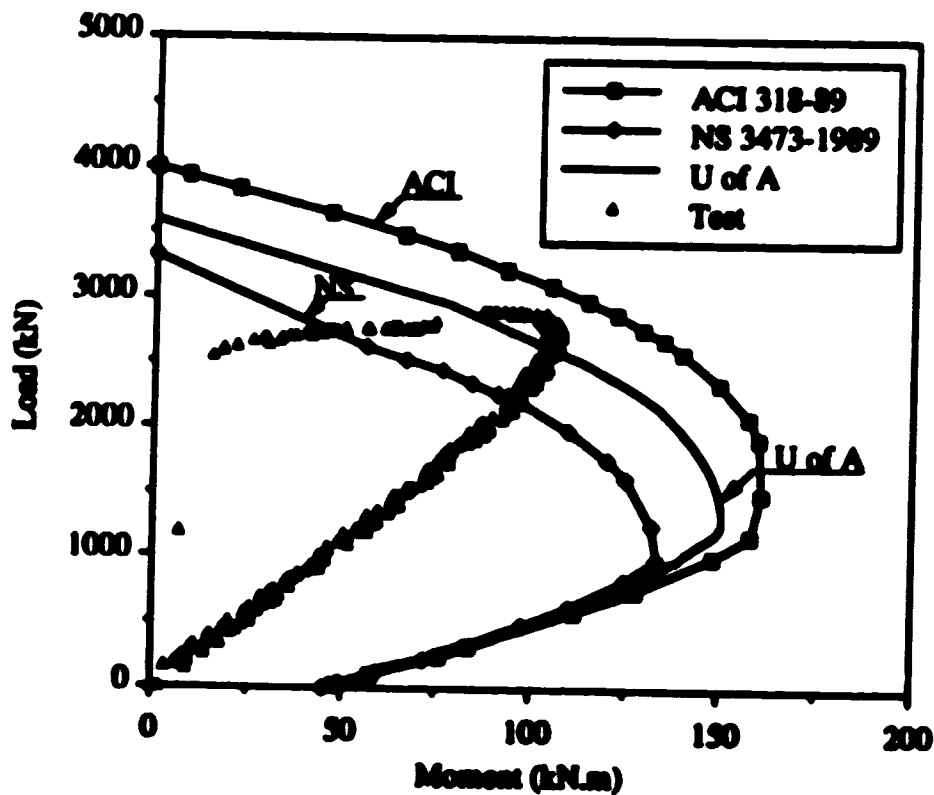


Figure 7.16 Tests of Specimen V13 with Compressive Strength of 72.5MPa

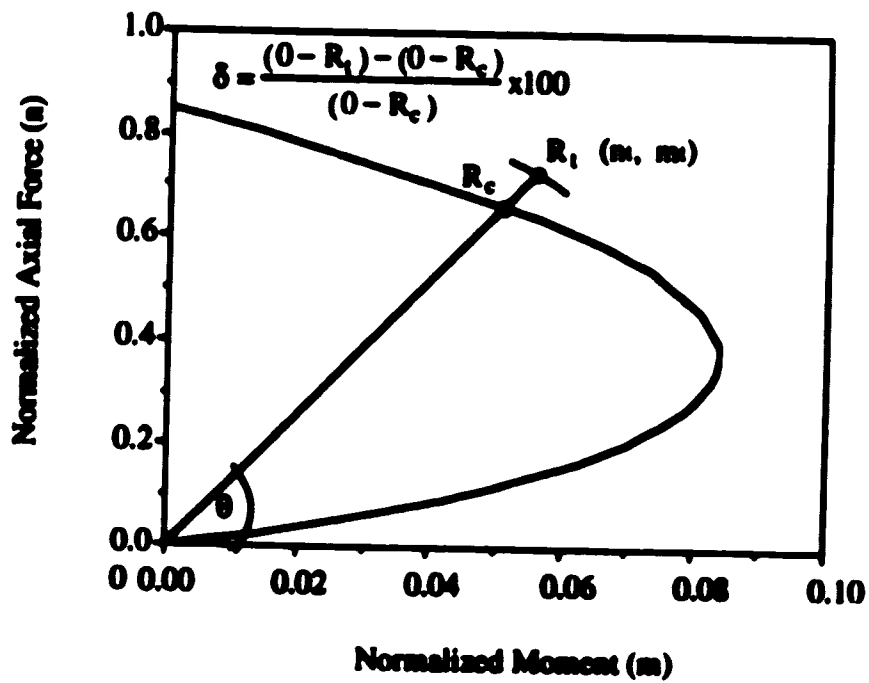
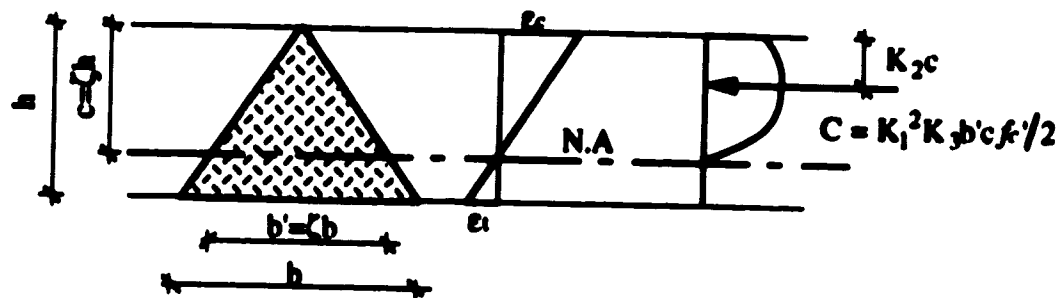


Figure 7.17 ACI Normalized Interaction Diagram for Triangular Plain Concrete Sections

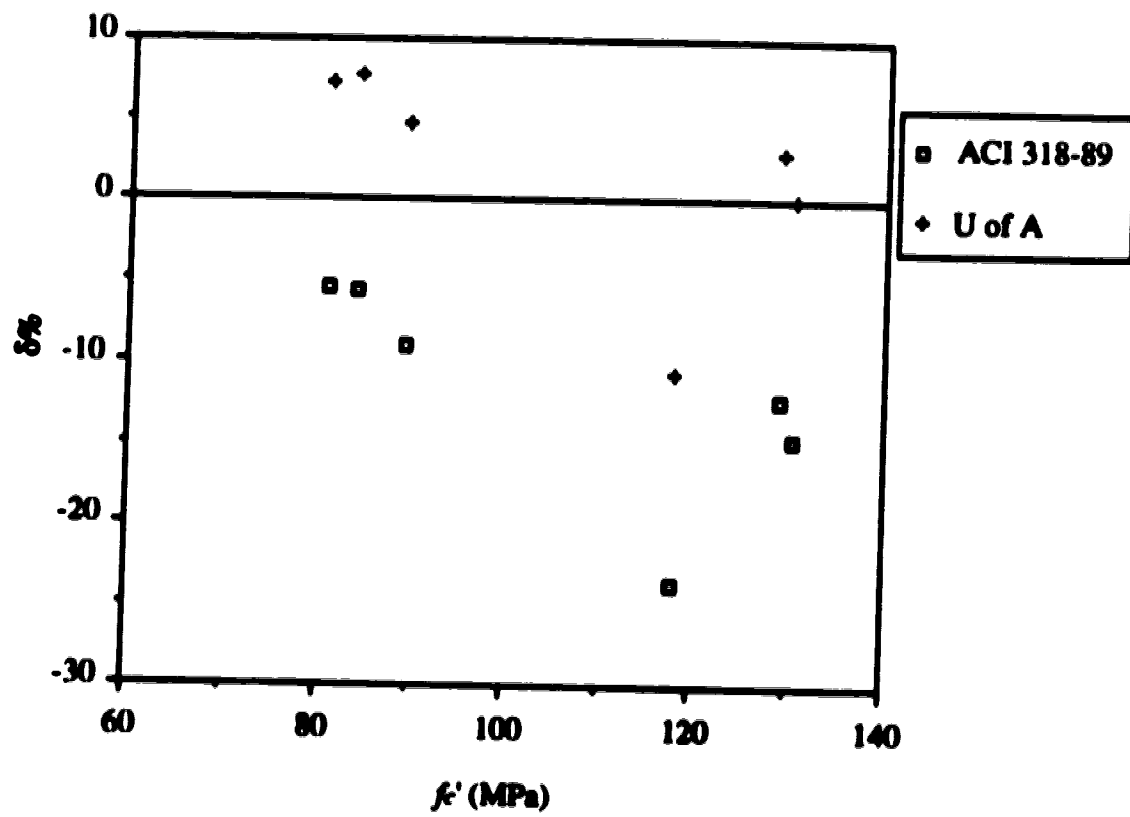


Figure 7.18 Values of δ for the Triangular Specimens versus the Compression strength

8- Modeling the Behavior of the Rectangular Specimens

8.1 General

Different analytical models that describe the behavior of plain and rectilinearly confined HSC were discussed in Section 2.3. These models (Shah et al. (1983), Muguruma et al. (1989), Yong et al. (1988) and Bjerkeli et al. (1990)) were based primarily on test results of concentrically loaded specimens.

The stress-strain curves of the concrete core observed in the tests were presented in Chapter 6. These curves showed lower modulus of elasticity than that reported from previous test series of HSC columns and for most of the specimens the descending branch was very short and steep.

In this Chapter, the capacity of the rectangular reinforced specimens in terms of loads and moments are compared with the calculated capacity using different analytical models. Specimen V2 and V14 were excluded from this study. Specimen V2 was tested under constant eccentricity and did not show any descending behavior. Test of specimen V14 was terminated when the cover spalled off as described in Section 4.2.2. The reliability of each model in predicting the behavior of the specimens during different loading stages is also discussed and a modified model is presented.

8.2 Analytical Analysis

8.2.1 Modeling of Concrete Cover and Concrete Core

Four different models were used to predict the behavior of the rectangular specimens. For each model, except for the one by Shah et al. (1983), the cross-section was treated as a composite section consisting of the concrete cover and the concrete core as illustrated in Figure 6.4. The model by Shah et al. (1983) describes the stress-strain relationship of unconfined concrete (Section 2.3.1). A stress-strain relationship, with a peak stress equal to f_c' and a continuous descending branch to $f_c = 0.0$, was used to describe the behavior of both the concrete cover and the concrete core.

The confinement model by Yong et al. (1988) (Section 2.3.3) was used to describe the stress-strain relationship of the confined core. The same model was also used to describe the stress-strain relationship of the concrete cover where the volumetric ratio of the vertical and the horizontal reinforcement were taken equal to zero. The model by Muguruma et al. (1988) has two different expressions for the confined and unconfined concrete (Section 2.3.2). The expression for confined concrete was used to describe the stress-strain relationship of the concrete core while the expression for unconfined concrete

with a peak stress equal to f_c' was used to describe the stress-strain relationship of the concrete cover. The confinement model by Bjerkeli et al. (1990) was used to describe the stress-strain relationship of the confined core (Section 2.3.4). The unconfined concrete strength in this model was taken equal to f_c' . For the unconfined cover, the authors suggested the use of the stress-strain expression that is given by the Norwegian Concrete Code NS. 3473-1989. This expression is given in Section 7.2.2.

8.2.2 Method of Analysis

A computer program was written in FORTRAN to simulate the behavior of the specimens during the test. The first step of the program is to calculate the loads and the moments that are applied to the cross-section of the test region using any of the previously described models for any assumed strain configuration. The loads and the moments are calculated using numerical integration. To do that each of the concrete cover and the concrete core is divided into 999 rectangular strips parallel to the zero strain face. The stresses are calculated at the boundaries of each strip using the equations of each model. For any strip, if the strain values at the boundaries of the strip are higher than the ultimate strain given by the model, the stresses at these boundaries are taken equal to zero. The loads and the moments carried by each strip are calculated by assuming a linear distribution of the stresses inside the strip. The total loads and moments are then calculated by summing the loads and moments from each strip.

The second step of the program is to take into consideration the second order effect due to the deflected shape of the specimen. To do that, half of the test region, because of symmetry, is divided into 9 strips as shown in Figure 8.1. During the analysis, the strain distribution that was imposed during the test is only applied to the mid section (section 10 in the figure). The other sections (from 1 to 9 in the figure) are allowed to have different strain distributions. The strain distributions of these sections are slightly different than the strain distribution of the mid section due to the second order effect caused by the deflected shape of the specimen. In this analysis the deflected shape is determined at each loading stage and the applied moments at each section are accordingly adjusted. The deflected shape is calculated using the conjugate beam method. Figure 8.1 shows a sketch of the curvature diagram and the equations used to calculate the deflections at the edge and at the mid section of the specimen. Since the deflected shape is required to calculate the moments at each section and the moments are required to calculate the curvature and hence the deflections, iteration is required in the analysis. Figure 8.2 shows a flow chart of the different steps of the computer analysis.

Due to the second order effect, the calculated strains at the compression face of the mid section are slightly higher than the strains at any other section of the test region at the same loading stage. This means that, in the analysis, the first spalling of the concrete cover would occur at the mid section. From the observation of different tests, although the strain at the mid section were slightly higher than any other section, the spalling usually started close to the top of the test region possibly because of the stress concentration or vertical migration of water in the plastic concrete. This observation should not affect the accuracy of the analysis since the spalling of the cover extended to the mid section at later stages of the test.

8.3 Comparison between the Tests and the Calculated Behavior

8.3.1 Maximum Moment Capacity

The calculated maximum moment capacity using each confinement model is compared with the actual maximum moment capacity obtained from each test. The bending moment is calculated about the center line (C.L) of the gross cross-section and about the neutral axis (N.A). The maximum moment calculated about the C.L occurs prior to spalling of the concrete cover and represents the gross cross-section maximum capacity. After spalling of the cover the actual position of the C.L of the cross-section is not well defined. The maximum moment calculated about the N.A might occur before or after spalling of the cover depending on the degree of confinement. For highly confined specimens, it occurs after spalling of the cover and for relatively lightly confined specimens it occurs prior to the spalling of the cover.

Tables 8.1 and 8.2 show the loads and moments at the maximum moment capacity with the moments relative to the C.L of the cross-section and the N.A respectively. The tables include values obtained from the test and calculated values using the four different models. The tables also give the percentage of $((\text{the calculated capacity} - \text{test})/\text{test})$ for each specimen. The mean value of this percentage for each model is referred to as δ and the standard deviation as σ .

Table 8.1 shows that all the models, except for the model by Bjerkeli et al., have positive values of δ for both the load and moment capacities with moments relative to the section center line. The model by Yong et al. gives the highest unconservative predictions to the section capacity. The values of δ are 10.08% and 8.71% for the loads and moments respectively (test/calculated capacity = 0.908 and 0.92) with a standard deviation of 9.268% and 9.16% (coefficient of variation of 0.102 and 0.0996). The model by Bjerkeli et al. is conservative by -8.82% and -4.09% in the prediction of the loads and moments

respectively (test/calculated capacity = 1.096 and 1.043) with a standard deviation of 8.26% and 9.03% (coefficient of variation of 0.0753 and 0.0866).

Table 8.2 shows that the model by Yong et al. overestimates the load and moment capacities with moments relative to the neutral axis. The values of δ are 20.7% and 15.72% for the loads and moments respectively (test/calculated capacity = 0.829 and 0.864) with a standard deviation of 14.6% and 10.83% (coefficient of variation of 0.1762 and 0.1253). The model by Bjerkeli et al. gives good prediction to the value of δ for both the loads and moments. These values are +2.91% and -1.63% respectively (test/calculated capacity = 0.972 and 1.016) with a standard deviation of 11.04% and 6.8% (coefficient of variation of 0.1136 and 0.0669).

The confined model by Bjerkeli et al. gives the closest agreement between the average of all tests and of the calculated capacities. The confined model by Yong et al. and Muguruma et al. considerably overestimate the carrying capacity of the specimens. The unconfined model by Shah et al. gives better prediction to the carrying capacity of the specimens than the confined models of Muguruma et al. and Yong et al. The model is assumed to have a long descending branch from $f_c = f'_c$ to $f_c = 0.0$. This assumption allows the cover to contribute to the carrying capacity of the cross-section to higher strain values than the actual values measured during the test.

8.3.2 Loading Path

Figures 8.3 to 8.6 show the loads plotted versus the C.L moment for specimens V13, V15, V16 and V17. The figures show the test and the calculated behavior using the four models. Details of the reinforcement and the strength of the specimens are given in Table 3.1. The loading path of each specimen consists of an ascending part that occurred before spalling of the cover and a descending part that follows the ascending part. At early loading stages, the ascending part has linear portion where the moments proportionally increase with the increase in loads. Close to the spalling of the cover the rate of increase in the moments is less than the rate of increase in the loads. The descending part shows a continuous decrease in the moment values. For ductile behavior the decrease in the moments is accompanied with an increase in the loads. For less ductile behavior the loads decrease with the decrease in the moments. For a brittle behavior the descending part does not exist.

Figure 8.3 shows that for the HSC specimen V13, the four models give good agreement with the loading path at early stages. At higher loads, especially in the descending part of the loading path, the three confined models overestimate the capacity of the specimen. The model by Yong et al. gives the highest prediction to the capacity of the specimen. The unconfined model by Shah et al. shows good agreement with the test

results in the descending part. Figure 8.4 shows that for the UHSC specimen V15 all the models, except for the model by Yong et al., give good agreement with the test results. The model by Yong et al. overestimates the capacity of the specimen in the descending part.

Figure 8.5 shows that for the highly confined HSC specimen V16, the unconfined model by Shah et al. significantly underestimates the ductility and the capacity of the specimen in the descending part of loading. The model by Muguruma et al. underestimates the capacity of the specimen in the descending part of loading. The model by Yong et al. shows good agreement with the test in the first portion of the descending part. At later stages, the model underestimates the capacity of the specimen. The model by Bjerkeli et al. significantly underestimates the capacity of the specimen at the first portion of the descending part and gives close agreement at later stages. Figure 8.6 shows that for the highly confined UHSC specimen V17, in the descending part of loading, the unconfined model by Shah et al. significantly underestimates the ductility of the specimen. The confinement models, especially for the model by Yong et al. significantly overestimate the capacity of the specimen.

8.4 Modifications to the Model by Bjerkeli et al.

8.4.1 Reviewing the Equations of the Model

The empirical model consists of three parts as shown in Figure 2.5. The first part that describes the ascending branch is in the form:

$$\sigma = \frac{E_c \varepsilon}{1 + (E_c/E_0 - 2) (\varepsilon/\varepsilon_u) + (\varepsilon/\varepsilon_u)^2} \quad (2.25) \text{ and } (8.1)$$

where; σ is the concrete stress; ε is the concrete strain; $E_0 = f_u/\varepsilon_u$; and $E_c = 9500(f_c')^{0.3}$

The second part is a straight line that describes the first portion of the descending branch with an equation in the form of

$$\sigma = f_u - z(\varepsilon - \varepsilon_u) \quad (2.26) \text{ and } (8.2)$$

where; $z = 0.15 f_u / (\varepsilon_{.85} - \varepsilon_u)$

The third part is a horizontal line with a stress value of f_{γ} that describes the second portion of the descending branch. The equation that used to describe this part of the curve is not a function of concrete strength. This means that the ratio of f_{γ}/f_c' decreases with the increase in the concrete strength. The equation of f_{γ} is in the form of

$$f_{\gamma} = 4.87 \frac{d_{50} A_{sh} f_{sy}}{s_p A_c'} \quad (2.27) \text{ and } (8.3)$$

where; d_{so} is the shorter out-to-out of ties in mm; s_p is the spacing between the ties; A_{sh} is the total effective area of ties in direction under consideration; A_c' is the gross area of concrete section measured to center line of the outer ties and f_{ty} is the yield stress of confining reinforcement in MPa.

The parameters of the model are: the peak stress/strain (f_u, ϵ_u); the strain at 0.85 f_u in the descending part of the model ($\epsilon_{.85}$); and the horizontal part of the descending branch (f_{ty}). These parameters are determined based on the cylinder compressive strength f_c' , the geometry factor of the confined core K_g and the confining reinforcement.

The peak stress f_u is defined for sections with concrete strength lower than 90 MPa by the following equations

$$f_u = f_c' + K_g 4.0 f_r \quad 45\text{MPa} < f_c' \leq 80\text{MPa} \quad (2.28.a) \text{ and } (8.4.a)$$

$$f_u = f_c' + K_g 3.0 f_r \quad 80\text{MPa} < f_c' \leq 90\text{MPa} \quad (2.28.b) \text{ and } (8.4.b)$$

The geometry factor K_g expresses the remaining effective concrete core cross-section after compression arches begin to develop. This factor is taken as the larger value of K_{g1} and K_{g2} . The factor K_{g1} is associated with the development of compression arches in vertical direction between the confinement reinforcement layers, shown in Figure 2.6.a. The factor K_{g2} is associated with the development of compression arches between laterally supported longitudinal reinforcement, shown in Figure 2.6.b. The equations of K_{g1} and K_{g2} are as follows

$$K_{g1} = [1 - s_p/d_{so}] \quad (2.32.a)$$

$$K_{g2} = \left(1 - \frac{n c^2}{5.5 A_c}\right) \quad (2.32.b)$$

The confining pressure f_r is calculated assuming equilibrium between forces from the confining reinforcement at yielding and the lateral stresses in the concrete as shown in Figure 2.6.c. The equation of f_r is in the form of

$$f_r = (A_{sh} f_{ty} / h' s_p) \quad (2.31)$$

The equations for ϵ_u and $\epsilon_{.85}$ are defined as follows

$$\epsilon_u = 0.0025 + K_g 0.05 \left(f_r / f_c'\right) \quad (2.29)$$

$$\epsilon_{.85} = \epsilon'_{.85} + K_g 0.05 \left(f_r / f_c'\right) / (1 - F) \quad (2.30)$$

where; $\epsilon'_{.85}$ is the strain at $0.85f'_c$ on the descending branch of the curve of unconfined concrete. The equations for $\epsilon'_{.85}$ and F are as follows

$$\epsilon'_{.85} = 0.0025 \left((17.07/f'_c)^2 + 1 \right) \quad (2.33)$$

$$F = \frac{1}{1 + (1/(f_r K_8))^{1/4}} \quad (2.34)$$

8.4.2 Reasons for Modifications

The model by Bjerkeli et al. as shown in Tables 8.1 gives very conservative prediction for both the loads and moments at the maximum moment capacity with moments relative to the section center line. Figures 8.3 to 8.6 indicate that the model overestimates the ductility of the lightly confined specimens (especially for the HSC specimen V13). For highly confined specimens, the model significantly underestimates the ductility of HSC specimen V16 in the first portion of the descending part, while it significantly overestimates the ductility of the UHSC specimen V17.

The model needs to be modified in order to satisfy the following requirements. The modified model should give higher prediction to the maximum capacity (capacity of the section before spalling of the cover). The modified model should give lower prediction to the ductility of lightly reinforced sections and UHSC highly confined sections. It should also give higher prediction to the ductility of HSC highly confined sections.

8.4.3 Discussion and Suggested Modifications for some of the Equations

The strength of the confined concrete f_u is extended to cover concrete strengths that are higher than 90 MPa. The proposed equation takes into consideration the reduced effect of lateral confinement on the ductility of concrete sections with the increase in the concrete strength. The proposed equation is as follows:

$$f_u = f'_c + K_8 \cdot 2.0 f_r \quad f'_c \geq 90 \text{ MPa} \quad (8.4.c)$$

The strain values at peak stress of the confined concrete (ϵ_u), suggested by the equation of this model, are considerably higher than that of the unconfined concrete. The results of the experimental program reported here did not show that. The constant number in equation (2.29) is changed from 0.005 to 0.0025. The proposed equation for ϵ_u increases the calculated maximum capacity by the model. The equation of $\epsilon'_{.85}$ is modified accordingly. The equations of ϵ_u and $\epsilon'_{.85}$ are taken as follows:

$$\varepsilon_u = 0.0025 + K_8 0.025 \left(f_r / f_c' \right) \quad (8.5)$$

$$\varepsilon_{.85} = \varepsilon'_{.85} + K_8 0.04 \left(f_r / f_c' \right) / (1 - F) \quad (8.6)$$

The equation of the confining pressure f_r was examined to see whether it has to be modified or not. The equation assumes that, for a concentrically loaded column, the stresses in the confining reinforcement would reach the yield stress by the time that the maximum capacity of the confined core is reached. The strains at the confining reinforcement were not measured during the test. A nonlinear finite element analysis for the HSC specimens tested here showed that the ties yielded at strain values close to the spalling strain which means that using the term f_{ry} in the equation is appropriate. Before yielding of the ties, the stress distribution in the ties was close to linear with a maximum value at the part located close to the compression face and a minimum value (very close to zero stress) at the part located close to the zero strain face. After yielding the stress distribution was not linear. The yielding started to spread in portion of the ties with the increase in the axial strain. The stresses close to the zero strain face were still below yielding stress. These observations indicate that the stresses in the confining reinforcement and accordingly the lateral stresses in the concrete are function of the longitudinal strains (not uniform across the section). The current equation of the model for f_r seems to be appropriate for the case of strain gradient.

$$f_r = \left(A_{sh} f_{ry} / h' s_p \right) \quad (8.7)$$

where; A_{sh} is the total area of ties in direction under consideration; f_{ry} is the yield stress of confining reinforcement; h' is the out-to-out of ties in the direction under consideration and s_p is the spacing between ties.

A section geometry factor K_8 is included to account for the effective area of confined concrete within the hoops. Following the derivation by Bjerkeli et al. K_8 is taken as the larger value of K_{81} or K_{82} . According to Sheikh et al. (1982), the area of effectively confined concrete has the least value at a section midway between ties. This area is determined by the tie spacing in addition to the tie configuration. This means that the parameter K_8 should be taken as the product of K_{81} and K_{82} . This modification, with the change in the values of ε_u and $\varepsilon_{.85}$, would increase the slope of the descending branch of the model decreasing the calculated ductility of the section. The parameter K_8 , according to Sheikh et al. (1982), is taken as follows:

$$K_s = \left(1 - \frac{s_p}{2\Gamma}\right) \left(1 - \frac{s_p}{2H}\right) \times \left(1 - \frac{nc^2}{5.5A_c}\right) \quad (8.8)$$

where; s_p is the spacing between the ties; B and H are the dimensions of the concrete core measured from the center line, n is the number of laterally supported longitudinal bars; c is the center to center distance between the longitudinal bars and A_c is the core area enclosed by the center line of the outer tie.

This equation was derived for concentrically loaded columns where the concrete spalls off from the four faces of the section. For columns subjected to strain gradient, the spalling occurs in a different manner starting from the most compressed face. This means that the reduction in the area of the cross-section is less than for the case of concentrically loaded columns. Despite that, the same equation is used for simplicity and because the part of the section that spalls off in the strain gradient case carries higher loads and moments than the remaining parts.

Equation (8.3) that describes the horizontal part in the descending branch could not be examined because the strain values at that part of the model are much higher than the ultimate strain of the tested specimens.

8.5 Comparison between the Tests and the Modified Model

The maximum moment capacity calculated by the modified model is compared with the actual moment capacity obtained from each test. Tables 8.3 and 8.4 show the loads and moments at the maximum moment capacity, calculated about the C.L of the cross-section and the N.A respectively.

Table 8.3 shows that the mean value δ for the loads and moments about the C.L are -3.5% and -0.465% respectively (test/calculated capacity = 1.036 and 1.005) with a standard deviation of 6.15% and 7.81 (coefficient of variation = 0.0593 and 0.0777). The values of δ for the loads and moments about the N.A are +0.74% and -0.87% respectively (test/calculated capacity = 0.993 and 1.009) with a standard deviation of 8.95% and 7.026% (coefficient of variation of 0.0902 and 0.06965).

Figures 8.7 to 8.15 show the loading paths of the specimens compared earlier and the calculated behavior using the modified model. The figures show good agreement between the actual and the calculated behavior for most of the tests. The model shows a conservative prediction of the capacity of the highly confined HSC specimen V16 in the descending part of loading and a non conservative prediction to the capacity of the highly confined UHSC specimen V17 in the first portion of the descending part. Despite that, the

calculated behavior of these specimens using the modified model was much closer to the actual behavior of the specimens than that of any of the other models.

8.6 Equations of the Modified Model for Confined Concrete

A summary of the equations of the modified model for confined concrete is presented. The modified model has the same basic three parts that were described in Section 8.4.1. The equations that are required to determine the parameters of the model are as follows

$$f_u = f_c + K_g 4.0 f_r \quad 45\text{MPa} < f_c' \leq 80\text{MPa} \quad (8.4.a)$$

$$f_u = f_c + K_g 3.0 f_r \quad 80\text{MPa} < f_c' \leq 90\text{MPa} \quad (8.4.b)$$

$$f_u = f_c' + K_g 2.0 f_r \quad f_c' \geq 90\text{MPa} \quad (8.4.c)$$

$$e_u = 0.0025 + K_g 0.025 \left(\frac{f_r}{f_c'} \right) \quad (8.5)$$

$$e_{.85} = e'_{.85} + K_g 0.04 \left(\frac{f_r}{f_c'} \right) / (1 - F) \quad (8.6)$$

$$f_r = \left(A_{sh} f_{ry} / h_{sp} \right) \quad (8.7)$$

$$K_g = \left(1 - \frac{s_p}{2B} \right) \left(1 - \frac{s_p}{2H} \right) \times \left(1 - \frac{nc^2}{5.5A_c} \right) \quad (8.8)$$

$$e_{.85'} = 0.0025 \left(\left(17.07 / f_c' \right)^2 + 1 \right) \quad (8.9)$$

$$F = \frac{1}{1 + (1/(f_r K_g))^{1/4}} \quad (8.10)$$

Table 8.1 Maximum Moment Capacity @ the C.L

Specimen	Test Results		Shah et al.		Yong et al.		Bjerfæli et al.		Meguruma et al.	
	Load (kN)	BM (kN.m)	Load (kN)	BM (kN.m)	Load (kN)	BM (kN.m)	Load (kN)	BM (kN.m)	Load (kN)	BM (kN.m)
V1	3203	58.4	3440 +7.4%	64.9 +11.1%	3140 -2.0%	63.4 +8.56%	2920 -8.84%	58.8 +0.68%	3330 +3.97%	74.6 +27.7%
V7	3013	140.3	3170 +5.21%	145 +3.35%	3340 +10.85%	149 +6.2%	3020 +0.23%	136 -3.06%	3170 +5.2%	149 +6.2%
V8	4422	203	4300 +1.76%	214 +5.42%	4890 +10.58%	221 +8.87%	3910 -11.58%	194 -4.43%	4490 +1.54%	216 +6.4%
V11	3743	177.6	4450 +18.89%	210 +18.2%	4820 +28.8%	216 +21.6%	3810 +1.8%	190 +6.98%	4620 +23.43%	212 +19.37%
V12	3960	180.2	4320 +9.09%	202 +12.1%	4660 +17.68%	206 +14.32%	3680 -7.07%	182 +1.0%	4440 +12.12%	202 +12.1%
V13	2718	108	2870 +5.59%	126 +16.67%	2960 +8.9%	125 +15.74%	2750 +1.18%	117 +8.33%	2830 +4.12%	132 +22.22%
V15	4424	226	4380 -1.0%	207 -8.41%	4690 +6.01%	209 -7.52%	3710 -16.14%	187 -17.26%	4400 -0.54%	209 -7.52%
V16	2729	110.6	2500 -8.39%	102 -7.78%	2630 -3.63%	105 -5.06%	2300 -15.72%	91.3 -17.45%	2340 -14.25%	106 -4.16%
V17	4218	179.8	4480 +6.21%	207 +15.1%	4790 +13.56%	208 +15.68%	3240 -23.2%	159 -11.57%	4640 +10.0%	209 +16.24%
Average Value (δ)			+4.97%	+7.31%	+10.08%	+8.71%	-8.82%	-4.09%	+5.06%	+10.95%
Standard Deviation (σ)			7.016%	9.42%	9.268%	9.16%	8.26%	9.03%	9.61%	11.16%

Table 8.2 Maximum Moment Capacity @ the N.A

Specimen	Test Results		Shah et al.		Yong et al.		Bjerkeli et al.		Magnuma et al.	
	Load (kN)	BM (kN.m)	Load (kN)	BM (kN.m)	Load (kN)	BM (kN.m)	Load (kN)	BM (kN.m)	Load (kN)	BM (kN.m)
V1	3645	1382	3720 +2.06%	1424 +3.07%	4180 +14.68%	1564 +13.17%	3620 -0.69%	1377 -0.36%	3800 +4.25%	1449 +4.89%
V7	3130	609	3020 -3.5%	589 -3.3%	3830 +22.36%	699 +14.8%	3020 -3.5%	589 -3.28%	3440 +9.9%	649 +6.57%
V8	4422	872	4720 +6.74%	913 +4.7%	5330 +20.53%	992 +13.76%	4100 -7.28%	805 -7.68%	4880 +10.36%	931 +6.77%
V11	3743	739	4670 +24.77%	902 +22.06%	5300 +41.6%	991 +34.1%	4340 +15.95%	786 +6.36%	4850 +29.57%	926 +25.3%
V12	3975	775	4540 +14.21%	873 +12.65%	5110 +28.55%	952 +22.84%	4170 +4.91%	754 -2.71%	4660 +17.23%	888 +14.58%
V13	2908	526	2960 +1.8%	558 +6.08%	3360 +15.54%	609 +15.78%	2750 -5.43%	529 +0.57%	3100 +6.6%	587 +11.6%
V15	4449	898	4600 +3.39%	889 -1.0%	5310 +19.35%	972 +8.24%	4330 -2.67%	778 -13.36%	4800 +7.89%	920 +2.45%
V16	3570	581	2990 -27.45%	481 -17.21%	3120 -12.6%	542 -6.71%	3460 -3.08%	551 -5.16%	2960 -17.09%	485 -16.52%
V17	4219	812.6	4710 +11.6%	904 +11.2%	5750 +36.29%	1020 +25.52%	5400 +28.0%	901 +10.87%	4930 +16.85%	942 +15.9%
Average Value (\bar{b})			+3.74%	+4.25%	+20.7%	+15.72%	+2.91%	-1.63%	+9.51%	+7.95%
Standard Deviation (σ)			13.56%	10.47%	14.6%	10.83%	11.04%	6.8%	11.85%	10.87%

Table 8.3 Comparison of Modified Model to Test Values of Maximum Moment Capacity @ the C.L.

Specimen	Test Results		Modified Model	
	Load (kN)	BM (kN.m)	Load (kN)	BM (kN.m)
V1	3203	58.4	3100 -3.22%	59.1 +1.2%
V7	3013	140.3	3110 +3.2%	137 -2.35%
V8	4422	203	4020 -9.09%	198 -2.46%
V11	3743	177.6	4000 +6.87%	196 +10.36%
V12	3960	180.2	3860 -2.53%	188 +4.33%
V13	2718	108	2770 +1.91%	118 +9.26%
V15	4424	226	3910 -11.62%	193 -14.6%
V16	2729	110.6	2560 -6.2%	98.9 -10.6%
V17	4218	179.8	3760 -10.8%	181 +0.67%
Average Value (δ)			-3.5%	-0.465%
Standard Deviation (σ)			6.15%	7.81%

Table 8.4 Comparison of Modified Model to Test Values of Maximum Moment Capacity @ the N.A

Specimen	Test Results		Modified Model	
	Load (kN)	BM (kN.m)	Load (kN)	BM (kN.m)
V1	3645	1382	3740 +2.6%	1412 +2.2%
V7	3130	609	3110 -0.64%	604 -0.82%
V8	4422	872	4210 -4.79%	824 -5.5%
V11	3743	739	4170 +11.4%	815 +10.3%
V12	3975	775	3860 -2.89%	767 -1.03%
V13	2908	526	2880 -0.96%	550 +4.56%
V15	4449	898	4060 -8.74%	792 -11.8%
V16	3570	581	3240 -9.2%	517 -11.0%
V17	4219	812.6	5060 +19.9%	855 +5.22%
Average Value (δ)			+0.74%	-0.87%
Standard Deviation (σ)			8.95%	7.026%

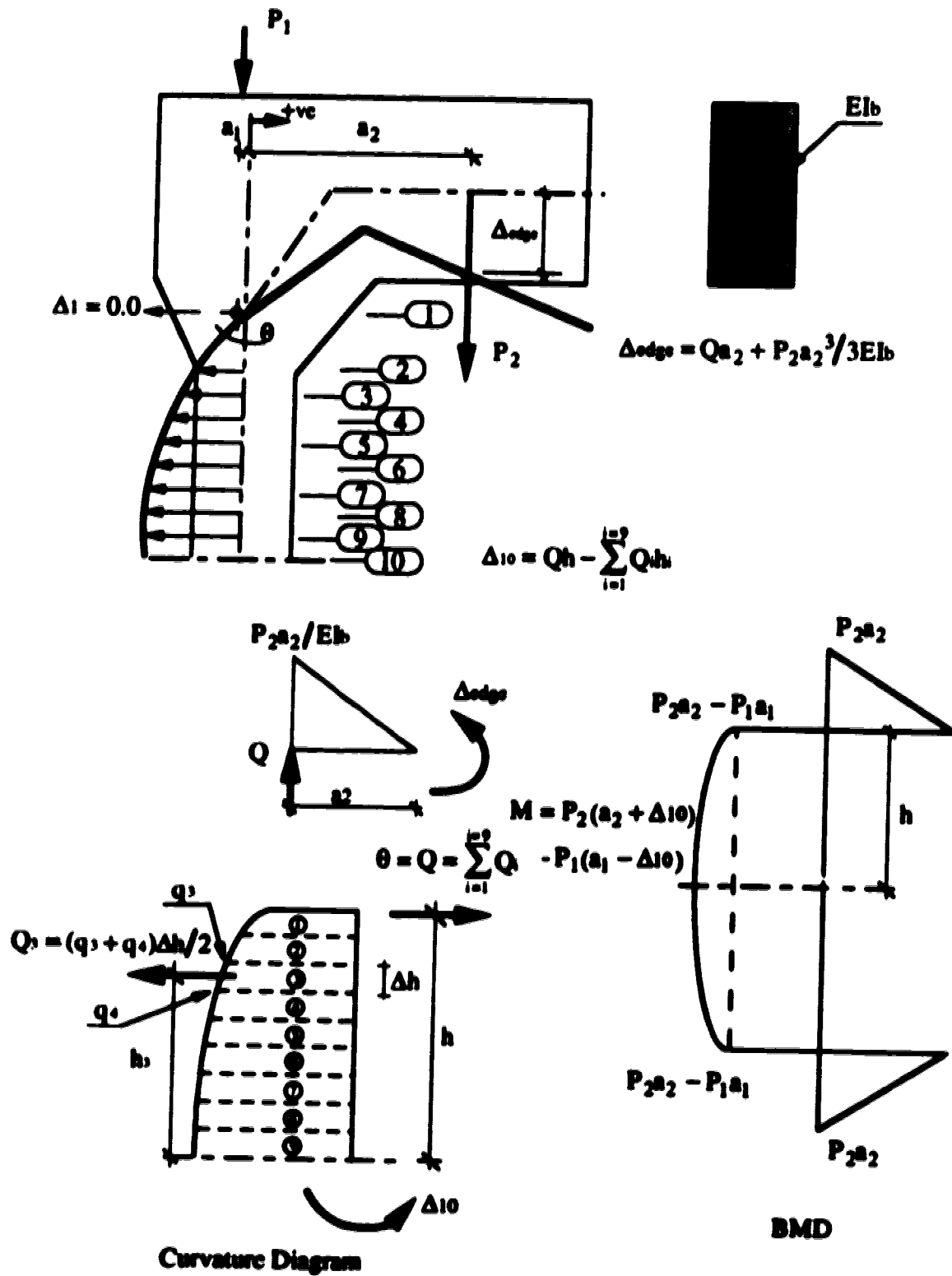


Figure 8.1 Calculations of the Lateral Deflection of the Specimen

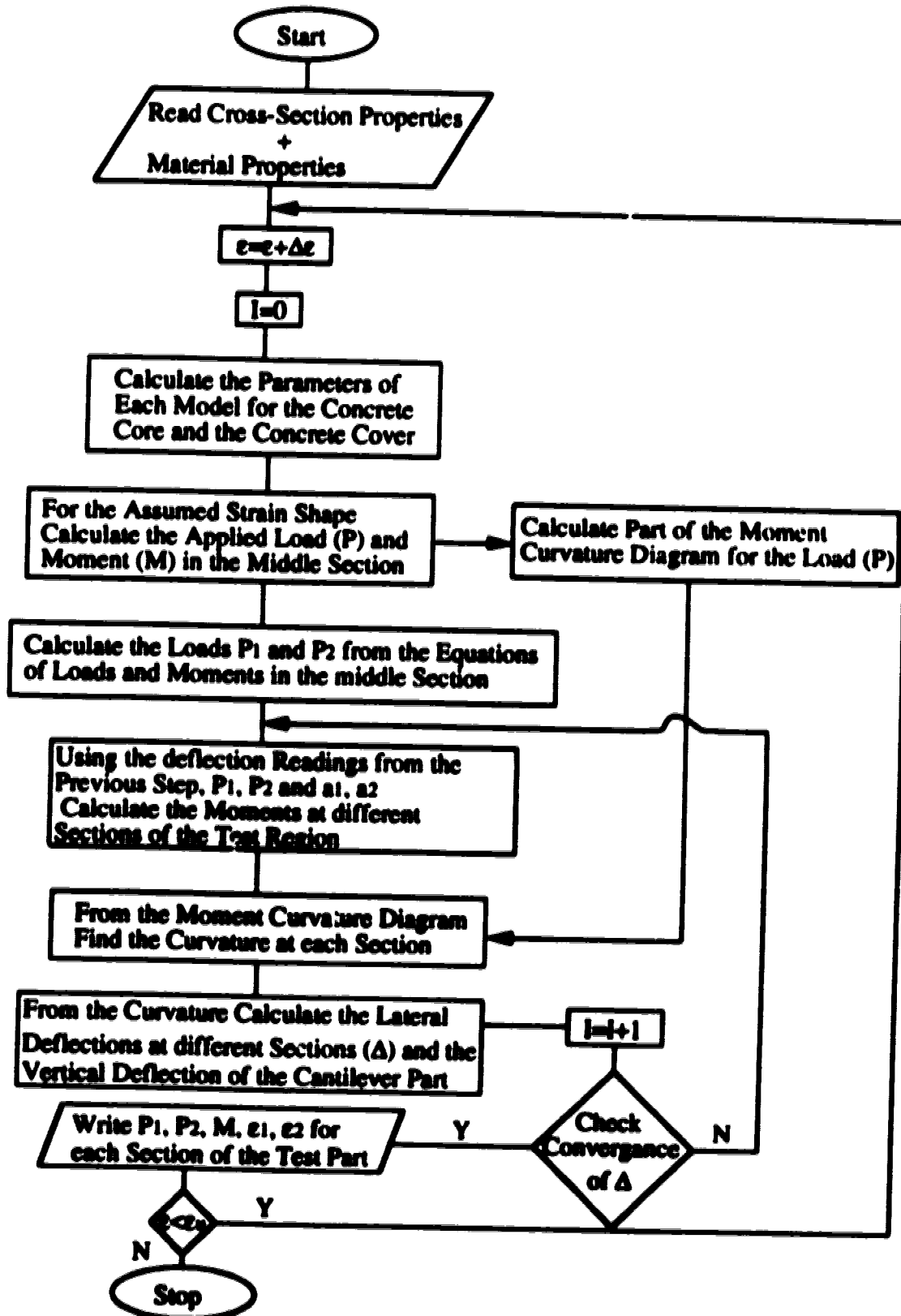


Figure 8.2 Flow Chart of the Computer Analysis

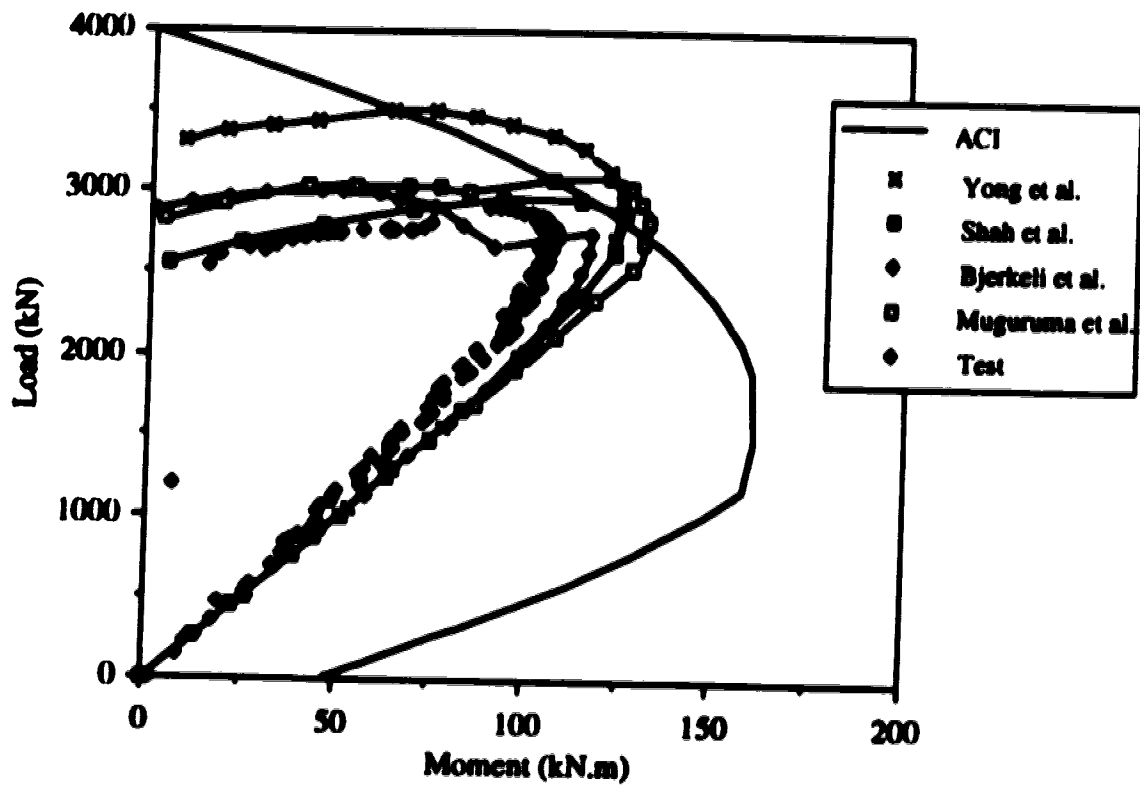


Figure 8.3 Test and Calculated Behavior of Specimen V13

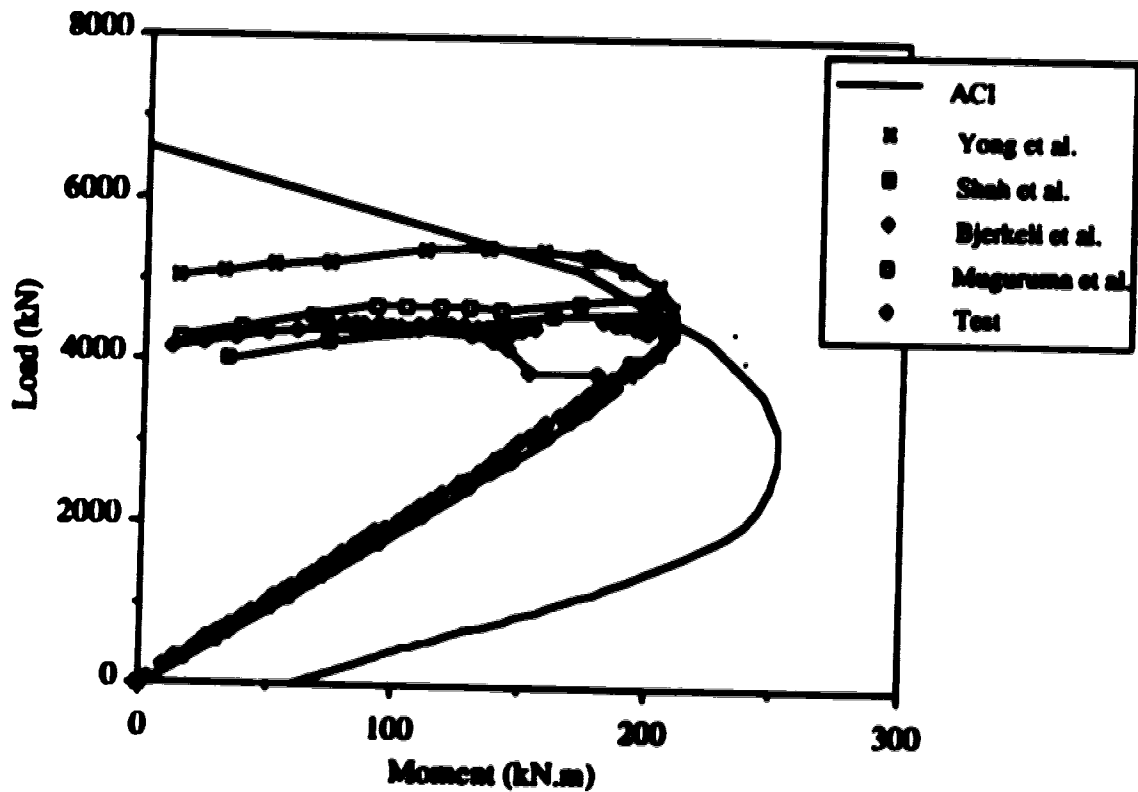


Figure 8.4 Test and Calculated Behavior of Specimen V15

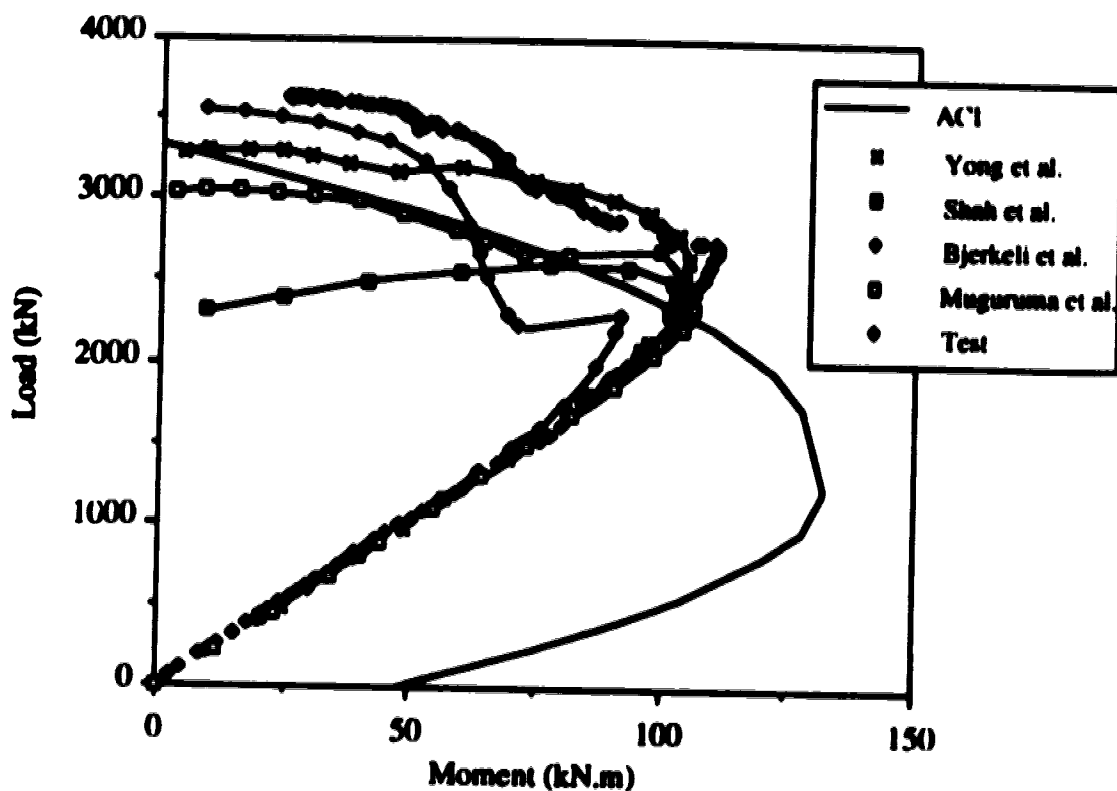


Figure 8.5 Test and Calculated Behavior of Specimen V16

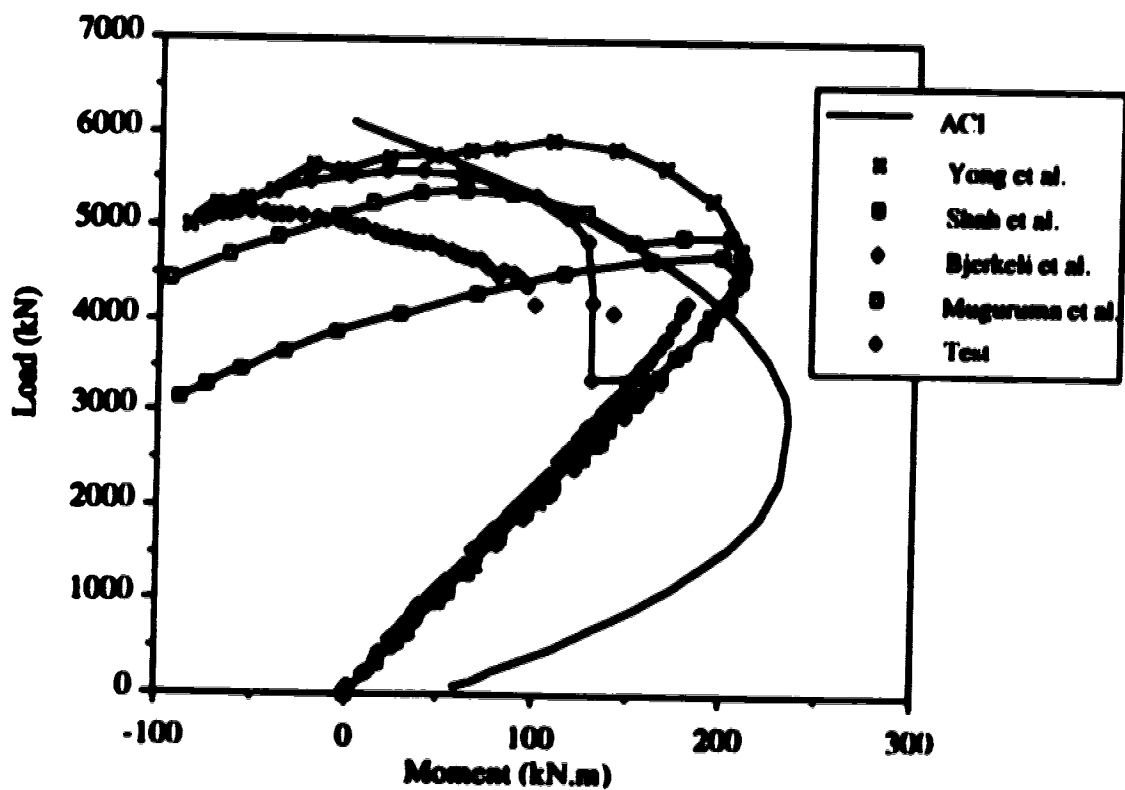
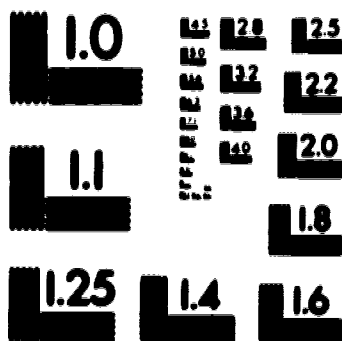


Figure 8.6 Test and Calculated Behavior of Specimen V17

3 1 of/de 3

PM-1 3 1/4" x 4" PHOTOGRAPHIC MICROCOPY TARGET
NBS 1010a ANSI/ISO #2 EQUIVALENT



PRECISION[®] RESOLUTION TARGETS

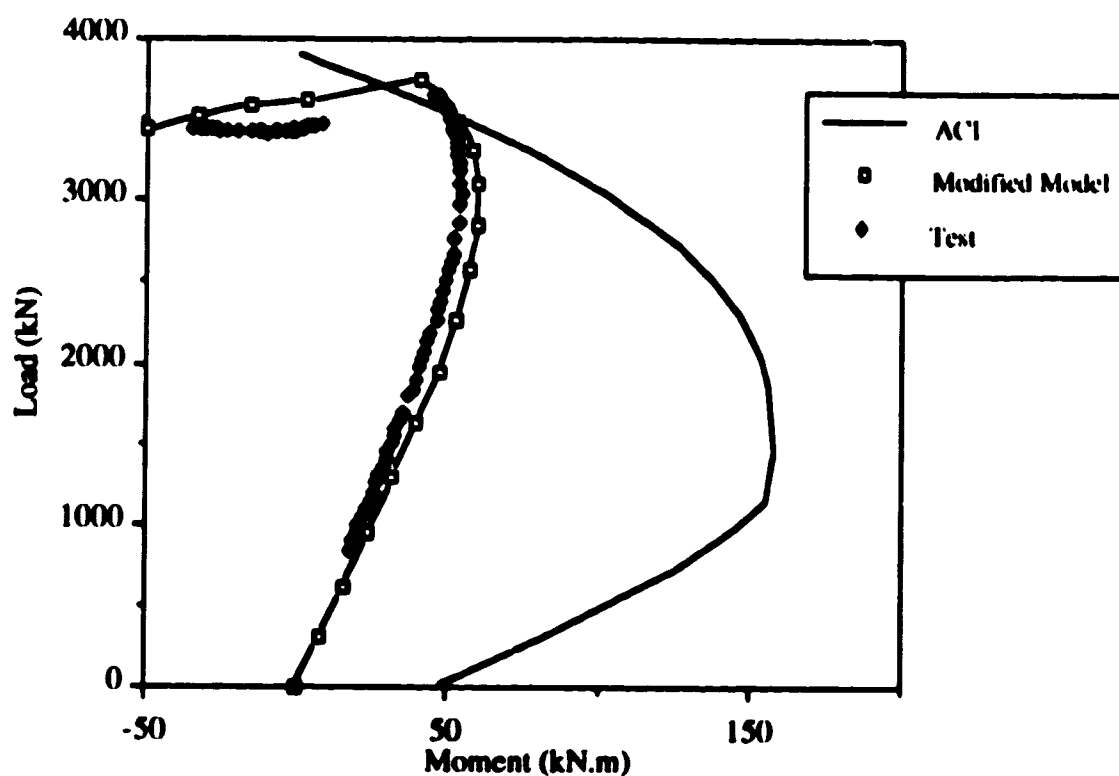


Figure 8.7 Test and the Calculated Behavior of the Modified Model for V1

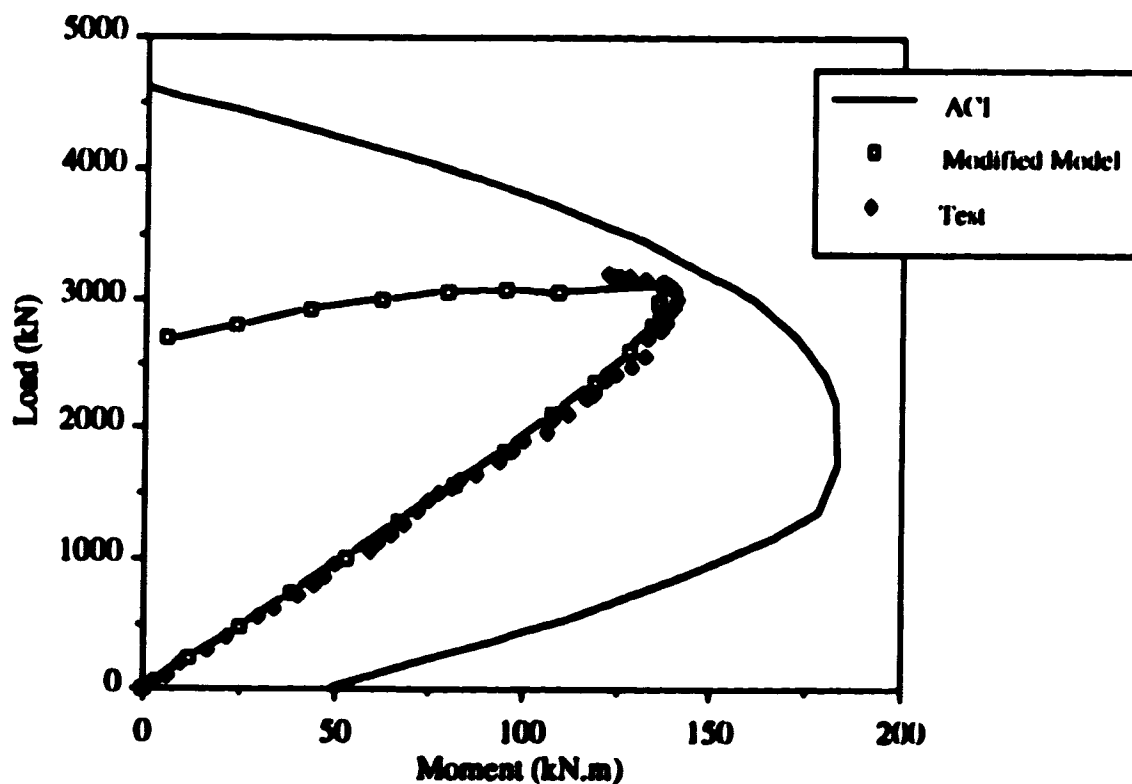


Figure 8.8 Test and the Calculated Behavior of the Modified Model for V7

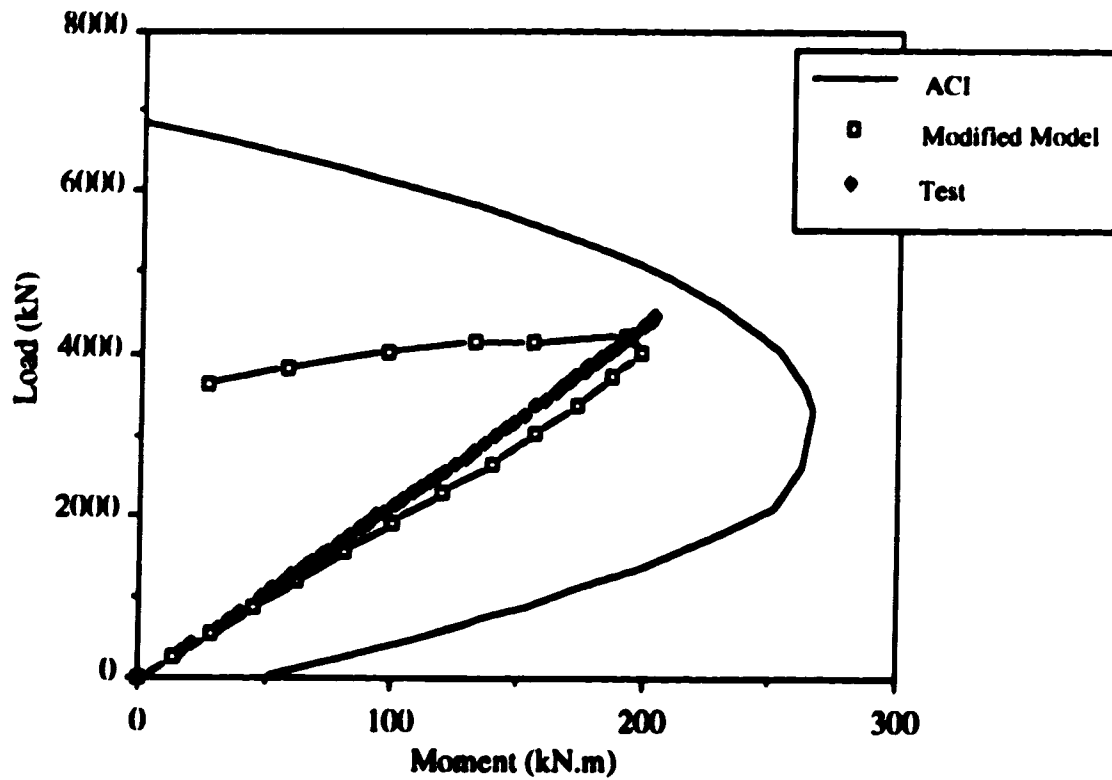


Figure 8.9 Test and the Calculated Behavior of the Modified Model for V8

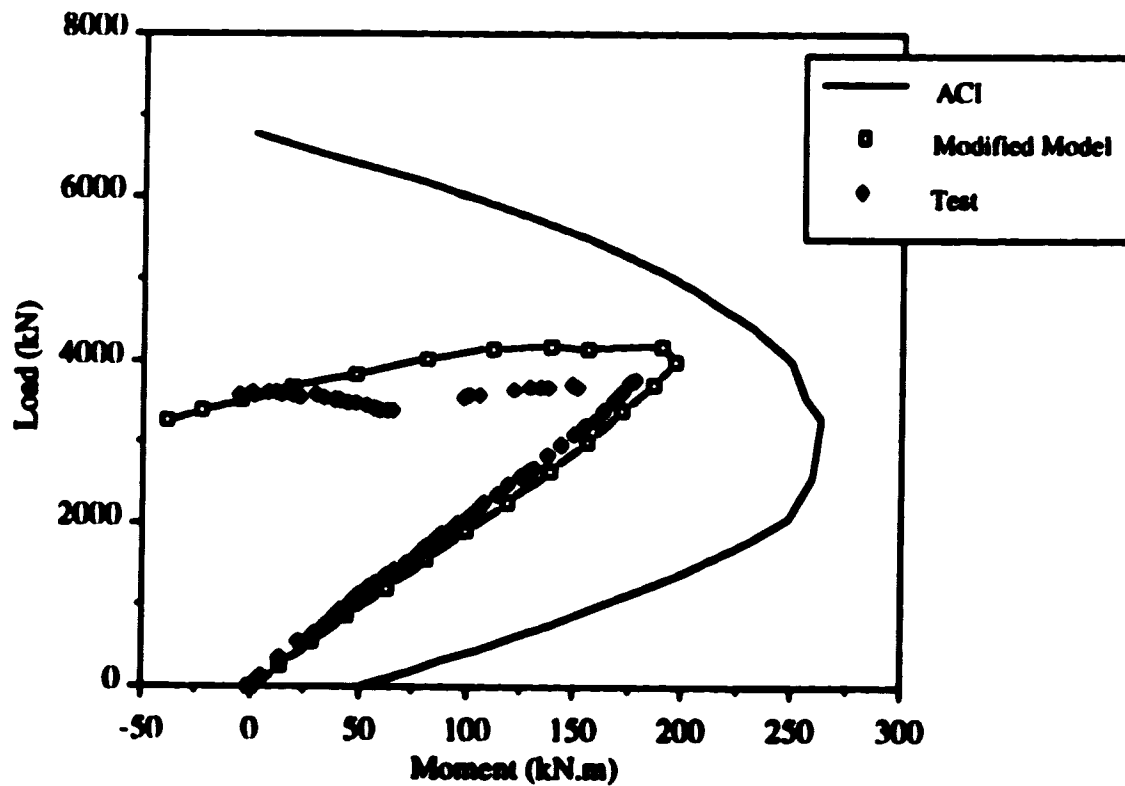


Figure 8.10 Test and the Calculated Behavior of the Modified Model for V11

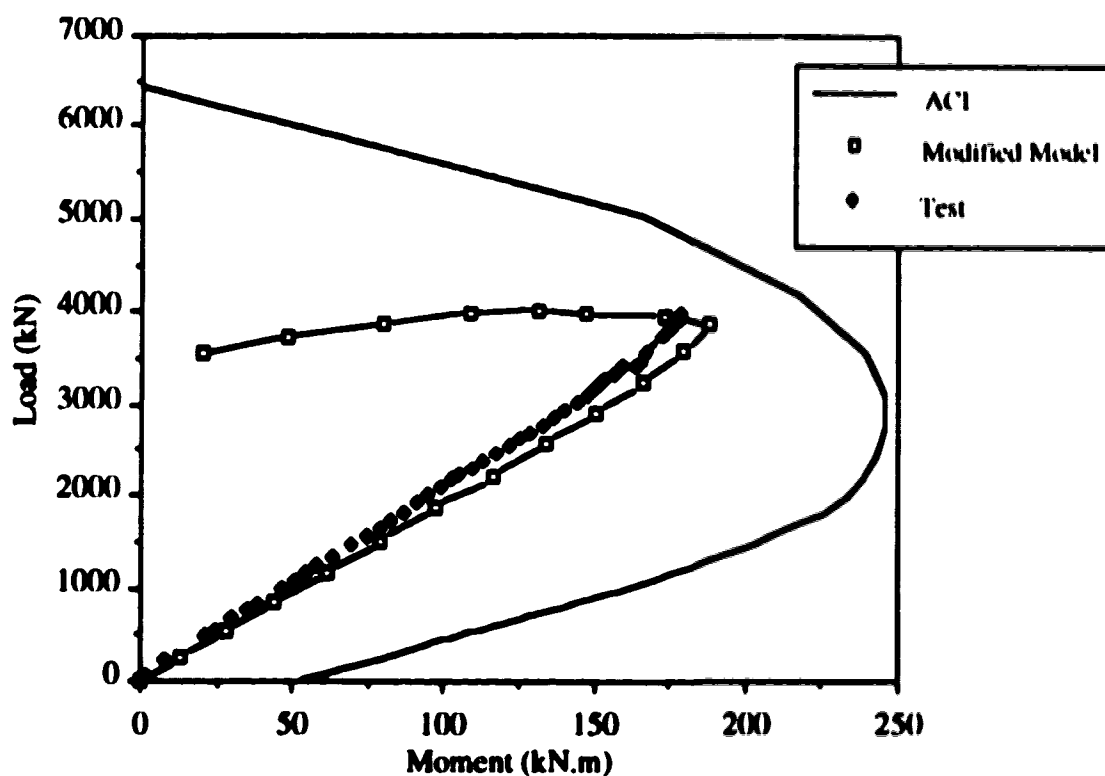


Figure 8.11 Test and the Calculated Behavior of the Modified Model for V12

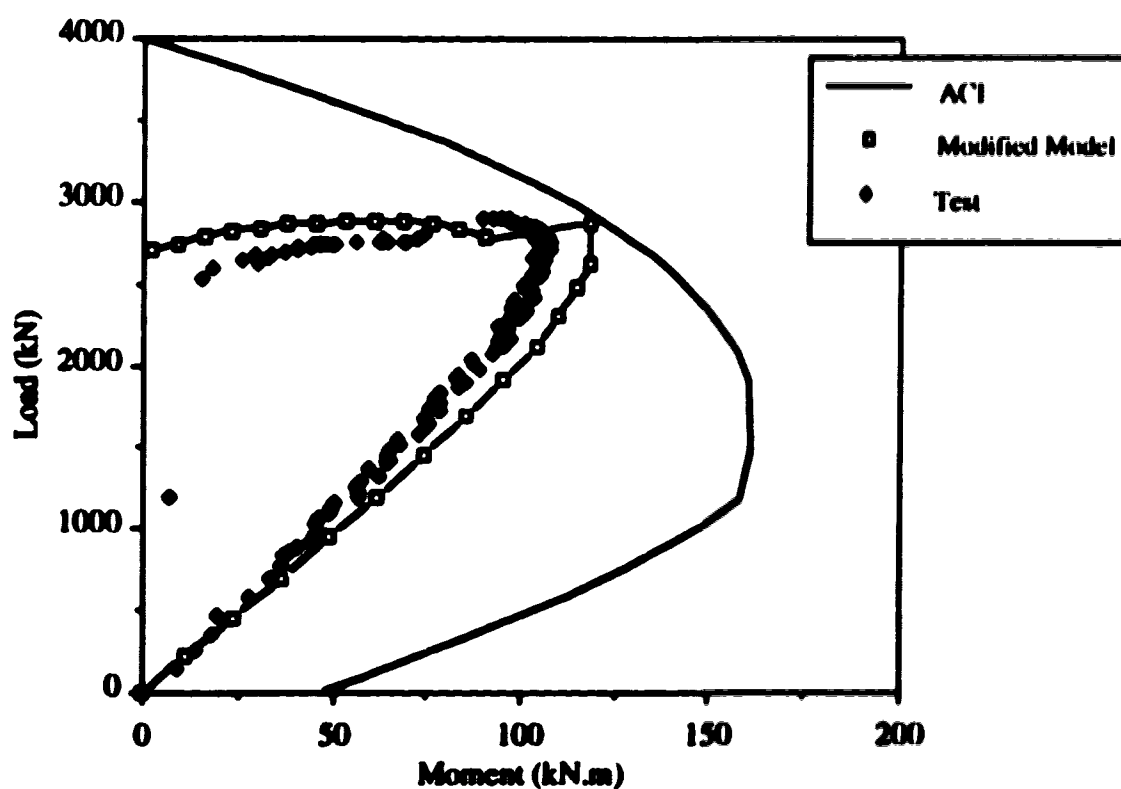


Figure 8.12 Test and the Calculated Behavior of the Modified Model for V13

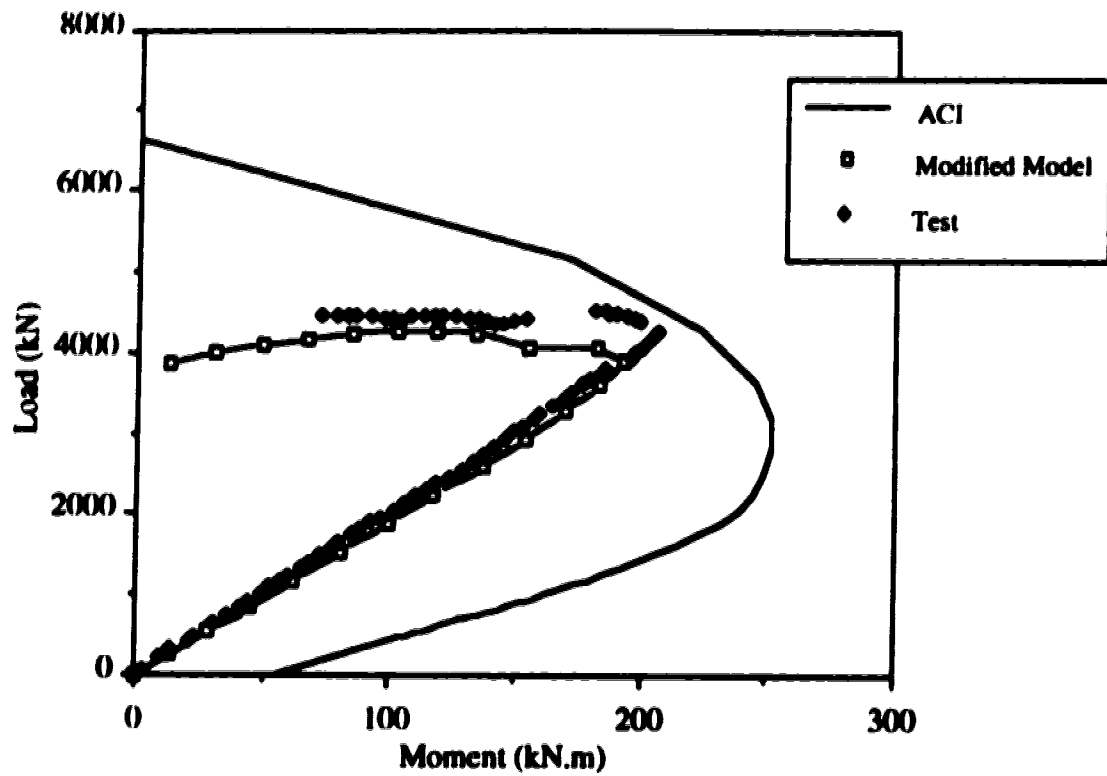


Figure 8.13 Test and the Calculated Behavior of the Modified Model for V15

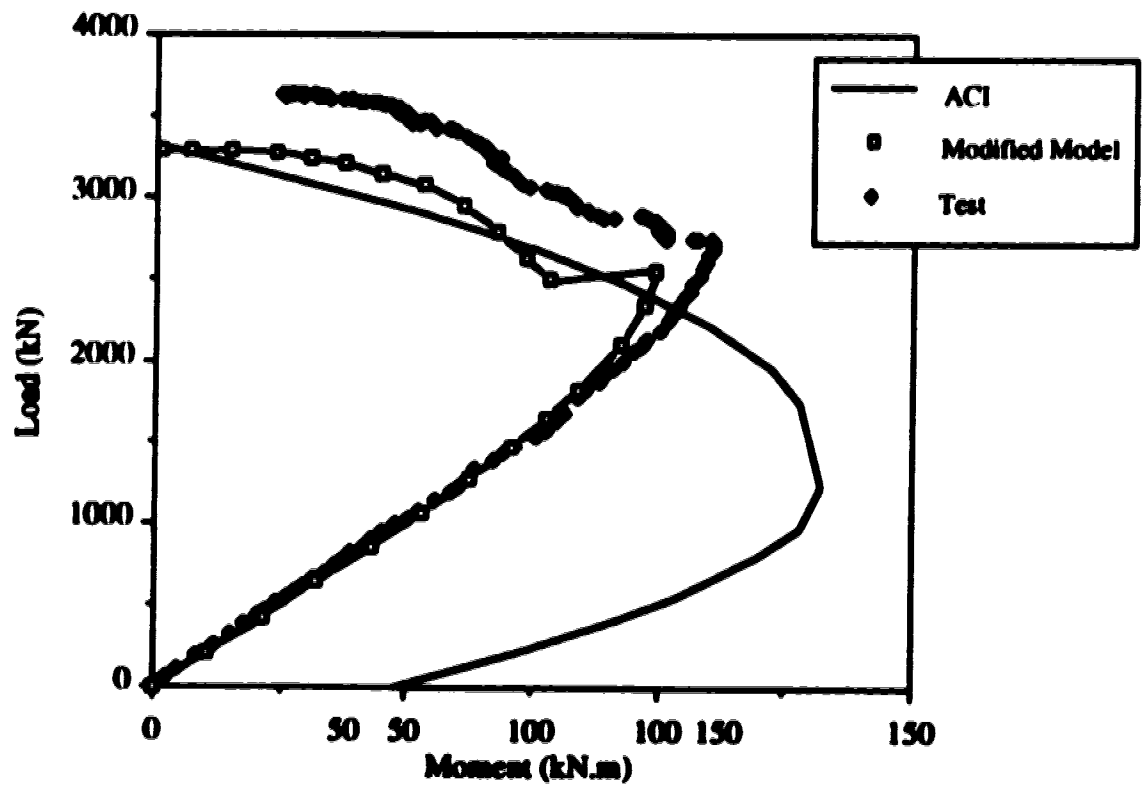


Figure 8.14 Test and the Calculated Behavior of the Modified Model for V16

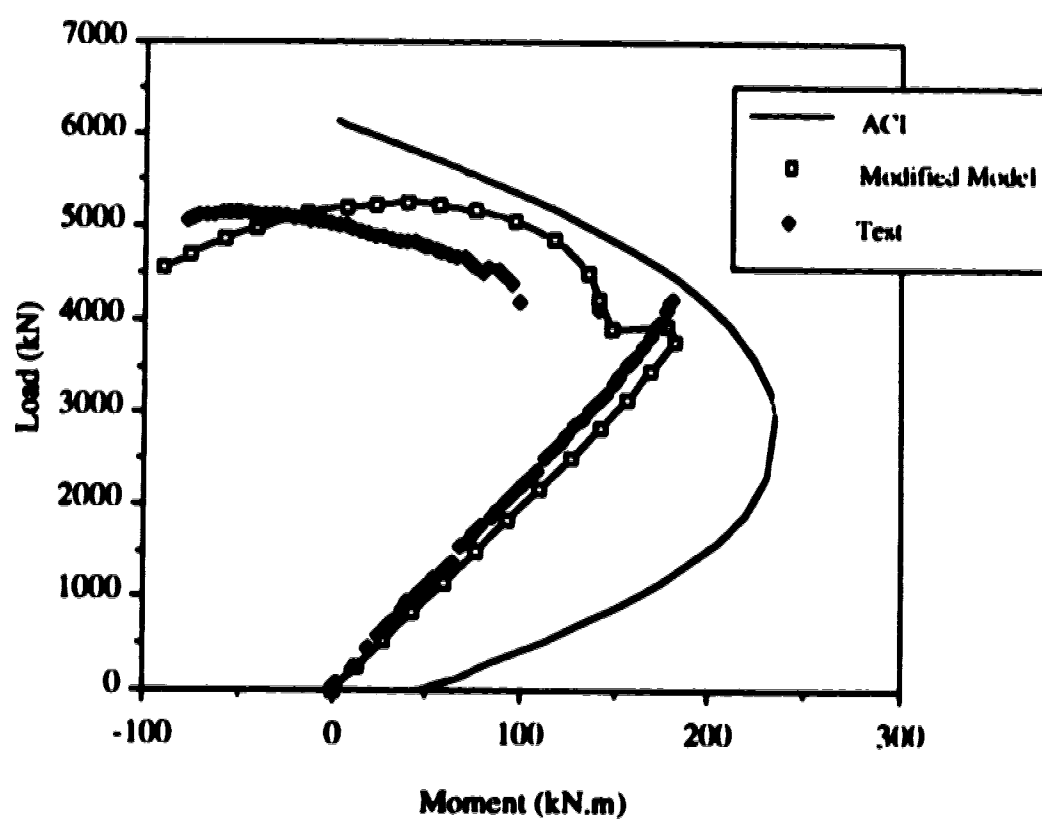


Figure 8.15 Test and the Calculated Behavior of the Modified Model for V17

9- Summary, Conclusions and Recommendations

9.1 Summary

The behavior of high strength concrete (HSC) and ultra high strength concrete (UHSC) columns subjected to axial loads with small eccentricities was investigated.

The experimental program had two phases. The first phase included tests of 15 rectangular cross-section specimens, 8 HSC specimens with f_c' ranging from 59.3 to 98.8 MPa, and 7 UHSC specimens with f_c' ranging from 121.1 to 127.7 MPa. The main parameters were concrete strength and confinement steel (diameter, spacing and volumetric ratio). The second phase included tests of 6 triangular cross-section specimens, 3 HSC specimens with f_c' ranging from 81 to 89.4 MPa, and 3 UHSC specimens with f_c' ranging from 117.8 to 130.6 MPa. The main parameters were concrete strength and confinement steel (spacing and volumetric ratio). The study was limited to relatively low longitudinal and confinement reinforcement ratios.

The columns were tested under the action of two applied loads in order to maintain zero strain at a predetermined point during each test. The design of the test was similar to the one originally adopted by Hognestad et al. (1955), with new added features by applying both loads in a stroke controlled manner rather than a load controlled manner and testing triangular compression zones. Using stroke control for both loads was important in order to obtain the post peak behavior of the specimens. All except two specimens, were tested with the neutral axis position maintained at one of the faces of the test region. Specimen V1 was tested with the neutral axis maintained at 161.5 mm outside the specimen, while specimen V2 was tested under constant eccentricity.

The analytical work included studying the flexural stress-strain relationships of HSC and UHSC sections and the effect of lateral confinement on the ductility of the section. The validity of the ACI rectangular stress block for the design of rectangular and triangular HSC and UHSC sections was investigated and new equations for the parameters of the ACI rectangular stress block are suggested. Different analytical models that describe the behavior of confined HSC sections were compared with the test results. A modification of one of these models which gives a better fit to the test data is suggested.

9.2 Conclusions

Despite the limited number of specimens tested (21) and the limited data, the following conclusions can be drawn from the results of this investigation and the discussion of the preceding chapters:

1- The plain concrete specimens showed a brittle failure. The failure of the UHSC specimens was more explosive than the HSC specimens. The triangular specimens showed less brittle failure with higher deformation capacity than the rectangular specimens. For same type of specimens the ultimate compressive strain was almost the same for different concrete strengths.

The assumption of linear strain distribution in compression zones was found to be true even for strain values that are very close to failure. Values of Poisson's ratio in the elastic range were comparable with those of low strength concrete.

2- The reinforced concrete specimens had different behavior depending on the amount of lateral reinforcement. The spacing of the ties and the volumetric ratio of the confinement steel were the main factors that affected the behavior of the reinforced concrete columns. Rectangular specimens with very light confinement reinforcement failed when the concrete cover spalled off with buckling of the longitudinal bars near the compression face. The deformation capacity of these specimens was close to that of the plain concrete specimens. Other specimens with more confinement steel had short and steep descending branches, however their failure was not explosive like the plain concrete specimens. Only the highly confined specimens showed a ductile descending behavior.

The UHSC rectangular specimens were less ductile than the HSC specimens with similar reinforcement, while opposite was true for triangular specimens. The UHSC triangular specimens were tested in older ages than the HSC specimens. The triangular specimens showed higher ductility than the rectangular specimens with the same degree of confinement. The constant eccentricity specimen failed at the peak load and did not exhibit any descending behavior.

3- The code recommendation for maximum tie spacing in non seismic regions was found to be too liberal for the design of HSC and UHSC sections. An eccentrically loaded column that is designed with the maximum tie spacing may have a sudden and brittle failure at the spalling of the concrete cover.

4- The flexural stress-strain curves of the reinforced rectangular specimens prior to spalling of the concrete cover were similar to the stress-strain curves of the plain concrete specimens with similar concrete strength. The curves of the HSC specimens had short descending branches while the curves of the UHSC specimens did not have descending branches.

The flexural stress-strain curves of the rectangular cross-sections were very similar to the cylinder stress-strain curves in the ascending part of the curves with an average value of K_3 of 0.92. A cylinder stress-strain curve with a peak stress equal to $0.85 f'_c$ can

conservatively represent the stress-strain curve of an eccentrically loaded column in the ascending part of loading. In the descending part of loading the behavior of the column is different and the cross-section of the column should be treated as a composite section consisting of the concrete cover and the concrete core.

The flexural stress-strain curves of the triangular specimens were not similar to the cylinder stress-strain curves in the ascending and descending branches. This may result from the fact the concrete at the tip of the triangular had only a small effect on the behavior of the section.

5- The stress-strain curves of the confined core could be obtained by subtracting the contribution of the concrete cover in the total applied loads and moments. The stress-strain curves of the confined core, for most of the specimens, did not show significant differences from that of the unconfined sections. Despite that the highly confined HSC specimen showed that, a well confined HSC core can exhibit very ductile stress-strain curves and reach a second peak at higher strain value.

6- The parameters that define the ACI rectangular stress block are not conservative for the design of rectangular or triangular HSC and UHSC sections. This conclusion is based on data from the tests reported here and previous tests of concentrically and eccentrically loaded columns.

New parameters for the rectangular stress block are suggested in Chapter 7. The new parameters are as conservative as the current ACI parameters for the design of low strength concrete sections. For HSC and UHSC sections the new parameters provide more conservative design than the current ACI parameters.

The limiting strain value as suggested by the code was found to be suitable for the design of HSC and UHSC sections. The triangular compression zones can even have higher limiting strain value than the rectangular compression zones.

7- The lateral confinement of the cross-section seems to have no effect on the maximum capacity of the section prior to spalling of the concrete cover. This conclusion is based on the results of the tests reported here only.

8- Three analytical models that describe the behavior of confined HSC columns overestimated the maximum capacity and ductility of the rectangular specimens. A proposed modification of one of the models gave reasonable accuracy in predicting the behavior of the HSC and UHSC rectangular specimens. The parameters of the modified

model are determined based on the concrete strength, section geometry and confining reinforcement.

9.3 Recommendations for Future Study

- 1- The number of tests for triangular compression zones included in this analysis was limited to 6 specimens. More tests of HSC and UHSC triangular section subjected to axial loads with small eccentricities is needed in order to be sure that the rectangular stress block is suitable for the design of these sections.
- 2- More tests are required to study the ductility of rectangular sections under combined axial load and bending. It is suggested that tests should be conducted on C-shaped specimens with a cross-section that does not have concrete cover. The existence of the concrete cover produces difficulties in the test control. It also produces difficulties in the analysis because the assumptions required to calculate the load carrying capacity of the cover could affect the accuracy of the analysis.
- 3- More work is needed to investigate the reasons why the HSC columns can suffer from early spalling of the concrete cover, as reported in some of previous column tests.

References

- Abeles, P.W., and others (1956), Discussion of a Paper by Hognestad et al. (1955), "Concrete Stress Distribuion in Ultimate Strength," ACI Journal, Disc. 52-28, Vol. 52, December, pp. 1305-1330.
- ACI Committee 363 (1984), "State of Art Report on High Strength Concrete," ACI Journal, Vol. 81, No. 4, July-August, pp. 364-411.
- ACI 318-89 "Building Code Requirements for Reinforced Concrete," ACI Committee 318, American Concrete Institute, Detroit, 1989, 353 pp.
- Ahmad, S.H., and Shah, S.P. (1982) "Stress-Strain Curves of Concrete Confined by Spiral Reinforcement," ACI Journal, Vol. 79, Nov.-Dec., pp. 484-490.
- Ahmad, S., and Shah, S.P. (1987), "High Strength Concrete - A Review," Utilization of High Strength Concrete, Proceedings, First International Symposium in Stavanger, Norway, pp. 255-268.
- Alca, N., and MacGregor, J.G. (1993), "Effect of Size on Flexural Behavior of High Strength Concrete Beams," M.A.Sc. Thesis, Structural Report No. 186, Department of Civil Engineering, University of Alberta, Edmonton, May, 93 pp.
- ASTM Standard C39-83b, "Standard Test Method of Compressive Strength of Cylindrical Concrete Specimens," American Society for Testing Materials, 1984, pp. 24-29.
- Bažant, Z.P., and Cedolin, L. (1991), "Stability of Structures: Elastic, Inelastic, Fracture, and Damage Theories," Oxford University Press, New York.
- Bjerkeli, L., Tomaszewicz, A., and Jensen, J.J. (1990), "Deformation Properties and Ductility of High Strength Concrete," Utilization of High Strength Concrete, Proceedings, Second International Symposium in Berkeley, California, pp. 215-238.
- CAN3-A23.3 M84, "Design of Concrete Structures for Building," Canadian Standard Association, Rexdale, Ontario, Canada, December, 1984, 280 pp.
- Carrasquillo, R.L., Nilson, A.H., and Slate, F.O. (1981), "Properties of High Strength Concrete Subject to Short-Term Loads," ACI Journal, Vol. 78, May-June, pp. 171-178.

Carreira, D.J., and Chu, K.H. (1985) "Stress-Strain Relationship for Plain Concrete in Compression," *ACI Journal*, Vol. 82, Nov.-Dece., pp. 797-804.

CEB/FIP Model MC90, Committee Euro-International du Beton, Bulletin d'Information No. 195 and 196, Lausanne, March, 1990, 348 pp.

CEB/FIP (1990), "High Strength Concrete State of the Art Report", CEB Bulletin d'Information No. 197, 61 pp.

Cole, D.G. (1967), "Some Mechanical Aspects of Compression Testing Machines," *Magazine of Concrete Research*, Vol. 19, No. 61, December, pp. 247-251.

Corley, M. (1966), "Rotational Capacity of Reinforced Concrete Beams," *J. Struct. Div., ASCE*, Vol. 92, ST5, October, pp. 121-146.

Cusson, D., and Paultre, P. (1992), "Behavior of High-Strength Concrete Columns Confined by Rectangular Ties under Concentric Loading," Department of Civil Engineering, University of Sherbrook, Report SMS-92/02, August, 39 pp.

Garcia, D.T., and Nilson, A.H. (1990), "A Comparative Study of Eccentrically Loaded High Strength Concrete columns," Research Report No. 90-2, Department of Civil Engineering, Cornell University, Ithaca, New York, January, 206 pp.

Hillerborg, A. (1988), "Fracture Mechanics Concepts Applied to Moment Capacity and Rotational Capacity of Reinforced Concrete Beams," *The International Conference on Fracture of Concrete and Rock*, Vienna, July 4-6, pp. 1-11.

Hognestad, E., Hanson, N.W., and McHenry, D. (1955), "Concrete Stress Distribution in Ultimate Strength Design," *ACI Journal*, Proceedings Vol. 52, Dec., pp. 455-479.

Høiseth, Hoff, and Jensen (1983), "Høyfast Betong," Delrapport 2. Søyler Under Sentrisk Last., SINTEF Report STF65 A83049.

Kaar, P.H., Hanson, N.W., and Capell, H.T. (1978a), "Stress-Strain Characteristics of High Strength Concrete," *ACI sp 55-7*, Douglas McHenry International Symposium on Concrete and Concrete Structures, ACI, Detroit, pp. 161-185.

Kaar, P.H., Fiorato, A.E., Carpenter, J.E., and Corley, W.G. (1978b), "Limiting Strains of Concrete Confined by Rectangular Hoops," *PCA, Research and Development Bulletin RD053.01D*, 12 pp.

- Kotsovos, M.D. (1982), "A Fundamental Explanation of the Behavior of Reinforced Concrete Beams in Flexure Based on the Properties of Concrete under Multiaxial Stress," *Materials and Structures, RILEM*, Vol. 15, No. 90, Nov.-Dec., pp. 529-537.
- Kotsovos, M.D. (1983), "Effect of Testing Techniques on the Post-Ultimate Behavior of Concrete in Compression," *Materials and Structures, RILEM*, Vol. 16, No. 91, January-February, pp. 3-12.
- Leslie, K.E., Rajagopalan, K.S., and Everard, N.J. (1976), "Flexural Behavior of High Strength Concrete Beams," *ACI Journal*, Vol. 73, No. 9, Sept., pp. 517-521.
- Lessard, M., Chaallal, O., and Aitcin, P.C. (1993), "Testing High Strength Concrete Compressive Strength," *ACI Material Journal*, Vol. 90, No. 4, July-August, pp. 303-308.
- Loov, R. (1991), "A General Stress Strain Curve for Concrete - Implications for High Strength Concrete Columns," *CSCE Annual Conference, Vancouver*, pp. 302-311.
- MacGregor, J.G. (1992), "Reinforced Concrete Mechanics and Design," Second Edition, Prentice Hall, Englewood Cliffs, New Jersey.
- Martinez, S., Nilson, A.H., and Slate, F.O. (1982), "Short-Term Mechanical Properties of High-Strength Light-Weight Concrete," Department Report No. 82-9, Structural Engineering Department, Cornell University, Ithaca, New York, August, 98 pp.
- Martinez, S. (1983), "Spirally Reinforced High Strength Concrete Columns," PhD Thesis, Cornell University, Ithaca, New York, January.
- Mattock, A.H., and Kriz, L.B. (1961), "Ultimate Strength of Nonrectangular Structural Concrete Members," *ACI Journal*, Vol. 57, January, pp. 737-765.
- Muguruma, H., Watanabe, F., Iwashimizu, T., and Mitsueda, R. (1983), "Ductility Improvement of High Strength Concrete by Lateral Confinement," *Trans., Japan Concrete Institute*, Vol. 5, pp. 403-410.
- Muguruma, H., Watanabe, F., and Komuro, T. (1989), "Applicability of High Strength Concrete to Reinforced Concrete Ductile Column" *Trans., Japan Concrete Institute*, Vol. 11, pp. 309-316.
- Nedderman, H. (1973), "Flexural Stress Distribution in Very High Strength Concrete," M.A.Sc. Thesis, Department of Civil Engineering, University of Texas, Arlington.

- NS 3473 (1989), "Norwegian Standard for Design of Concrete Structures," The Norwegian Council for Building Standardisation, N.B.R., Oslo, Norway.
- Park, R., Priestley, M.J.N., and Gill, W.D. (1982), "Ductility of Square-Confined Concrete Columns," J. Struct. Div. , ASCE, Vol. 108, ST4, April, pp. 929-950.
- Pastor, J.A. (1985), "High Strength Concrete Beams," PhD Thesis, Cornell University, Ithaca, New York.
- Polat, M.B. (1992), "Behavior of Normal and High Strength Concrete under Axial Compression," M.A.Sc. Thesis, Department of Civil Engineering, University of Toronto, 175 pp.
- Prentis, J.M. (1951), "The Distribution of Concrete Stress in Reinforced and prestressed Concrete Beams when Tested to Destruction by a Pure Bending Moment," Magazine of Concrete Research, Vol. 2, No. 5, January, pp. 73-77.
- Priestley, M.J.N., Park, R., and Potangaroa, R.T. (1981), "Ductility of Spirally-Confined Concrete Columns," J. Struct. Div. , ASCE, Vol. 107, ST1, January, pp. 181-202.
- Rak MK4 (1989), "National Building Code of Finland, Concrete Structures," Concrete Association of Finland.
- Richart, F.E., Brandtzaeg, A., and Brown, R.L. (1929), "The Failure of Plain and Spirally Reinforced Concrete in Compression," University of Illinois Engineering Experiment Station, Bulletin No. 190, Urbana, April, 73 pp.
- Richart, F.E., and Brown, R.L. (1934), "An Investigation of Reinforced Concrete Columns," University of Illinois Engineering Experiment Station, Bulletin No. 267, Urbana, June, 91 pp.
- Richart, F.E., Driffin, J.O., Olson, T.A., and Heitman, R.H. (1947), "The Effect of Eccentric Loading, Protective Shells, Slenderness Ratio, and Other Variables in Reinforced Concrete Columns," University of Illinois Engineering Experiment Station, Bulletin No. 368, Urbana, November, 128 pp.
- RILEM Draft Recommendation (1985), "Determination of the Fracture Energy of Mortar and Concrete by Means of Three-Point Bend Tests on Notched Beams," Submitted by

50FMC Committee, Fracture Mechanics of Concrete, Materials and Structures, RILEM, Vol. 18, No. 106, July-August, pp. 285-290.

Rokugo, K., Ohno, S., and Koyanagi, W. (1986), "Automatical Measuring System of Load-Displacement Curves Including Post-Failure Region of Concrete Specimens," Fracture Toughness and Fracture Energy of Concrete, Edited by F.H. Wittmann, Elsevier Science Publishers B.V., Amsterdam, pp. 403-411.

Rüsch, H. (1955), "Tests on the Strength of the Flexural Compression Zone," Bulletin No. 120, Deutscher Ausschuss Für Stahlbeton, Berlin, 94 pp.

Rüsch, H. (1960), "Researches Toward a General Flexural Theory for Structural Concrete," ACI Journal, Proceedings Vol. 57, July, pp. 1-28.

Sargin, M. (1971), "Stress-Strain Relationships for Concrete and the Analysis of Structural Concrete Sections," Study No. 4, Solid Mechanics Division, University of Waterloo, Waterloo, Ontario, Canada.

Sargin, M., Ghosh, S.K., and Handa, V.K. (1971), "Effects of Lateral Reinforcement upon the Strength and Deformation Properties of Concrete," Magazine of Concrete Research, Vol. 23, No. 75-76, June-September, pp. 99-110.

Schade, J.E. (1992), "Flexural Concrete Stress in High Strength Concrete Columns," M.A.Sc Thesis, Department of Civil Engineering, University of Calgary, Calgary, Alberta, September, 156 pp.

Shah, S.P., Fafitis, A., and Arnold, R. (1983), "Cyclic Loading of Spirally Reinforced Concrete," J. Struct. Div., ASCE, Vol. 109, No. 7, July, pp. 1695-1709.

Sheikh, S.A., and Uzumeri, S.M. (1980), "Strength and Ductility of Tied Concrete Columns," J. Struct. Div., ASCE, Vol. 106, ST5, May, pp. 1079-1102.

Sheikh, S.A., and Uzumeri, S.M. (1982), "Analytical Model for Concrete Confinement in Tied Columns," J. Struct. Div., ASCE, Vol. 108, ST12, December, pp. 2703-2722.

Smith, R.G., and Orangun, C.O. (1969), "Evaluation of the Stress-Strain Curve of Concrete in Flexural Using Method of Least Squares," ACI Journal, Vol. 66, July, pp. 553-559.

Soliman, M.T.M., and Yu, C.W. (1967), "The Flexural Stress-Strain Relationship of Concrete Confined by Rectangular Transverse Reinforcement," Magazine of Concrete Research, Vol. 19, No. 61, December, pp. 223-238.

Sundararaj, P. (1991), "High Strength Concrete Columns Under Eccentric Load," M.A.Sc Thesis, Department of Civil Engineering, University of Toronto, 261 pp.

Swartz, S.E., Nikaeen, A., Narayan Babu, H.D., Periyakaruppan, N., and Refai, T.M.E. (1985), "Structural Bending Properties of High Strength Concrete," ACI sp 87-9, American Concrete Institute, Detroit, pp. 147-178.

Thorenfeldt, E., Tomaszewicz, A., and Jensen, J.J. (1987), "Mechanical Properties of High Strength Concrete and Application in Design," Utilization of High Strength Concrete, Proceedings, First International Symposium in Stavanger, Norway, pp. 149-159.

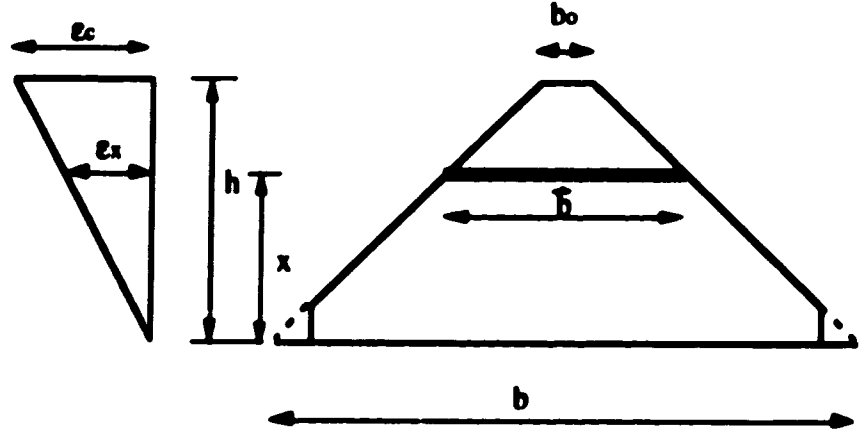
Vallenas, J., Bertero, V.V., and Popov, E.P. (1977), "Concrete Confined by Rectangular Hoops and Subjected to Axial Loads," Report No. UCB/EERC-77/13, Earthquake Engineering Research Center, University of California, Berkeley, Calif.

van Mier, J.G.M. (1986), "Multiaxial Strain-Softening of Concrete," Part I: Fracture, Materials and Structures, RILEM, Vol. 19, No. 111, May-June, pp. 179-190.

Wang, P.T., Shah, S.P., and Naaman, A.E. (1978), "Stress-Strain Curves of Normal and Lightweight Concrete in Compression," ACI Journal, Vol. 75, November, pp. 603-611.

Yong, Y.K., Nour, M.G., and Nawy, E.G. (1988), "Behavior of Laterally Confined High-Strength Concrete under Axial Loads," J. Struct. Div., ASCE, Vol. 114, No. 2, February, pp. 332-351.

Appendix A
Derivation of Equations 5.9 and 5.10 for Triangular Specimens



$$\frac{e_x}{e_c} = \frac{x}{h} \quad (\text{A-1})$$

$$dx = \frac{h}{e_c} de_x \quad (\text{A-2})$$

$$\bar{b} = b_0 + 2(h - x) = b_0 + 2h \left(1 - \frac{e_x}{e_c} \right) = (b_0 + 2h) - 2h \frac{e_x}{e_c} \quad (\text{A-3})$$

The load and moment equations can be written as follows:

$$C = \int_0^h f(e_x) \bar{b} dx = f_0 \left(\frac{b_0 + b}{2} \right) h = f_0 A \quad (\text{A-4})$$

$$M = \int_0^h f(e_x) \bar{b} x dx = m_0 \left(\frac{b_0 + b}{2} \right) h^2 = m_0 Ah \quad (\text{A-5})$$

By substituting Equations (A-2) and (A-3) into Equations (A-4) and (A-5), the following equations are obtained

$$C = \int_0^{e_c} f(e_x) \left((b_0 + 2h) - 2h \frac{e_x}{e_c} \right) \frac{h}{e_c} de_x = f_0 A \quad (\text{A-6})$$

$$M = \int_0^{e_c} f(e_x) \left((b_0 + 2h) - 2h \frac{e_x}{e_c} \right) \frac{h^2}{e_c^2} e_x de_x = m_0 Ah \quad (\text{A-7})$$

By rearranging and differentiating the load equation with respect to e_c , the following expressions are obtained

$$\frac{h(b_0 + 2h)}{e_c} \int_0^{\frac{e_c}{h}} f(e_x) de_x - \frac{2h^2}{e_c^2} \int_0^{\frac{e_c}{h}} f(e_x) e_x de_x = f_0 A \quad (A-8)$$

$$-\frac{h(b_0 + 2h)}{e_c^2} \int_0^{\frac{e_c}{h}} f(e_x) de_x + \frac{h(b_0 + 2h)}{e_c} f_c + \frac{4h^2}{e_c^3} \int_0^{\frac{e_c}{h}} f(e_x) e_x de_x - \frac{2h^2}{e_c} f_c = \frac{df_0}{de_c} A \quad (A-9)$$

$$\frac{boh}{e_c} f_c - \frac{h}{e_c^2} \int_0^{\frac{e_c}{h}} f(e_x) \left((b_0 + 2h) - 2h \frac{e_x}{e_c} \right) de_x + \frac{2h^2}{e_c^3} \int_0^{\frac{e_c}{h}} f(e_x) e_x de_x = \frac{df_0}{de_c} A \quad (A-10)$$

$$\frac{boh}{e_c} f_c - \frac{1}{e_c} f_0 A + \frac{2h^2}{e_c^3} \int_0^{\frac{e_c}{h}} f(e_x) e_x de_x = \frac{df_0}{de_c} A \quad (A-11)$$

$$f_c = \frac{A}{boh} \left(f_0 + \frac{df_0}{de_c} e_c \right) - \frac{2h}{boh^2} \int_0^{\frac{e_c}{h}} f(e_x) e_x de_x \quad (A-12)$$

By rearranging and differentiating the moment equation with respect to e_c in the same way as has been done for the load equation, the following expressions are obtained

$$\frac{h^2}{e_c^2} (b_0 + 2h) \int_0^{\frac{e_c}{h}} f(e_x) e_x de_x - \frac{2h^3}{e_c^3} \int_0^{\frac{e_c}{h}} f(e_x) e_x^2 de_x = m_0 Ah \quad (A-13)$$

$$-\frac{2h^2}{e_c^3} (b_0 + 2h) \int_0^{\frac{e_c}{h}} f(e_x) e_x de_x + \frac{h^2}{e_c} (b_0 + 2h) f_c + \frac{6h^3}{e_c^4} \int_0^{\frac{e_c}{h}} f(e_x) e_x^2 de_x - \frac{2h^3}{e_c} f_c = \frac{dm_0}{de_c} Ah \quad (A-14)$$

$$-\frac{2h^2}{e_c^3} \int_0^{\frac{e_c}{h}} f(e_x) \left((b_0 + 2h) - 2h \frac{e_x}{e_c} \right) e_x de_x + \frac{boh^2}{e_c} f_c + \frac{2h^3}{e_c^4} \int_0^{\frac{e_c}{h}} f(e_x) e_x^2 de_x = \frac{dm_0}{de_c} Ah \quad (A-15)$$

$$-2m_0 \frac{Ah}{e_c} + \frac{boh^2}{e_c} f_c + \frac{2h^3}{e_c^4} \int_0^{\frac{e_c}{h}} f(e_x) e_x^2 de_x = \frac{dm_0}{de_c} Ah \quad (A-16)$$

$$f_c = \frac{A}{boh} \left(2m_0 + \frac{dm_0}{de_c} e_c \right) - \frac{2h}{boh^3} \int_0^{\frac{e_c}{h}} f(e_x) e_x^2 de_x \quad (A-17)$$

Equations (A-12) and (A-17) are used to calculate the stress-strain curve for the triangular cross-section. These equations follow the basic assumptions that were used to derive the equations of the rectangular cross-sections (see Section 5.2.1). Since the equations have integration terms that include the stress and the strain, a certain shape for the stress-strain relationship that can be integrated should be assumed. In the same time the experimental values for f_0 and m_0 should be fitted into regression equations that have the same shape and order of the equation assumed for the stress-strain relationship.

Appendix B
Procedures for Obtaining the Stress-Strain Curves
of the Rectangular Cross-Sections

- 1- Input the following test data, prior to spalling of the concrete cover, into a work sheet :
 - a- The applied loads P_1 , P_2
 - b- Average strain at the compression face
 - c- Deflection measurements at loading points and mid section of the specimen
- 2- Calculate the total applied loads and the moment about the neutral axis for the mid section of the specimen using the data from Step (1).
- 3- Calculate the force carried by each reinforcement bar using the strain values calculated at the center line of the bar and the load-strain curve obtained from tension tests of specimens taken from the bars used.
- 4- Calculate the quantities f_o and m_o as explained in Equations (5.5) and (5.6).
- 5- Use polynomial equations to fit the experimental data of the quantities f_o and m_o . In this step polynomial equations with different orders were tried and the equations that gave the best fit to the experimental data were chosen.
- 6- Calculate the stress-strain curves using the fitted data for f_o and m_o as explained in Equations (5.3) and (5.4).
- 7- Modify the force carried by the reinforcement bars by subtracting the force that could be carried if the same area of the bar was occupied by concrete using the stress-strain curves obtained from Step (6).
- 8- Repeat Steps (4 to 6) using the modified values from Step (7) to obtain the stress-strain curves of the specimen.

Appendix C
Data from Eccentrically Loaded Plain and Reinforced Concrete Columns

No.	f'_c (MPa)	$K_1 K_3$	K_2	Remarks
1	5.3	1.052	0.487	PCA Test Series By Hognestad et al. (1955). on Plain Concrete C-Shaped Specimens with Cross-Section Dimensions of (127x203.2 mm)
2	9.9	0.91	0.484	
3	11.6	0.954	0.483	
4	11.6	0.903	0.473	
5	15.1	0.877	0.48	
6	19.8	0.819	0.442	
7	20.5	0.806	0.455	
8	21.1	0.897	0.433	
9	25.8	0.742	0.477	
10	26.9	0.80	0.484	
11	31.6	0.761	0.432	
12	35.6	0.729	0.452	
13	36.9	0.632	0.442	
14	37.8	0.716	0.471	
15	39.6	0.671	0.413	
16	41.9	0.642	0.416	
17	44.7	0.65	0.394	
18	45.0	0.65	0.418	
19	46.7	0.645	0.406	
20	52.1	0.632	0.374	
21	52.7	0.652	0.406	
22	70.8	0.568	0.394	
23	71.9	0.555	0.381	

No.	f_c' (MPa)	K_1K_3	K_2	Remarks
1	10.0	0.868	0.452	Eccentric Compression Tests By Rüsch (1955), on Plain Concrete Prisms
2	18.7	0.813	0.419	
3	23.6	0.816	0.416	
4	30.9	0.787	0.41	
5	32.2	0.761	0.407	
6	36.5	0.768	0.394	
7	48.2	0.697	0.365	
8	55.4	0.71	0.374	
1	95.5	0.59	0.37	Test Series By Nedderman (1973), on Plain Concrete C-Shaped Specimens with Cross-Section Dimensions of (127x203.2 mm)
2	95.5	0.55	0.39	
3	96.6	0.61	0.37	
4	97.6	0.59	0.38	
5	79.3	0.57	0.34	
6	89.4	0.58	0.36	
7	85.7	0.58	0.36	
8	83.1	0.56	0.38	
9	84.1	0.55	0.38	
1	57.9	0.855	0.41	Test Series By Swartz et al. (1985), on Plain Concrete C-Shaped Specimens with Cross-Section Dimensions of (127x127 mm)
2	64.8	0.657	0.37	
3	66.8	0.508	0.35	
4	66.8	0.70	0.41	
5	66.8	0.69	0.41	
6	77.1	0.745	0.43	
7	77.1	0.698	0.37	
8	77.1	0.721	0.37	
9	77.1	0.611	0.34	

No.	f'_c (MPa)	K_1K_3	K_2	Remarks
1	44.8	0.76	0.45	PCA Test Series By Kaar et al. (1978a), on Plain Concrete C-Shaped Specimens with Cross-Section Dimensions of (127x203.2 mm)
2	47.6	0.72	0.45	
3	58.4	0.65	0.39	
4	71.8	0.63	0.37	
5	64.7	0.64	0.36	
6	78.2	0.69	0.36	
7	96.5	0.58	0.34	
8	91.6	0.71	0.37	
9	45.3	0.72	0.42	
10	48.9	0.66	0.42	
11	58.1	0.61	0.40	
12	67.7	0.62	0.38	
13	69.6	0.62	0.41	
14	77.1	0.71	0.36	
15	88.7	0.59	0.38	
16	102.4	0.62	0.36	
17	77.8	0.64	0.37	
18	87.5	0.64	0.36	
19	94.5	0.59	0.38	

No.	f_c' (MPa)	K_1K_3	K_2	Remarks
1*	105.9	0.560	0.357	U of C Test Series By Schade (1992), on Plain and Reinforced Concrete C-Shaped Specimens with Cross-Section Dimensions of (250x250 mm)
2	105.9	0.604	0.357	
3	105.9	0.576	0.355	
4	105.9	0.609	0.365	
5	105.9	0.599	0.360	
6	105.9	0.603	0.365	
7	109.6	0.636	0.349	
8	109.6	0.627	0.351	
9	109.6	0.652	0.371	
10	109.6	0.640	0.360	
11	109.6	0.631	0.358	
12*	109.6	0.587	0.365	

1- (*) Column (1) and Column (12) were discarded in the original report because their strain readings could not be explained and did not fit into the other test results. They had the lowest total load readings. These values were included in this study.

2- Column 1-6 were plain concrete specimens cast from the same concrete mix.

3- Column 7-12 were reinforced concrete specimens cast from the same concrete mix.

END

2 8 1 0 8 1 9 6

FIN